Max-Planck-Institut für Kolloid and Grenzflächenforschung

Complex Bioactive Fiber Systems by Means of Electrospinning

Dissertation
zur Erlangung des akademischen Grades
"doctor rerum naturalium"
(Dr. rer. nat.)
in der Wissenschaftsdisziplin "Kolloidchemie"

eingereicht an der
Mathematisch-Naturwissenschaftlichen Fakultät
der Universität Potsdam

von

Rafael Gentsch

Potsdam, im April 2010

Table of content

1 Introduction

The increase of life expectancy is an achievement of today's welfare and recent developments in the health sector. However, this prolongation of life led to an increased physical stress on the human body. Therefore, a growing need for the replacement of nonfunctional and damaged tissues or organs has arisen. The annual health care costs in the United States related to tissue loss and end-stage organ failure exceed US$400 billion.[1] The utilization of living tissue/organ is a strategy, nevertheless, it is not practical as only limited numbers of adequate donors are available. Conventional implants and vascular grafts are another possible alternatives, but their usage, as of yet, is normally restricted between 5 to 15 years. In addition, there are still several tissues which cannot be replaced adequately, i.e. central nerve system. Nowadays, only limited numbers of tissue replacements are commercially available such as artificial skin for severe body burns, cartilage, bone or pancreas. In this context, tissue engineering, a relatively new concept, arrose which deals with the *in vitro* culture of cells within an artificial three-dimensional (3D) scaffold.[1]

Modern approaches towards 3D materials with bioactive interfaces are increasingly important not only for tissue engineering, but also for production of biointegrated materials and biomimetic materials. Advances in understanding how materials passively interact or actively communicate with biological systems via designed material-biology interfaces demand precise means to fabricate macroscopic and nano-structured materials. Recently, modern materials and technology platforms are developed to produce bioactive scaffolds, providing spatial control of mechanical, chemical and biochemical signals at the biointerface in combination with tailored pore architecture and surface topology.

Fibrous scaffolds, in particular, which cover different length scales seem to be very promising in that respect since these provide a natural or biomimetic environment for biological systems. In addition such structures provide inherently an interconnected pore system, which is beneficial for cell infiltration and waste/nutrient transport. In this context, electrospinning is a powerful tool to produce fiber webs from different materials. While conventional fiber fabrication methods (e.g. conventional extrusion) spin fibers in the micrometer range, electrospinning is able to obtain submicron to nanometer-sized fibers. Such meshes composed of nanofibers are very attractive for tissue engineering as they fit the dimensions of the extracellular matrix and therefore are believed to provide the proper physical cues for tissue regrowth. However, the cellular infiltration and vascularization of such fiber meshes remain a difficult task.

The scope of this thesis was to establish straightforward approaches to fabricate complex structures fabricated by electrospinning, which are structurally and chemically bioactive, to allow cell infiltration. The first part addresses the control of the mesh porosity. A new approach to obtain bimodal structures composed of micro and nanofibers is introduced. Its characterization and comparison with conventional micro and nanofibers is then evaluated. These meshes were used as matrices for fiber directed crystallization and for investigation of the cell ingrowth for biomedical applications. A second part expounds on fiber functionalization strategies to decorate the fiber surface with biomolecules such as peptides and sugars. A hybrid-conjugate molecule (peptide-block-polymer) is blended with a commodity polymer for electrospinning fibers where the peptide part of the conjugate is surface segregated by means of demixing and interface stabilization. In addition, a modular approach to create functional fibers is developed. A one-step process is shown to generate fiber meshes with reactive fibers, which are functionalized in a second step with peptide and sugar molecules for potential biomedical applications.

2 Basic principles

2.1 Bioactive nanostructures

Precisely controlling the interface between synthetic materials and biological systems might be one of the most important, but also most demanding tasks of modern materials sciences. The resulting opportunities will however assure progress in several research areas, ranging from medical technology (e.g. implantation medicine), tissue engineering, regenerative cell biology, stem cell research, toward biointegrated materials design as well as bio-assisted compound synthesis.[2-6] To rationally design materials that actively interact with biological systems to guide or even dynamically communicate with biological entities such as cells or tissues requires a high level of structural and functional control.

Fundamental research that focused on planar interfaces reveals the applicability of basic concepts of bioadhesion and functional signaling in two dimensions.[7-9] Despite this progress, biological systems are three dimensional in nature and moreover exhibit often hierarchical organization levels.[10, 11] This makes the spatial control of surface structure, pore architecture, mechanical properties and functionality as well as of complex functions mandatory (Figure 2.1).[6] Cells are roughly 10-100 µm in size. Cell sensing takes place with about 5-10 nanometer precision and signaling (cell communication) can follow multidimensional concentration gradients with nanometer accuracy.[7] Hence cells are sensitive to chemistry and topography on the meso-, micro-, and nanoscale.[12] It is exactly the range of length scales which makes materials design at the interface to biology an exciting, but also highly complex task.

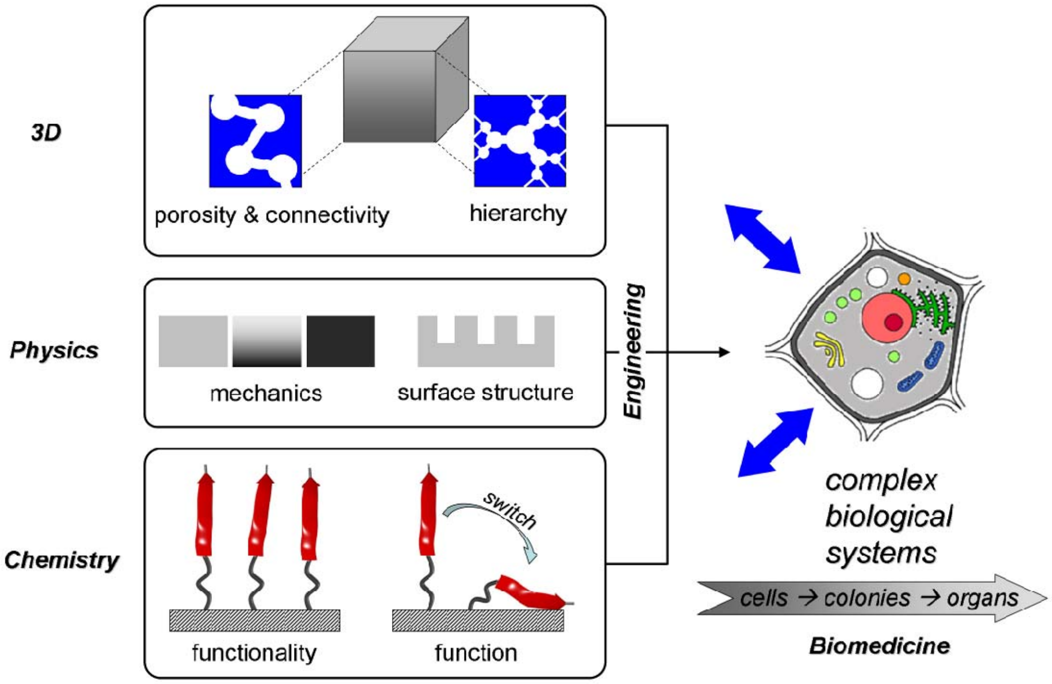

Figure 2.1. Constructing scaffolds to mimic the microenvironment of cells in biological systems is a complex task because engineering of chemistry (bioactivity), physics (mechanics, roughness) and 3D control over the pore system (pore size, connectivity, hierarchy) is required.

Initial approaches focused on the design of macroscopic material scaffolds to provide cell support, which matches the dimensions of organs. However, the importance of the nano scale structure has been underestimated for a long time. The significance of the nanoscopic dimension has been set into focus by progressively understanding the structure, functionality and function of the extracellular matrix (ECM).[10, 13] Cells in complex biological systems exist in a highly fiber structured environment. The ECM provides not only mechanical support, but also directional orientation to the cells and thus presents an instructive grid. The fiber structures of the ECM are mainly composed of proteins of the collagen type.[14] For instance type II collagen is accounting for about 90-95% of the matrix collagen. Its high ratio of carbohydrate groups leads to rather polar fibrillar nanostructures. Other collagen types are present in the ECM, too. Sometimes they are enriched at specific regions, but the function is often not fully understood.[15]

The fibrils are embedded into an elastin network to modulate mechanical properties of the ECM. The interfibrillar spaces within the matrix are filled to a large extend with proteoglycans, which are macromolecules composed of about 5% proteins and 95% polysaccharides.[16] No covalent bonds between the collagen fibers, and proteoglycans, or hyaluronic acids are found. However, ECM viscoelasticity is adjusted by these molecules, as proteoglycans and hyaluronic acids regulate water balance and osmotic pressure within the ECM. Besides these main constituents, the ECM consists of a multitude of other proteins, e.g. adhesion proteins such as fibronectins[17] or laminins[18] as well as of growth factors[19] and low molecular weight compounds that are exchanged with adjacent cells to realize cell communication.[20] Thus, a highly defined and very specific three dimensional microenvironment is created. This is considered to be essential to ensure the function of cells, cell colonies, tissues and complete organs from the early embryogenesis toward adult repair of damaged tissues.[21] The extracellular matrix supports and directs the adhesion and migration of cells. Moreover, the ECM contacts influence cells deeply on their regulatory processes on the metabolism level.

To mimic the complex environment of the ECM the production of macroscopic-nanostructured materials is mandatory. In these synthetic systems mechanical properties, porosity, pore connectivity, and functionality should be spatially controlled. Ideally, those parameters should be locally adaptable with high precision to meet the requirements of cells, tissues up to full organs. The 3D control of functionality in nanostructured materials is still posing difficulties in materials design and synthesis. However, research addressing planar bio-interfaces, progressively elucidates the mechanisms of ligand positioning, ligand surface densities, synergistic ligand clustering as well as the precise biological responses of cells toward those positional functionalities.[22-24] Taking into account that the micro environment of the ECM *in vivo* controls cell function, it seems to be achievable that synthetic materials can provide precise handles to regulate cells to generate custom made tissues on demand.[8, 25]

Biomimetic ECM systems can be engineered on the one hand from naturally derived materials such as polypeptides, polysaccharides, or minerals as hydroxyapatite or their composites. These biomaterials have excellent physicochemical activities, mechanical properties close to natural tissues, biological degradability and most importantly, they mediate cell adhesion by borrowing natural motifs e.g. from collagen or fibrin. On the other hand fully synthetic polymers can be manufactured in a highly reproducible manner. Frequently, they do not impose the inherent risk of antigenicity or complex degradation toward immunogenic side products. However, difficulties with synthetic polymers arise more from contaminations such as remaining catalysts, solvents, or residual monomers. These impose clearly toxicity issues. Moreover, to mediate specific bioactive contact, cell adhesion peptides/proteins and signaling molecules (growth factors) have to be incorporated which might be already present in biological materials. Ultimately a hybrid material might combine favorable properties of synthetic materials and biological macromolecules in a synergistic manner. In those hybrids the synthetic materials introduce tailored mechanical and degradative properties as well as ease of processing. The biomacromolecule components of the hybrids could transport specific bioactivity via precisely positioned functional labels.

2.2 Effect of nanostructures on biological systems

Nanostructured materials have been put into focus as with the arise of nanotechnology, tools became available to design, manipulate and characterize such dimensions. This is reflected in various developments in the field of biomedicine and biotechnology. For example microarrays of DNA[26], proteins[27] or carbohydrates[28] are used for high-throughput screening. This includes studying the cellular responses on nanostructure, materials properties and chemical functionality (Figure 2.1).[29] Cells as basic components of tissues interact with their surrounding either by soluble factors e.g. growth factors, or via direct cell-cell as well as cell-ECM contacts. Whether the cell proliferates, differentiates, or dies, is supposed to depend aside of intrinsic cell factors also on the extrinsic signals from their microenvironment.

Nanometer texture: In a first generation, synthetic two dimensional (2D) materials with nanometer textured surfaces have been fabricated by sophisticated technologies like for instance dip-pen printing[30] or e-beam lithography[31] to elucidate the interactions of cells with defined surfaces. Cell-nanostructure interactions were studied from the gene expression level (cell metabolism) up-to the microscopic cell behavior. Understanding of the influences of nanostructure on cell adhesion, orientation, motility, proliferation, migration, or differentiation is accessible.[32] In terms of adhesion, proliferation and migration, nanogratings seem to regulate cell behavior more effectively than nanoposts and pillars (the latter has not been studied much).[33] However, despite the intense investigations, still no widely accepted hypothesis for proliferation is available. In cell differentiation and formation of cell superstructures, nanotopography seems to have a profound effect and hence a high potential to direct cells.[34] Within 5–500 nm to 7–10 µm, topography can alter cell behavior independent of the underlying material chemistry.[35] Cells primarily respond to chemistry, if the topography is below their minimum size scale for sensing.[36] In addition, certain cell types show higher interaction with nanometer scaled pattern than other. For example, osteoblasts seemed to win the adhesion race against chondrocytes, fibroblasts and smooth muscle cells on carbon nanofiber.[37] This is nowadays already exploited for the design of implant surfaces. For instance, implants are treated by sand-blasting generating rough surfaces, where osteoblasts are desired to attach.[38]

Porosity: Proceeding further to design synthetic 3D structured scaffolds a variety of top-down and bottom-up approaches are established as we will discuss on selected examples in chapters 2.4/5. While building up 3D materials, the aspects of internal surfaces, porosity and interconnectivity come into play. Cells need to effectively penetrate such architectures, and colonalization of 3D-scafflods requires bridging of the pores to fully fill the scaffold finally. In addition nutrient and waste transport are necessary. To realize this, a hierarchical pore system might be of advantage (Figure 2.1). Depending on the fabrication methods different pore sizes, geometries, distributions and other porosity characteristics are obtained. For example, scaffolds made out from fibers have mostly an interconnected pore system and inherently an anisotropic nature. This anisotropy can be tuned by fiber alignment as will be illustrated at electro spun scaffolds to direct neurite outgrowth (Sections 2.5/6). As the meshes are composed of sub-micrometer thin fibers, the pore size is direct correlated to the fiber diameter.[39] Conventional textile technologies like braiding, carding or knitting are not straight forward applicable to control the fiber assembly. The difficulties arise mainly from the handling of submicron to nanosized fibers.

Mechanical properties: The porosity of nano- or microstructures might not only be biofunctional in terms of geometry and inner surface topography. Moreover, structure is also modulating the mechanics of a corresponding scaffold as shown in natural hierarchical systems (e.g collagen fiber based tissues).[15] The mechanical properties e.g. stiffness, affect cellular behavior as well. Discher *et al.* showed in their pioneering work that the elasticity of acrylamide gels with different cross-link densities can direct stem cell lineage specification due to mechanical differences.[8] The cells seem to sense mechanically and geometrically the matrix environment and translate this to a cellular response (mechanosensing → mechanotransduction → mechanoresponse).[12, 13] The translation might occur due to unfolding of proteins triggered to extern sensed forces and thereby exposing cryptic binding cites.[12]

2.3 Biological activity of 3D-surfaces

In cellular infiltration of artificial or natural 3D scaffolds, the cells have to overcome the biophysical resistance given by the surrounding microenvironment. How to evenly distribute cells into such scaffolds while still maintaining or controlling the cell phenotype turns out to be a challenging task.

In Nature there are two strategies available involving proteolyic and nonproteolytic cell migration.[40] In the proteolytic way the cells clear their path through secreting and activating proteases which locally and specifically degrade components of the pericellular matrix. The nonproteolytic pathway is conducted through amoeboid forward migration, where cells adapt in their shape or deform the microenvironment.[2] For artificial 3D scaffolds cell-adhesive ligands for traction are required and cell infiltration via nonproteolytic pathway is enhanced by providing adequate pore sizes and scaffold elasticity for cell migration. The degradation of a scaffold is the first step to an active remodeling of an artificial matrix. Degradation is often based on hydrolytic ester cleavage, which proceeds with a tunable rate depending on surface area, hydrophilicity, crystallinity and ester type. Recently, there have been different bioinspired approaches described, which include the introduction of degradation sites for proteolytic (i.e. enzyme catalysed) cleavage.[41, 42] Healing processes, in which ECM remodeling takes place by MPP proteases inspired a scaffold that can be selectively degraded by proteases. In this biomimetic strategy, the cell itself produces the required enzymes to pave the way for infiltration.[42]

In both the proteolytic and non-proteolytic pathways the question remains how to facilitate cell penetration into a preformed scaffold. Aside afore mentioned requirements, seeding strategies are highly relevant. While static seeding relies on active cell migration into the pore system, dynamic seeding in bioreactors can actively assist the cell transport by a directed flow field. Appling flow perturbation increases additionally the transport of nutrient and waste.[43] However, a flow field applies stress on the cell culture. This may influence the cellular behavior and thus limits the application of dynamic seeding. An elegant approach is the direct implantation of scaffold into a patient’s body to detour the artificial bioreactor.[44]

More frequently an approach is applied, where a scaffold precursor is homogeneously mixed with cells. Subsequently, a scaffold is formed with response to temperature, pH, or crosslinking molecules. The *in situ* encapsulation strategy provides often systems with homogeneously integrated cells.[5] A similarly promising strategy includes the fabrication of a structured 3D scaffold directly into a dispersion of cells in an appropriate medium (Chapter 2.4/5: electrospinning and plotting).

The 3D environment alters mechanosensing and cell adhesion from those provided in 2D. The cell-adhesion sites (i.e. integrins), integrin ligation, cell contraction and associated intercellular signaling occurs substantially different in 3D.[11, 45, 46] In addition, the solute diffusion and the binding of proteins (i.e. growth factor, enzymes) are effected by the 3D structure thus creating gradients. 3D scaffolds might be essential to direct morphogenetic and remodeling events. There is an interplay between cell-generated forces, adhesion-ligand density and matrix stiffness. The mechanics of the scaffold as the cells migrate into the structure displays certain cell functions depending on the contraction-response. In mammary epithelia for example, the increase in gel stiffness across a range disrupts morphogenesis and promotes proliferation.[10] Furthermore, scaffold geometry dictates cell adhesion and migration. For example, the minimum fiber diameter needed for fibroblast to adhere and migrate on a single fiber was shown to be approximately 10 µm, and an interfiber distance of up to 200 µm was the maximum gap that could be used to bridge 2 fibers.[47]

Combinatorial 3D polymer scaffold libraries for screening might be promising to evaluated the so far discussed issues. However in the reported case only 3D scaffold by salt leaching were constructed.[48] The geometry is here not as defined and reproducible as in designer scaffold (SFF, Chapter 2.4). Nonetheless this methodology might be translated to those techniques.

In order to **functionalize** scaffolds to mimic the native cell environment, different strategies are available. Recombinant DNA technology can be used to design artificial ECM proteins to avoid the afore mentioned complications with naturally derived materials.[49] However, there is little known about the long term *in vivo* performance of such synthetic biomaterials. Other approaches are directed to compose hybrid structures out of biocompatible synthetic polymers like poly(lactic-*co*-glycolic acid) (PLGA) or poly(ethylene oxide) (PEO).

Cell adhesion on a non-functional scaffold is mediated dominantly by non-specific, entropically favored adsorption of a layer of cell adhesion proteins, excreted by the cell itself.[50] In order to obtain and retain native functions of these proteins attempts are being made to tune hydrophilicity/hydrophobicity of the scaffold surfaces.[51] Different methods towards surface activation are commonly applied, *e.g.* blending, copolymerization, plasma treatment, etching, radiation, chemical surface modification, coatings and combinations of those.

On such modified surfaces some of the attached proteins are recognized by cytoskeletally associated receptors in cell membrane. So eventually the extracellular substrate is mechanically connected with the intracellular cytoskeleton, which may secrete its own adhesion proteins. Integrins, as important class of cell receptors,[52] bind to small domains on their adhesion proteins e.g. the oligopeptide sequence arginine-glycine-aspartic acid (RGD) common in fibronectin.[53]

In order to facilitate cell adhesion before mentioned oligopeptides or adhesion protein are chemically or physically attached to scaffolds in advance (i.e. cell adhere specifically). The strategy to attach peptide sequences to surfaces instead of proteins has the advantage not to deal with the before mentioned antigenicity as well as the loss of functionality through protein denaturation or degradation. The so created adhesion sites show a biphasic cellular response i.e. too low and too high ligand densities have adverse effect on cell spreading and migration.[24, 54] Additionally, for example for RGD-containing peptide sequences, different aspect like peptide sequences (i.e.

flanking residues), forms (linear, cyclic), immobilization strategies (substrate material, linker), and nanopatterning [23, 55] will be important for cellular behavior.

Nonetheless, RGD-containing scaffolds seem to only partially exhibit the functions of native fibronectin as mentionend by Vogel and coworkers. Additionally, the importance of the preservation of native protein structure, especially fibronectin as it occurs in the extracellular fibrils, is highlighted.[46] Cell biologists commonly enhance cell adhesion onto e.g. polymer surfaces by the adsorbtion of fibronectin. In a ground-breaking essay, Vogel hypothesized that the preservation of the native fibronectin structure would not enhance cell adhesion, but moreover be critical for vascularization of a scaffold. The latter is certainly one of the most important demands for *in vivo* scaffolds, where additional blood vessels have ultimately grow into the scaffold and supply the cells with nutrition. Functionalize scaffolds with fibronectin (or potential other ECM components) while preserving the native structure, remains an unsolved problem on the track to engineering an artificial tissue.

Other functionalization strategies deal with shelf binding and release of signaling molecules triggered by cellular events. Heparin binds with high affinity various morphogens i.e. growth factors. Therefore heparin is used to functionalize scaffolds for example through electrostatically bound growth factors.[56] The release of these factors can be triggered by specific enzymes with occur i.e. in ECM remodeling to degrade heparin. This bioactive route is clearly of advantage compared to common approaches where physical triggers like pH, or temperature are exploited to release bioactive factors.[4] The advantages of such approaches rely on the fact that growth factors are well controlled in 3D position, concentration and time. Additionally, the growth factors might be more functional by immobilization than by being dissolved in cell media as shown in the case of vascular endothelial growth factor (VEGF).[57]

In overall, the concepts and effects of 3D architectures and functionalization mentioned so far, shall now be addressed to selected bottom-up and top-down designed scaffold.

2.4 Bottom-up approaches

Templated synthesis:

Porous polymer materials with a continuous polymer phase consisting e.g. of a homo- or a statistical copolymer can be accessed via template strategies. These involve the dispersion of a porogen e.g. gaseous, liquid or solid into a fluid phase of a polymer. The removal of the porogen leads to macroporous materials with pore sizes >>50 nm.[58] For bioapplications often salt crystals are used, which can be leached easily with water, generating systems with porosities up to 90% and pore sizes in the range of 5-600 µm.[59, 60] These simple and convenient processes are suitable for a range of biomaterials. However, templated strategies do not offer optimal control over pore structure and connectivity. Miscibility gaps and density differences make homogeneous dispersion difficult and result in inhomogeneous materials with imperfect interconnectivity. Advanced control toward hierarchical pore systems via templating processes is only in some special cases possible. Often physicochemical demixing hampers the templating of mixtures of particles with strongly different sizes.[61]

Organization of polymers:

Microcellular foams can be produced by thermally induced phase separation (TIPS).[59, 60, 62] The induced spinodal decomposition can be optimized to generate e.g. polylactide scaffolds with the porous morphology and physico-mechanical characteristics of a foam. Interesting materials are able to be constructed in a simple process. These materials exhibited bundles of channels with a diameter of ~100 µm. The internal walls of the tubular macropores have a porous substructure with pore diameters of ~10 µm. It is remarkable that the channels have a preferential orientation in the cooling direction. TIPS is easily implemented by using freeze-drying methods. The porosity of the resulting materials is < 90%, average pore sizes are in the range of 5-600 µm and large interconnectivity can be achieved.[63]

Materials generated by the template or the organization method can be functionalized. The introduction of signaling entities to decorate the pore walls with biologically active molecules is feasible but rather limited. Often biopolymers such as gelatin (degraded collagen) are blended into the polymer matrix to be statistically exposed on the pore surface. Moreover, physicochemical adsorbtion e.g. of fibronectin can be performed in a posttreatment step of the materials. The simplicity of both functionalization methods is strongly limiting the precise spatial control of bioactive entities.

Self-assembly of polymers:

Block copolymers, which combine polymer segments with different properties are presumably the most widely examined system for the study of self-assembly to larger scale structures with controlled structural and functional features on the nanometer length scale.[64] Phase segregation of block copolymers followed by selective degradation of one polymer block leads to highly ordered porous 3D-structures.[65] The obtainable pore dimensions are in the micro- and mesoporous range (< 50 nm), which do not meet the requirements for cellular infiltration.

However, the controlled self-assembly of macromolecular building blocks is probably the closest strategy, compared to the concepts found in biology to generate e.g. collagen fibers which structure the ECM. New strategies emerged in the field of soft-matter structure formation, which paved the way to precisely generate fibrillar or fiber-like nanostructures.[66-68] These can exhibit appropriate mechanical properties in the regime of biological matrix fibers and even provide the possibility to present the required biological signal entities at their surfaces.[67, 69, 70]

Particularly *de novo* designed peptides proved to be a versatile tool for the bottom-up assembly of fibrillar structures.[71-74] A broad set of different biomimetic filaments are described. These can be accessed via the controlled self-assembly of peptides, peptide amphiphiles, peptide-polymer conjugates and proteins (Figure 2.3).[69, 71, 75] Nowadays, there is a general understanding of the rules determining the relationship of peptide amino acid sequence and secondary structure motifs. For materials and biomedical science applications, mostly the β-sheet, but also the α-helical coiled-coil motif has been indentified as organization motifs to generate nanofibers.[67, 76, 77] The peptide building block together with the assembly motif determines the inner nanostructure, the dimensions and the mechanical properties of the resulting filaments.[78, 79]

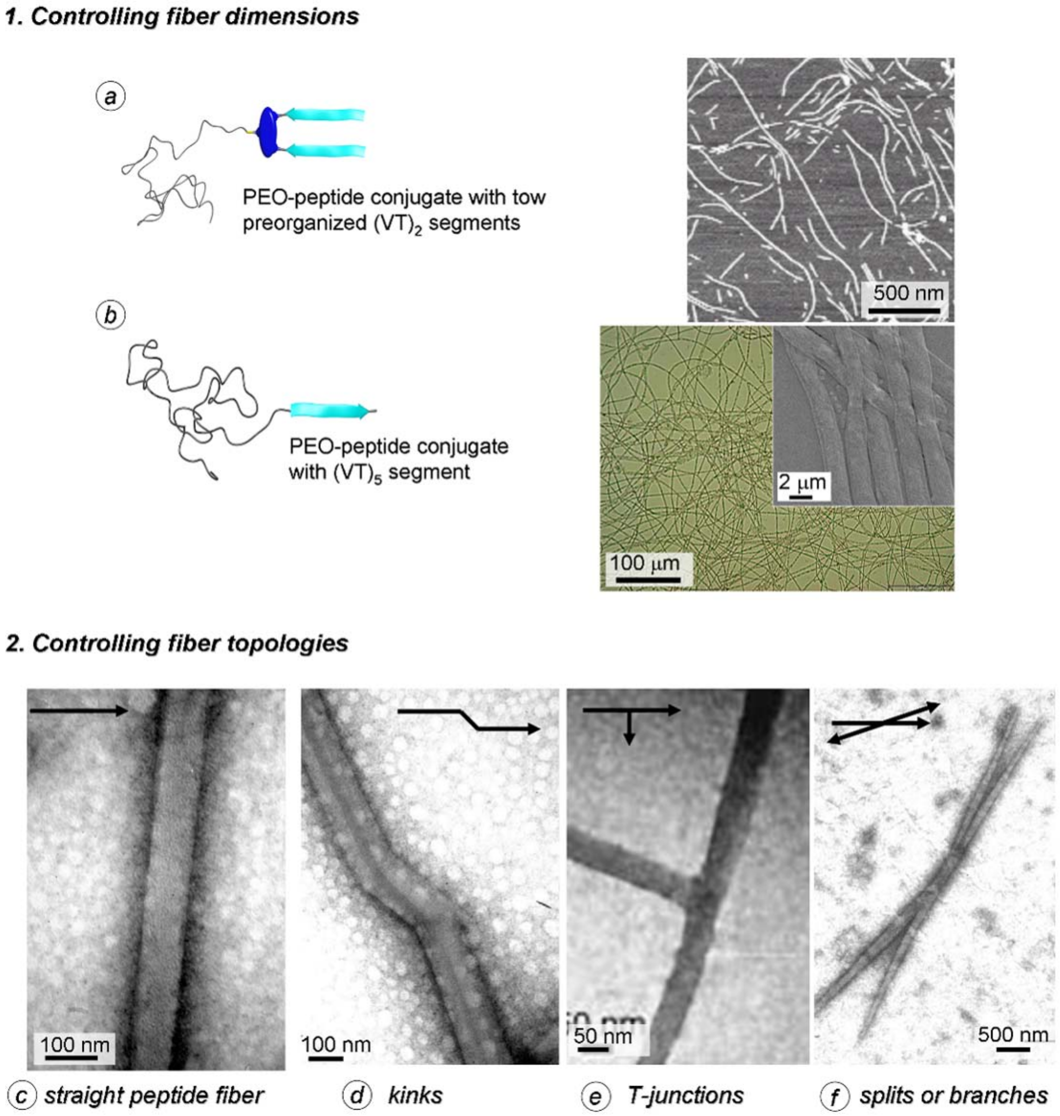

Figure 2.2. Controlling dimensions and topology of self-assembled fibrils. Controlled self-assembly of peptide-polymer conjugates allows tuning of fiber sizes and shapes from nanotapes with 1.2×17 nm cross section (a) to microtapes with 50 nm×2 µm cross section (b). Self-assembling coiled-coil-peptides leads to straight nanofibers (c), fibers with kinks (d) or branched fibers (f) as well as fibers with T-junctions. [80-83]

Börner *et al.* demonstrated that peptide-polymer conjugates can assemble to nanotapes with persistence lengths close to actin filaments (composes one part of the intercellular skeleton).[80, 81] The generated nanostructures are flat ribbons (1.2 nm × 17 nm × 2 µm (h/w/l)) with a peptide β-sheet core and a polymer shell (Figure 2.2). Similar to the basic structure element of collagen (rod like tripel helix), the strong anisotropic nature of the synthetic core shell ribbon is reflected in a high tendency to pack into bundles with nematic substructure.[81] The vast structural variability of the present concept has been indicated by the fact that a slight variation in the peptide part of the peptide-polymer conjugate led to macroscopic tapes with a cross section of 2 μm × 50 nm and lengths of several millimeters (Figure 2.2).[82]

Woolfson *et al.* described impressively the design of peptide fibers based on α-helical coiled-coil building blocks.[79] By programming at the amino-acid sequence level, the fibers could be fine-tuned from thick rigid rods to thinner, more flexible fibrils.[78] Advanced control could be achieved, including the tailoring of the fiber topology. The amino acid sequence could be used to rationally equip peptide nanofibers with kinks, branches or cross-links (Figure 2.2).[83, 84]

Despite the fact that peptide or bioconjugate based filaments are not covalently assembled and the building blocks hold together via soft interactions (e.g. hydrogen bonding, hydrophobic or ionic interactions), excellent mechanical properties might be achievable. Smith *et al.* have shown that insulin for instance creates fibrils with strengths of up to 0.6 GPa, comparable to that of steel, and with a Young's modulus of 3.3 GPa, corresponding to that of silk.[85] Moreover, the latter is perhaps the most prominent example of a protein based, high performance fiber. Silk threads combine high modulus fibers elasticity with enormous toughness, which is still unmatched by synthetic fiber materials.[86]

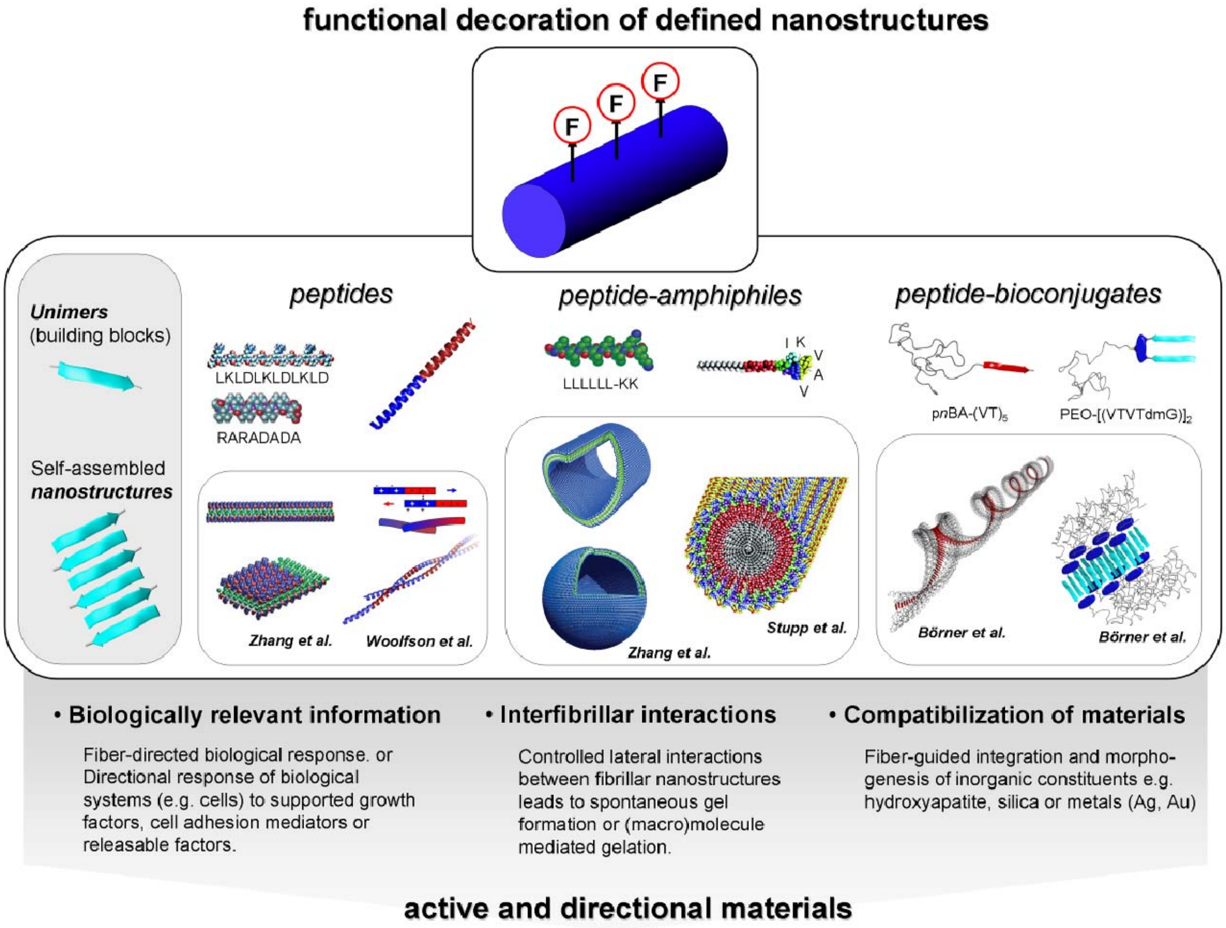

- **Biologically relevant information**

Fiber-directed biological response. or Directional response of biological systems (e.g. cells) to supported growth factors, cell adhesion mediators or releasable factors.

- **Interfibrillar interactions**

Controlled lateral interactions between fibrillar nanostructures leads to spontaneous gel formation or (macro)molecule mediated gelation.

- **Compatibilization of materials**

Fiber-guided integration and morphogenesis of inorganic constituents e.g. hydroxyapatite, silica or metals (Ag, Au)

Figure 2.3. Functional decoration of self-assembled nanofibers to mimic fibrillar structures of the ECM. The monodisperse nature of the building blocks and the precise assembly motifs lead to nanostructures with well defined functional surfaces. Adjusting of these faces enables the generation of bioactivity by presenting biorelevant epitops.[68, 69, 71, 75, 87]

The utilization of peptide self-assembly allows additionally to the control of structural parameters the rational control of the functionalities, which are displayed at the nanofiber surface. This makes the presentation of biological signals and thus the introduction of bioactivity feasible. Stupp and coworkers investigated the self-assembly of peptide-amphiphiles (Figure 2.3).[68, 87] The resulting worm-like, cylindrical nanostructures consist of a hydrophobic core that is formed by the alkyl chains of the amphiphiles. The polar peptide segments, instead, are exposed to the water phase on the fiber surface.[88] For instance, the self-assembly of a peptide-amphiphile with a RGD domain leads to nanostructures with RGD surface functionalities.[87] A similar system has been equipped with an epitope of laminin. This is an ECM protein that signals complex information, influencing and regulating neurite outgrowth. The resulting nanofibers presented the bioactive epitope and have been apparently capable to stimulate differentiation as well as growth of neural cells in a directional manner.[88]

Moreover, self-assembled nanofibers with distinct functional surfaces might enable more than designing cell-fiber-systems. Since peptides and nanofibers direct the growth of inorganic mater in biological systems, the controlled integration of composites into the field of tissue engineering might be feasible.[89] For example, functional faces of nanotapes composed of peptide-poly(ethylene oxide) conjugates could be adjusted to mimic fibrillar proteins such as silicatines.[73, 90] The functionality programs the nanofibers to have a high affinity to inorganic precursors and ultimately controls the rapid formation of a complex composite material with 6 hierarchy levels. This might be useful for biomedical applications e.g. plotted dental inlays.[91] Hartgering and Stupp *et al.* presented different self-assembled nanofibers, which could control the crystallization of hydroxyapatite.[92] Since silica and hydroxyapatite are important inorganic components in biological composite materials, interesting biocomposites might be envisioned. In the future defined cellular integration could be potentially combined with hierarchically structured inorganic-bioorganic composites, which might lead to interesting biointegrated composite materials.

Programming functionalities on the nanofiber surface makes the adjustment of interfibrillar interactions possible. Biology probably controls the hydrophobicity of the fibers in the ECM by using different types of collagen with different degrees of glycosylation. Even if the entire function of the collagen family is not clear, it might be likely that a variable glycosylation is one tool to regulate the hydrophobicity of the collagen fibers, which adjust lateral fiber interactions. Furthermore, biological ECM fibers show soft and reversible multipoint interactions that can be mediated by ligands for specific cross-linking. For example, peptide amphiphile nanofibers mimicked this by presenting heparin binding peptide sequences on their fiber surfaces. The effective cross linking of the nanofibers could be mediated by the addition of heparin to a delude fiber solution.[93]

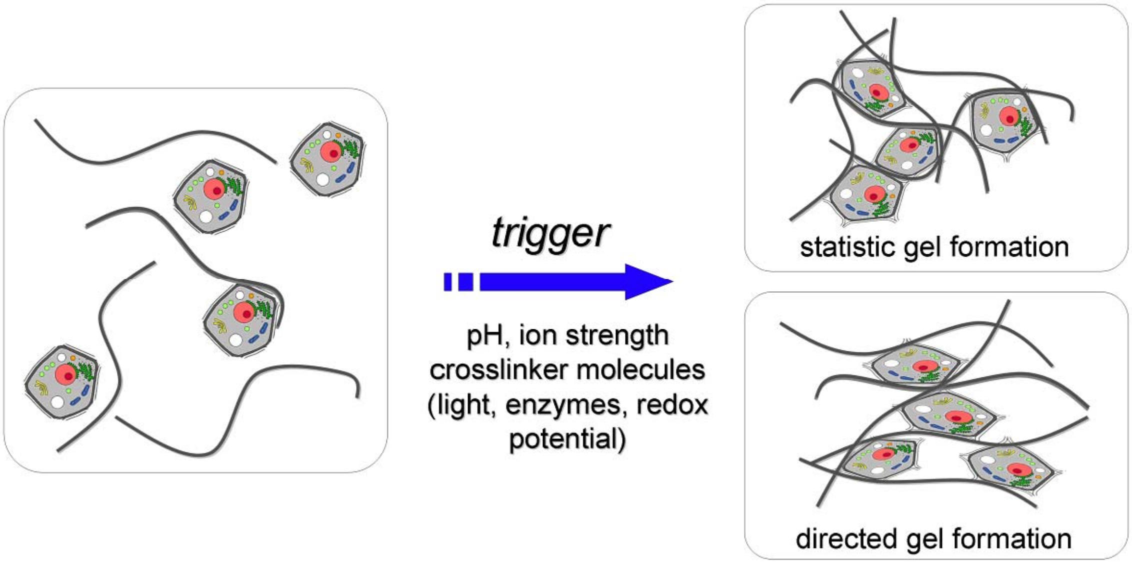

Figure 2.4. Schematic illustration of the formation of isotropic (top) or anisotropic (bottom) hydrogels. Gel formation can be triggered by inducing lateral interactions between fibrillar nano objects.

Ultimately, self-assembled nanofibers can possess a fluid-gel transition and thus generate 3-dimensional fiber structured materials (Figure 2.4). Preferably resulting gels should have a high porosity, preserved structural dynamic and low solid content.[94] Several different systems based on peptides, amphiphiles and bioconjugates have been described that lead to the formation of hydrogels or organogels.[71, 95, 96] While the latter are more relevant for materials science applications,[97] aqueous media are required for biomaterial scaffolds e.g. useful for tissue engineering.[70, 96, 98] A common form of scaffolds is a fiber structured gel in which cells can be encapsulated (Figure 2.4).[99] The above mentioned nanofibers based on peptide-amphiphiles formed spontaneously hydrogels at a concentration of about 0.5%. The high aspect ratio of the fibers span pores of about 200-800 µm leaving enough dynamic for cellular penetration but still preserving tight cell-fiber contact to influence the included cells. *In situ* gelation in the presents of different cell lines has been demonstrated, making the gels interesting for tissue engineering.[88] The artificial nanofiber scaffolds had a distinct effect on cell differentiation due to the bioactive epitops presented on the fiber surface.

Zhang *et al.* investigated a variety of peptides with alternating hydrophobic-hydrophilic amino acid sequences.[69, 77] The polarity sequence meets the requirements for β-sheet formation, leading to fibrils that show a reversible cross-linking to hydrogels. Charged residues, present in the sequence of the peptide were used to control the self-assembly process via pH or ionic strength. It is noteworthy, that cells which are entrapped into this type of gels are rapidly stimulated to enhance the production of ECM.[100] The rapid reconstitution of the native biological environment makes the non-toxic peptides good candidates to be used in repair strategies of cartilage tissue.

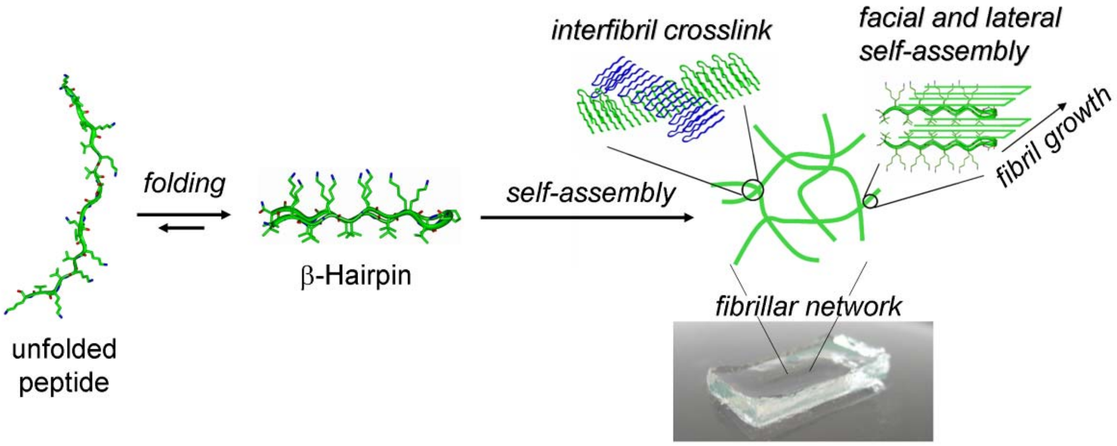

Figure 2.5. Illustration of the triggered self-assembly of a peptide β- hairpin that forms fibrillar structures which show facial and lateral self-assembly to hydrogel networks.[74]

Schneider *et al.* described a highly interesting peptide having a β-hairpin structure (Figure 2.5).[101] The amino acid sequence determines the folding of the peptide into a β-sheet-turn-β-sheet tertiary structure. This can self-assemble in a pH-controlled manner into branched nanofibers which form hydrogels.[102] The self-assembly kinetics is strongly depending on temperature. Under physiological conditions the aggregation of the peptide proceeds slow at 10°C but highly rapid at 20°C. This is indeed interesting for injection tissue engineering, where rapid gelatin is required at body temperature, but fluid flow should be preserved before injection.[103]

The examples described above reveal the versatility and potentials of bottom-up approaches to generate structures with controlled substructures and moreover, positioned functionalities to modulate the material-biology interfaces. Certainly, this toolbox will be further explored and exploited to program nanostructures for interfacing to biology. However, the control of self-assembly processes over several length scales from the nanostructure to macrostructure is still highly challenging. Therefore an interesting technological interface has been set into focus, where existing polymer processing technologies are evaluated to produce structured materials for biomedical applications. The available processes and the resulting possibilities are discussed in the next chapter.

2.5 Top-down processing

Solid freeform fabrication:

For an adequate scaffold for tissue engineering mechanics and porosity have to be optimized preferably by the design of hierarchical porous structures. As putting the holes determines the mechanical properties, it also will effect the mass-transport required for cell nutrition and cell migration. The computational topology design (CTD) enables to construct such structures by creating libraries of particular unit cells at different physical scales. The unit cells are then the building units of the overall structure.[104] From these microstructures stiffness and permeability can be calculated. Using topology optimization, a tailored microstructure can be created, in which cell migration and mechanical properties of the addressed tissue e.g. bone are considered.[105] Custom-made implants can be fabricated. The exact shape of a specific anatomic defect in a patient can be nowadays diagnostically determined with computed tomography or magnetic resonance imaging. This data can then be directly intersected with the microstructure database, to design an optimized scaffold.[106]

The scaffolds for implants can be manufactured by mean of solid freeform fabrication (SFF), relaying on a layer-by-layer composition of 3D materials. The step-by-step assembly proceeds in a highly precise manner enabling one to accurately defined pore size, interconnectivity and the scaffold form of an i.e. anatomically shaped structure. SFF requires expensive equipments, the technology is certainly limited in resolution and does not allow the fabrication of all complex geometries generated by computational design (CTD). However, different materials like polymers, ceramics and metal biomaterials can be processed into scaffolds. Due to an accurate inner geometry and shape, SFF scaffolds have typically better mechanical properties than those produced via other methods e.g. from porogen leaching, or gas foaming. Therefore, SFF is attractive for mechanical supports of hard tissue with elastic moduli of 10-1500 MPa.[107] There is a large variety of SFF systems established, which all have in common that they use a triangular facet structure to replicate a representation of the optimal scaffold. Technology platforms can be divided into three groups by the way the material is deposited into laser-, printing- and nozzle-based systems. Three examples are schematically shown in Figure 2.6.

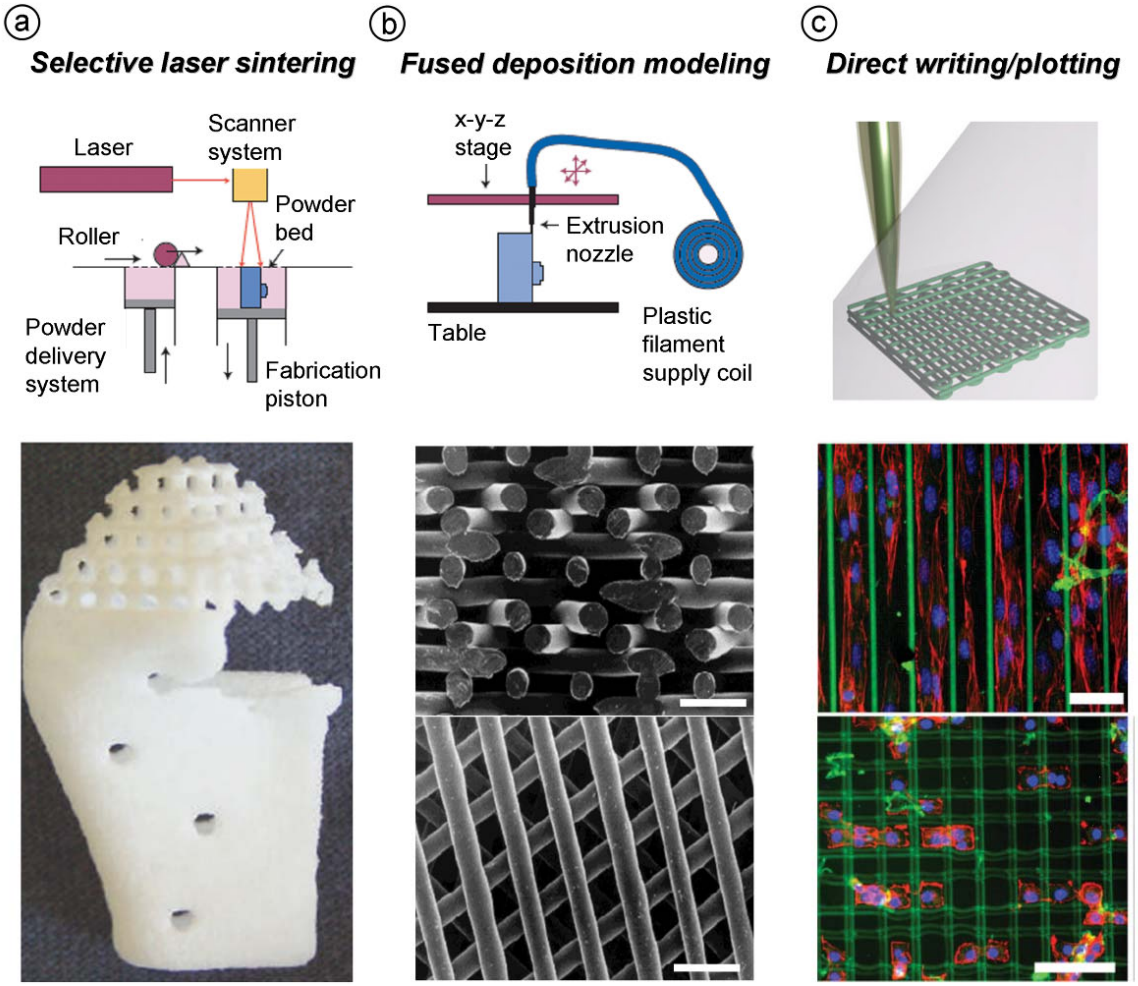

Figure 2.6. Schematics of 3 examples of SFF are presented: selective laser sintering, fused deposition modeling and direct writing/plotting. Their corresponding scaffolds can be seen in the pictures below, where in the last part fibroblasts are incorporated and adapt to the 3D environment (scale bars: b) = 1 mm, c) = 100 µm).[108, 109]

The laser-based systems are stereolithography (SL) and selective laser sintering (SLS). In **SL** a liquid monomer is photo-polymerized, restricting the range of materials to polymers, which are compatible to UV-curing. SL provides scaffolds with porosities of < 90% and a pore size ranges of 20-1000 µm.[110] **SLS** uses powders preferable with narrow size distribution. These are sintered to geometries with < 40% porosity and 30-2500 µm pore sizes.[111] In the second group, either a chemical binder is printed onto powder (**3D printing**) or wax is directly deposited. The powder needs to have a narrow size distribution to compose scaffolds with porosities < 45-60% and pore sizes in the range of 45-1600 µm.[112] The last technology exploits extrusion through a nozzle either using melts (fused depositing modeling (**FDM**)) or solutions that are directly structure forming or upon for example radiation (Plotting/direct writing (**DW**)). FDM applies thermoplastics to form structures with porosity < 80% and ranges of pore sizes of 100-2000 µm.[113] Malda *et al.* compared the oxygen gradients in an 3D-scaffold fabricated by FDM with one produced by porogen leaching. Both scaffolds have been seeded with chondrocytes. Two weeks after *in vivo* implantation the FDM scaffold showed, compared to the other scaffold, significantly higher cell densities in the center and higher glycosaminoglycan content. This suggests a better cell infiltration, lower oxygen gradients and better cell colonalization in the FDM scaffold and highlights the importance of rationally designed scaffolds for tissue-engineering applications.[114] To achieve smaller feature sizes below the resolution of the FDM process, simple surface roughening by NaOH etching is applied. This improves early matrix deposition in FDM scaffolds and facilitates bone formation in a rabbit model.[115] Direct writing scaffolds comprise porosities of < 90% and pore sizes of 5-100 µm. Therefore this method shows the best resolution. However, the long manufacturing time is a clear disadvantage of the method. DW is especially interesting for using direct writing of cells,[116] biomaterials like hydrogels (Figure 2.6),[109, 117] or self-assembling systems.[118] The latter shows the possibility of combining bottom-up with top-down approaches. This provides means to macroscopic nanostructured scaffolds, where the inherent nanostructure is aligned to the macroscopic drawing direction.

In order to functionalize the scaffolds, blending seems to be a feasible approach, as shown in the FDM of poly(ε-caprolactone)/calcium phosphate composites.[113] These scaffolds exhibit favorable degradation and resorption kinetics, combined with excellent mechanical properties and an optimal hydrophilicity.[119] Biochemical advantages of such structures are the improved cell seeding. Moreover, an enhanced control of the position of supported growth factors e.g. bone morphogenetic proteins (BMP) is established as shown in *in vitro* and *in vivo* studies.[120] The functional biomolecules are mostly added after the scaffold fabrication as the fabrication method might effect the functionality, as non-mild conditions are used. The tricalcium phosphate (TCP) incorporated provides a high binding affinity for BMP proteins. The functionality of growth factors is expected to increase by presenting them together with specific co-factors, such as heparin sulphate (HS) together with osteoconductive scaffolds. HS is a rather robust biomacromolecule that tolerates harsh processing conditions and thus the direct incorporation is of HS during scaffold processing is feasible.[119] In contrast to FDM, the direct writing method is compatible with several functionalization strategies. Even the direct incorporation of cells or proteins is feasible, as solutions can be easily processed. Detailed approaches for *in situ* and post functionalization will be discussed in the following section.

Electrospinning (ES)

Although the principle of this technique is quite old, ES has been developed toward a powerful tool to design fiber meshes with fiber diameter ranging from ~ 10 µm down to a few nanometers as well as mesh porosities of < 90% and pore sizes of < 1-100 µm (Figure 2.7) [121, 122]

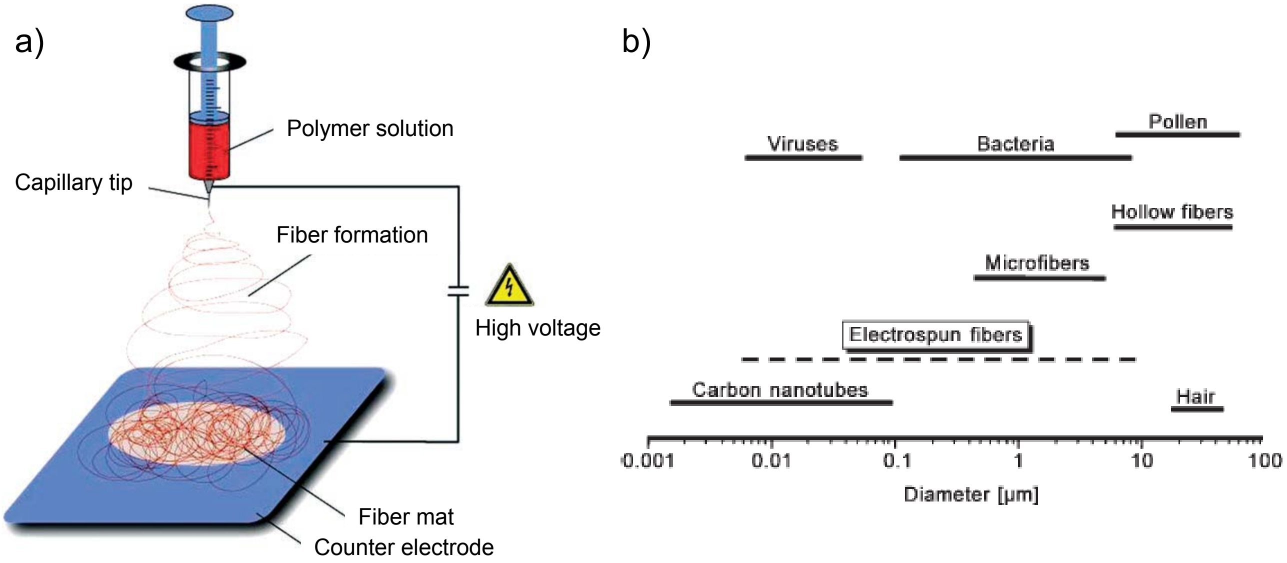

Figure 2.7. The schematics of electrospinning (a) shows the simplicity of the process which is able to form fibers in the size range from ~ 10 µm down to a few nanometers (b).[122]

Typically, viscous solutions or melts (not further discussed here) composed of polymers (synthetic, natural), precursors (ceramics, metals) or composite materials are able to be processed. During ES the viscous solution is extruded through a needle, which is charged at the tip with high voltage. Deposition of the meshes takes place on a grounded collector. Given by its simplicity regarding equipment needed and versatility (materials, structures), the ES process becomes highly popular across different disciplines. Applications range from mesh production for wound dressings, tissue engineering to drug delivery systems. The fact that the fiber dimensions can reach the order of magnitude of fibrillar structures of the ECM makes it a feasible approach to mimic the natural environment of cells. In addition, features like high interconnectivity of pores, high porosity, and high surface area make the resulting non-wovens attractive for example to be infiltrated with cells.

It should be noted that mechanisms involved in ES are rather complex and some details are still under heavy discussion. The ionized drop at the tip is first deformed to a Taylor cone or more precisely a hyperboloidal shape. Then, after overcoming surface tension and viscosity a so called liquid jet is ejected and accelerated, undergoing different instabilities before deposition.[123] An interplay of solution properties (surface tension, viscosity, molecular weight, conductivity, solvent volatility, solvent-solute interaction, dielectric constant), apparatus constraints (voltage, tip to collector distance, feeding rate, collector geometry, assembly) and environmental conditions (humidity, temperature, atmosphere) influence the process and can be used to control the outcome. For example by using different concentrations and molecular weights, beads (i.e. electrospraying), beaded fibers and fibers with different diameters can be constructed. This depends on the interaction of surface tension and polymer entanglements with the pulling force.[124] The latter depends on feed rate, voltage applied, gap distance, dielectric constant and conductivity of the used solution. Depending on the solution/solute system and the applied "sophisticated" set up (e.g. a coaxial setup[125]) meshes with special features can be obtained consisting of porous,[126] hollow,[127] wrinkled,[128] branched,[124] flat,[129] coiled[130] and barbed[131] fibers. A variety of factors influence the assembly mechanism of the non-woven meshes and hence determine essential parameters such as final fiber-to-fiber distance, porosity and mechanical properties of the resulting meshes. The amount of remaining solvent, humidity, the collector material and the elasticity of the polymer might play a dominant role on screening or grounding of charges, fiber bonding and on buckling of fibers. However further investigations must be performed to clarify this aspects, which are tightly coupled with each other. By using rotating drums, patterned electrodes or post-drawing at elevated temperature an aligned fiber mat or bundle can be obtained.[132, 133] Interestingly, reducing the gap distance enables the technology of direct writing (near field ES).[134] In order to increase productivity of the ES process, multi-nozzle setups or a porous tube spinnerets are used to produce various jets in parallel, making industrial scale fabrication feasible.[135]

Cell studies on scaffolds of nano-/submicrometer scaled fibers have shown that these dimensions promote not only the cell adhesion, but also have beneficial effects on proliferation and differentiation of cells.[136-138] These effects are more prominent with decreasing fiber diameters. It seems relevant that the cells can be guided and bridged by the artificial fibers. Particularly meshes with aligned fibers are promising e.g. for guiding the growth of nerve cells (Figure 2.8).[139]

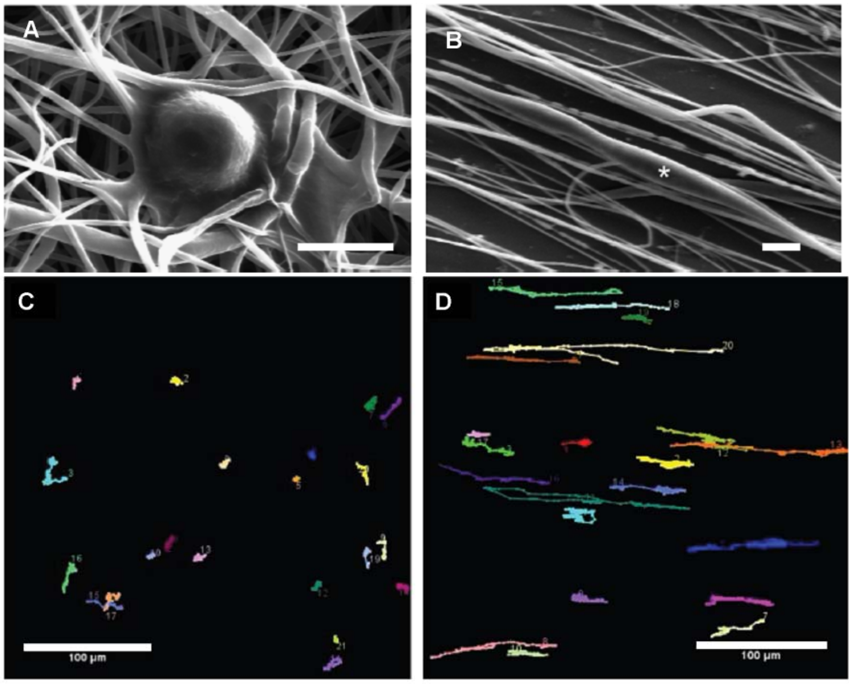

Figure 2.8. Nerve cells adjust their adhesion and migration to the corresponding structure as seen here on random (A, C) and aligned (B, D). PCL nanofibers (SEM pictures (A, B)) and motion cell-tracking are shown (C, D) (20 individual trajectories (C, D) were traced manually after a total tracking period of 36 h; Scale bars: (A, B): 10 µm, (C, D): 100 µm).

It is noteworthy, that aligned fibers compared to randomly oriented ones seem to stimulate fibroblasts to increase the production of ECM proteins. This was rationalized by a more controlled microenvironment providing adequate topology and stimulating mechanotransduction.[140] However, quantitative evaluation is not straightforward, as frequently appropriate 2D reference surfaces are not available. Furthermore, the cellular behavior dependents on the cell line, e.g. endothelial cells seem to prefer flat surfaces more than nanofibers.[141] Explanations could be complex but also rather trivial as projected area of fibers is smaller compared to flat surfaces.[142] In addition, it was found that cells proliferated faster on scaffolds with peak pore diameters greater than 6 µm. In case of further increase of the peak pore diameter to 12 or even 23 µm, cells began to align along single fibers, instead of attaching to multiple fibers via multiple attachment points.[143]

Early reports of electrospun scaffolds suffered from poor **cellular infiltration**.[137] Frequently, cells adhered at the surface and thus coated the nano- or submicrometer scaled electrospun meshes due to small pore sizes. In order to overcome this limitations pore sizes were increased by combining ES with other methods. These approaches include the coating of microfiber with nanofibers,[144] or the combination of electrospinning and electrospraying.[145] Moreover, sequential[146] or simultaneous electrospinning with a two syringe setup was described. There either nano- and microfibers were deposited[147] or one fiber type was selectively removed in a subsequent step to increase the porosity and pore sizes.[145, 148] Other strategies involved electrospinning combined with salt leaching,[149] or freeze-drying[150] but also blowing agents,[151] or ice templates[152] have been introduced. Another attempt is to use bioreactors to encourage the cell penetration into the fiber meshes.[143] Other approaches include direct spinning of cells by encapsulation into PDMS by coaxial ES.[153] However, there might be some long term effects which can be induced to cells by the strong electric field. More harmless in that regard seems to be spinning into the cell culture and then sequential seeding of cells. The interesting procedure and the resulting sandwich scaffolds are schematically outlined in Figure 2.9.[154]

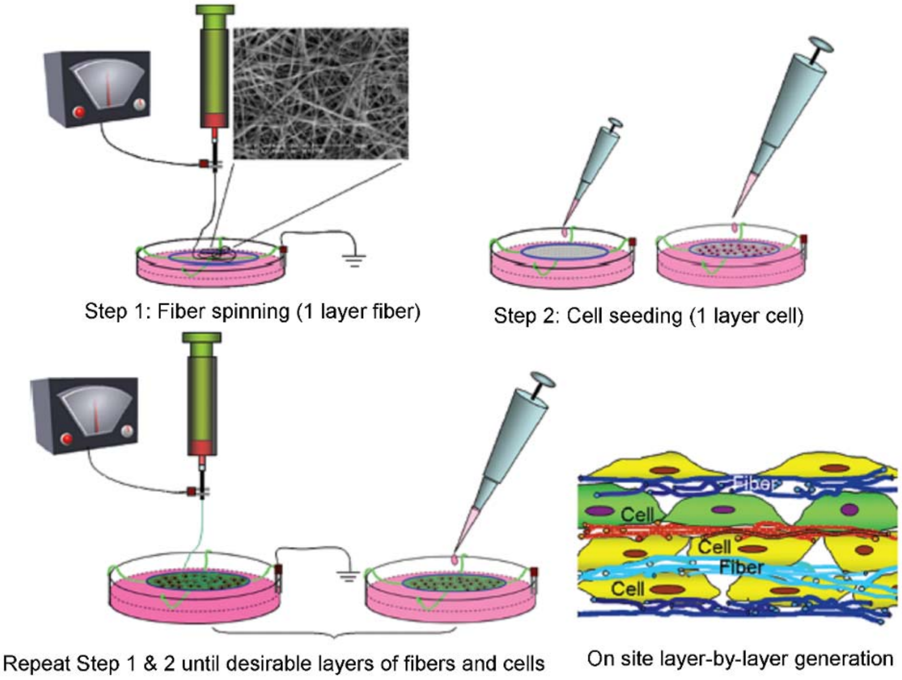

Figure 2.9. Cell-fiber sandwiches can be constructed by L-b-L cell/fiber assembly. This way the cells are sandwiched between layers of electrospun fiber mashes. The mesh thickness and cell loading can be controlled within this process.

To improve, and control cell-fiber interactions, the fiber meshes can be either composed of biomacromolecules or post-functionalized with appropriate biomolecules. The question arises which materials can be electrospun? In principle all polymers can be spun, that provide in solution enough entanglements and adequate interactions between the solvent and solute. Particularly, biopolymers show dominant H-bonding and/or polyelectrolyte effects, which lead to strong viscosity increase or poor solvent evaporation. In order to prevent such effects H-bond breaking or charge screening agents are added into the solution to facilitate spinning. Changing the interaction between the molecules might however change the conformation of biopolymers like proteins.[155] The most popular strategy is blending with easily spinnable polymers such as high-molecular-weight PEO.[156] Another interesting approach is described by using a coaxial-ES setup. A polymer which is difficult to spin is placed in the core and an easily spinnable will assist fiber production by forming the shell. Subsequently, shell-leaching provides eventually fibers from the "difficult" polymer.[157]

Furthermore, meshes have been composed of multilayers consisting of different polymers. Matsuda and coworkers produced bilayer meshes of a thick polyurethane microfiber mesh and a thin nanofiber mesh composed of type I collagen. The material decouples mechanical properties with biochemical functionality of collagen to form a prototype scaffold for artificial grafts.[158]

In principle, the functionalization strategies can be subdivided into methods allowing (1.) direct incorporation of the functionality during spinning and (2.) post-functionalization of the fibers after mesh production.

Coaxial-ES is a straight forward technology to produce meshes with functional fibers. These individual fibers can consist of a synthetic, nonfunctional core and biofunctionalized shell. However the process is not trivial, as control over multiple feeding rates and incompatibility issues occurring.

Spinning of homogeneous blends of two polymers usually imposes compatibility problems. However, these can be overcome by i.e. common solvents, solvents mixtures, or surfactants. The control of the position and distribution of the functionality within the fiber is a complex task, but essential for this form of functionalization. Several studies described the ES of solution blends of PEO and PCL. Both polymers have a wide range of common solvents, but PEO is water soluble, which requires a cross-linking step to preserve the meshes.

A systematic strategy to enrich a functional compound at the surface during electrospinning is difficult. Particularly, bioactive compounds are frequently expensive substances e.g. proteins or peptides and hence not available in large quantity. In addition, the biomolecules that are at the surfaces of fibers may quickly undergo dissolution. In that respect block-copolymers with a biofunctional part and a part compatible with a synthetic fiber forming polymer are an attractive approach. In a model study a small amount of a PEO-peptide conjugate was field enriched on a PEO fiber, leading to meshes with a PEO core and a functional peptide shell.[159] In other approaches block-co-polymers were spun to provide fibers with concentric lamellar like substructures after annealing. Such compartments might be useful for incorporating functional systems i.e. nanoparticles, drugs or biomolecules.[160] In addition, emulsions-ES seems to be a feasible method to encapsulate and spin diverse biomolecules or drugs.[161] Further evaluation has to show if the surfactants might impose a risk to sensitive biological systems.

Post-funtionalization strategies are frequentlly applied and therefore well described in literature.[162] They often involve multistep procedures such as fiber surface activation, linker attachment, introduction of a functional entity. In PLGA/PLGA-*b*-PEG-NH_2 blend system GRGDY-peptide sequence was immobilized at the fiber surfaces through an ethylene glycolbis(sulfosuccinimidyl-succinate) coupling agent.[163] In another study the surface of PCL fibers was first activated by plasma treatment and the generated carboxylates allowed the coupling of gelatin by carbodiimide chemistry.[71] In RGD and gelatin functionalized meshes the cell proliferation and growth was superior to the unfunctionalized ones. However, bioactivity was still lower compared to established tissue culture plates. Also the layer-by-layer method, which has been mainly used for planar surfaces can be applied to charged electrospun fiber in order to introduce functional entities.[164]

In general, ES provides despite the difficulties to understand the intricate mechanisms involved, a wide range of tools to structure fiber surface or to compose a mesh at different length scales.

2.6 Biological aspects

Synthetic nanofibrillar matrices can provide physically and chemically stable, 3-dimensional surfaces for *ex vivo* growth of cells. Meiners and coworkers showed that fibroblast or rat kidney cells which have been grown on electrospun polyamide nanofiber meshes displayed all characteristics of their counterparts *in vivo*.[165] In addition, breast epithelial cells underwent morphogenesis to form multicellular spheroids containing lumens.

Synergistic effects of nanotopography and chemical signaling in synthetic scaffolds can certainly mimic the physical and biochemical properties of native matrix fibrils to guide cells. Patel *et al.* functionalized aligned PLLA fibers with heparin, a basic fibroblast growth factor (bFGF) and laminin as an ECM protein.[133] If the aligned nanofibers were compared to randomly oriented meshes, a significant induction of neurite outgrowth (Figure 2.10) and the enhancement of skin cell migration during wound healing could be observed with the same treatment. In addition, the immobilized biochemical factors synergized with the aligned nanofibers to promote highly efficient neurite outgrowth and to a less extent improved skin cell migration (similar to soluble bFGF) compared to untreated aligned PLLA fibers.

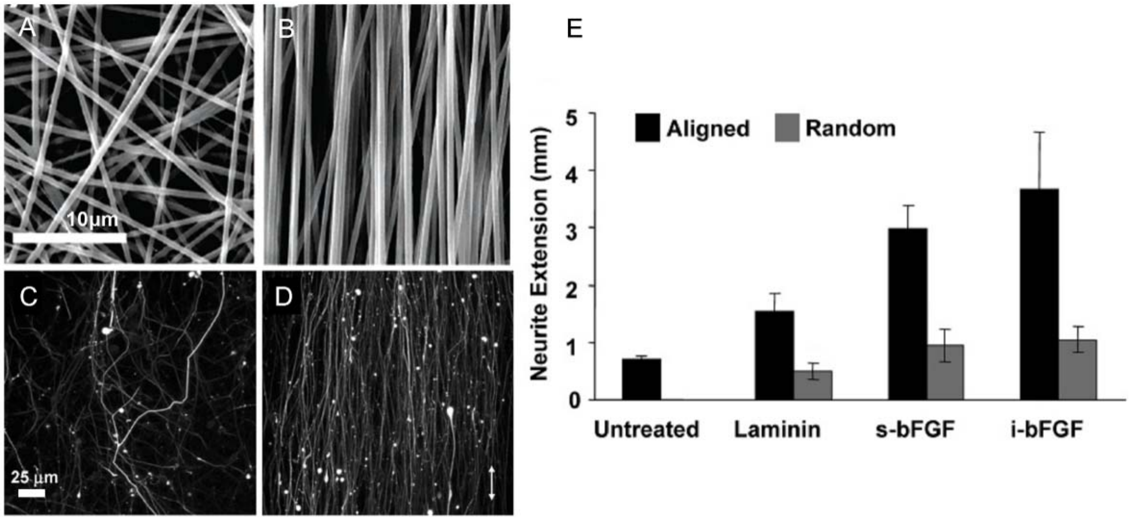

Figure 2.10. Synergistic effects of nanostructure and chemical signaling on cell guidance. The SEM micrographs of random (A) and aligned (B) PLLA nanofibers show a strong effect on neurite morphology. High-magnification confocal microscopy images indicate an isotropic growth on random (C) and the directed growth on aligned (D) PLLA nanofibers. A quantitative evaluation of neurite outgrowth on nanofibers suggests benefits from aligned, functionlized nanofibers (E, s-bFGF: immobilized with laminin, soluble bFGF, i-bFGF: immobilized laminin and bFGF); Scale bars: (A, B) 10 µm, (C,D) 25 µm).

Another interesting approach is to use nanofiber scaffolds as crystallization matrix to mimic biological composites. Xia and coworkers were able to produce meshes with a gradient of calcium phosphate content to mimic the tendon-to-bone insertion site.[166] The variation in composition led to an interesting spatial gradient in stiffness of the scaffold. This was also reflected in an activity gradient of seeded mouse preosteoblast cells.

Injectable self-assembling peptide nanofibers seems to be promising as they can create for example *in situ* intramyocardial microenvironments for endothelial cells. [167] Davis *et al.* injected self-assembling peptides into a male C57BL/6 mice. The resulting nanofibrillar microenvironment recruited progenitor cells that expressed endothelial markers too a larger extent as a reference matrigel. After 14 days vascular smooth muscle cells are additionally recruited to form functional, vascular structures and potential myocyte progenitors. When exogenous donor neonatal cardiomyocytes were co-injected with self-assembling peptides, the transplanted cells survived in the artificial microenvironment and recruited further augmented endogenous cells.

In order to create systems with larger dimensions, fibers can be processed into yarns with improved mechanical properties and enhanced cellular infiltration capabilities. For example, electrospun poly(L-lactic acid) (PLLA) nanofibers with uniaxial alignment were fabricated into braided wires. These yarns were applied as tissue sutures after coating with chitosan. The handling problem of nanofibers was overcome by initially preparing entire bundles of electrospun fibers via hot-stretch and twisting which could be used then for braiding. The braided PLLA yarns exhibited comparable tensile and knot strengths to commercially available suture. This enables tying wounded tissues for a complete healing period. The yarns showed in an *in vivo* study no cyto-toxicity, promote cell in-growth and the results suggested a improved histological compatibility compared to silk suture.[168] Another strategy to form yarn is to use oppositely charged electrospun nanofibers by coupled spinnerets.[169]

Even more feasible seems an approach from Moutos *et al.*, who used 104 µm sized, commercial available PGA multifilaments to weave into 3D structures. As shown in Figure 2.11, interlocking of multiple layers led to porous scaffolds with ~ 70-75% porosity. For cell growth purposes a composite structure was fabricated by vacuum assisted infusion of a hydrogel. The resulting scaffolds had mechanical properties similar to artricular cartilage.[170]

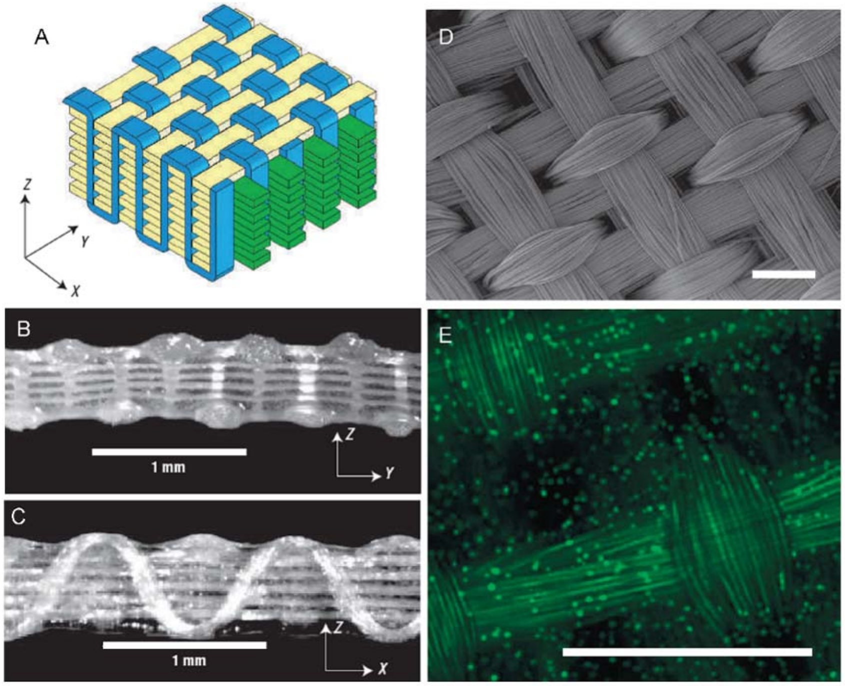

Figure 2.11. Fiber architecture of a 3D orthogonally woven structure for cartilage tissue engineering. (A) Schematics: interlocking multiple layers of two sets of in-plane fibres (x-/y-direction) with a third set of fibers in the z-direction as shown in B and C (cross-sectional view: Y–Z plane and X–Z plane, respectively). View of the X–Y plane (SEM) shows the 104 µm thick bundles composed of 8 µm PGA fibers. Fluorescent image of a freshly seeded construct shows the uniform initial distribution of porcine articular chondrocytes (label: calcein-AM; Scale bars: 1 mm (B,C) and 300 µm (D,E)).

2.7 Selected characterization methods

X-ray photoelectron spectroscopy (XPS)

In XPS, X-rays are directed onto the sample surface and electrons escape due to the photoelectric effect. The emission process is fast, so that the photoelectrons create an ionized atom, which will relax subsequently into the ground state by recombination. Electrons have a very limited mean free path in matter, which leads to the surface selectivity of XPS. Therefore, only electrons from a 2-10 nm depth region can leave the surface without loosing energy. The sample surface is located in an ultra-high vacuum (UHV) chamber during the measurement, so that photoelectrons from the sample surface can freely travel to the spectrometer. The kinetic (E_{kin}) energy of the electrons is measured in an electric field. The binding energy (E_{bind}) of the electron can be calculated by knowing the energy of the initial x-ray (E_{photon}) and the work function of the spectrometer (E_{work}), using the following equation:

$$E_{bind} = E_{photon} - (E_{kin} + E_{work})$$

The primary information provides the atomic surface compositions of each element except for H and He. However, secondary information about the chemical environment, oxidation number, depth profile, overlayer thickness, plasmons, shake-ups, inelastic background and Fermi level can be obtained. The nominal sensitivity is 10^{13} atoms/cm^2 (~ 1%) and an lateral imaging resolution of ~ 10 μm is possible.[171]

Scanning electron microscopy (SEM)

In 1932 Max Knoll and Ernst Ruska constructed the first prototype electron microscope in order to further increase the spatial resolution provided by light microscopy. In SEM, the surface of a sample is scanned with a highly energetic (~ 100 keV) electron beam. The reflected secondary and backscattered electrons are detected through an electromagnetic lens system in the same way as light by convex lenses in optical microscopy. The resulting electronic image reflects the electron-emissivity of the surface, which depends on the local conductivity, microstructure and chemistry of the sample. SEM is an UHV technique as XPS. The measurement of non-conducting samples is difficult due to charging effects and therefore samples are often coated with a thin layer of electrically conductive material, typically Au or Pd. By microscopic methods, the structure of a sample is magnified and the obtained picture gives primary information about its morphology and topology. Secondary information can reveal details of its crystallographic structure. Only a small part of the sample is analyzed and the method is susceptible to artifacts or distortions due to radiation effects. The resolution of a microscope is limited by the wavelength λ of the incident beam, and has to be short in order to resolve fine details. The wavelength of the electron beam depends on the accelerating voltage, which is typically between 1 and 50 kV. The resolution of SEM is ~ 5 nm.[172]

Atomic force microscopy (AFM)

Binnig, Quate, and Gerber first introduced AFM in 1985 to image samples with very high resolution under nonvaccuum conditions.[173] Direct force is typically measured between a sharp tip (probe) on a cantilever and the sample surface. The deflection of the cantilever is monitored using a reflected laser beam which is detected using a four-segment photodiode. By this, normal (cantilever deflection) and lateral (cantilever torsion) forces can be detected. When the normal force signal is applied to control the vertical tip position in a feedback loop, the sample surface can be laterally scaned by the tip using constant force mode. Therefore, the computer aquires a 3D image of the samples (i.e. sample topology). In contrast, a topology image can also be created using a constant tip-surface distance mode, but this is more susceptible to tip damage and therefore less used. The tip-surface interactions can include Van-der-Waals forces, electrostatic interactions, specific interactions and capillary forces. Therefore, this instrument is very attractive for nondestructive investigation of biomaterials. Different variants of the AFM technique have been developed since the early 1990s as for example the tapping mode, which is very interesting for biological surfaces because of its gentleness. In this mode the vertical tip position is modulated at the resonance frequency of the cantilever. Shifts of resonance-frequency and phase (due to tip-surface interaction) are used to gain additional information from the sample surface. In addition, the tip on the cantilever is for certain applications omitted and replaced by a bead to probe samples.[174]

Generally, AFM image has a high lateral and depth resolution of ~ 0.1 nm, but it can be very complex to interpret. The primary information is obtained about topography and tip-surface forces. Additionally, secondary information about local mechanical properties and interactions forces as for example in nano-tribology (friction) can be derived.[175]

Porosimetry for electrospun fiber meshes

Several methods are available to characterize the porosity of electrospun nonwoven membranes like for example capillary flow porosimetry. Its principle is based on the difference in flow rates of a gas through the dry membrane and the membrane wetted with a low surface energy fluid. It characterizes the mean flow pore diameter, which indicates the size of the smallest constriction in the pores through which 50% of the gas flows when the membrane is dry. While this method is of interest for transport applications, it does not provide information about the distribution of pore volume within the membrane. In this context, mercury intrusion porosimetry and liquid extrusion porosimetry are employed. The intrusion method is based on the measurement of the volume of a non-wetting liquid, e.g. mercury, penetrating the pores of the membrane as pressure increases. In contrast, liquid extrusion relies on the volume measurement of a wetting liquid that is extruded from the pores of the membrane as pressure is elevated. The wetting or non-wetting of a liquid depends its contact angle (θ) with the membrane material. The pressure (P) at which a wetting liquid is extruded from, or a non-wetting liquid is intruded into, the pores with diameter D can be calculated by the Washburn equation:

$$P=+/-\ 4\gamma \cos \theta / D$$

In the equation, γ is the surface energy of the liquid. The positive algebraic sign corresponds to liquid extrusion where $\cos \theta > 0$, and the negative prefix is applied to liquid intrusion, where $\cos \theta < 0$. Mercury is typically the preferred liquid for intrusion porosimetry, because of its high contact angle of 130-140° with most materials. On the one hand, mercury intrusion porosimetry measures more accurately the total pore volume of the membrane than liquid extrusion porosimetry because of symmetry considerations.[176] On the other hand, intrusion porosimetry potentially suffers from inaccuracies due to the high pressures that are frequently applied to intrude mercury into the smallest pores of the membrane. For very compliant materials like electrospun nonwoven fiber mats composed of small fiber compared to conventional fiber fabrics this issue is in particular serious. Similar problems have been indentified in the porosity characterizations of xerogels and aerogels.[177]

3 Matrices with controlled porosity

3.1 Fabrication of bimodal fiber meshes

The pore sizes of nanofiber meshes are inherently small given by the fiber diameters of nanofibers and the nature of the electospinning process. So far, approaches reported to increase pore sizes include additional steps and processes aside from continuous one-syringe electrospinning, which make the mesh production more complicated. Electrospinnning (ES) produces fibers with a distribution of diameters. Normally, the intent is to keep the range as narrow as possible. For cellular infiltration however the other extreme might be of advantage. The goal of this Chapter is to use a single-step process to obtain bimodal fiber meshes, where diameters differ by one order of magnitude.

Poly(ε-caprolactone) (PCL) and its copolymers are considered as one of the most important polyester classes for biomedical engineering.[178, 179] For this reason, PCL was investigated in this study to spin bimodal meshes exhibiting biocompatibility and sufficient stability due to the slow biodegradation characteristics of PCL. The electrospinning behavior of PCL has been extensively described.[138, 146, 149, 151, 152, 178] However, commonly chloroform ($CHCl_3$) at higher spin rates or solvent mixtures for example $CHCl_3$ with dimethylformamid (DMF) were applied to generate meshes with well-controlled fiber diameters. While prior work focused on the electrospinning in the axial stable regime (or normal regime of bending instability) of the process to produce uniform PCL meshes, the spinning at the borderline of the stability of the process was investigated here to generate mixed meshes. The electrospinning was performed on a standard setup (Chapter 6.1.1.3) using aluminum foil as collector, a fixed tip-to-collector distance of 7 cm, and applying 4-7 kV to generate a single spin jet. The spinning of high concentration solutions of 15% w/v PCL in $CHCl_3$ lead to bimodal meshes when rather reduced feed rates down to 0.2 mL/h were applied. Figure 3.1(d) shows a scanning electron microscopy (SEM) image of the resulting mixed meshes, indicating an interwoven fiber system that combines 200-600 nm small-sized fibers with 4-9 µm large-sized fibers. The porosity seen on the surface of the larger fibers is a common feature of electrospinning from highly volatile solvents, and can be explained either by vapor[180] or by temperature induced phase separation.[126]

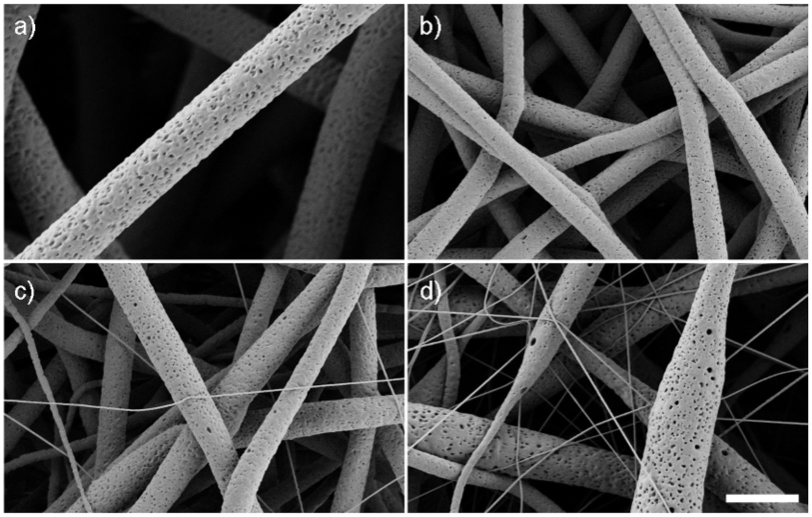

Figure 3.1. SEM micrographs of PCL fiber meshes obtained after electrospinning at different feed rates (a) 1, b) 0.4, c) 0.3, d) 0.2 mL/h. The number of thin fibers increased with decreasing feed rate (15% w/v PCL / $CHCl_3$; 52% humidity; scale bar 10 µm).

In order to obtain deeper insight into the process, a parameter screen was performed to examine the occurrence of bimodal fiber meshes by systematically changing PCL concentration, spin rates and humidity. The importance of the concentration was evaluated. For this purpose, PCL solutions in $CHCl_3$ with 10, 15, 20, and 25% w/v (PCL/$CHCl_3$) were electrospun at a spin rate of 1 mL/h and with an intermediate humidity of 47-68%. The SEM images of the meshes show, with increasing polymer concentration, the well-known transition of electrospraying (not shown), to electrospun beaded fibers to porous fibers with uniform cylindrical shape (Figure 3.2).[181]

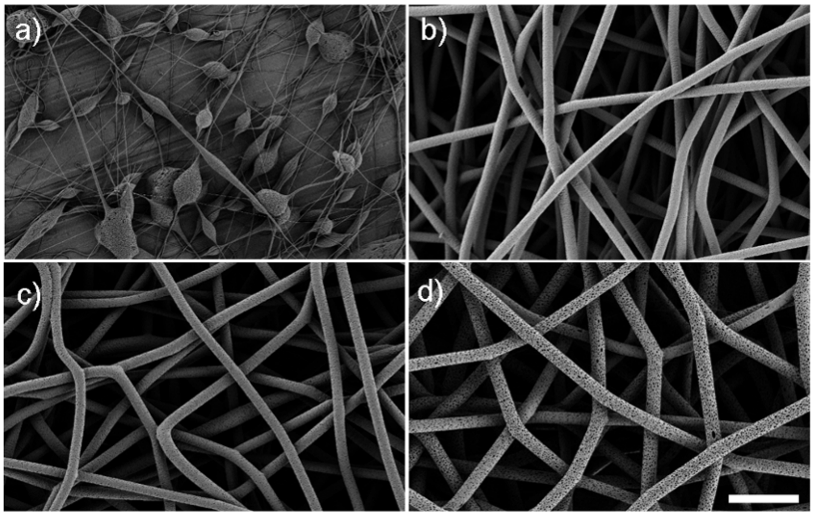

Figure 3.2. SEM images of electrospun fibers obtained by spinning PCL/$CHCl_3$ solutions with different concentrations of a) 10, b) 15, c) 20 and d) 25% w/v (rate of 1 mL/h, scale bar: 50 µm).

Bead-free fibers were formed at a concentration of 15% w/v or higher. The bimodal regime could be reached by reducing the spinning rates. Compared to the high rates, e.g. 1-18 mL/h that are commonly used to produce uniform PCL fibers,[137, 138, 145, 146, 152] the reduction to rates of 0.2 mL/h resulted in mixed meshes. Figure 3.1 shows the effect of the spinning rates on the mesh morphology. The decrease of the spinning rate from 1 to 0.4 mL/h only led to a minor decrease of the fiber widths from roughly 7 μm to 3-4 μm (Figure 3.1a and b). However, at a rate of 0.3 mL/h, bimodality of the meshes started to become evident (Figure 3.1c). The amount of thin fibers increased while further decreasing the spin rates to 0.2 mL/h (Figure 3.1d). The thick fibers exhibited obvious undulations in the fiber diameter and occasionally thinning to the size of the small ones could be found (Figure 3.1d). The occurrence of bimodal meshes at spin rates of 0.2 mL/h was evident also for higher concentrations. However, the diameter of both the small and the large fibers increased to ~ 1 μm and 10 μm respectively, upon increasing the concentration (Figure 3.3).

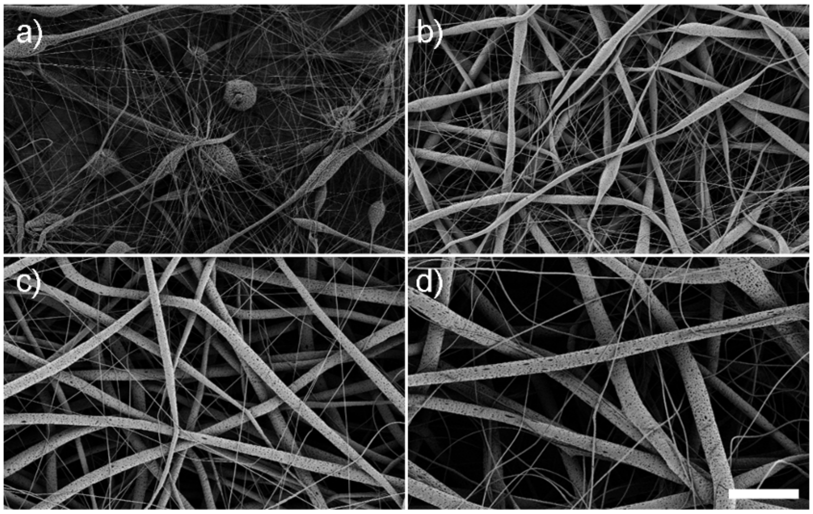

Figure 3.3. SEM picture series of electrospun fibers obtained after spinning PCL/$CHCl_3$ solutions with different concentrations such as a) 10, b) 15, c) 20 d) 25% w/v at reduced spin rates of 0.2 mL/h (scale bar: 50 μm).

In addition to the rate of spinning, the humidity was also found to affect the bimodality. A decrease of the humidity from 52% to 39% preserved the bimodality when spinning a 15% w/v PCL solution at rates of 0.2 mL/h. Consistent with the literature, the reduction of the humidity led to a reduced surface porosity of the larger fibers (Figure 3.4a).[180]

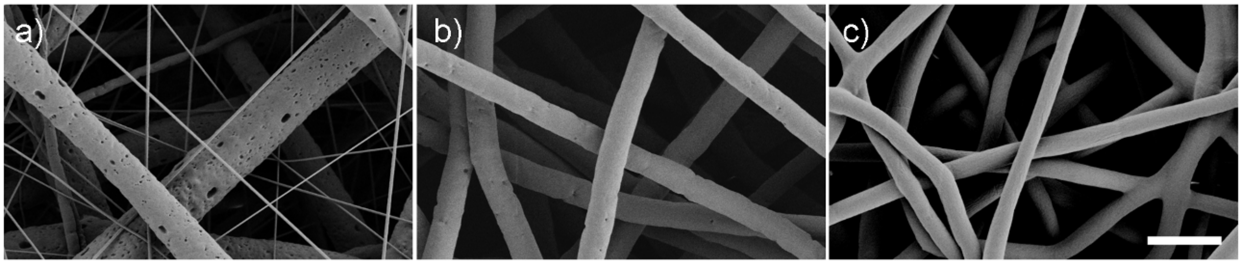

Figure 3.4. SEM pictures of PCL fibers obtained by electrospinning a PCL/CHCl$_3$ solution at variable humidity such as a) 39%, b) 31% and c) 13% humidity (concentration: 15% w/v, feed rate: 0.2 mL/h, scale bar: 10 µm).

Further decrease of the humidity to 31% resulted in unimodal 3.5 ± 0.5 µm thick fibers with a few surface pores, whereas a humidity of 13% led to fibers that showed no surface porosity and a uniform width of 2-3 µm. The effect of humidity on electrospinning has so far not been deeply investigated. An exception is the effect on surface porosity of fibers spun from volatile solvents.[180] Apparently, a minimum humidity seems to be required to reach the bimodal regime.

To elucidate the mechanism that generates bimodal fiber meshes, the SEM micrographs were evaluated (Figure 3.5a1). It was evident, that thick fibers underwent stretching which led to thinning. Occasionally, it was observed that also the thin fiber segments thickened ones as seen *e.g.* in Figure 3.1d and Figure 3.5a1. Thus a periodically changing stretch rate could be identified to cause the bimodality. This can be explained by the occurrence of axial-symmetric instability in the spin jet as it has been already predicted in the operating diagrams of Hohman *et al.* for low feed rates and field strengths.[182] Therefore, the process proceeds not in the regime dominated by bending instabilities, but rather in an oscillatory bistable mode.

The periodic modulation of the thickness of the spin jet was conclusively confirmed by analysis of high speed camera images of the spin jet. Figure 3.5a2 shows that the origin of fiber bimodality can be located to the early spin phase as it occurs closely after the needle orifice. The sequence of images shows the presence of thick and thin parts in the jet, which remain in phase looking at the different high-speed frames. This is in contrast to a uniform, straight jet that was developed when micron-sized fiber meshes were produced (Figure 3.5b1/2).

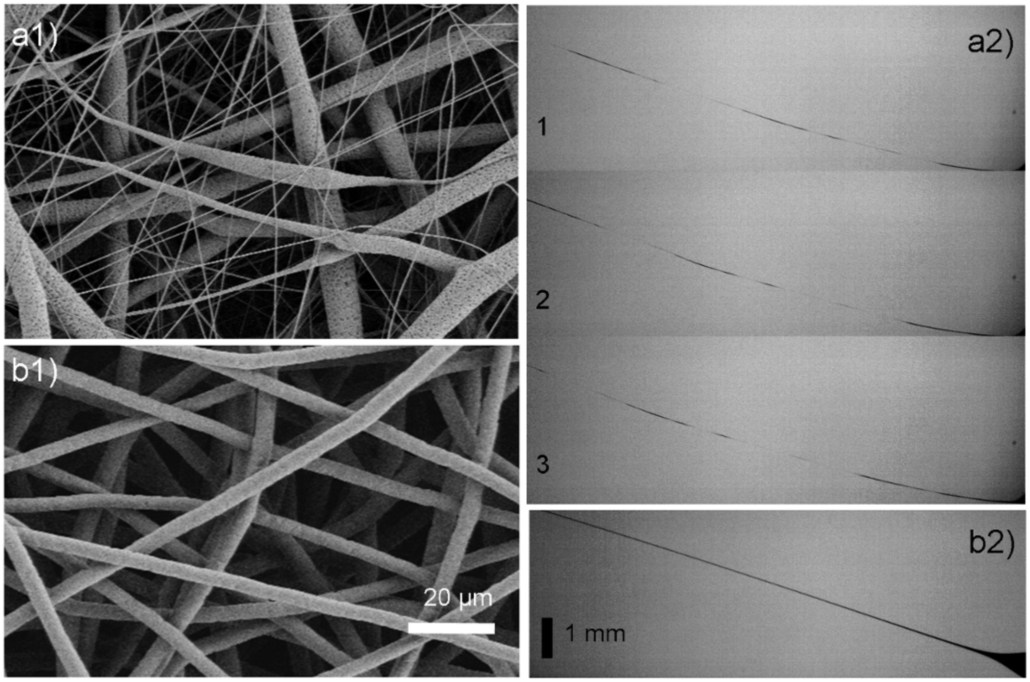

Figure 3.5. SEM micrographs showing the PCL nonwovens with bimodal fiber size distribution as directly obtained by spinning a 15% w/v PCL/$CHCl_3$ solution at a rate of 0.2 mL/h and ~ 50% humidity. Thick and thin fibers caused by different stretch rates can be observed (a1). At ~ 30% humidity unimodal fibers (rate: 0.2 mL/h) were processed (b1). High speed images of the spin jet leading to the bimodal fiber mashes (a2: 1-3) and as comparison, the corresponding straight jet that leads to unimodal, microsized fiber meshes are shown (b2) (a2/b2: spin direction from right to left, pictures are taken at 1995 fps close to the syringe tip, 50 ms exposure time).

Interestingly, these modulations suggest an oscillating process and exclude branching in the early phase as well as the existence of multiple asymmetric jets.[183] The physics behind the phenomenon can probably be rationalized by considering the related mechanism of extended bead formation.[181] However, beading usually takes place at much lower concentrations and much higher spin rates (Figure 3.2). In the present case highly elongated beads were formed due to the high viscosity of the solution, providing sufficient entanglements of the polymer molecules to produce not the common beads but homogenous fiber segments (microfibers). A simple analogy can be found when the flow rate of water from a tap is reduced resulting in the known transition of a straight water jet to a periodically modulated jet to a chain of drops, known as Plateau-Rayleigh-instability.[184] As this axial instability in a fluid flow jet is driven by surface tension, and the latter is dominating especially in the early phase of spinning process, an influence of the humidity appears to be very likely. The surface tension of the jet can be either changed by the condensation of water onto the jet surface or partial dissolution into the chloroform solution. Therefore, the increase in humidity might have resulted in the earlier occurrence of the axial instability and shifted the spinning process already at higher flow rates into the bimodal regime, where periodically changing stretch rate was promoted.

To investigate if the occurrence of the bimodal regime is a generic effect in electrospinning, other polymers such as poly(lactic-*co*-glycolic acid) (PLGA), poly(methyl methacrylate) (PMMA) and polystyrene (PS) were electrospun from chloroform solutions (solution properties given in Table 1). Electrospinning conditions have been applied, where bimodality should occur. The SEM images show bimodality in the PLGA fiber meshes, whereas spinning of PMMA and PS led to unimodal sized fibers (Figure 3.6).

Table 1. Different properties of polymer and their corresponding chloroform solutions.

Polymer systems	**Mn [kDa]**	**PDI**	**Tg / Tm [°C]**	**conc. [% w/v]**	**dyn η [mPa.s]**	**conduct. [µS/cm]**
PCL	78	1,65	(-60) / 57	15	830	0.01
PLGA	161	2,08	57	5	513	0.01
PMMA	173	1,88	123	20	317	0.01
PS	103	2,33	102	27	375	0.01

(M_n= number average molar mass, PDI = polydispersity index, Tg/Tm = glas/melting temperature, conc. = concentration, dyn. η = dynamic viscosity, conduct. = conductivity; σ_{CHCl3} = 0.01 µS/cm)

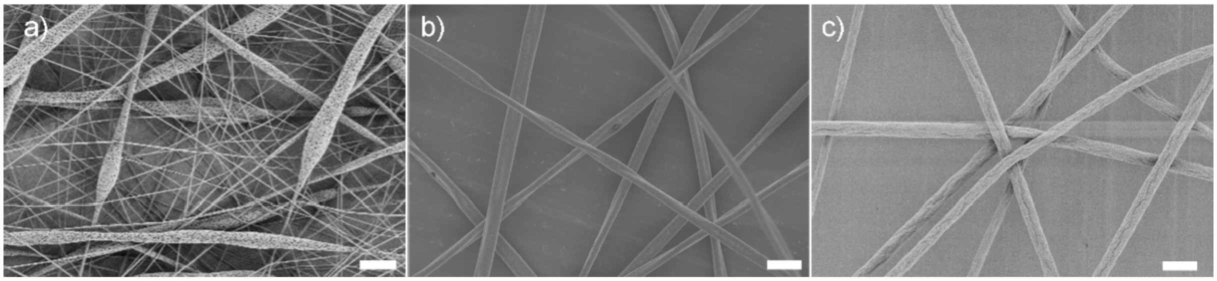

Figure 3.6. a) Bimodal PLGA, b) unimodal PMMA and unimodal PS fibers were obtained while electrospinning under conditions were bimodality should occur (solvent: chloroform, rate: 0.2 mL/h, humidity: 45%, SEM scale bars 10µm).

Conductivity can be excluded as a key parameter because it is generally dominated by the solvent. It was apparent that PCL and PLGA solutions exhibited higher viscosities at lower polymer concentrations compared to the PMMA and PS solutions. Moreover, the thermal bulk properties between the PCL/PLGA and PMMA/PS were different. In a good solvent, differences in T_g or T_m are not relevant. However, as chloroform is highly volatile, polymer concentration increased rapidly after the solution left the nozzle, making potential demixing phenomenon relevant. Therefore, the role of bulk properties progressively became important. Considering the high polymer loading, the glass transition in the PMMA/PS systems probably suppressed the viscoelastic behavior which is certainly required for the periodically changing stretch rate mechanism. Here, it has to be pointed out that the effect of bimodality appeared to be a complex phenomenon and the cause was probably a coupling of the low flow rate, humidity, viscosity and nature of the polymer solution (viscosity, solvent-solute interaction) and the polymer properties itself (solubility, Tg).

In order to evaluate the three-dimensional pore structure of the electrospun bimodal fiber mesh, mercury porosimetry was performed (Figure 3.7). The results were compared to two reference meshes, exhibiting on the one hand uniform microfibers with widths of 5-6 µm and on the other hand nanofibers of 0.2-1.2 µm in width. All samples were electrospun onto water, providing thick, self-sustained meshes, which are required for biological testing. It had been shown that the fiber diameters and diameter distribution of fibers were apparently not dramatically dependent on the ground used. Bimodal fiber meshes could be observed under similar conditions, regardless if water or aluminum foil was applied as ground (Chapter 6.1.1.3). In the literature, electrospun fiber meshes are frequently characterized by the overall porosity and the mean pore size. These are, however, volume average values not fully representing the properties of the meshes, which are relevant for cellular infiltration. More conclusive values are the pore size distribution and the number of pores in the relevant regime of 10-100 µm. [144]

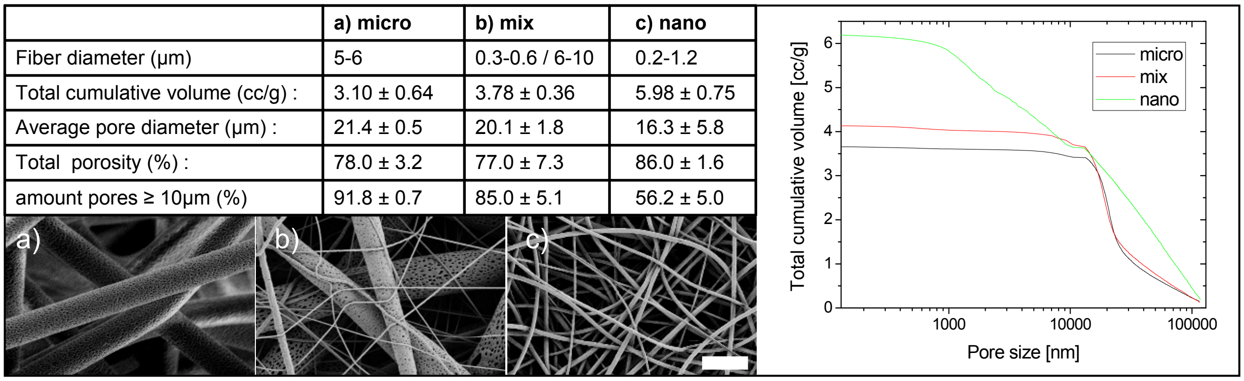

	a) micro	**b) mix**	**c) nano**
Fiber diameter (µm)	5-6	0.3-0.6 / 6-10	0.2-1.2
Total cumulative volume (cc/g) :	3.10 ± 0.64	3.78 ± 0.36	5.98 ± 0.75
Average pore diameter (µm) :	21.4 ± 0.5	20.1 ± 1.8	16.3 ± 5.8
Total porosity (%) :	78.0 ± 3.2	77.0 ± 7.3	86.0 ± 1.6
amount pores ≥ 10µm (%)	91.8 ± 0.7	85.0 ± 5.1	56.2 ± 5.0

Figure 3.7. Results of the mercury porosimetry and the corresponding SEM pictures of a) micro, b) mix, and c) nanosized electrospun fiber meshes (scale bar: 10 µm).

The microfiber meshes exhibited over 90% of their pores between 10-100 µm and had a maximum increase of total cumulative volume near 20 µm as shown in Figure 3.7. The mixed fiber meshes exhibited comparable pore characteristics as the microfiber meshes. However, a stronger increase in cumulative volume at 20 µm was evident, resulting in a higher overall pore volume.

While the microfiber meshes showed a reduced overall porosity compared to the mixed ones, the pore size and pore distribution in both systems could facilitate ingrowth of cells. As expected, the nanofiber meshes had large pore volumes. Nonetheless, only 56% of the total cumulative pore volume will be accessible for cells. Hence, porosimetry suggests that the pores are too small for effective cell infiltration, which is consistent with previous observations describing poor cellular infiltration in sub-microfiber networks.[144]

3.2 Biocomposites by fiber directed crystallization

Inspired by the biomineralization in Nature, the nonwoven meshes discussed in the previous section were used to direct crystallization processes and obtain inorganic-organic hybrids. This section discusses the selection and use of calcium carbonate and calcium phosphate as two biologically relevant systems. In the case of calcium carbonate, the idea was to design composite materials, which could be precursors for porous crystals. The nanofiber-enhanced composite material has the pores fully filled by the organic phase that modulates the mechanics of the inorganic network. In Nature, such concepts are present in nacre where the organic phase dramatically increases the fracture toughness of the composite material. Regarding the architecture, the present approach can be considered, to some extent, like a “steel reinforced concrete construct”.

Instead, using calcium phosphate is interesting to coat fibers while still maintaining the porous structure for potential cell infiltration. In bone, for example, collagen fibrils are used as crystallization matrix of calcium phosphate. From that point of view, using electrospun nano/micro sized nonwovens might be a feasible approach to generate materials by abstracting the bioconcepts of bone.

3.2.1 Calcium Carbonate

Nonwoven meshes composed of micro and/or nanosized poly(ε-caprolactone) (PCL) fibers (Chapter 3.1) are used as templates for crystallization processes to facilitate the generation of fiber enhanced or directed $CaCO_3$ composites as well as porous crystalline materials potentially with bimodal pore systems as shown schematically in Figure 3.8. The task was here to fully fill the pores of nano and/or micronsized fiber meshes within $CaCO_3$ crystals (poly- or single crystal). The fibers would then be removed by means of calcination or leaching. Porous single crystals would be attractive for electronic, optical or sensory applications.

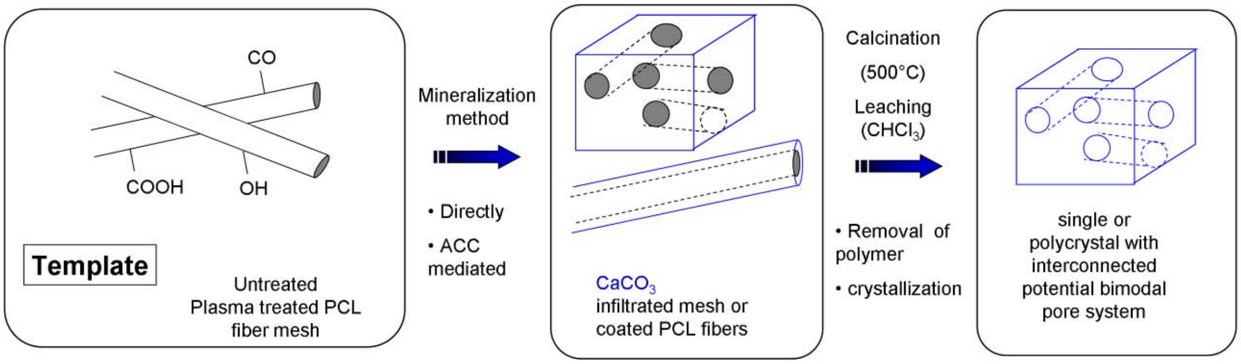

Figure 3.8. Electrospun meshes are used as template for different crystallization methods for creation of $CaCO_3$/PCL composite or porous $CaCO_3$ crystals.

To effectively fill the pore systems of the meshes, different crystallization routes have been explored. Direct crystallization methods were conducted in first attempts while amorphous calcium carbonate (ACC) mediated pathways performed in a second set of experiments. The latter was inspired by biomineralization in nature where ACC is believed to play an important role as a precursor form. The meshes were mineralized by means of gas diffusion, double diffusion, saturated solution, precipitation, centrifugation and vacuum-assisted infiltration with a transient amorphous ACC phase (Table 2, more details see Chapter 6.1).

Table 2. Different mineralization routes and their effects on mesh coating.

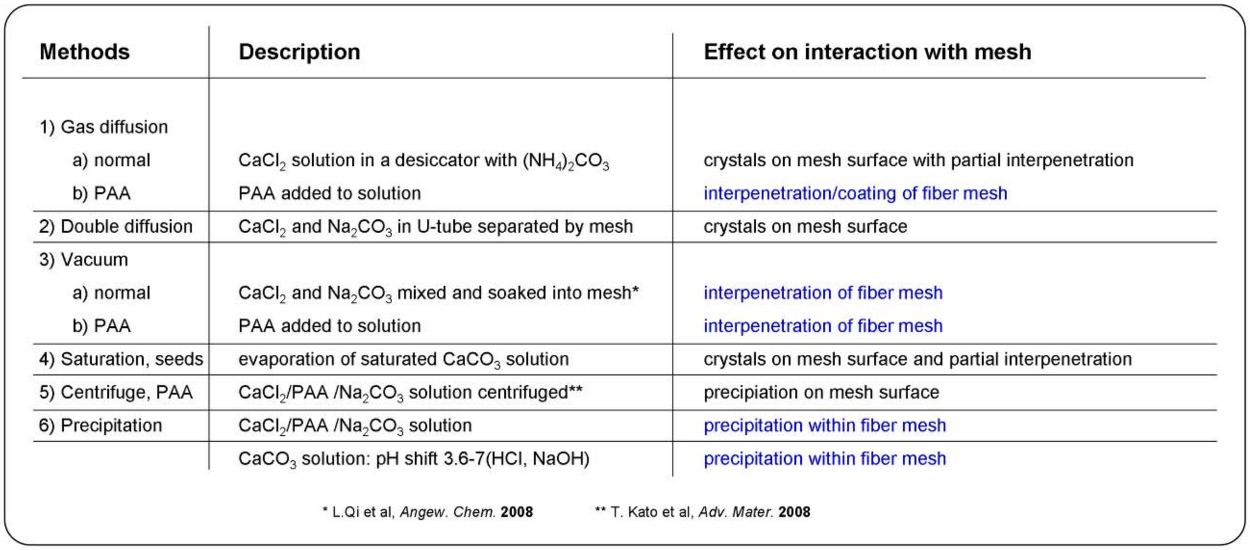

Methods	Description	Effect on interaction with mesh
1) Gas diffusion		
a) normal	$CaCl_2$ solution in a desiccator with $(NH_4)_2CO_3$	crystals on mesh surface with partial interpenetration
b) PAA	PAA added to solution	interpenetration/coating of fiber mesh
2) Double diffusion	$CaCl_2$ and Na_2CO_3 in U-tube separated by mesh	crystals on mesh surface
3) Vacuum		
a) normal	$CaCl_2$ and Na_2CO_3 mixed and soaked into mesh*	interpenetration of fiber mesh
b) PAA	PAA added to solution	interpenetration of fiber mesh
4) Saturation, seeds	evaporation of saturated $CaCO_3$ solution	crystals on mesh surface and partial interpenetration
5) Centrifuge, PAA	$CaCl_2$/PAA /Na_2CO_3 solution centrifuged**	precipiation on mesh surface
6) Precipitation	$CaCl_2$/PAA /Na_2CO_3 solution	precipitation within fiber mesh
	$CaCO_3$ solution: pH shift 3.6-7(HCl, NaOH)	precipitation within fiber mesh

* L.Qi et al, *Angew. Chem.* **2008**   ** T. Kato et al, *Adv. Mater.* **2008**

As a starting point, gas diffusion was employed where an untreated nanofibrous PCL mesh in aqueous solution of 10 mM $CaCl_2$ was crystallized in a vessel by decomposition of $(NH_4)_2CO_3$ into CO_2, H_2O and NH_3. Most of the resulting crystals did not show inclusion of fibers, but rather expelled and lifted the fibers onto their top surface as visible in Figure 3.9a. In order to improve the interaction between $CaCO_3$ crystals and PCL fibers during crystallization, the fiber scaffold was plasma activated (1 min, air, 18 W). During treatment, the ester bonds on the fiber surface are supposed to be cleaved and reacted to hydroxyl, carbonyl and carboxyl groups.[185] Plasma-treated fibers were increasingly integrated into the calcite crystals as shown in Figure 3.9b. However, the crystals seemed to grow from the fiber mesh, rather than inside the fiber mesh. Attempts to switch the top side of the fiber mesh upside down after one day of crystallization in order to promote the ingrowth of crystals into the fiber mat were not successful. An alternative approach was to disturb the crystallization at the mesh surface by perturbation (Chapter 6.1.3.1). This improved the crystal incorporation into the mesh, but led to increasingly defected morphology of crystals with time.

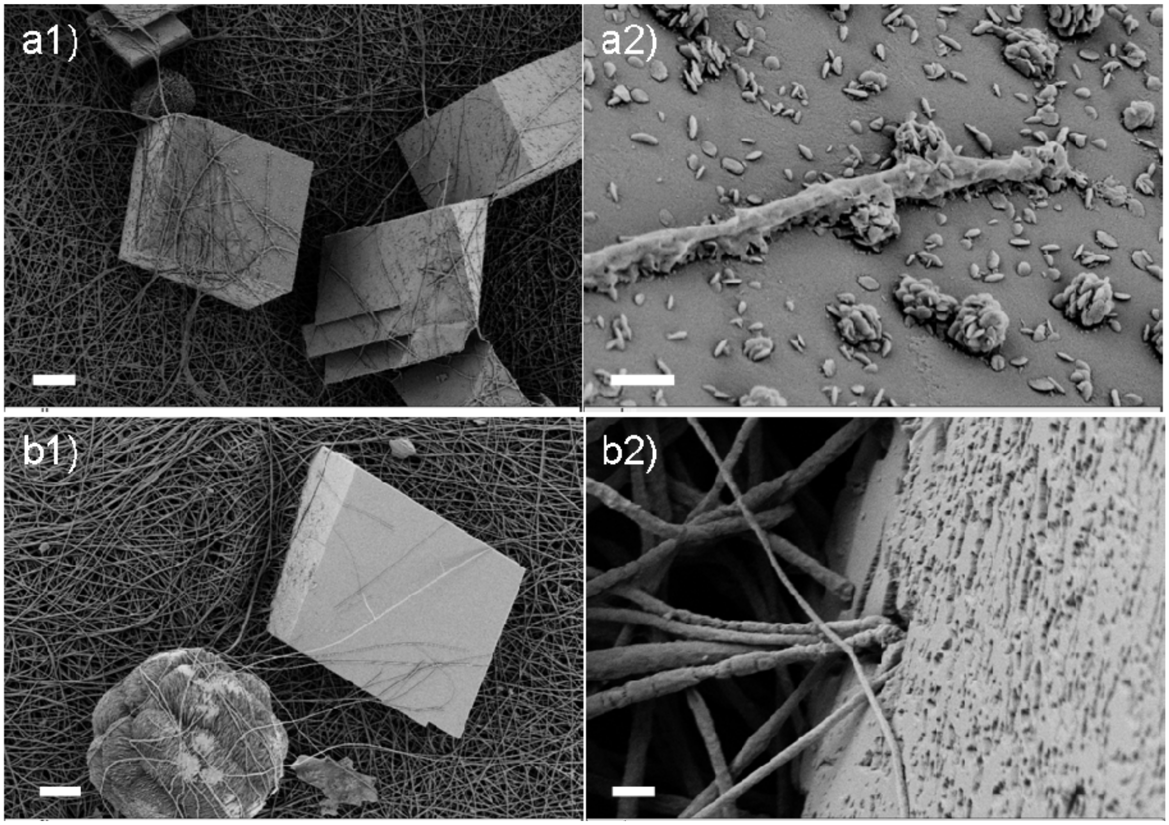

Figure 3.9. SEM imagas of calcium carbonate crystallization revealed an improved interaction of plasma-treated (b) versus untreated (a) PCL nanofiber by means of gas diffusion (conditions: $CaCl_2$=10 mM, 3 days, plasma: 1 min, 18 W, scale bars: a/b1 = 20 µm, a/b2 = 1 µm)

To improve the limited integration of $CaCO_3$ into the fiber mesh, a double diffusion experiment was conducted. The mesh was placed between two half U-tube arms, which were simultaneously filled with aqueous solutions of $CaCl_2$ and Na_2CO_3 (10 mM each). This procedure clearly improved the $CaCO_3$ incorporation, as can be seen from fully fiber-penetrated calcite crystals shown in Figure 3.10. Nonetheless, there seemed to be a larger number of small crystals compared to those formed during gas diffusion. This suggests many nucleation points. In addition, there were still some crystals growing from the surface of the meshes. Experiments using untreated PCL, variation of both concentrations and reaction times did not change the results dramtically (Chapter 6.1.3.1). Another attempt was to use the resulting small crystals as seeds for crystal extension in saturated $CaCO_3$ solution. However, this resulted in coating the mesh surface and did not improve infiltration.

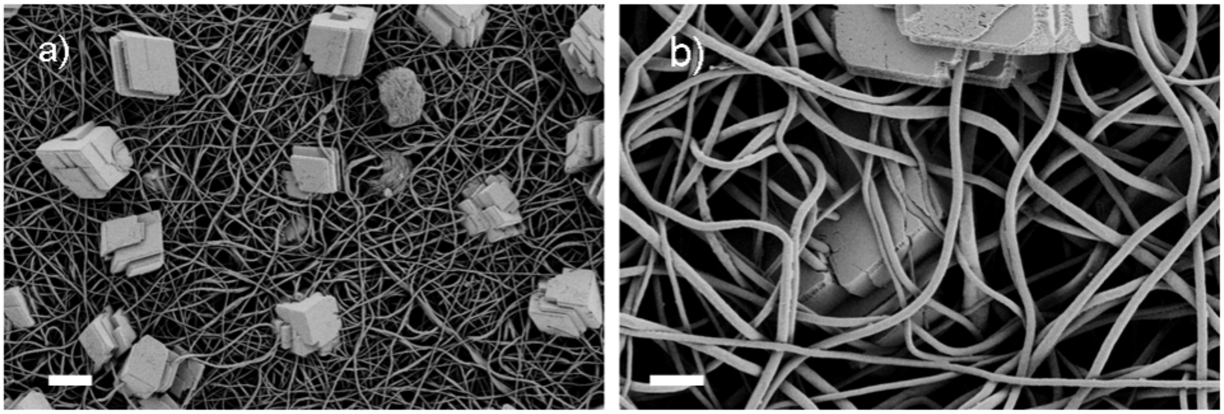

Figure 3.10. SEM images indicate that some calcium carbonate crystals were fully incoporated in the fiber mesh, while others were still on the surface (double diffusion: 10 mM $CaCl_2$ and Na_2CO_3, 2 days, scale bars: a) = 20 µm, b) = 5 µm).

Theoretically, the ideal case would be one nucleation point in the middle of the fiber mesh leading to a large single crystal. Practically, this is time-consuming as low oversaturation and hydrophobic surfaces are typically needed to prevent many heterogeneous nucleation sites. However, this might be bypassed using ACC intermediates inspired by nature. By this means, the pores might be filled with a liquid-like ACC, which converts directly into a crystal or by introduction of a second crystallization step as shown by Qi *et al.*[186] In addition Meldrum *et al.* showed that the ACC stability could be increased by cooling the anion/cation solutions prior to start of the crystallization.[187] This was applied in a double diffusion experiment, however, the results did not improve the situation shown in Figure 3.10.

The concept of cooling solutions in advance was also applied to a vacuum-assisted method adapted from Qi *et al.*.[186] This procedure was applied to a plasma-treated nanosized PCL mesh. Cooled aqueous $CaCl_2$ and Na_2CO_3 solutions were mixed, obtaining a translucent phase, which then served as infiltration solution for the fiber mesh upon applying vacuum. Figure 3.11 summarizes the results using two differently concentrated solutions.

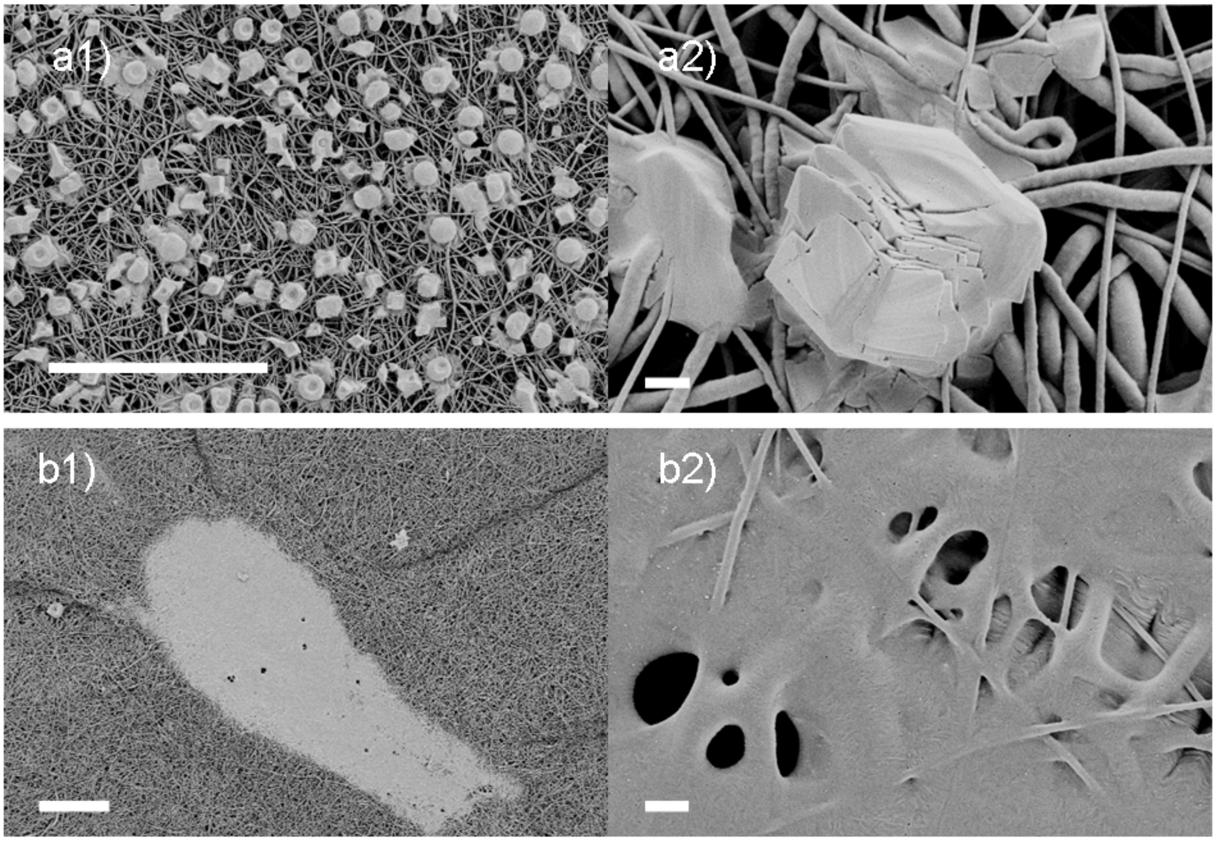

Figure 3.11. SEM images of PCL fiber meshes infiltrated by ACC precursor solutions. The incorporation of $CaCO_3$ was conducted by a vacuum-assisted protocol. a) 16 mM or b) 8 mM solutions of $CaCl_2$ and Na_2CO_3 were mixed and then ~ 0.5ml of the mixture was sucked into the mesh within ~ 1 min (scale bars: a1/2 = 100 µm, a/b2) = 2 µm).

A solution containing 8 mM calcium and carbonate ions (Figure 3.11a) resulted in small calcite-like structures after drying. Decreasing the concentration to 4 mM (Figure 3.11b), led to a large (200×500 μm^2) incorporation of amorphous-like $CaCO_3$ into the fiber mat. The wide angle x-ray diffraction (WAXS) pattern from the latter composite structure indicated no peak assigning to the $CaCO_3$ (Figure 3.12). The peaks visible were attributed to the semicrystalline orthorhombic PCL.[188] The lack of a crystalline peak might be an indication of amorphous calcium carbonate (ACC) which was in agreement with the liquid-like morphology of the $CaCO_3$. However, a low mineral content could be alternative explanationl.

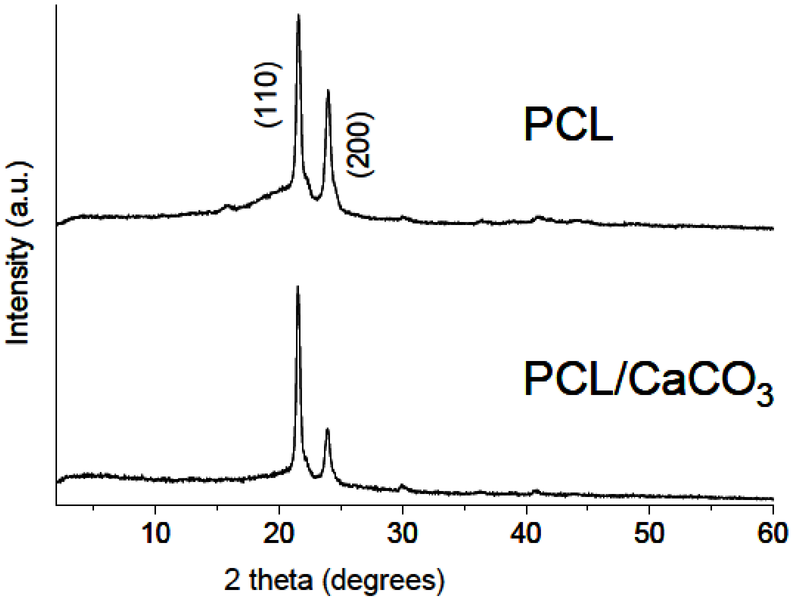

Figure 3.12. Wide angle x-ray diffraction pattern indicated no crystalline peak attributed to the $CaCO_3$.

While the $CaCO_3$ incorporation into the fiber mesh looked promising, the goal was to create larger, infiltrated patches. In order to do so, solution temperature, volume, or the infiltration time were changed for 4 mM [Ca^{2+}] and [CO_3^{2-}] ion concentrations (Chapter 6.1.3.1). However, no general trend or major improvement could be established. It seemed that $CaCO_3$ patches as large as 200×500 μm^2 represented the maximum size achievable with this method.

To further increase the inorganic mass ratio in the composite, a method adapted from Kato *et al.* was applied.[189] A paste was generated by mixing an aqueous solution containing $CaCl_2$ and poly(acrylic acid) (PAA) with an aqueous Na_2CO_3 solution reaching a concentration of 50 mM of each component in the final mixture. By aging ~20-60 min and subsequent centrifugation of the resulting precipitate into the fiber mesh, deposition was mainly observed onto the mesh surface (Figure 3.13a). In contrast, using vacuum-assisted infiltration succeeded in the incorporation of fibers within the dried $CaCO_3$ crust as evident in a cross section of the film in Figure 3.13b. The $CaCO_3$ film was probably broken by drying or handling. Nonetheless, the production of large scale (> 1 mm^2) incorporation of PCL fibers was accomplished. The $CaCO_3$ film itself consisted of small particulates (Figure 3.13b2) which might be composed out of ACC as suggested by Kato *et al.*.[189]

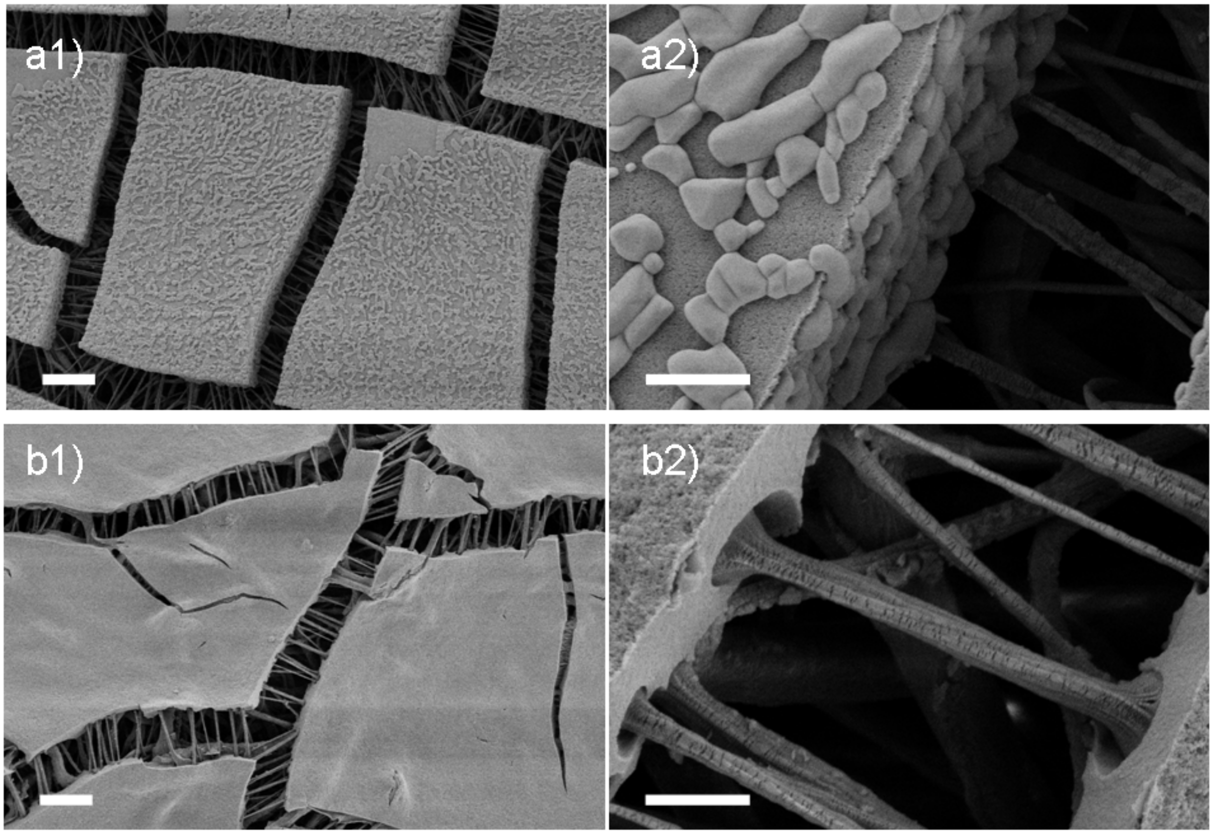

Figure 3.13. SEM images of $CaCO_3$ films coating (a) or incorporating (b) PCL meshes. An ACC paste stabilized by PAA (Mw=2 kg/mol) was infiltrated into the electrospun PCL nanofibers network by a) centrifuge and b) vacuum-assisted means (aging time: a) ~ 60min, b) ~ 20 min, scale bars: a/b1) = 10 µm, a/b2) = 2 µm).

In order to verify the composite structure, WAXS was performed. No crystalline peak which could be assigned to $CaCO_3$ was observed in the diffractogram. This suggests an amorphous form of calcium carbonate and is in agreement with the observations made from Kato *et al.*, who reported a stability of the ACC for at least 200 days at ambient conditions.[189] This procedure can also be transferred onto mixed sized fiber meshes, however here the ageing time had to be prolonged (Chapter 6.1.3.1). This revealed that the method is feasible for meshes with larger pore sizes. In addition, the precipitation could occur directly into the mesh by simple adding the mesh prior to ageing. The coverage was lower than by using the vacuum assisted procedure. Overall, this method was feasible with coating large mesh area within short period of time.

Another precipitation method was introduced and applied to mixed fiber meshes. $CaCO_3$ powder was dissolved in an acidic aqueous solution (saturated at pH 3.6, adjusted with HCl) and then its pH was shifted to neutral conditions (pH 7, NaOH). This method seemed feasible, especially in coating large fibers within the mixed fiber meshes and maintaining the pore structure (Figure 3.14).

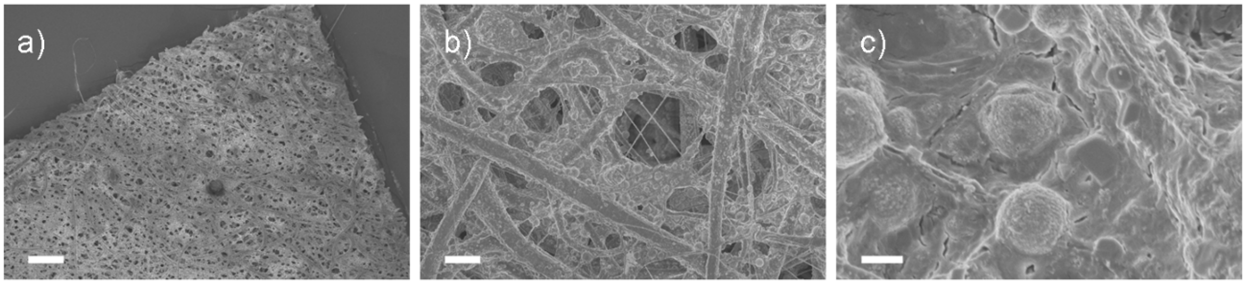

Figure 3.14. SEM of bimodal fiber meshes crystallized with calcium carbonate into a using a precipitation method by shifting the pH of a calcium carbonate solution from 3.6-7 using HCl and NaOH (mineralization time:12 h, scale bars: a) = 100 µm, b) = 10 µm, c) = 10 µm).

As a last approach, the gas diffusion method was applied using the concept of PAA as ACC stabilizer. A solution of 25 mM $CaCl_2$ and 50 mM PAA was employed so that potentially every Ca^{2+}-ion could be coordinated by a carboxylate group of the PAA. The resulting composites can be seen in Figure 3.15. The inorganic composition could be gradually increased by the crystallization time. The crystallization proceeded in particle-like precipitates, which partially coated the entire fiber and mesh surface after 4.5 days (Figure 3.15b/d). In Figure 3.15d, it can be seen that some of the ACC-like particles transformed into calcite-like polycrystals. After one week, large areas (> $1mm^2$) were coated as shown in Figure 3.15c. In summary, composite fabrication was successful using different approaches ranging from vacuum-assisted methods, precipitation and gas diffusion. It seemed to be promising to use ACC intermediates and rather high concentrated solutions for convenient pore filling.

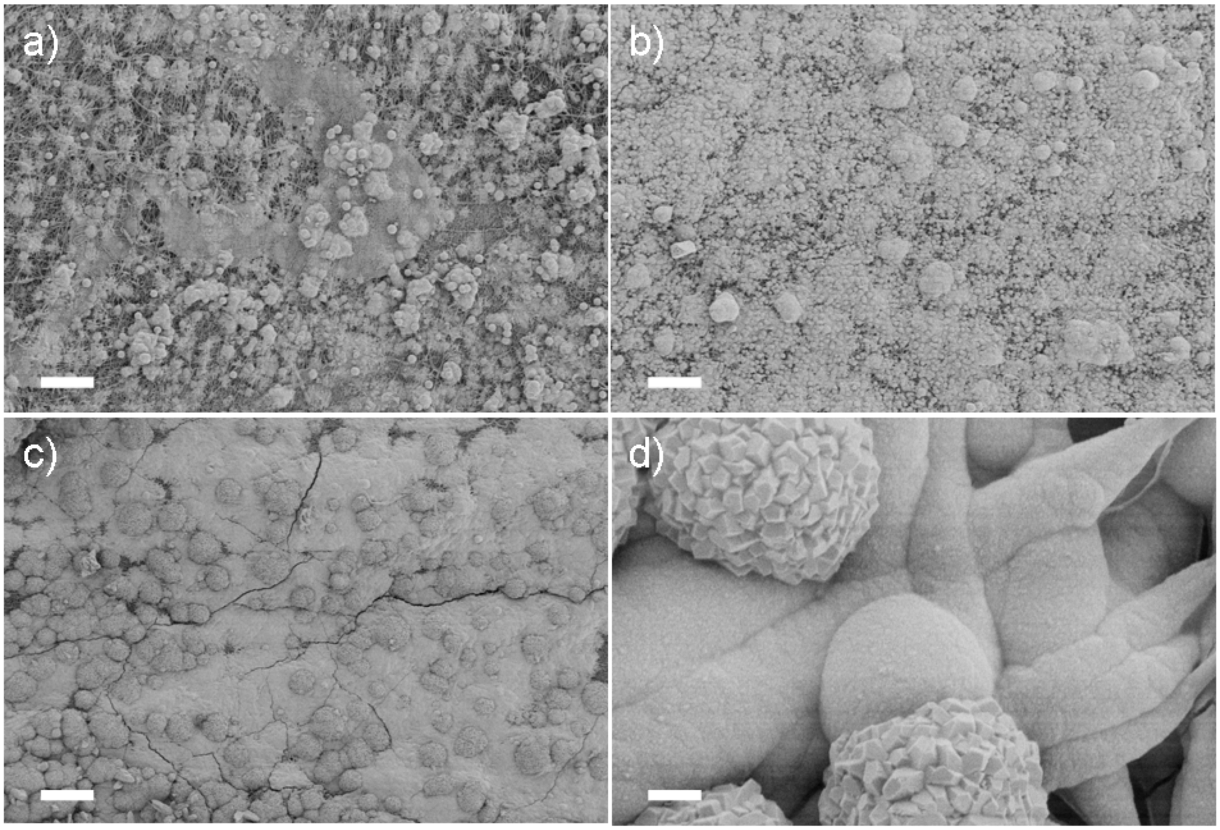

Figure 3.15. SEM images showed an increased $CaCO_3$ coating on the PCL fiber meshes with increasing crystallization time using PAA as a ACC stabilizer (Gas diffusion, $CaCl_2$: 25mM, ACC: 50mM) during a) 1, b)/d) 4.5 and c) 7 days, scale bars: a-c) = 100 µm, d) = 2 µm).

To create porous crystals and to reveal the homogeneity of the coating, the organic fibers had to be removed. For this purpose, leaching with chloroform and calcination at 500°C (~ 10°/min, 3 h dwell time) in air atmosphere were performed. While direct calcination seemed to only partially retain the replica of the nanofibrous fiber mesh, leaching of the sample nicely showed the traces of the initial fibers (Figure 3.16). To some extent, the porous structure of the mesh was kept because the fiber mesh was not completely infiltrated, i.e. fibers were just partially coated. The resulting porous body could then be fired while maintaining the pore system, while direct firing as mentioned before was not feasible.

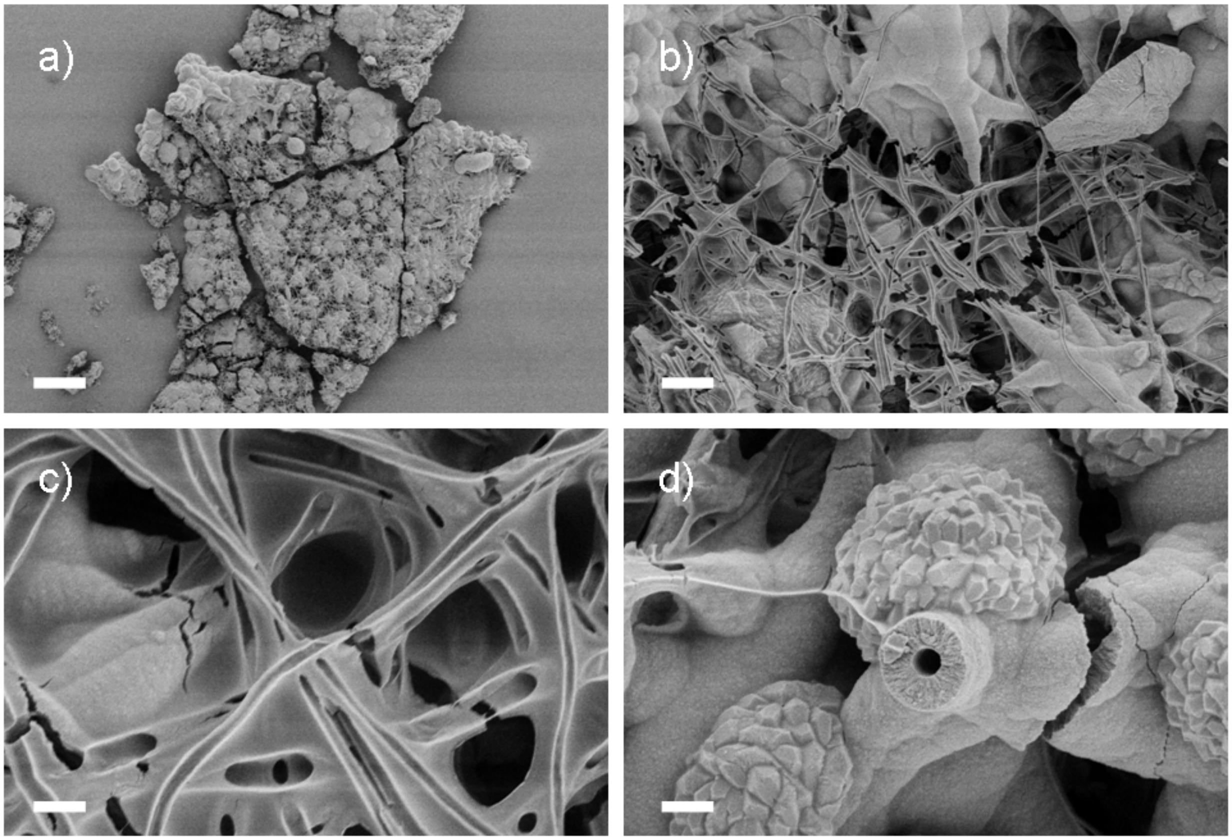

Figure 3.16. SEM images of $CaCO_3$ demonstrated an intact replica of the PCL fibers upon subsequent leaching (chloroform, 1 day). The sample was crystallized using gas diffusion during 4.5 days (scale bars: a) = 100 µm, b) = 10 µm, c/d) = 2 µm).

Analysing the leached $CaCO_3$ body shown in Figure 3.16 with x-ray diffraction suggested calcite crystals (Figure 3.17). The main peak at 29.5° 2 theta was not accompanied by large neighbouring peaks as common for vaterite or aragonite. In addition most side peaks could be assigned to different calcite crystal planes as indicated by the miller indices. The remaining small peaks (not tagged) could be attributed to vaterite. Overall, this suggested mainly calcite formation which is consistent with the SEM pictures where small calcite-like crystals grow from probable initially formed ACC particles. In addition, the composite and its leached form showed similar diffractograms. Furthermore no polymer peak is visible suggesting a large inorganic content, supporting the impressions from the SEM images (Figure 3.15b/d).

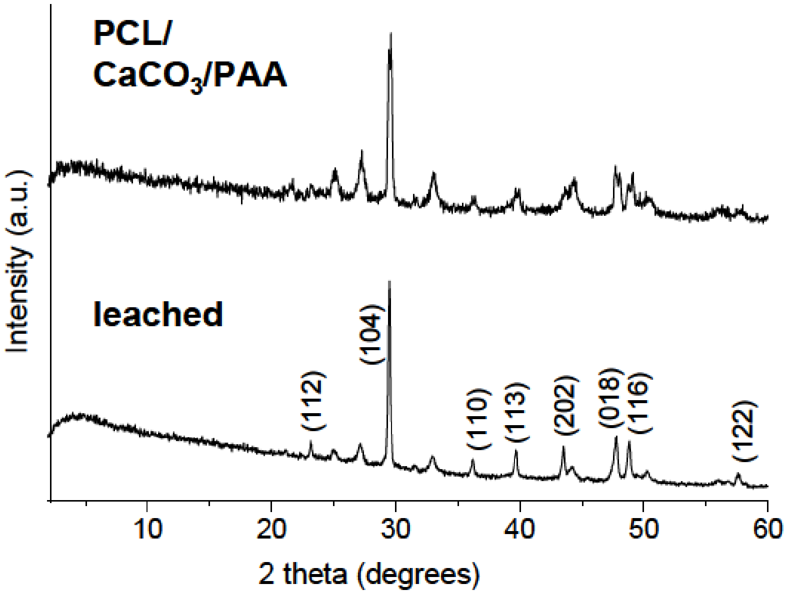

Figure 3.17. The WAXS diffractogram reveal no substancial difference between composite and leached $CaCO_3$ body. The main peak suggests mainly calcite crystals.

Porous polycrystals or $CaCO_3$/PCL composites were successfully realized, whereas the creation of porous single crystals with dimensions larger than 1 mm seemed to be challenging. While porous $CaCO_3$ could be interesting for release systems (e.g. drugs) composites might have improved mechanical properties. For this mechanical testing (e.g. tensile testing) required a large $CaCO_3$/PCL composite sample area (~ 3×3 cm^2), in addition to homogenous inorganic distribution throughout the mesh. Whilst composite materials were successfully synthesized the fabrication of larger specimens were not fully realized as the mesh encapsulation with $CaCO_3$ was not complete.

3.2.2 Calcium Phosphate

While in the case of $CaCO_3$ crystallization methods were mostly applied on a small scale (~ 10 mL), calcium phosphate crystallizations were conducted with simulated body fluid (SBF)[190] to produce larger specimens (50-100 mL) for potential mechanical testing and cell studies. SBF is an aqueous salt solution, which simulate the ion concentrations of the human blood plasma. Nanofiber, mixed fiber and microfiber meshes, were used to eventually coat them with a homogenous calcium phosphate layer. The goal was to maintain the porous structure of the scaffolds for cellular infiltration. In addition, the role of the mesh structure on the crystallization behavior was elucidated.

In a preliminary experiment, a mixed fiber mesh was mineralized using a 2×SBF solution for 2 weeks under dynamic conditions. The resulting materials demonstrated a rather inhomogenous coating, composed of small particles and blocks, which fully encapsulated areas of the fiber mesh (Figure 3.18a-c). The latter, however, only occurred in partial regions within the crystallization time so that the porous structure of the mesh was maintained. From the thermogravimetric analysis (TGA) of the composite at 550°C 13 wt% residual mass was observed. Bulk PCL showed 1 wt% residual mass at 500°C. Therefore, the composite was composed of 12 wt% inorganic coating.

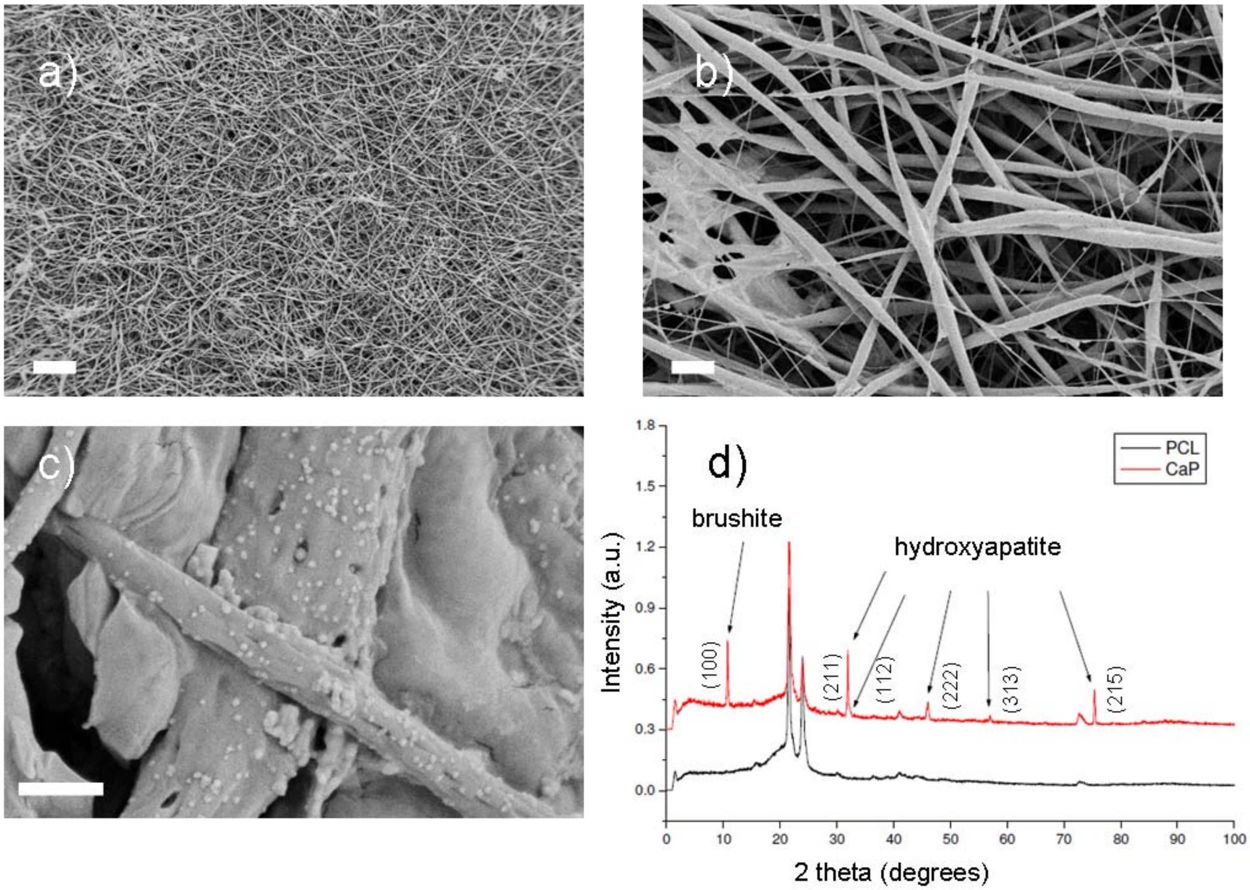

Figure 3.18. a-c) SEM micrographs showing the calcium phosphate (CaP) coating on a plasma-treated mixed sized mesh using a 2x SBF solution for 2 weeks. The WAXS pattern (d) shows peaks attributed to brushite and hydroxyapatite (the 2 peaks at 21.6° and 24° 2 theta are assigned to the PCL fiber mat, scale bars: a) 200 µm, b) 20 µm, c) 1 µm).

The WAXS diffractogram of the composite (CaP) showed a peak at 10.8° 2 theta corresponding to brushite (dicalcium phosphate dehydrate, DCPD), which is a known precursor for hydroxyapatite (Hap) normally formed at low pH, but it can coexist with Hap until a pH of ~ 7.[191] The double peak at 31.9° and 32.3° 2 theta could be attributed to HAp. From the area ratio of the peaks, a weight ratio of 1.15/1 of DCPD/HAp could be calculated. In addition, peaks at higher angles could be assigned to hydroxyapatite, too. In general, the WAXS diffractogram suggested successful apatite formation, whereas the morphology of the crystals was not apatite-like and the coating inhomogenous. Furthermore, it had to be considered that PCL might start to chemically degrade during 2 weeks in 2×SBF solution. Increased brittleness of the fiber mesh, by pulling manually on the fiber mesh, compared to pure PCL confirms this concern.

To improve the afore described composite, a 10×SBF crystallization procedure first introduced by Tas *et al.*[192] was used. This protocol was already successfully applied to coat electrospun nanofibers with apatite and had the advantage that it decreased the crystallization time to hours, thereby decreasing the risk of PCL degradation.[193] A stock solution of NaCl, KCl, $CaCl_2 \cdot 2H_2O$, $MgCl_2 \cdot 6H_2O$ and Na_2HPO_4 in 1L water was prepared in advance, where the pH was set between 4.2-4.4. The mineralization was then started after addition of $NaHCO_3$ which raised the pH as can be seen in Figure 3.19. After an initial fast increase above pH 6, a first maximum is reached at pH 6.2. After that, the pH decreases to 6, from where the pH steadily increases to 6.5 after 2 h and to more than 7 after 5 h. The decrease might be connected to a first precipitation with crystals, while the increase of the pH could be caused by the CO_2 release upon hydrogen carbonate decomposition and/or the reduced buffer capacity upon phosphate precipiation. The increase in pH might induce further precipitation, which is addressed in the next section examining the calcium phosphate coated meshes by SEM.

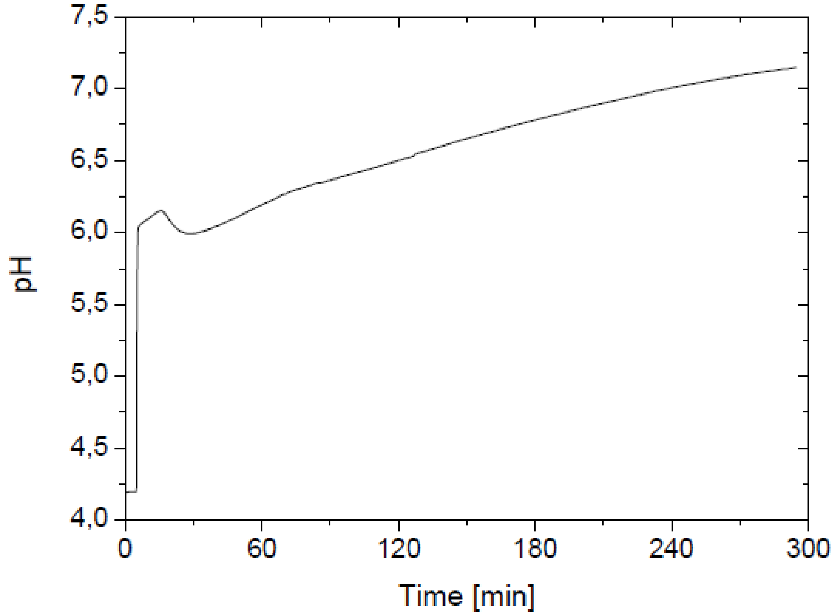

Figure 3.19. pH – time evolution of 10×SBF crystallization is shown initiated by $NaHCO_3$ addition.

Mixed sized fiber meshes were initially plasma-treated on each side for 1 min using 18 W for adequate hydrophilization as larger meshes were used compared to the calcium carbonate. The meshes were added to 50 ml stock solutions while the pH remained at 4.2. Then, $NaHCO_3$ was added to the solutions to start the crystallization. Initially, 2 separately conducted crystallizations were performed for 120 min and 140 min under static conditions (Figure 3.20 a1-3 and b1-3).

Although the difference in reaction time was quite small (i.e. 20 min) the coating thickness on the fiber meshes were quite different. This might be explained by a higher precipitation rate at higher pH with increasing crystallization time as mentioned before (Figure 3.19). Whereas in Figure 3.20a3, just some crystals coat the micro and nanofibers, Figure 3.20b2 suggests a rather homogenous coating on both fiber types. However in both cases, a laterally inhomogeneous coating was visible over the whole mesh surface (Figure 3.20a1 and b1).

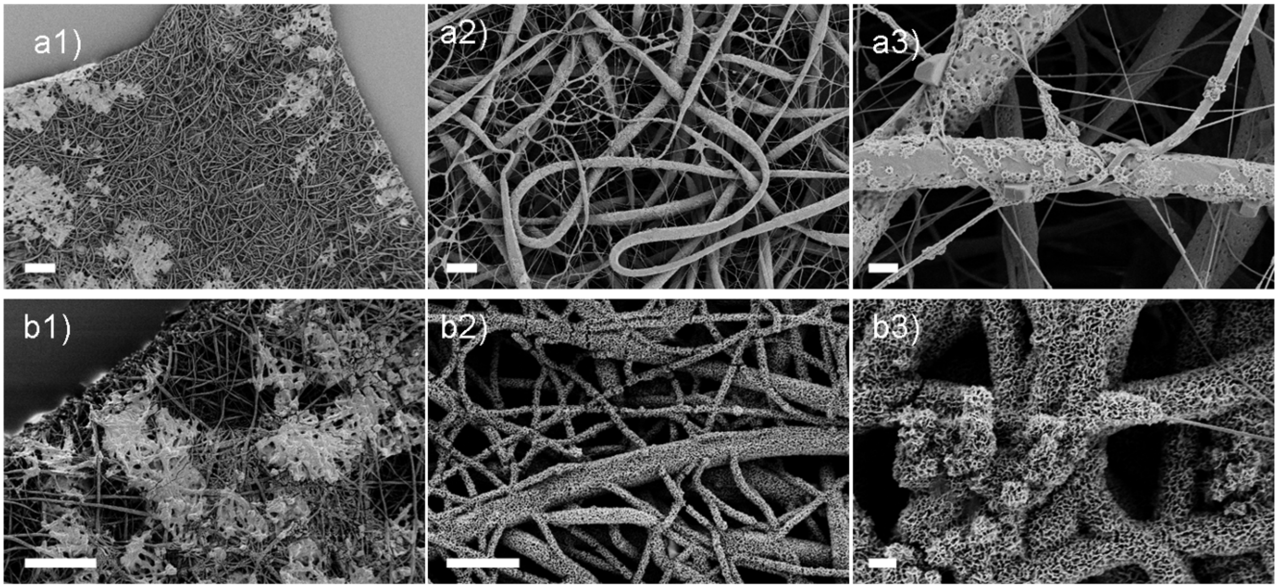

Figure 3.20. SEM images showed calcium phosphate coated PCL mats, obtained after crystallizations on plasma treated fiber meshes for a1-3) 120 min and b1-3) 140 min (plasma: 18W, 2x1min, air; scale bars: a/b1 = 200 µm, a/b2 = 20 µm, a/b3 = 4 µm).

In the next step, the meshes were initially soaked in the stock solution for 40 min before $NaHCO_3$ was added. This might ease the crystallization process and serve beneficial for homogeneity. The coating increased in thickness suggesting an effect of the prior soaking step as can be seen from the SEM micrographs (Figure 3.21 versus Figure 3.20a1-3). Nonetheless the homogeneity was still an issue (Figure 3.20a1). Increasing crystallization time to 5.5 h resulted in film and particle formation.

WAXS analysis of the sample shown in Figure 3.21a indicated a main peak at ~ 32° 2 theta, which can be attributed to the (211) crystal plane of hydroxyapatite. With increasing crystallization time (sample: Figure 3.21b) this peak increased dramatically, while no peak at ~ 11° 2 theta was visible at any crystallization time. This suggests no brushite formation which is in contrast to literature were normally brushite is formed.[193]

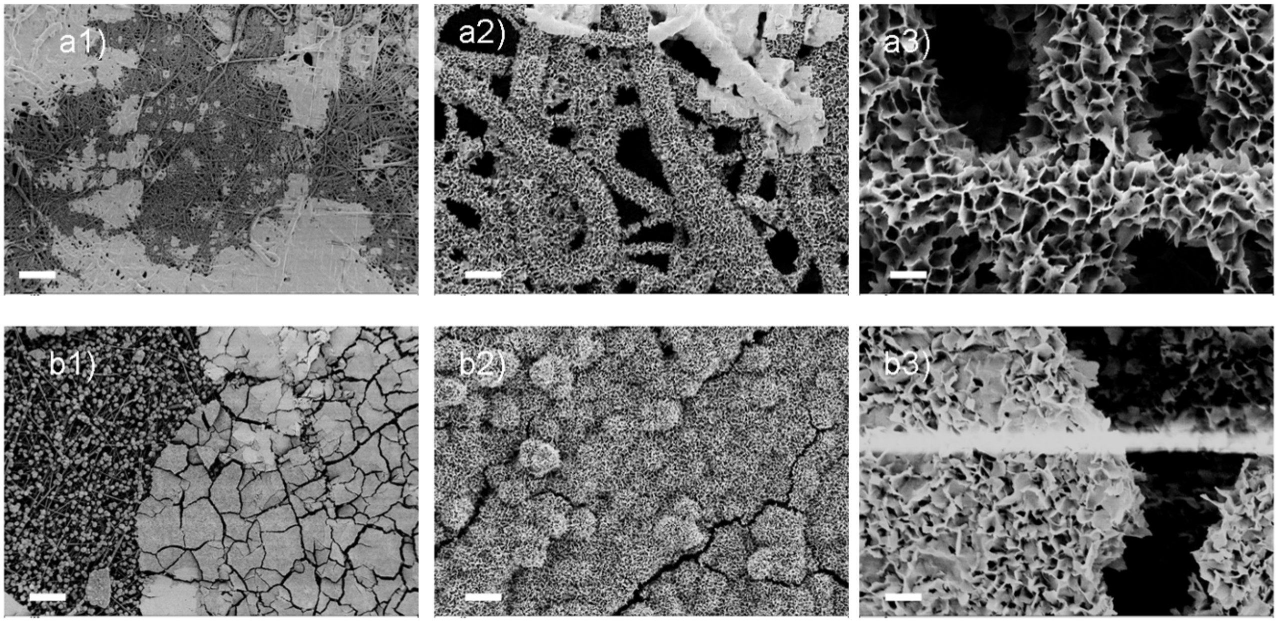

Figure 3.21. SEM images indicated a rather thick fiber coating after 2 h of crystallization (a1-3), whereas after 5.5 h a complete film or particles were forming (b1-3) (plasma: 2x1min, air, 18W; scale bars: a/b1) = 100 µm, a/b2) 10 µm, a/b3) = 2 µm).

To determine if the inhomogeneity was connected to the length of the plasma treatment, the number of chemical groups introduced was investigated by examining untreated, and plasmatreated PCL meshes (time: 30 s, 60 s and 120 s, 18 W).. In order to quantify the surface chemistry, XPS measurements were performed. Plasma-treated meshes resulted in increased C/O ratios and a decrease of C-C binding states accompanied by an increase of carbonyl and ester groups compared to untreated meshes. This might be attributed to ester cleavage, but also to surface cleaning of carbon-contaminated surfaces. However, the measurements did not show a steady increase of oxygen and oxygen-carbon binding states on increasing treatment time. This was plausible by the fact that reorganization of activated groups into the fiber bulk occurred. PCL might have softened during the measurement because of its low melting point (Table 1), and therefore promoted the reorganization.

In order to evaluate the influence of surface chemistry on coating homogeneity, differently treated meshes (e.g. plasma time) were used for calcium phosphate crystallization (Chapter 6.1.3.2). Here, crystallizations in 10 mL solutions were also performed so that smaller pieces of mats were used and the full mesh could be easily characterized by SEM in terms of homogeneity. A micron-sized fiber mesh was plasma-treated for 2×10 min, pre-soaked for 30 min and further crystallized for 135 min. At a first glance, the fibers were nicely coated (Figure 3.22b/c) similar to Figure 3.21a3. In Figure 3.22b the coating seems homogenous as well, however looking at Figure 3.22a a dark patch is visible with a diameter of ~ 1.4 mm indicated within quarter circle. This corresponded to an area where the coating exists (Figure 3.22a/b)) and can be found in other parts of the mesh. In the brighter areas, no coating or less coating was found. It seemed similar to the calcium carbonate that crystallization proceeded at different points, however, here the distance between the "nuclei sites" (here meant the point from which the coating proceeds) seemed larger.

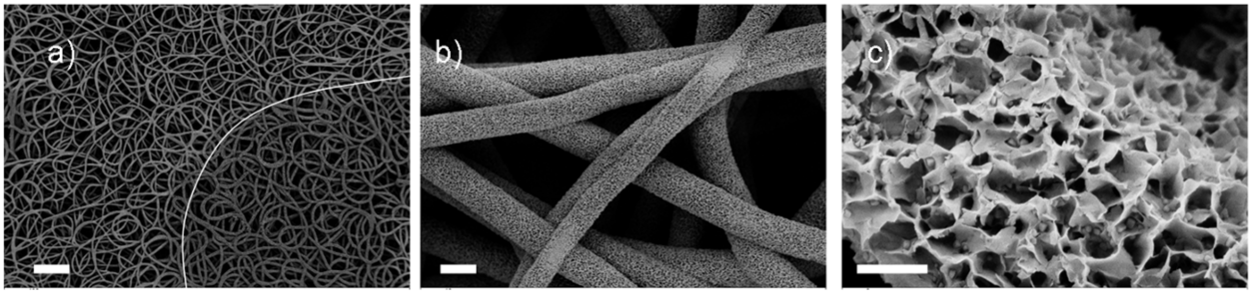

Figure 3.22. Crystallized micron-sized PCL fiber mats were nicely coated (b,c), however the increase in plasma treatment time revealed no dramatic increase in coating area (dark zone indicated in a) (135 min crystallization time, 30min pre-soaked, 2x10min plasma, air, 18W; scale bars: a) 100 µm, b) 10 µm, c) 2 µm).

Modulation of the fiber surface chemistry by plasma treatment (e.g. plasma power, time, atmosphere) but also using other functionalized meshes (e.g. NaOH treated, untreated) seemed not to show a common trend how to improve homogeneity. Surface chemistry effect on the crystallization seemed somehow limited, maybe attributed to the large oversaturation conditions.[193] In general, improvement of homogeneity seemed to fail using other conditions, indicating difficulties to produce centimeter-sized homogenous scaffolds (Chapter 6.1.3.2).

Since a basic understanding of the factors involved in calcium phosphate mineralization was investigated, coating of large sized meshes with nano, mixed and micro sized fibers were addressed. As visible in Figure 3.23 all the mesh types can be readily coated using 50 or 100 mL crystallization solution. The nanofibers (Figure 3.23a) were already coated with a thick layer and complete encapsulation had occurred in other regions (not shown). This was obvious by comparing the diameter of the coated nanofibers which was in the same order of magnitude like the coated microfiber or mixed sized fiber mesh (Figure 3.23b/c). Leaching of the calcium phosphate coated micron-sized fiber mesh maintained the overall mesh structure as seen in Figure 3.23e and Figure 3.23f. This suggests that calcium phosphate crystallization occurred within the fiber mesh. The microfiber composite mesh shown in Figure 3.23c was examined with TGA at 550°C, resulting in 9 wt% calcium phosphate. In contrast, the mixed sized fiber mesh was composed of 53 wt% calcium phosphate, suggesting a beneficial effect of nanofibers in the mixed sized fiber meshes on mineral incorporation. Interestingly, this difference in inorganic content is purely attributed to the PCL architecture, in contrast to calcium phosphate content differences found in literature between crystallization of two nanofiber meshes which differ by chemical means (PLGA versus PLGA/collagen) by means of a dipping method.[194]

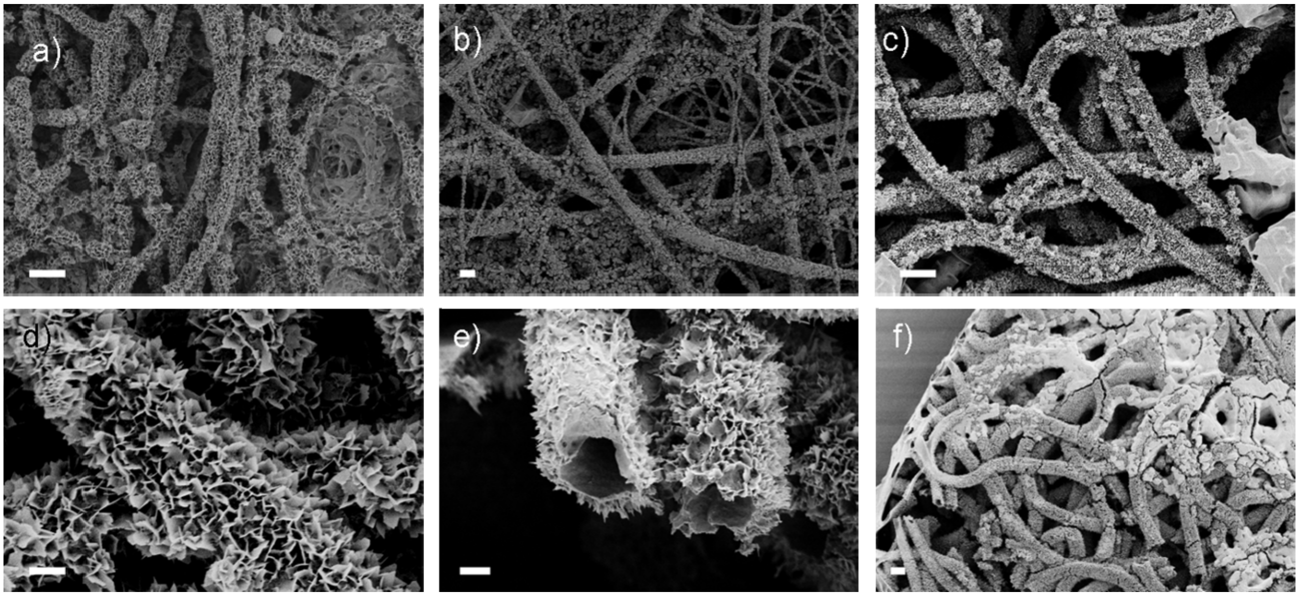

Figure 3.23. Different mesh types, namely nano (a), mixed (b) and micro (c/d) were coated with calcium phosphate. In e) and f) the micronsized fiber were leached with chloroform to show the distribution of the inorganic phase (crystallization time: a) 2.5 h, b) 2.25 h and c/d) 2h, air plasma, 18W, time: a/b) 5min, c) 15+10min; scale bars: a-c, f) = 10 µm, d,e) = 2 µm).

To further investigate the effect of nanofibers and micronfibers on crystallization, samples were taken from the crystallization solution at different times. The pictures (Figure 3.24) underline the impression that nanofibers seem to promote the crystallization by the increased surface area of the nanofibers. In addition, the shown coating for nanofibers after 30 min (Figure 3.24a) coincided with the pH minima observed in Figure 3.19. The coating then increased in thickness after 1.5 h, where as after 2.5 h film formation is observed. In contrast the microfibers were not coated to a large extent after 30 or 90 min. Finally, after 2.5 h the fibers were fully coated. Overall, this implies in a simplified way that nanofiber within compartments of human body may enhance the precipitation of biominerals. However, for tissue engineering, microfibers might be more suitable as narrowing the pores in the case of nanofibers increases the problem of effective cellular infiltration.

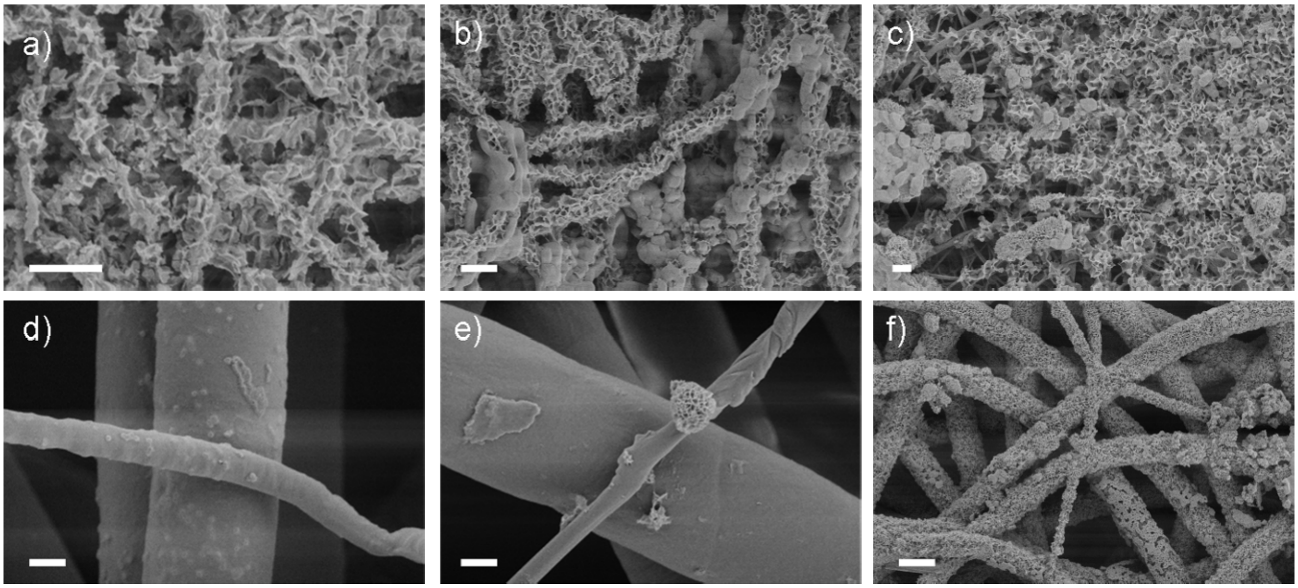

Figure 3.24. Calcium phosphate crystallization on nano (a-c) and micron (d-f) sized fiber meshes, revealed the increased crystallization speed on nanosized fiber (time: a/d) 30 min, b/e) 1.5 h, c/f) 2.5 h, plasma: 5min, air, 18 W; scale bars: a-e) = 2 µm, f) = 10 µm).

As a last point, crystallizations under dynamic conditions using a shaker were performed. This technique suggests a decrease in diffusion path and therefore faster crystallization compared to static conditions. This could be shown macroscopically by formation of platelets and by faster coating of the microfibers. In addition, the patches where coating occurred (Figure 3.22a, millimeter sized) increased in size from 2h to 4h, which could be seen macroscopically without microscopy aid to centimeter-sized patches. This increase in the area of homogenously coated patches indicated the advantage of using dynamic conditions for microfiber meshes. Furthermore the coating of individual fibers increased in thickness, as observed before for longer crystallization times using static conditions (Figure 3.19). For nanofibers, however, the dynamic conditions mainly led to accelerated platelet formation, and the nanofibers were not coated after 4h (Chapter 6.2, Figure S1). The WAXS analysis indicated for the crystals formed under dynamic conditons peaks which could be attributed to hydroxyapatite and brushite crystal planes. This is in contrast to static conditions, where only hydroxyapatite peaks were observed. The brushite formation might be promoted by dynamic conditions and seemed to be correlated to the observed platelets formation which is in agreement with the reported platelet-like morphology of brushite.[195]

Overall, it was shown that nanofibers seemed to accelerate calcium phosphate crystallization in contrast to microfibers as shown by crystallization kinetic studies. In addition, initial soaking, longer crystallization times and the use of dynamic conditions were beneficial for crystallization rate and final coating (thickness, homogeneity, area). The dynamic conditions however promoted brushite formation. In order to maintain the initial fiber structure, the findings suggest that nanofibers might preferentially need lower crystallization time and/or static conditions. In contrast, to coat microfiber meshes, dynamic conditions and/or longer crystallization times are beneficial.

3.3 Basic biomedical evaluation

To apply the above described materials for potential biomedical applications like tissue engineering, basic tests have to be performed. *In vitro* tests are in most cases the first step to evaluate the biological activity of scaffolds. In preliminary studies, epithelial cells were used before going further to chondrocytes and osteoblasts. In order to evaluate the suitability of such meshes in *in vivo* applications, mechanical testing and degradation studies were performed.

3.3.1 Cell tests

Cellular infiltration of meshes with epithelial cells

The promising properties of the micro- and mixed-sized fiber meshes for cell penetration were investigated by initial cell-infiltration studies using the well-established model system CHO-K1 (in collaboration with Dr. A. Lankenau, Fh-IBMT, Golm). For that, two different microfiber meshes (fiber diameter: 1.5 ± 0.5 µm (*i.*) and 4 ± 0.2 µm (*ii.*)) were used as references, which could be compared to the mixed fiber mesh (Figure 3.5a1). Although the fiber diameter of the reference meshes only differed by a factor of about two, a distinct effect was evident. In the 1.5 µm mesh, more than 80% of the cells adhered close to the mesh surface (in the first depth segment that summarizes the upper 43 µm of the mesh) (Figure 3.25b and d). This sieve effect would be even more pronounced with nano fiber meshes.[137] In contrast to this, the 4 µm fiber mesh and the mixed fiber mesh exhibited superior penetration characteristics having only 48% and 57%, respectively, of the cells in the first depth segment. In all mesh systems, the number of cells found in deeper regions decreased with penetration depth. However, the decrease was most dramatic in the 1.5 µm fiber mesh and less obvious with both the 4 µm mesh and the mixed mesh. Therefore, the cellular infiltration tests were consistent with findings from SEM and porosity analyses.

Taking into account that static perturbation conditions have been used, an infiltration under more realistic flow conditions leads usually to even better penetration characteristics. Moreover, the cellular infiltration under flow perturbation condition usually increases the trend that can be observed under static conditions.[146] While the micrometer fibers in the mixed meshes generate the open pore structure, the submicrometer fibers support cell adhesion and facilitate cell bridging of the large pores. This was revealed by initial cell penetration studies, showing superior ingrowth of epithelial cells into the bimodal meshes compared to *e.g.* a mesh which was composed of unimodal 1.5 µm fibers.

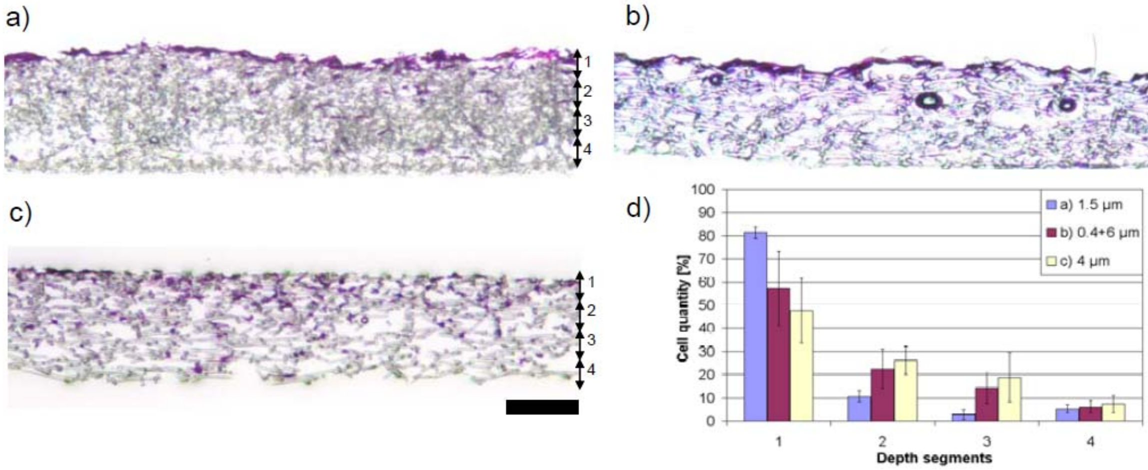

Figure 3.25. Light microscopy images (a-c) illustrating the different cellular infiltration characteristics of the bimodal fiber mesh compared to two reference meshes which are composed of uniform fibers. Freeze cuts showing the cell-populations in the different PCL meshes (~ 1.5 µm (a); mixed ~ 0.4 µm + ~ 6 µm (b) and 4 µm (c); Scale bar = 100 µm). d) The cell penetration depth analysis summarizing cell populations in four different depth segments in the meshes (penetration depth 1: 0-43 µm, 2: 43-86 µm, 3: 86-129 µm, and 4: 129-172 µm).

Mixed meshes (*e.g.* nano- and microfiber fabrics) are surveyed for their potential to combine the benefit of microfibers that span an open pore structure with properties of nanofibers, which are known to enable cell adhesion and proliferation.[196] To study the interactions of the cells with the mixed fibers (micro-nano structures), epithelial cells were seeded onto the mixed meshes. Using a low cell density of ~1750 cells/cm^2, the cell adhesion on the individual fibers could be investigated.

Figure 3.26 reveals that cell spreading occured dominantly on the nano-sized fibers, which is consistent with the literature.[138] The mode of interaction is evidently shown in the inset of Figure 3.26.

These initial results are consistent with the literature and suggest that the small fibers promote the three-dimensional colonization of the electrospun mesh, assisting to bridge the gaps of the large pores provided by the microfibers. This might be a design principle similar to that illustrated in Figure 3.27. As epithelial cells are known to be more receptive to planar surfaces, interactions of such meshes with osteoblasts and chondrocytes are discussed in the next section.

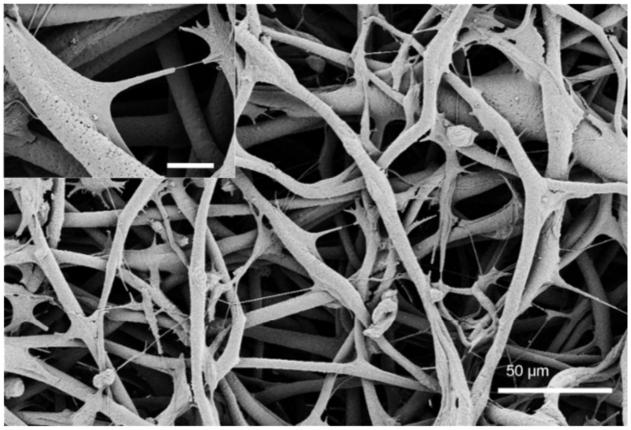

Figure 3.26. SEM micrograph of cell attachment on an electronspun mixed fiber mesh (small and large fiber diameter: ~ 400 nm and ~ 6 µm). In the inset small fibers guide the spreading of cells (scale bar inset = 10 µm). The cells were grown for 8 days with an initial seeding density of 1750 cells/cm^2.

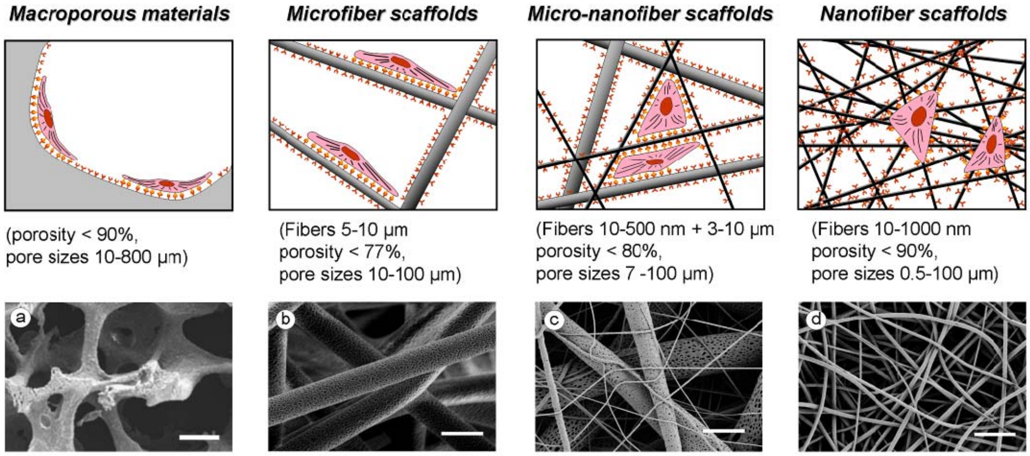

Figure 3.27. Scaffold architecture affects cell binding and spreading. The examples shown below were obtained by a) phase separation/leaching combination[59] and b-d) electrospinning (porosity data roughly estimated; note: nanofiber classically structure < 100 nm, here < 1000 nm as found commonly in the biomedicine field; scale bars: a) = 500 µm, b-d) = 10 µm).

Osteoblast and chondrocyte cell culture

Mixed and micron-sized fiber meshes were investigated in preliminary cell culture experiments with osteoblasts and chondrocytes. The studies were performed in collaboration with Prof. D.W. Hutmacher (QUT, Australia). Human primary osteoblasts were seeded on the PCL fiber mesh and adhered well as can be seen in Figure 3.28.

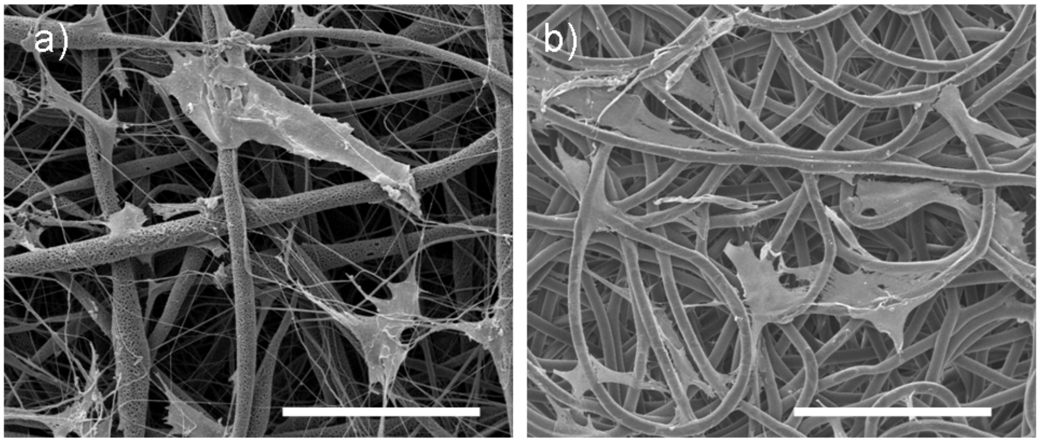

Figure 3.28. SEM images of osteoblast attachment on mixed- (a) and micron-sized fibers (b) suggested filopodia guidance through the nanofibers (a) (1 day cell culture, ~ 700000 cells/cm^2; scale bars = 100 µm)

Osteoblasts showed a preferable attachment to the nanofibers in the mixed fiber mesh (Figure 3.28a). Such guidance was less obvious in micron-sized fiber meshes (Figure 3.28b) where cells have to overcome the gaps by self-bridging the pores.

After 14 days in culture (Figure 3.29), the meshes were entirely coated with a cell sheet, suggesting a normal cell growth behavior. The cell layer seemed to be more tightly attached to the mixed fiber mesh, which might be linked to the preferred nanofiber-cell attachment. After 28 days of cell culture, in some of the meshes calcium phosphate could be detected with an alizarin red staining assay. However, cellular infiltration seems to be limited. A potential cause is the hydrophobicity of the meshes. In an ongoing study using plasma-treated fiber meshes this issue will be addressed.

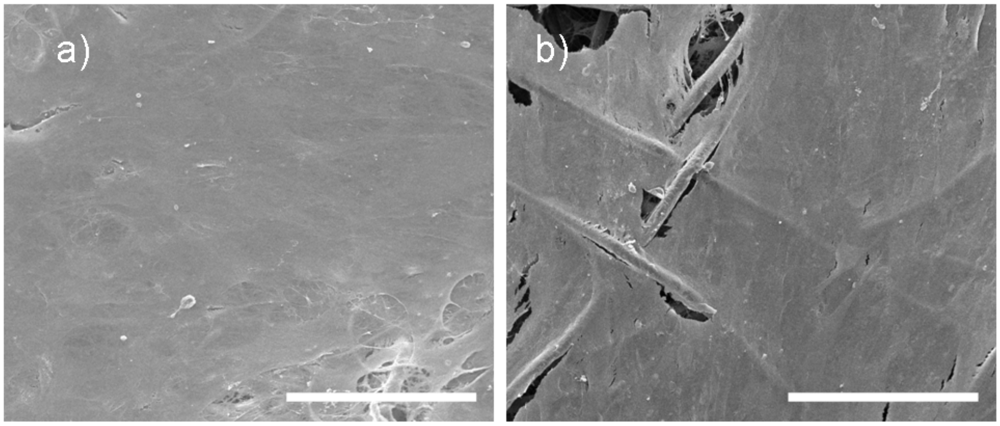

Figure 3.29. After 14 days in cell culture, the osteoblasts mainly coat the fiber mat as revealed in the SEM images. In mixed sized fiber meshes (a) the cell sheet seems to be tightly bonded in contrast to the micronsized fiber mats (b) (scale bars = 100 µm).

In a second set of experiments, bovine chondrocytes (P2) were cultured on the meshes for 18 days in expansion (LG-DMEM, 10% FBS, 100 µM ascorbic acid) and chondrogenic media (HG-DMEM, 1.25 mg/mL BSA, 1 µM DEX, 1 µM ITS+1, 100 µM ascorbic acid). Under both conditions the hydrophobic meshes supported chondrocyte attachment and growth, as shown after 18 days of cell culture in Figure 3.30.

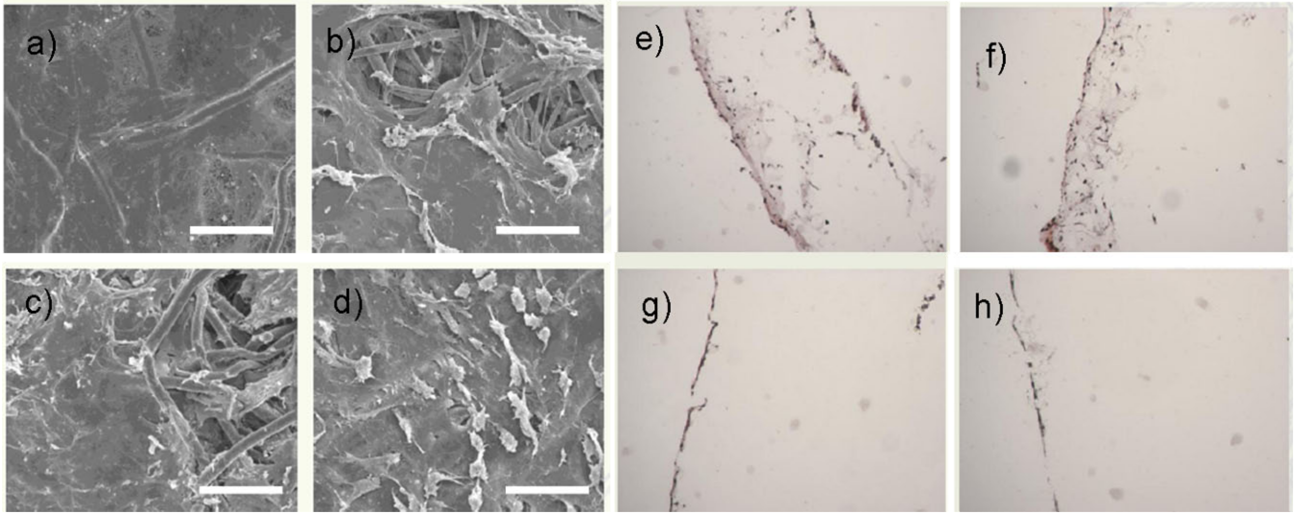

Figure 3.30. Micron- (a, c, e, g) and mixed-sized (b, d, f, h) fiber meshes were cultured in expansion (a, b, e, f) and chondrogenic (c, d, g, h) media. In the SEM pictures (a-d) chondrocyte showed confluent growth on both mesh types and in both media. The safranin-O/haematoxylin stained frozen sections (e-h) suggest superior penetration in expansion media (scale bars SEM images = 50 µm).

No major difference in cell attachment was observed between the mesh types. In all cases, chondrocytes showed a fibroblastic morphology. Safranin-O and haemtoxylin (stain glycosaminoglycans (GAG) orange/red and nuclei blue, respectively) histology (Figure 3.30e-h) showed higher degree of chondrocyte infiltration and GAG accumulation in meshes cultured with the expansion media compared to the chondrogenic media. However, the Von Gieson stain (collagen) showed no dominant difference (data not shown). For further GAG analysis, the DMMB (1,9-dimethyl methylene blue) assay was performed to quantify the amount of GAG in media.[197] GAGs are sugar molecules that serve as basic building blocks of extracellular matrix in cartilage and its levels are typically associated with chondrocytes' ability to produce cartilage-associated matrix.The average GAG released in the chondrogenic media was similar to the expansion media. In addition, there could not be a difference discerned between the mixed and micro-sized fiber meshes. In a more extensive study, further chondrocytes and osteoblasts cell culture are currently performed using nano-, mixed- and micron sized fiber meshes together with calcium phosphate coated mats.

3.3.2 Degradation studies

The degradation behavior of PCL is rather slow as reported in literature. However, increased surface area given by electrospun mats suggest a faster degradation behavior, which was investigated using differently structured fiber meshes. In order to simulate the degradation behavior *in vivo*, a protocol by Hutmacher *et al.* was used to evaluate nano-, mixed- and micron-sized fiber meshes.[198] Mats were immersed in 5 M NaOH solution and shaken for 1, 2 and 3 days at ambient conditions (Figure 3.31).

From the mixed sized fiber meshes, it is evident that nanofibers at the surface are missing (day 1) as compared to the reference (day 0). This suggests faster degradation behavior of the nanofibers. As expected, surface erosion depends on surface area. The degradation behavior of nanofibers is described in literature with a four-stage model of structure and morphology changes (Figure 3.32).[199] As seen in the SEM pictures of nanofibers of days 1-3 (Figure 3.31), the lamellar stacks are visible, which might be attributed to crystallization steps (stage I-II). Thermally induced crystallization and lamellar stacks are formed and then cleavage-induced crystallization of thinner lamellae/lamellar stacks occured. At day 3 some fibers break down, probably because of the accelerated mass loss rate within large amorphous regions (stage III). Stage IV, where lamellar stacks start to collapse and accelerated mass loss proceeds, was not observed within the examined timeframe.

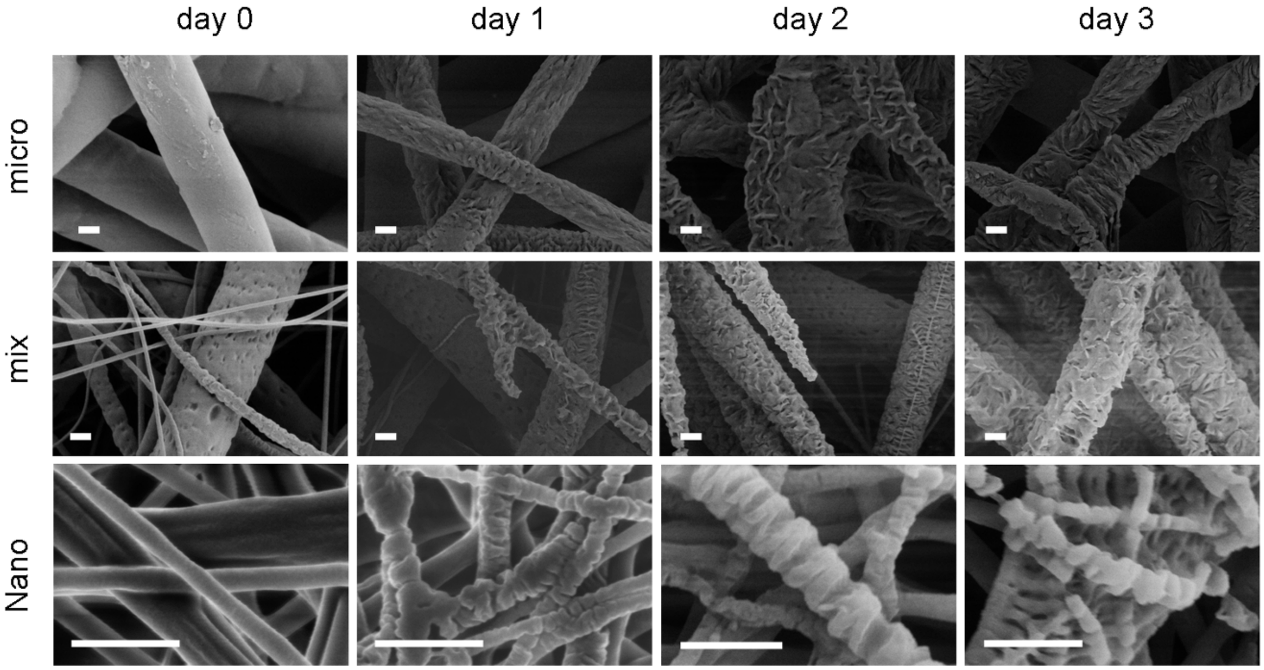

Figure 3.31. Micro-, mixed- and nanosized fiber meshes were hydrolytically degraded by using 5M NaOH solution. Nanofibers degraded faster than microfibers as depicted from the mixed sized fiber mesh where the nanofibers at the surface (day 0) are degraded (SEM scale bars = 2 µm (micro/mix), = 1 µm (nano)).

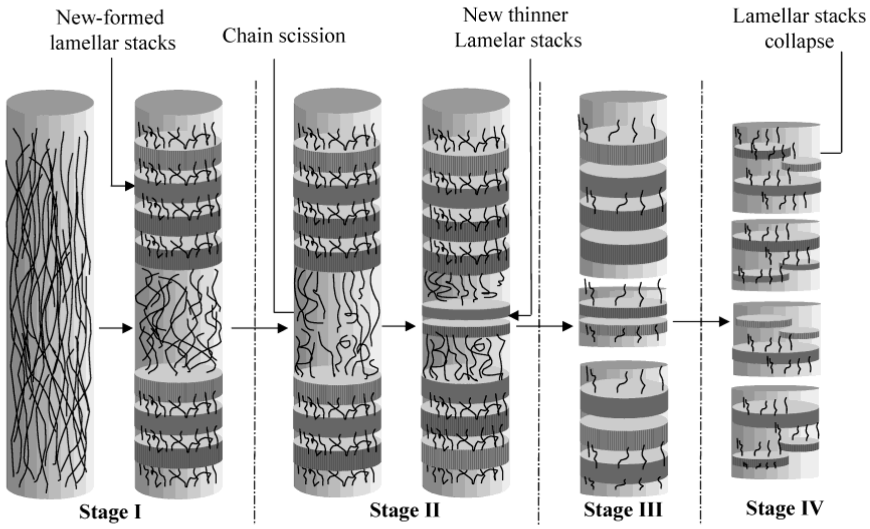

Figure 3.32. Four-stage model of structure and morphology changes of electrospun nanofibers during degradation. [199]

In addition, no dramatic difference between days 1-3 can be deduced from the SEM pictures in Figure 3.31. This is probably because the 5M NaOH solution did not penetrate the fiber mesh, thus the mesh surface eroded layer by layer. The meshes slowly degraded leading to smaller and smaller macroscopical pieces. In another set of experiments the fibers were initially plasma-treated to wet the complete fiber architecture. Here the degradation was much faster, disintegrating the nanofiber mesh within 1 day into small flake-like parts. The mixed and micronfiber meshes fell into parts after 3 days. That suggests again the faster degradation behavior of the nanofibers. In addition, it shows that wetting behavior of the fiber mesh is critical for the degradation behavior. In the wetted fiber mesh, the starting point for degradation is not only the mesh surface, but also the whole surface area given by the fibers composing the mesh.

3.3.3 Mechanical testing

Tensile testing

In order to evaluate mechanical properties of the micro-, mix- and nano-sized fiber meshes, tensile tests were performed in collaboration with Dr. M. Eder and Dr. I. Burgert (MPIKG, Dept. of Biomaterials). The stress-strain curves, shown in Figure 3.33, indicate a different behavior of the various structured fiber meshes. In the elastic zone, the micro-sized fiber meshes showed the highest slope (elastic modulus, E) whereas mats composed of mixed- and nano-sized fiber showed rather similar E-moduli. In addition, the E-modulus seemed to depend on the thickness of the sample, as indicated for thicker micro fiber meshes (micro2), possibly by a reduced Poisson´s ratio due to larger resitance in thickness compression during longitudinal stretching. Upon entering the plastic regime, the micro- and mixed sized fiber meshes reached the yield point faster than the nanofiber meshes. From a strain of roughly 0.1, the expansion of the mesh proceeded only with slight increase of stress. In contrast, the stress is continuously increased dramatically in the case of nanofibers, suggesting a higher strength of the nanofiber mesh.

The observed behavior can be explained by the enhanced entanglement in the case of the nanofiber meshes. Therefore, the fibers got stuck frequently when increasingly stretched. In contrast, microfiber and mixed fiber meshes seemed to untangle when further stretching occurs. For deeper insights, SEM analysis of the stretching process and dynamic stretching studies are ongoing.

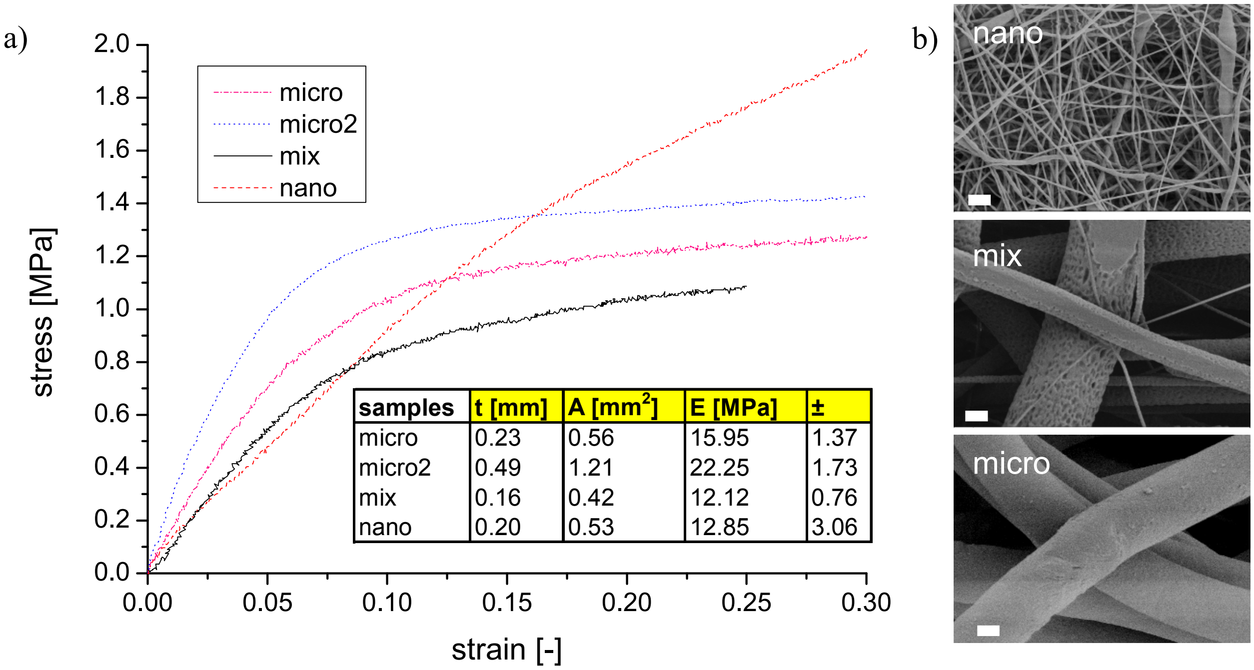

samples	t [mm]	A [mm^2]	E [MPa]	±
micro	0.23	0.56	15.95	1.37
micro2	0.49	1.21	22.25	1.73
mix	0.16	0.42	12.12	0.76
nano	0.20	0.53	12.85	3.06

Figure 3.33. a) Stress-strain curves of micro-, mixed- and nano-sized fiber meshes (b) are presented. The E-moduli (E) are highest for micro-sized fiber mesh. An increased thickness t of the micro-sized fiber mesh (micro2) increased the E-modulus (4 samples/mesh type were measured; porosity was not included in the cross section, A, SEM scale bars = 2 µm).

Force deformation measurements by AFM using a colloidal probe

While tensile testing values might be useful information for implantation and performance as structural support, it might not reflect the mechanical interactions between cells and fiber meshes. To learn more about mechanical properties of meshes in the micrometer range the nano- and micron-sized fiber mats have been probed using AFM in colloidal probe configuration as shown schematically in Figure 3.34a. This investigation was performed in collaboration with D. Kluge and Prof. A. Fery (University of Bayreuth). Force-displacements curves were recorded (i.e. a plot of the applied force versus the probe-sample distance). In order to obtain a force displacement curve, the probe (or the sample) was displaced along the vertical axis, while the cantilever deflection, as well as its diplacement was measured. To study mechanical material properties, like the sample spring constant, it was required that the force imposed by the AFM probe actually deformed the sample. In this configuration the cantilever and the sample form a coupled spring with a springconstant k_{tot}, which can be expressed as **$1/k_{tot}=1/k_c+1/k_s$ (eq. 1)**, with k_c and k_s being the spring constants of the cantilever and sample, respectively. The term displacement is the sum of the cantilever deflection and the sample deformation. In this work the sample spring constants was determined by measuring the slope of force-displacements curves, which gave the total spring constant, k_{tot}, and the sample spring constant k_s as described by **(eq. 1)**

In preliminary studies a ~ 35 µm-sized glass particle was used to indent different points of the fiber mat, probing the mechanics of meshes on a scale that mimics the cell mesh interaction (Chapter 6.1). The force-displacement curves of nano- (Figure 3.34b) and micron-sized fiber meshes (Figure 3.34c) indicate a different mechanical behavior. Meshes composed of nanofibers seemed to behave as an adaptive system, where after some displacement the stiffness k_s increased from ~ 0.3 N/m to ~ 1 N/m. In contrast, the microfibers showed a constant slope of ~ 4.5 N/m.

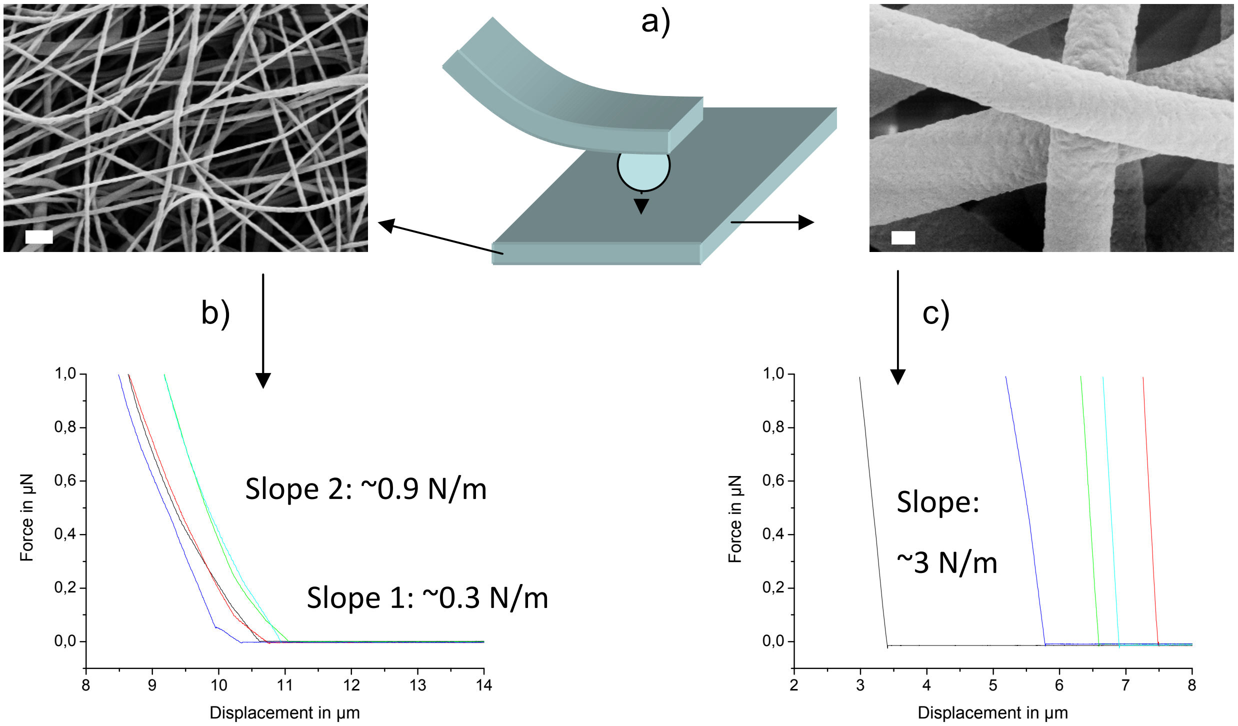

Figure 3.34. Nano- and micro-sized fiber meshes were mechanically probed using a glass bead as illustrated in a). Force-displacement curves were recorded on b) nano- and c) micro-sized fiber meshes indicating different slopes i.e. k_{tot} (substrate: glass slide, particle: ~ 35 µm, maximum force: 1 µN, k_c: 8.93 N/m, SEM scale bars = 2 µm).

Interestingly, the increased slope of the microfibers is qualitatively consistent with the findings from the tensile testing. This might establish a valuable relationship between macroscopically applied force in tensile testing and microscopic force applied in colloidal force probing. In order to further quantify the mechanics from the colloidal probing, single fiber mechanics are planned in the near future. The single fiber behavior of nanofiber and microfiber could ultimately give a deeper understanding of structure-mechanics relationship between single fiber and mesh.

4 The facile fabrication of biofunctionalized fibers

4.1 Processing of peptide-polymer blends

Physicochemical means such as demixing and interface stabilization have been used to functionalize electrospun fibers with bioactive molecules (e.g. peptides). In a blend of a commodity polymer, poly(L-lactic-*co*-glycolic acid) (PLGA), and an RGD containing polymer-peptide conjugate, poly(L-lactic acid)-*b*-CGGRGDS (PLLA-*b*-CGGRGDS) the peptide part is segregated to the surface. The polymer part of the conjugate helps to compatibilize the latter into the fiber bulk as shown schematically in Figure 4.1. From this simple mixture of PLGA and PLLA-*b*-CGGRGDS a core-shell like fiber morphology is successful electrospun. The enriched peptide at the fiber surface is anchored by the polymer part of the conjugate.

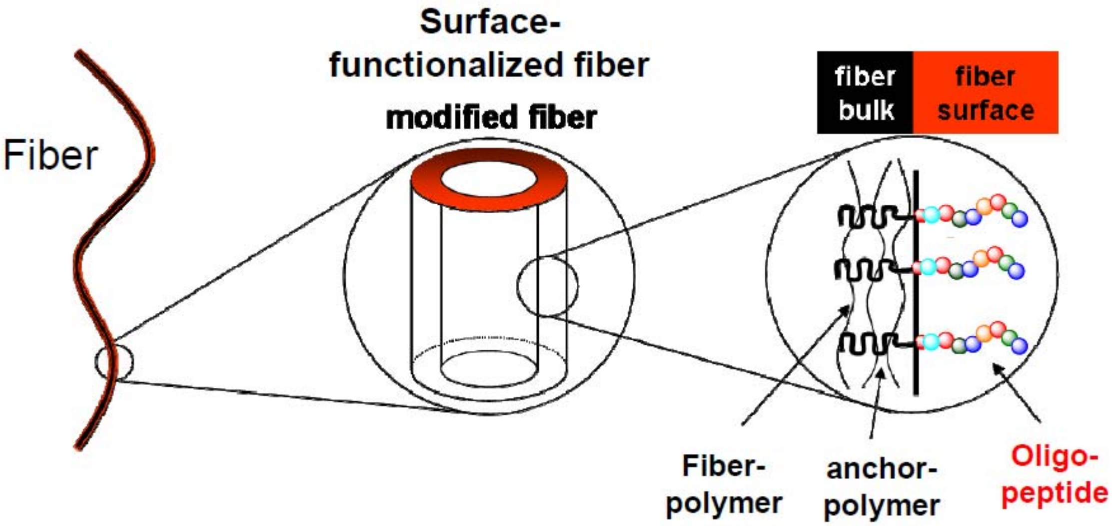

Figure 4.1. Schematic design of peptide functionalized fiber surfaces, where the surface is enriched with the peptide part of the polymer-peptide-conjugate.

4.1.1 Electrospinning of polymer-peptide conjugate/polymer blends

While the PLGA is a commercially available polymer the PLLA-*b*-CGGRGDS had to be synthesized using a 4-step protocol (Chapter 6.1.3.3). On the one hand, end functionalized PLLA was accessed via ring-opening anionic polymerization initiated by a furan protected maleimide initiator. Removal of the furan protective group yielded a PLLA-maleimide with a molecular weight of $M_{n,NMR} = 2600$ g/mol and a $M_w/M_{n,GPC} = 1.48$. On the other hand, the peptide CGGRGDS was obtained by solid-phase supported peptide synthesis.[200] Ultimately, PLLA-maleimide and peptide were chemically linked by using maleimide-thiol coupling chemistry ligating the terminal maleimide (PLLA) and thiol moiety of cysteine (peptide).[201]

In the first strategy, PLLA-*b*-CGGRGDS was blended with PLGA (9 wt% peptide-polymer conjugate/total solid composition) using chloroform as solvent. It was hypothesized that a non-polar solvent might facilitate field enrichment of the peptide to the surface in analogy to previously reported in literature.[159] To estimate the solution concentration electrospinning behavior of PLGA and the PLLA-*b*-CGGRGDS in chloroform were evaluated. Electrospinning of PLGA from a 5% w/v solution was feasible, resulting in a bimodal fiber meshes at conditions described in Chapter 3 whereas the conjugate alone, using a 10% w/v solution, led to electrospraying and resulted in particles due to the low molecular weight of the bioconjugate ($M_{n,\ PLLA,\ GPC}$ = 3.0 kg/mol; $M_{CGGRGDS,\ LC\text{-}ESI\text{-}MS}$ = 650 g/mol). A blended solution of 9.1 wt% PLLA-*b*-CGGRGDS solid composition was electrospun producing porous fibers with enhanced uniformity (diameter 1.16 ± 0.47 µm, Figure 4.2a) as compared to electrospun fibers from of PLGA without PLLA-*b*-CGGRGDS addition.

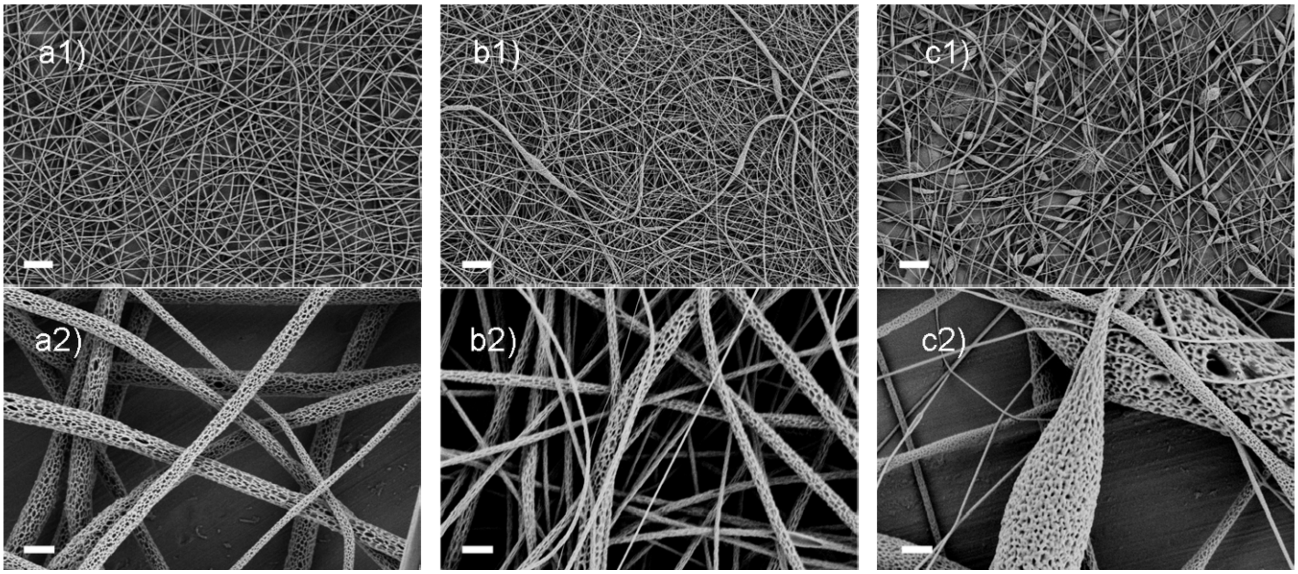

Figure 4.2. SEM images of PLGA/PLLA-*b*-CGGRGDS fiber fabricated by electrospinning under different conditions (a-c) using a 5% w/v (related to PLGA mass) solution in chloroform (solid composition: 9.1 wt% PLLA-*b*-CGGRGDS, conditions: rate: 0.2 mL/h, distance: 7 cm a) 5.5 kV, 72%, b) 14-15 kV, ground at needle tip, 67.5%, c) 4.7 kV, 46% humidity; scale bars: a1-c1) = 20 µm, a2-c2) = 2 µm).

This observation suggests that the addition of peptide-polymer conjugate to relatively nonpolar polymers facilitates the spinnability of such polymers, thought to be the result of increased conductivity which overweights the increase in viscosity (Chapter 6.2 Table S1/2). Phenomenologically, an earlier onset of the bending instability was visible to the eye, suggesting a stability increase and thus more uniform fibers compared to electrospinning pure PLGA.

To evaluate if the polarization of the applied field effects the enrichment, the ground position was inverted. The postulation of a field assisted process was assumed here. A reversing of the ground from bottom (collector) to top (needle) (b), resulted in similar structures, however with decreased fiber diameter and increased fiber diameter distribution (0.92 ± 0.62 µm). To overcome the surface tension in this configuration, higher voltages had to be applied, which might explain the different outcome. In addition, it was observed that a decrease in humidity increased the number of beads created at a similar applied field, underlining the influence of humidity by modulating surface tension (chapter 3.1).

In order to quantify the chemical nature of the fiber surface XPS measurements were performed on a thick fiber meshes. For comparison, films fabricated by drop-drying spin-coating were also prepared. As an additional reference, the electrosprayed peptide-polymer-conjugate particles were measured. In order to quantify the peptide content, the nitrogen concentrations were compared as shown in Table 3. In PLGA no nitrogen was present, so the two molecules can be differentiated.

Table 3. XPS analysis of fibers and references processed from $CHCl_3$ solutions to evaluate peptide enrichment at the fiber surface.

samples	c [% w/v]	form	N [at%]	±	N_{corr} [at%]	±	N_{theo} [at%]
PLLA-*b*-CGGRGDS	10	particles	4.6				4.9
PLLA-*b*-CGGRGDS	1	film (DD)	3.7	0.1	3.8	0.1	
PLLA-*b*-CGGRGDS	1	film (SC)	1.6	0.0	2.7	0.4	
PLLA-*b*-CGGRGDS/PLGA (9.1wt%)	1	film (DD)	2.1	0.4	3.0	1.5	0.4
	1	film (SC)	1.5	0.0			
PLLA-*b*-CGGRGDS/PLGA (9.1wt%)	5	fibers	0.8	0.7	1.1	0.8	
invers	5	fibers	0.8	0.3	0.9	0.5	

The nitrogen (N) composition was measured for PLLA-CGGRGDS and PLLA-CGGRGDS/PLGA blends with 9 wt% PLLA-CGGRGDS (DD: drop-drying, SC: spin-coating 2000 RPM, fibers: electrospinning, particles: electrospraying, corr: correction for background and impurities, see chapter 6.1.1.4, theo: theoretical calculated values assuming homogenous mixture and $M_{bioconjugate}$ = 3250 g/mol.

Although values for both electrospun fibers were higher than the theoretical values based on homogeneous blends, the related drop-dried and spin-coated films exhibited still higher values. This suggests that the surface enrichment was not dominated by a field-driven process under conditions used. Apparently in the investigated polymer/peptide system, phase separation and interface stabilization might cause the peptide-enrichment, as the slow process of drop-drying led to the highest peptide values amongst the blends. This was also valid for pure peptide-conjugate films. However values of spin-coated and drop-dried films are lower than the calculated average value for peptide-conjugate, implying lower peptide content at the film surface than calculated assuming homogenous distribution within the films. The N-values measured for electrosprayed particles, are slightly lower than theoretical values, suggesting that more PLLA of the bioconjugate particle is on the particle surface than calculated.

In order to investigate field-enrichment versus phase separation, a different solvent system of methanol/chloroform (ratio 1:3 (v:v)) was used. Although methanol is a non-solvent for PLLA or PLGA, it dissolves peptides well and thus acts as a compatibilization aid for electrospinning.

The behavior of the pure PLGA and the peptide-polymer conjugate in this solvent mixture was elucidated. Formation of unimodal fibers resulted using the same concentration as before for spinning of PLGA/$CHCl_3$ solutions (Chapter 6.2, Figure S2a). This might be attributed to a strong increase in conductivity and decrease in overall viscosity (Chapter 6.2 Table S1/2). Interestingly, fibers prepared from this solution seemed to be not round-shaped in cross-section, but rather wrinkled. Similar behavior had been already described in literature.[128, 202] The cross-section seemed eight shaped, like two fibers (~ 300 ± 100 nm) glued together to one (~ 900 ± 200 nm). The formation was caused probably by a collapse of a not yet solidified core, which is attributed to the solvent mixture, where methanol is less volatile than chloroform. In addition, the polymer concentration was varied, resulting in different fiber diameters (Chapter 6.2, Figure S3) Attention had to be paid to the methanol mediated degradation of the PLGA, which reflected the decrease of molecular weight in formation of particles. Therefore, preparing fresh solutions was here a prerequisite for reproducibility. Using a solution of pure peptide-conjugate in the aforementioned solvent mixture resulted in similarly shaped particles as formed by electrospinning from pure chloroform. This implies that independent of the solvent, electrospraying takes places due to low molecular weight and the resulting lack of entanglements (Chapter 6.2, Figure S2b).

In the next step, electrospinning of a PLGA blend was conducted at the same concentrations (i.e. 9.1 wt% PLLA-*b*-CGGRGDS, 5% w/v solution related to PLGA) as for pure chloroform. The addition of the peptide-polymer conjugate led to unimodal sized fibers with decreased fiber diameters of 640 ± 180 nm (Figure 4.3) compared to fiber prepared from electrospinning of pure PLGA. The wrinkled fiber surfaces were again visible, but interestingly not to the same extreme wrinkled state as observed for PLGA fibers. Phenomenologically, the stability of the electrospinning process was increased further by the peptide additive, showing an early onset of bending instabilities. The addition of the peptide-polymer conjugates also increased the conductivity and the viscosity (Chapter 6.2 Table S1/2). This change in properties was thought to be responsible for the higher stability, decrease of fiber diameter and decreased wrinkling. However, the latter might also be dependent on humidity.

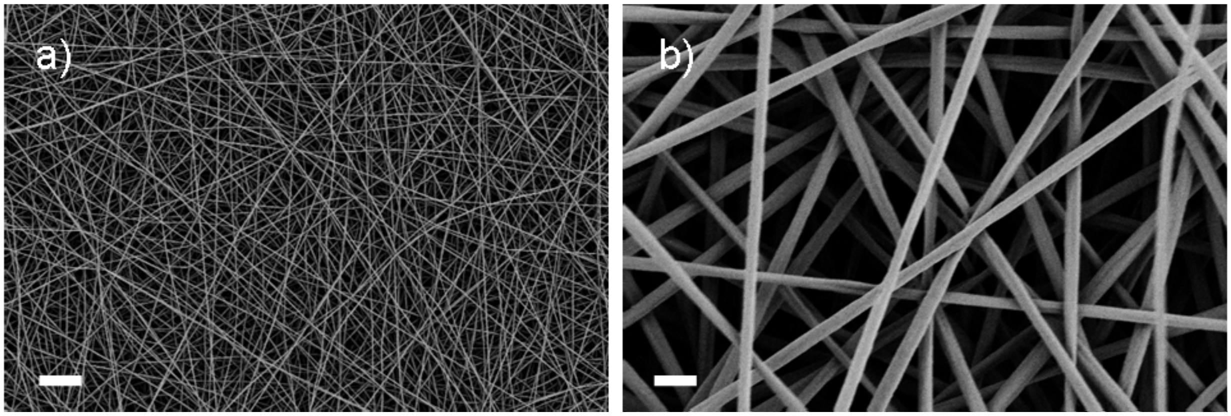

Figure 4.3. SEM images of uniform fibers of PLLA-*b*-CGGRGDS/PLGA electrospun from $CHCl_3$/MeOH (3:1) (9.1 wt% PLLA-*b*-CGGRGDS, parameters: rate 0.7 mL/h, 6.6 kV/ 10 cm, humidity 26.7%, 5% w/v solution related to PLGA mass; scale bars: a) = 20 µm, b) = 2 µm).

In order to evaluate peptide enrichment at the fiber surface, nitrogen content was obtained by XPS. As control samples, thin films of PLLA-*b*-CGGRGDS/PLGA blends in the solvent mixture were produced by spincoating and particles generated by electrospraying were also investigated (Table 4). Nitrogen concentrations irrespective of the sample preparation were higher than for corresponding samples prepared from chloroform solutions. N surface contents for polymer-peptide-conjugate/PLGA blends were roughly 10 times higher than theoretically calculated values. This suggests a dramatic improvement of the enrichment, also with the background that the values are similar to the value for the pure peptide conjugate. It is thought that mainly peptide-polymer conjugate is accessible at the fiber and film surface. Furthermore, the similar nitrogen surface composition of the films and fibers suggests the electric field plays a minor role, whilst changing the polarity of the solvent from a non-polar solvent to a polar mixture, seems to be primarily responsible for the enrichment of the peptide. This implied that the peptide is partially entrapped in the fiber bulk when using chloroform solutions, and increasingly enriched at the fiber surface upon addition of methanol.

Table 4. Nitrogen (N) composition of fibers and references processed from $CHCl_3$/MeOH (3:1) solutions derived from XPS for PLLA-*b*-CGGRGDS and PLLA-*b*-CGGRGDS/PLGA blends.

samples	c [% w/v]	form	N [at%]	±	N_{corr} [at%]	±	N_{theo} [at%]
PLLA-*b*-CGGRGDS	10	particles	5.0				4.9
PLLA-*b*-CGGRGDS/PLGA (9.1wt% PLLA-b-CGGRGDS)	5	film (SC 3000)	4.7		4.9		0.4
		film (SC 1000)	4.3	0.4	4.6	0.4	
		fibers	4.3	0.7	4.5	0.5	

peptide-polymer conjugate solid concentration: 9.1 wt%, solution concentration% w/v related to PLGA mass, film SC: spin-coating values RPM, fibers: electrospinning, particles: electrospraying, corr: correction correction see exp. section, theo: theoretical calculated values assuming homogenous mixture.

In order to further investigate the effect of the peptide concentration on the electrospinning and enrichment behavior, different PLLA-CGGRGDS/PLGA blend ratios were electrospun (Figure 4.4). Decreasing the peptide content resulted in an increase in fiber diameter, which is consistent with the larger sized PLGA-fiber. As aforementioned, this is attributed to a decrease in conductivity which seemed to prevail over the decrease in viscosity, which should decrease the fiber diameter.

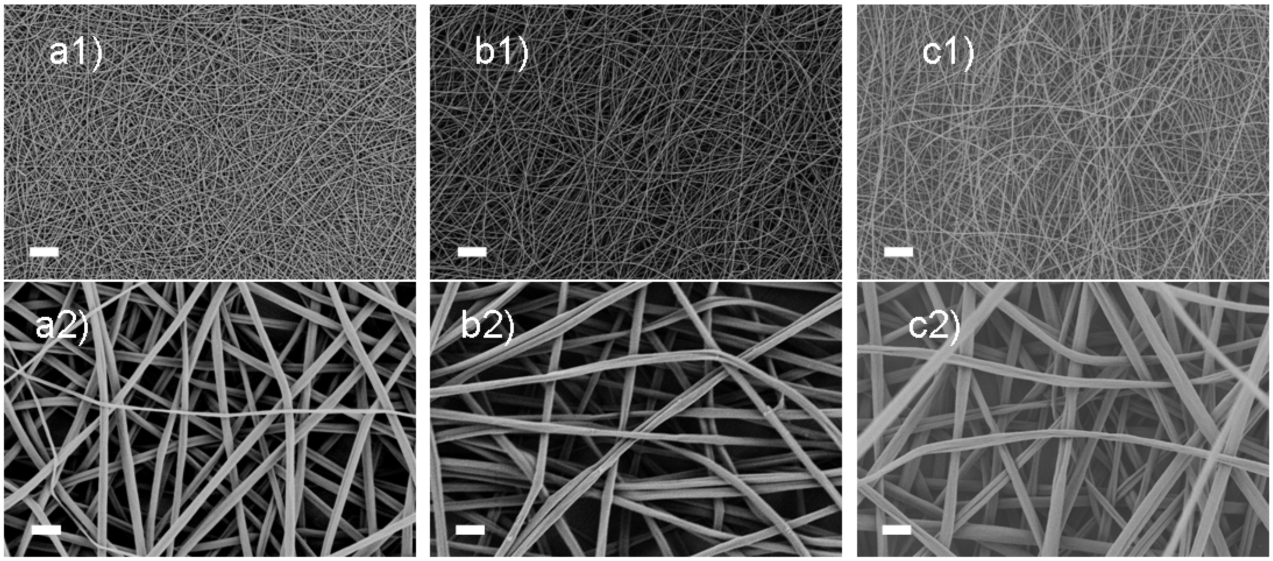

Figure 4.4. SEM images of electrospun PLGA/PLLA-*b*-CGGRGDS fibers prepared at decreasing peptide-polymer-conjugate concentration from 6.5 (a), 4.8 (b) down to 2 wt% (c) led to an increase of fiber (parameters: PLGA solution concentration 5% w/v $CHCl_3$/MeOH (3:1), 10 cm distance, a) 0.7 mL/h, 11.1 kV, 33.3%, b) 1 mL/h, 8.7-11.8 kV, 34.1%, c) 1 mL/h, 6.5 kV, 30.5%; scale bars: a1-c1 = 20 µm, a2-c2 = 2 µm)

Quantification of fiber surface composition was obtained by XPS, to measure the surface nitrogen concentration of fibers spun with increasing peptide-polymer-conjugate content (Figure 4.5). The amount of nitrogen increased in a dramatic fashion for both films and fibers. All experimental values were higher than the calculated values, assuming a homogeneous mixing of PLLA-*b*-CGGRGDS and PLGA. The nitrogen values for spin-coated films were found to increase steadily from 2 to 6.4 wt% PLLA-*b*-CGGRGDS, until leveling off upon increasing to 9.1 wt% polymer-peptide conjugate. In contrast, the N-contents for electrospun fibers increased slowly from 0 wt% to 4.8 wt% PLLA-*b*-CGGRGDS in the blend. Further increase in the PLLA-*b*-CGGRGDS/PLGA ratio resulted in a strong increase of the N content up to 9.1 wt% peptide-polymer conjugate content. This suggests a different enrichment mechanism attributed to the different confinement. Furthermore, the values for the fibers seemed to scatter more at higher polymer-peptide conjugate composition. As the XPS measured the surface composition of the fibers, warming up of samples was a potential issue. However, from SEM analysis no difference of the fiber surface before and after XPS measurement could be discerned.

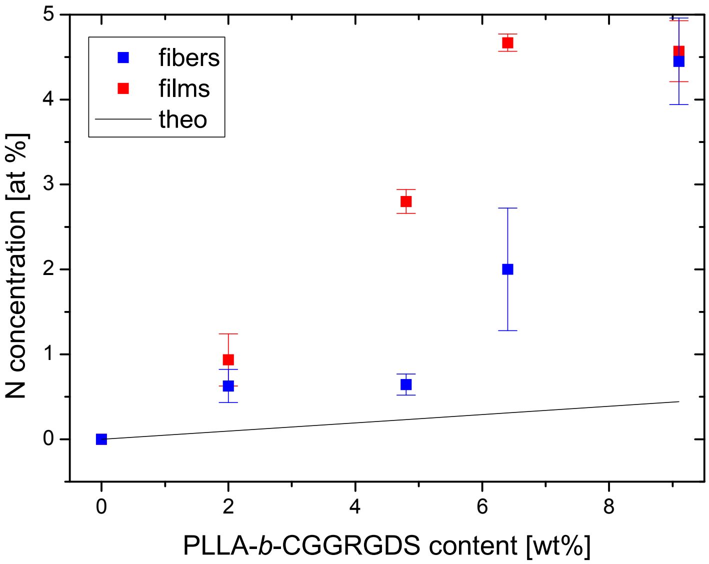

Figure 4.5. Nitrogen (N) concentration derived from the XPS spectra shows a dramatic increase by increasing the peptide-polymer conjugate content for electrospun fibers and spin-coated films with 1000 RPM (corrected N values are used, raw data is shown in Chapter 6.2, Table S3).

To verify peptide accessibility at the fiber surface, the wetting of the fiber mesh was examined. The peptide part of PLLA-*b*-CGGRGDS in principle should enhance the hydrophilicity of the mats, therefore electrospun mats and as reference spin-coated films were characterized using static contact angle measurements (Figure 4.6). Indeed, a clear increase in hydrophilicity was observed with increasing PLLA-*b*-CGGRGDS content within the electrospun fibers (2 wt% PLLA-*b*-CGGRGDS: 124° => 9.1wt% PLLA-*b*-CGGRGDS: 0°). In contrast, films produced by spin-coating presented only a slight decrease in contact angle from 72° to 50° when increasing the peptide content from 2 to 9.1 wt%, attributed to structural differences (e.g. roughness) between the planar film and fibrous 3D mesh morphology. Interestingly, the contact angle was found to decrease slowly until 4.6 wt% of PLLA-*b*-CGGRGDS and then dramatically reduce until H_2O droplet was soaked into the fiber mesh (i.e. contact angle of 0°). Once the surface energy reaches a critical value the droplet was soaked into the fiber mesh due to capillary forces. The contact angle measurements agreed well with previously discussed XPS measurements indicating a similar development of contact angles as a function of PLLA-*b*-CGGRGDS content compared to nitrogen contents as a function of PLLA-*b*-CGGRGDS concentration.

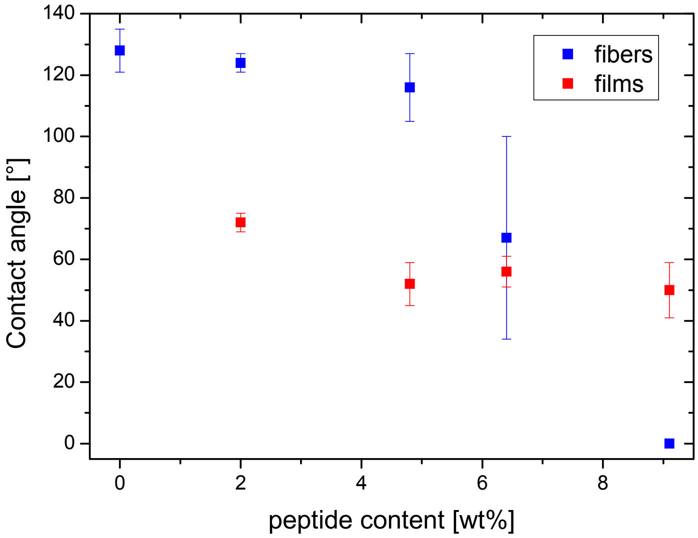

Figure 4.6. Static contact angle measurements indicate enhanced hydrophilicity with increasing PLLA-*b*-CGGRGDS content.

The maximal nitrogen concentration at the fiber surface was 5 at% resulting from spinning a blend of 9.1 wt% bioconjugate. To further improve peptide-enrichment, thinner fibers were fabricated to decrease transport distance and enhance segregation of the peptide-conjugate at the fiber surface. Reduction in fiber diameter is typically achieved via a decrease in solution concentration. Reducing the PLGA concentration from 5 to 3% w/v whilst keeping the relative amount of bioconjugate constant (2 wt%), led to electrospun fibers possessing diameters decreasing from 690 ± 190 nm (5% w/v of PLGA), to 460 ± 70 nm (4% w/v), to finally 270 ± 90 nm (3% w/v) (Figure 4.7). Again, wrinkling was common in all concentrations investigated as indicated from the higher magnification SEM images in Figure 4.7a-c2. As concentration was decreased, viscosity and resistance decreased, which reduced the fiber diameter by increased fiber stretching. In addition, less solid material was transported with the same feed rate, resulting in increased solvent evaporation and thus smaller fibers.

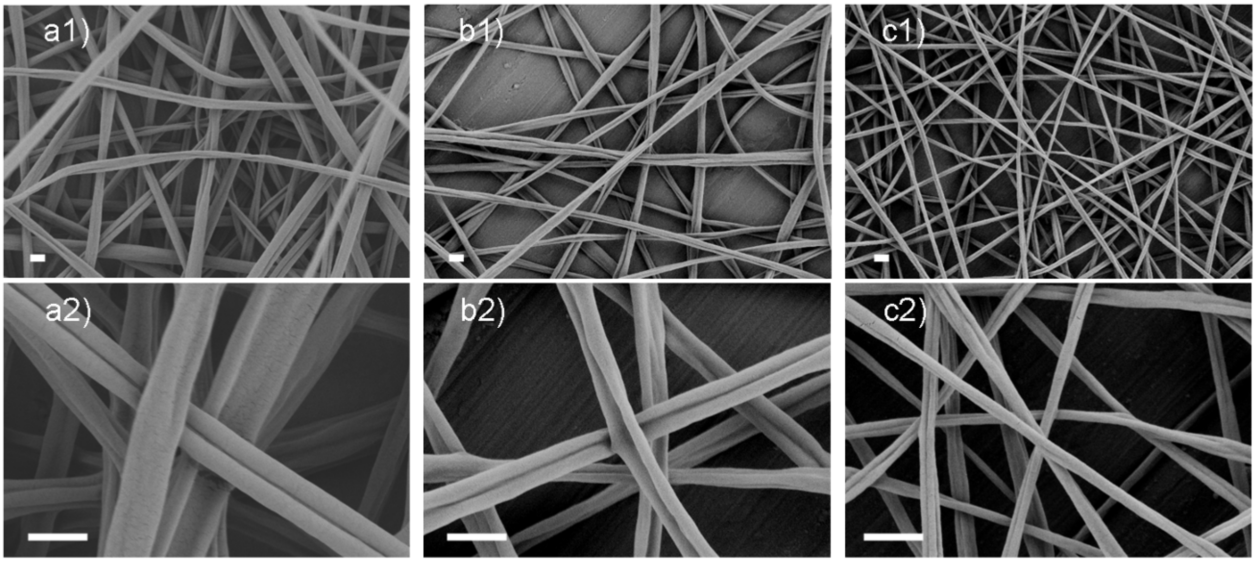

Figure 4.7. SEM images of fibers prepared as a function of polymer solution concentration: varied from 5 (a), 4 (b), to 3% w/v (c) at a fixed PLLA-*b*-CGGRGDS concentration (2 wt% solid ratio) for decreasing the fibers diameter (parameters: $CHCl_3$/MeOH (3:1), 10 cm, a) 1 mL/h, 6.5 kV, 30.5%, b) 0.7 mL/h, 5.1 kV, 26.7%, c) 1 mL/h, 6.9 kV, 23.5%; scale bars = 1 µm).

Electrospinning of 3% w/v solutions relative to PLGA but differing in the ration of PLGA and peptide-polymer conjugate gave fibers with a similar reduction in fiber diameter compared to fibers obtained using 5% w/v solutions (e.g. Figure 4.8a versus Figure 4.4b). Fiber diameters between the different weight compositions of 4.8, 9.1 and 18 wt% peptide/polymer blends varied from 230 ± 40, 340 ± 50 and 360 ± 80 nm, respectively. Such differences are thought to be a consequence of an overlaying effect, due to increased solution conductivity and viscosity are increased (Chapter 6.2, Table S1/2) This means that typically a viscosity increase leads to higher fiber diameter, whereas increased conductivity reduces the fiber diameter. Increasing the bioconjugate content from 2 wt% to 5 wt% resulted in a decrease in fiber diameter due to conductivity effects after which the fiber diameter increased due to viscosity. In addition, it was observed that the solutions investigated still remained electrospinable after some weeks but were not electrosprayed as for pure polymer. Similarly, higher concentrated polymer/peptide solutions (i.e. 5% w/v, 9 wt% PLLA-*b*-CGGRGDS) confirm this trend, where solutions were spinnable even after 5 months. This was thought to be the result of a decreased viscosity loss as compared to pure PLGA solutions, or the inhibition of polymer degradation related to a conductivity decrease at 18 wt% PLLA-*b*-CGGRGDS composition after 2 weeks (Chapter 6.2, Figure S4).

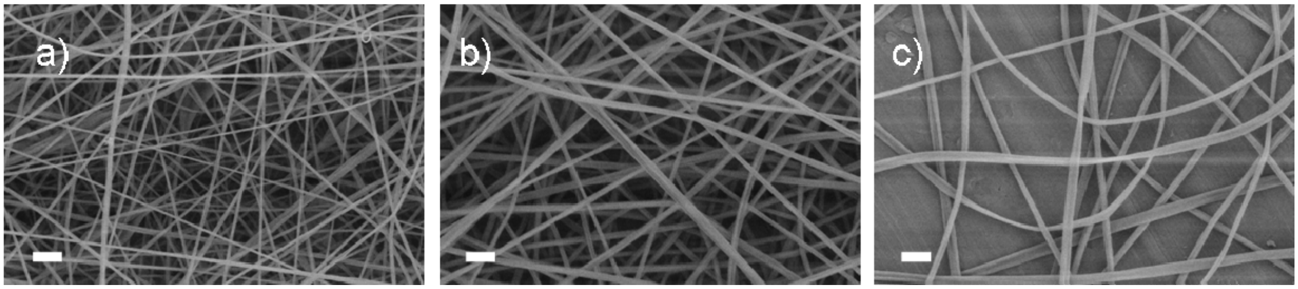

Figure 4.8. SEM images of fibers prepared at from 3% w/v solutions, indicating fiber mesh with different fiber diameters at variable PLLA-*b*-CGGRGDS concentration a) 4.8, b) 9.1 and c) 18 wt% (solid ratio: PLLA-*b*-CGGRGDS-conjugate/total solid content, solution concentration: PLGA content/volume $CHCl_3$/MeOH (3:1); parameters: 1 mL/h, 7-10 cm, 7-8 kV, 28%; scale bars = 2 µm).

For these thinner fibers prepared with different bioconjugate content as XPS was again employed to investigate surface peptide enrichment (Figure 4.8, Chapter 6.2, Table S3). Generally, all nitrogen concentrations are still higher than their calculated values based on homogenious distribution of PLLA and bioconjugates. However, surface enrichment is substantially smaller than for corresponding values from thicker fibers i.e. electrospun from 5% w/v. Nitrogen content for a 9.1 wt% bioconjugate/polymer blend was approximately half of that for fiber meshes spun from 5% w/v PLGA solutions. This was not expected as enrichment should proceed better in the case of smaller fibers due to shorter path lengths. An SEM analysis of the samples measured by XPS indicated that this seems to be linked to partial thermal softening as was observed from images taken before and after the measurement series (data not shown).

In order to overcome the aforementioned issues, electrostatic surface interactions studies were performed to determine the peptide labels availability at the fiber surface. Such interfacial interactions can be measured using colloidal-probe atomic force microscopy (AFM). Here attractive electrostatic interactions are measured between a negatively charged silica probe and positively charged PLGA/PLLA-*b*-CGGRGDS fibers. Using colloidal probe AFM the lateral resolution was also improved compared to the a few micrometer lateral resolution capability of XPS. In this technique a colloidal tip approached the sample until fiber contact was made in aqueous solution. Whilst the AFM tip approached the force was measured by deflection of the cantilever and the known cantilever spring constant. In the experiment single PLGA or peptide-functionalized fiber with two composition (i.e. 9 wt% and 18 wt%) were probed with a silica bead in aqueous solution.

To render attractive electrostatic probe-sample interactions possible the pH was set to 3.9 with HCl. Thereby, the peptide-conjugate is positively charged due to the protonated amines (~ 1.3 net charge, modeled with Sednterp, 1.09, 2006), whilst the silica bead is still negatively charged due to the dissociated silanol groups (isoelectric point at pH ~ 2).[203] Therefore the peptide-functional fibers should attract the silica bead in contrast to the pure PLGA fibers as schematically shown in Figure 4.9a.

Force displacement curves from the interaction between the RGD-functional fibers and the 10 µm sized silica bead show an attractive behavior (Figure 4.9b). Note, that the force curves represented approach cycles, where the probe was driven from the bulk towards the fibers. At a distance of ~ 10 nm attractive interactions emerged, bending the cantilever towards the fibers. In addition, the increased peptide content resulted in an enhanced attraction between fiber and probe (Figure 4.9c). In contrast repulsive interaction towards PLGA fibers were observed attributed to the potential negatively charged PLGA surface due to carboxyl groups derived from degradation and end groups (Figure 4.9b). Overall, small adhesion forces were observed for PLGA fiber whereas increased adhesion was monitored for RGD-functionalized fibers, where a double peptide input resulted in more than double the adhesion force. This clearly indicated the accessability of the peptide on the surface. Using AFM for mapping the attraction between probe and sample can be spatially resolved, which gives a measure of the distribution of the peptide on the surface. The attraction forces seemed to scatter along the fiber surface by the error bars shown in Figure 4.9c (Chapter 6.2 Figure S5). The variation increased with increasing peptide content.

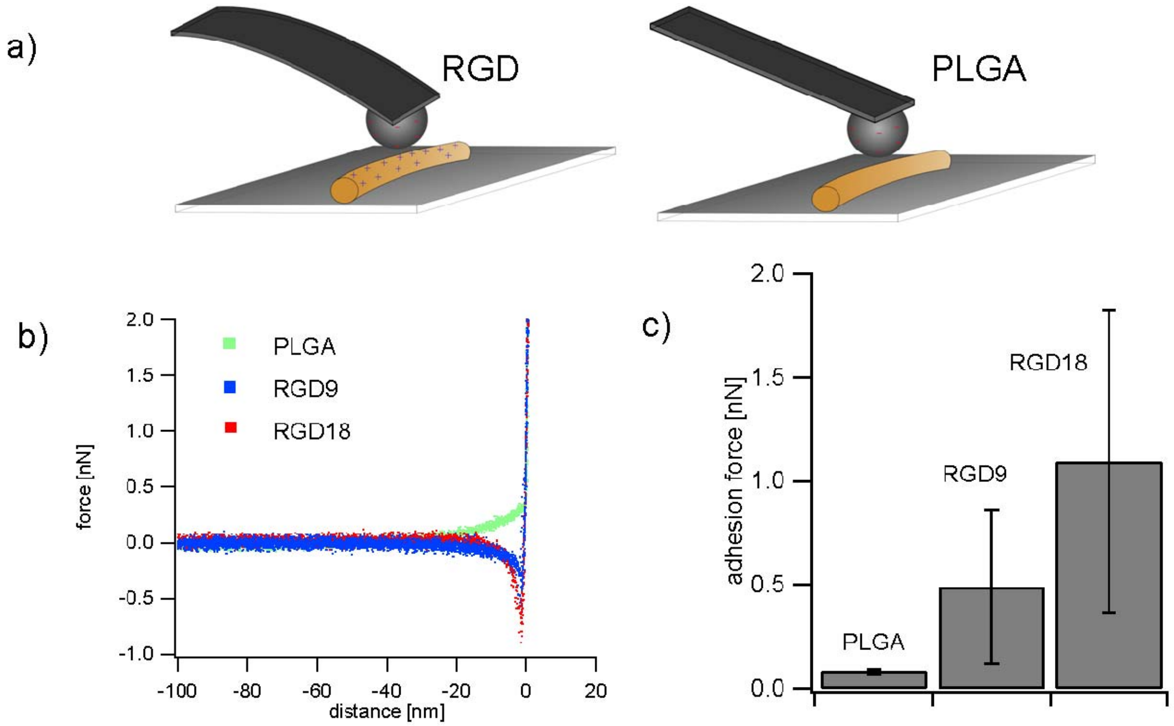

Figure 4.9. (a) Colloidal interaction probing is shown schematically for a RGD-functional and PLGA fiber. (b) Resulting force displacement curves for a silica bead and RGD-functional fiber compared to PLGA fiber and (c) Adhesion force as a function of PLLA-*b*-CGGRGDS content are shown (0, 9 and 18 wt%).

In summary, using 3 different characterization methods, it had been shown that the peptide part could be successfully enriched at the fiber surface. Using XPS analysis of fibers with 9.1 wt% PLLA-*g*-CGGRGDS spun from a 5% w/v solutions (relative to PLGA) indicates similar values to those obtained from spraying pure PLLA-*g*-CGGRGDS conjugate. This suggests that the fiber surface is especially composed of the bioconjugate. Contact angle and AFM analysis in tandem proved the peptide sequence is accessible.

To clarify the solvent dependency of peptide-polymer conjugate enrichment on PLGA fibers prepared by electrospinning, dynamic light scattering (DLS) was utilized. Solutions of peptide-polymer conjugate in chloroform/methanol solutions and pure chloroform were investigated. Pure bioconjugate solutions with ~ 1% w/v were prepared using two solvent systems ($CHCl_3$, $CHCl_3$/MeOH (3:1/v:v)). It was anticipated that the peptide-conjugate would aggregate in chloroform as the peptide part of the block copolymer drives assembly due to ion and hydrogen bonding interactions, whereas the PLLA block is well solubilized by the chloroform solvent. The addition of methanol (good solvent for peptides) results in more dynamic system. At the appropriate solvent ratio, the peptide-polymer conjugate should be molecularly dissolved. This behavior was confirmed with the dynamic light scattering (DLS) findings. As can be depicted from Figure 4.10, different aggregate classes can be observed. For the $CHCl_3$/MeOH system, small 0.29 nm sized species were observed, in contrast to much larger 2.08 nm sized aggregates in the chloroform system. While the $CHCl_3$/MeOH system suggests molecularly dissolved species of the bioconjugate with $M_n = 3300$ g/mol, the pure $CHCl_3$ solvent system promotes aggregate formation. In addition, there are some larger species found in both solutions probably attributed to larger aggregates. It is important to note however that as the DLS measurement is size-weighted, the dominating species are typically small species.

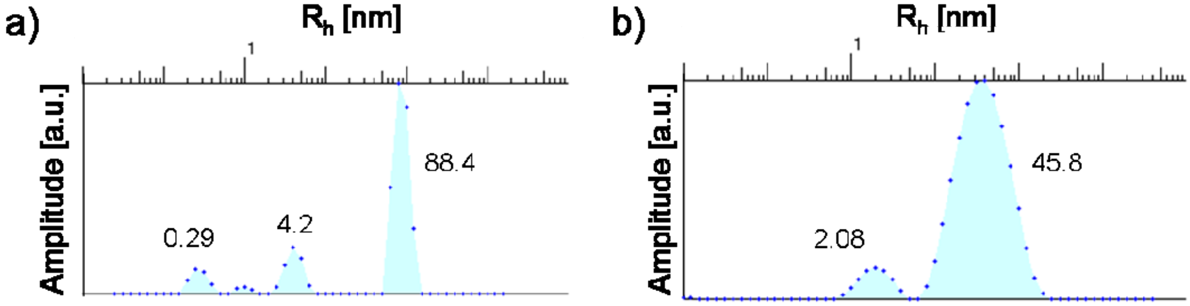

Figure 4.10. DLS measurement of PLLA-CGGRGDS solutions in a) $CHCl_3$/MeOH (3:1/v:v) and b) $CHCl_3$ demonstrated different sized aggregates (hydrodynamic radius, R_h).

It is assumed that the peptide-conjugate aggregation in chloroform occurs as the hydrophilic part of the block copolymer is assembles into micelle-like structures, with the PLLA part interacting with chloroform solvent molecules. By addition of methanol the peptide component is released from the aggregated state to the more molecularly dissolved state. This is in agreement with the DLS findings. For the electrospinning of PLGA/PLLA-*b*-CGGRGDS solutions, the situation becomes more complex. However, PLGA is thought not to contribute to a large extent to aggregate dissociation in $CHCl_3$. The aggregations formed in chloroform therefore might be entrapped within the fiber bulk, preventing them from surface segregation. In contrast the dissolved species of the peptide-conjugate is believed to promote such surface segregation. In addition, small species may diffuse at rates faster than aggregates favoring segregation.

4.1.2 Cell tests and spinning into cell culture

The RGD sequence in the bioconjugate is a common segment in the adhesion protein fibronection, thus promoting the cell adhesion. Therefore to clarify the bioactivity of as-synthesised peptide-funtionalised fibres, cell growth studies were investigated. Fiber meshes spun from a 9 wt% PLLA-*b*-CGGRGDS/PLGA blend were tested for cell culture with L929 fibroblasts (in collaboration with Dr. A. Lankenau, IBMT). Initially the interaction between cells and the RGD functionalized fiber meshes was examined. For this purpose the cells were plated for 1 day on a fiber coated glass slide. Cell attachment and spreading occurred and the adhesive areas localized at the cell periphery seemed to follow the fiber morphology (Figure 4.11).

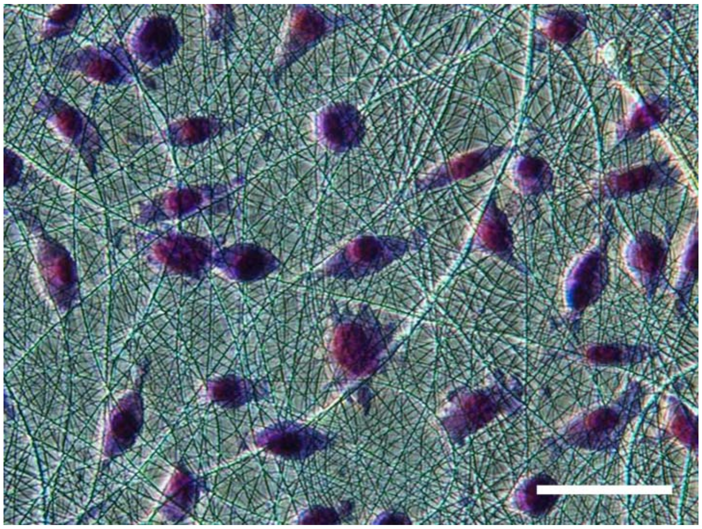

Figure 4.11. Image of L929 fibroblast adhesion on RGD-functionalized fiber mesh (9 wt% PLLA-*b*-CGGRGDS/ PLGA blend fiber, 1 day cell culture with 10% serum, giemsa staining, scale bar: 50 µm).

To elucidate if cell adhesion occurs specific through RGD-integrin-interaction or via non-specific means the RGD-functionalized meshes were compared against pure PLGA fibers meshes. The adhesion behavior was monitored after seeding with L929 at intervals for 1 h for 6 h and then after 24 h. In this culture conditions, no differences could be discerned between PLGA and RGD-functionalized fibers at any time. This might be explained by a too low RGD concentration on the fiber surface and a too high serum content that probably screens the few exposed RGD groups.

To overcome this two limitations, PLLA-*b*-CGGRGDS content was increased to 18 wt% with concurrently decrease in solution concentration from 5 to 3% w/v to reduce the fiber diameter. For this set of experiments, other fibroblasts like the NIH 3T3 (in collaboration with Dr. J. Polleux MPI of Metals Research) were tested in a culture medium with a low serum content. As displayed in Figure 4.12A/B in contrast to the previous experiments a better cell attachment and spreading on RGD-functional fiber was observed in comparison to pure PLGA after 4 h. After 20 h this trend was even more dominantly, showing mainly rounded cells on the PLGA fibres and spread cells in presence of RGD groups (Figure 4.12A2 versus Figure 4.12B2).

Additionally, RGD-functionalized fibers were annealed in water at ~ 40°C for several days in order to improve the homogeneity of the RGD distribution on the fiber surface. In a preliminary experiment using a lower cell density, the fibroblast adhesion was enhanced via fiber guided attachment of cells after 6 h and to a larger extent after 20 h (Figure 4.12C1/2).

Overall such fiber meshes are interesting by combining structural with chemical functionality, which might lead to synergistic effects. In addition biofunctional fibers are directly obtained without activation and/or grafting strategies which might compromise the polymer backbone or require additional linker chemistry.

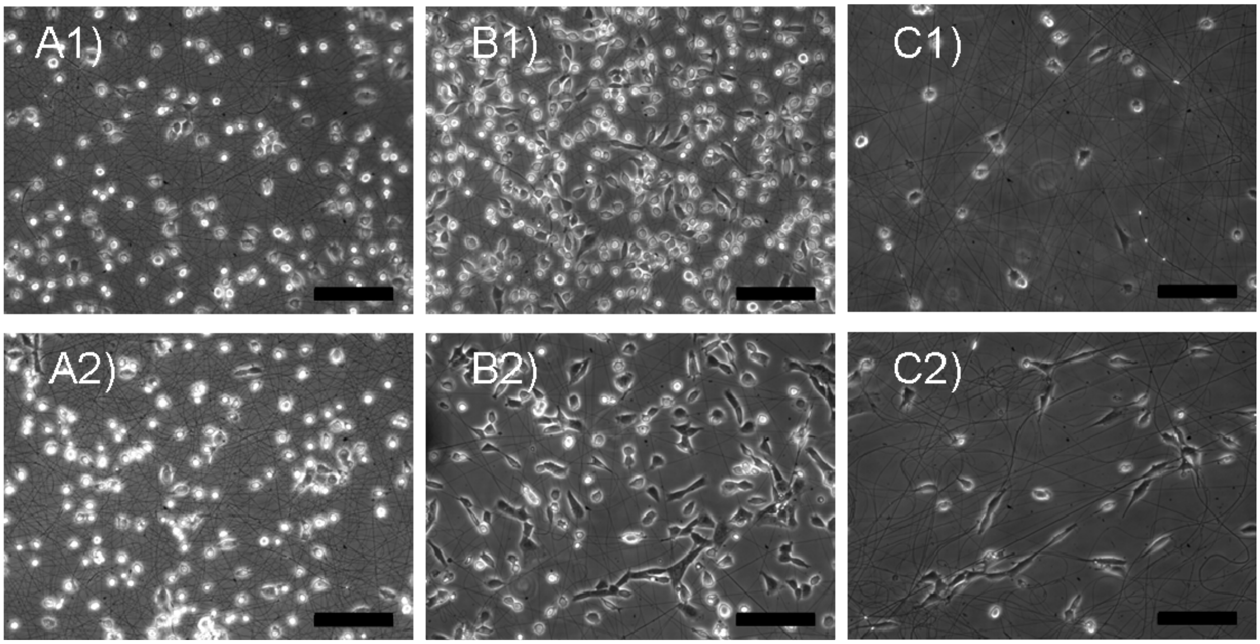

Figure 4.12. Cell attachment on electrospun fiber meshes indicates a superior adhesion on RGD functionalized fiber (B and C) compared to pure PLGA fiber (A) at different time points (A1/B1: 4 h, C1: 6 h, A2/B2/C2: 20 h cell culture, scale bar: 100 µm).

Interestingly, along side the observed increase in cell spreading on RGD-functionalised fibre mats, an increased hydrophilic surface directly after production was also observed. This is in contrast to non-functionalised PLGA fibrils that possess a hydrophobic surface as indicated by previously discussed H_2O contact angle studies. The difference are obvious and were visualized via wetting of Dulbecco's Modified Eagle Medium (DMEM) with electrospun fiber composed of pure PLGA fiber meshes and RGD-functionalized fiber mats (Figure 4.13a versus c). Whereas the mesh did not wetted in the case of pure PLGA, the medium soaked into the fiber mesh, as observed for nonwetted white area on the PLGA fiber meshes (Figure 4.13b). In contrast fully wetted RGD-functionalized fiber meshes, have a hydrogel-like appearance.

The hydrophilic behavior of RGD-funtional fiber meshes appears to be promising with regard to step-by-step fiber cell construction. Therefore fibres were spun onto a cell culture medium, then cells were seeded resulting in the eventual sandwiching of cells with another fibre layer. This procedure can then be repeated to produce in situ fabrication of cell/fiber sandwich composites; circumventing problems associated with limited cellular penetration (see Chapter 3).

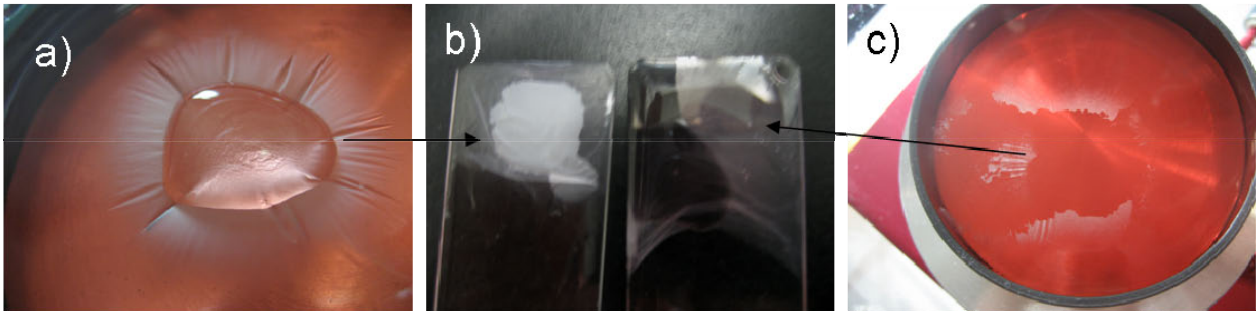

Figure 4.13. Wetting behavior of PLGA meshes and meshes spun from PLGA/PLLA-b-CGGRGDS blends with DMEM (a) versus c). Both meshes were then removed using a microscopy glass slide where the white part indicates nonwetted areas (b).

In order to investigate cell behavior in response to potential solvent residues or remaning charges, L929 cell proliferation was examined while fibres were directly electrospun into the cell culture (Figure 4.14a). Cells were grown on tissue culture plates (TCP) in advance. In a control experiment the normal proliferation of L929 was performed (Figure 4.14b). The comparison of the two proliferation lines did not indicate any adverse effect on cell behaviors indicating that solvent or applied field had no immediate effect on the cell culture after 2 or 4 d (data not shown).

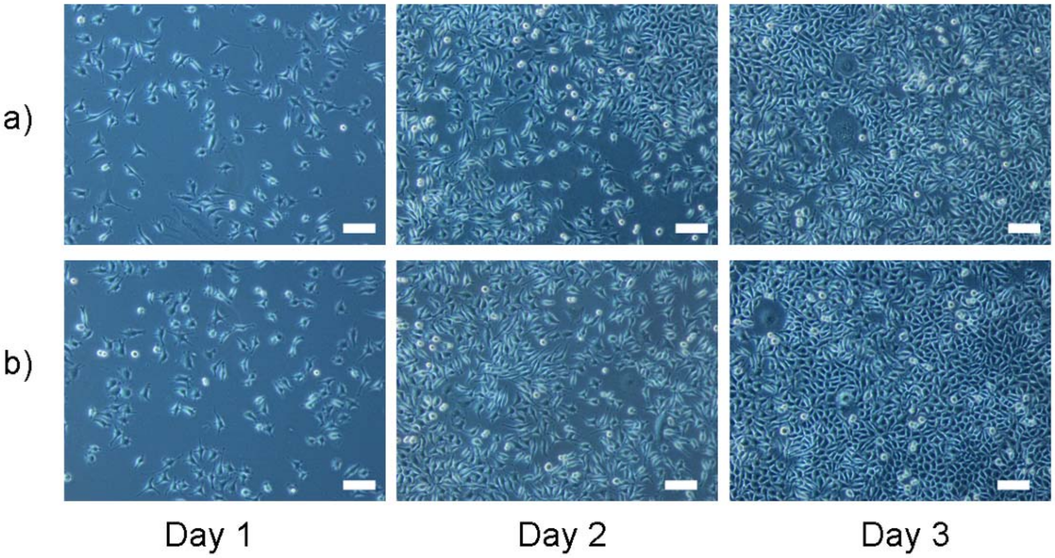

Figure 4.14. Cells proliferate without any adverse effect on tissue culture plates after spinning ~5 min PLGA/PLLA-*b*-CGGRGDS blend fiber into the cell culture (a). In (b) the control is shown for comparison (scale bar: 100 µm, a) day 1, the picture is taken before electrospinning).

In initial experiments, U2OS cells were used for the creation of sandwich fiber-cell-fiber structure. These cells are genetically modified in such a way, that they can be visualised live using fluorescence microscopy without additional staining. The meshes were immediately after sandwich fabrication shifted into another TCP to ensure only encapsulated to be within the fiber mesh. In addition, 3 days after sandwich fabrication, the sandwich was transferred on to another TCP to remove non-adherent cells. Fluorescence imaging indicated cell colonies present within the fiber meshes (Figure 4.15a). Although, this outcome was promising additional experiments related to the exact seeding and further handling as well as characterizations need to be conducted, which could not be accomplished within this work.

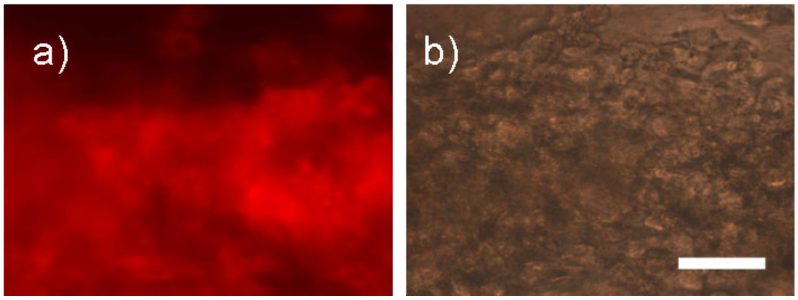

Figure 4.15. The fluorescence light micrograph visualized vial U2OS cells as indicated by the red stained areas shown in (a) which were grown in the fiber fabric for 5 days. In (b) a transmission light microscope image is shown (scale bar: 100 µm).

Overall, RGD-functionalised fibre meshes showed a pronounced effect on cell adhesion as compared to pure PLGA fibers. Furthermore, the instantaneous hydrophilicity offered by the fibre meshes makes the as-synthesised meshes attractive for cell infiltration. Initial experiment indicated that via a step-by-step fibre-cell-deposition, 3D constructs are relatively easily accessible. In addition, the hydrogel-like appearance of wetted RGD-functionalised fibre meshes are interesting candidate materials for chondrocytes cell studies, which are currently ongoing in the group of Prof. D.W. Hutmacher (QUT, Australia).

4.2 Fabrication of reactive polymer fibers

In this section a modular approach is described to the chemical functionalization of fiber meshes. An initial reactive fiber mesh was electrospun in a one-step process and then subsequently decorated by surface grafting of biomolecules without further activation (e.g. plasma) or additional linker chemistry. In contrast to one-step functionalisation (see Chapter 4.1), biomolecules will not be entrapped in the bulk fiber, making 100% of the attached molecules accessible. This attachment strategy is based on a polymer bound activated ester.[204] Amino-functionalized biomolecules nucleophilically substitute the pentafluorophenyl esters linked to the polymethacrylate backbone, forming an amide-linkage (Scheme 1). In addition, pentafluorophenol is released to be quantitatively measured via UV/Vis spectroscopy, thus allowing to determine the kinetics of the functionalization reaction.

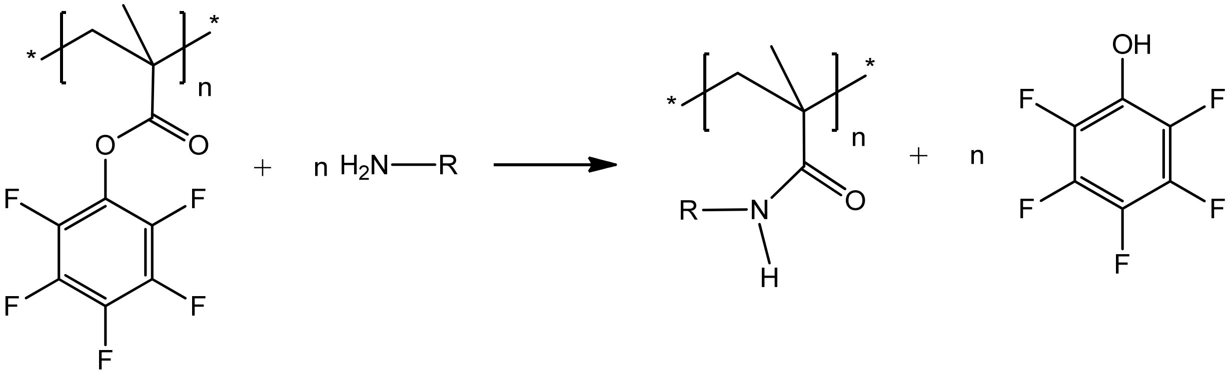

Scheme 1. Functionalization strategy of active ester functionalized fiber accompanied by pentafluorophenol release detectable with UV/Vis spectroscopy

4.2.1 Electrospinning of polymers with reactive esters

The base polymer poly(pentafluorophenyl methacrylate) (PPFPMA) with side-chain active esters was provided by the group of Dr. Patrick Theato (University Mainz). PPFPMA was synthesized by free radical polymerization as described elsewhere.[204] The PPFPMA used in this study had a molecular weight around M_n = 29.3 kg/mol (PDI = 1.67) and a glass transition point similar to PMMA (T_g = 125 °C).

In the first attempt the pure PPFPMA polymer was successfully electrospun to yield fibers independent of the low molecular weight. The electrospinning was optimized using different solvents and adjusting the concentration. Reducing the latter resulted in thinner fiber (Figure 4.16a-c and e-f), which is in agreement with previous reported results (see Chapter 4.1). Operating at high concentrations and with pure chloroform as solvent resulted in nozzle clogging within a short experimental time (Figure 4.16a). This is supposed to be caused by the lower solvent content and high volatility of $CHCl_3$. Therefore, DMF as a solvent of lower volatility was added (Figure 4.16b) which is frequently added because of its high polarity and conductivity.[121] As clogging was still an issue, the concentration was further decreased, whilst $CHCl_3$ was replaced by THF and DMF content was increased, improving spinning continuity (Figure 4.16c, e, f). A 17% w/v system yielded homogeneous fibers, while a further decrease in concentration induced partially beaded fiber. A common feature observed for this system was the increased deposition in the z-direction. The increase of this thickness dimension, which could be interesting for scaffold cellular ingrowth, was attributed to the high humidity (lower electrostatic repulsion) and the stiff nature of the polymer, caused by the relative stiff backbone.

Interestingly, the use of pure PPFPMA/DMAc solutions resulted in the formation of thick porous fibers and nozzle clogging (Figure 4.16d). These are common phenomena when using low volatile solvents. Both observations indicate that the solvent evaporated quickly, attributed to the low interaction between solvent and solute; considered the dominate factor, rather than solvent volatility.

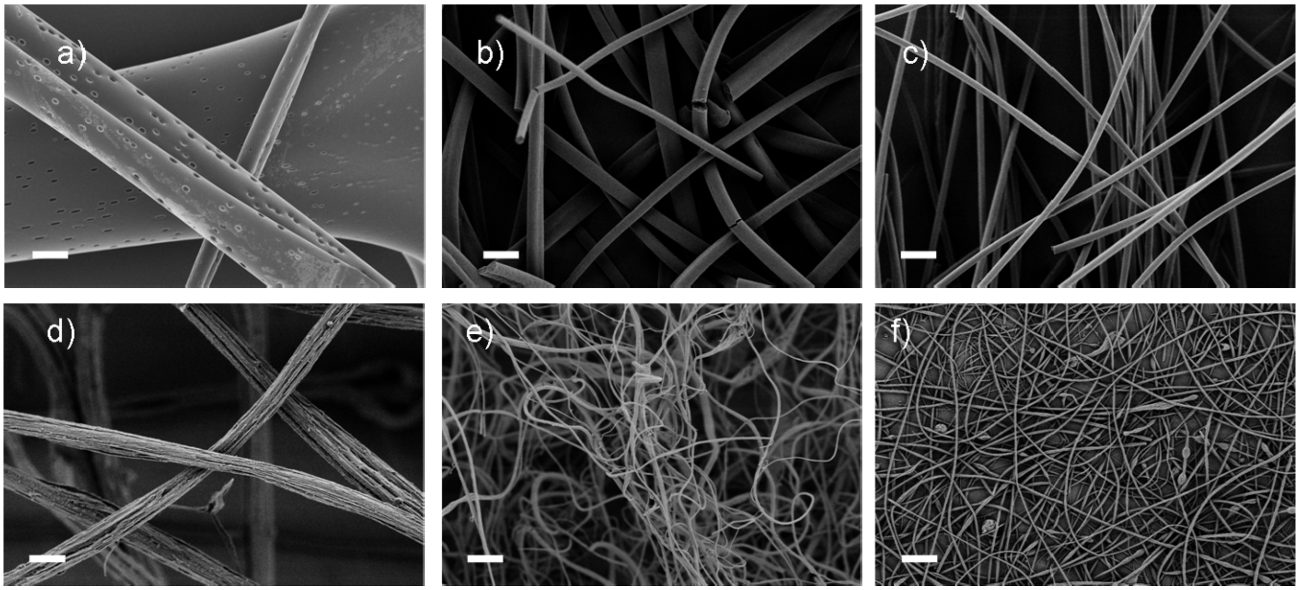

Figure 4.16. SEM images of electrospun pure PPFPMA fibers using different solvents and concentrations: a) 56% w/v, $CHCl_3$, b) 32% w/v, $CHCl_3$/DMF (3:1), c) 30% w/v, THF/DMF (3:1), d) 20.2% w/v, DMAc, e) 17% w/v, THF/DMF (1:1) and f) 15.7% w/v, THF/DMF (1:1) (all 7 cm, 0.2-4.7 mL/h, 5-10 kV, 56-64%; scale bars = 10 μm)

Electrospinning of pure PPFPMA was successful, therefore in the next step these meshes were used to be functionalized with aminoethanol (AE) as a model substance. The release of pentafluorophenol (PFP) during functionalization was detected with UV/Vis spectroscopy at λ = 267 nm for methanol solutions. A calibration curve was established prior to measurement (Chapter 6.1.1.4). The production of PFP was ascertained from the absorption intensity and together with the known initial mass of the PPFPMA mesh, a yield was calculated assuming quantitative conversion. This value however could not reach 100% as functionality remains entrapped in the bulk fibre and hence can not participate in the reaction.

The investigated meshes (i.e. 1-16 mg: Figure 4.16 a, b, d, e, f) were reacted with AE at room temperature using methanol as solvent (5 mL, 2-5 v/v% AE). In a first set of experiments static reaction conditions, 1-1.5 days reaction times and a high excess of AE were used (Table 5). As it could be expected, using meshes with a decreasing fiber diameter from 32 ± 9 μm to 4.3 ± 1.6 μm (Table 5a => b) increased the yield dramatically ~ 3 times. This trend was confirmed, by comparing fiber mats with 32 ± 9 μm fiber diameter (a) and with mats of fiber diameters of 6.8 ± 1.6 μm or 0.54 ± 0.29 μm (d or f) (Table 5, static). This comparison demonstrated a decrease in reaction time and AE excess resulted in similar or higher yields. While these initial experiments did not use dynamic conditions to prevent mechanical fiber degradation, gentle agitation was used in a secondary set of experiments to enhance reaction kinetics promoted by increased homogeneity. As a result yields increased by a factor of ~ 3 (Table 5d/f) relative higher values compared to static conditions. Using higher equivalences (eq.) of AE for the reaction with 0.81 ± 0.34 µm sized PPFPMA fiber mats ~ 4% (2.5h) and ~ 20% (19h) yield were reached. Control experiments using pure methanol indicated ~ 10 times smaller conversion compared to AE solutions (ref, without AE, Table 5d).

Table 5. Yields (y) of the reaction of PPFPMA meshes with AE derived from UV-Vis spectroscopy.

sample	conditions	time [h]	eq. AE	y [%]
a	static	36	111	6
b	static	36	135	16
d	static	24	65	5.3
f	static	24	84	7.9
d	ref, static	24	-	0.6
d	shaken	24	65	16.6
f	shaken	24	84	23.9
e	shaken	19	896	27.7
e	shaken	2.5	896	6.3
d	ref, shaken	24	-	3.3

reference (ref) were conducted in pure MeOH, equivalence (eq.) AE compared to PPFPMA repeat unit.

The fiber structure and functionalization of fibers with the AE model compound are promising. However the SEM image analysis of fiber meshes indicated a mechanical degradation during functionalization and sample handling. This suggests that the meshes are very brittle, which seem to be related to the low molecular weight and the high T_g of the polymer. Unfortunately such features hamper applicability during handling and shaking the reaction solutions (Figure 4.17a-c). Interestingly, the fibers presented some porous structuring within the fiber bulk, suggesting a possible phase separation during electrospinning.[126]

A common approach to overcome brittleness and to improve electrospinnability of a polymer is co-blending with another polymer which can be easily spun (Figure 4.17d). Therefore PEO, PnBA, PMMA, or PCL were blended with PPFPMA using $CHCl_3$ or THF/DMF as compatibilizing solvents. While the application of high molecular weight PnBA, PMMA, or PEO significantly improved the spinning behavior and resulting fiber morphology due to their higher molecular weight, the mat handling did not improve. For a PCL concentration of 12 wt% blended with PPFPMA, electrospinning was conducted using a 22.3% w/v solution in THF/DMF (1:1, v:v), resulting in a discernable elasticizer effect, generating significant plastic fracture behavior (Figure 4.17d).

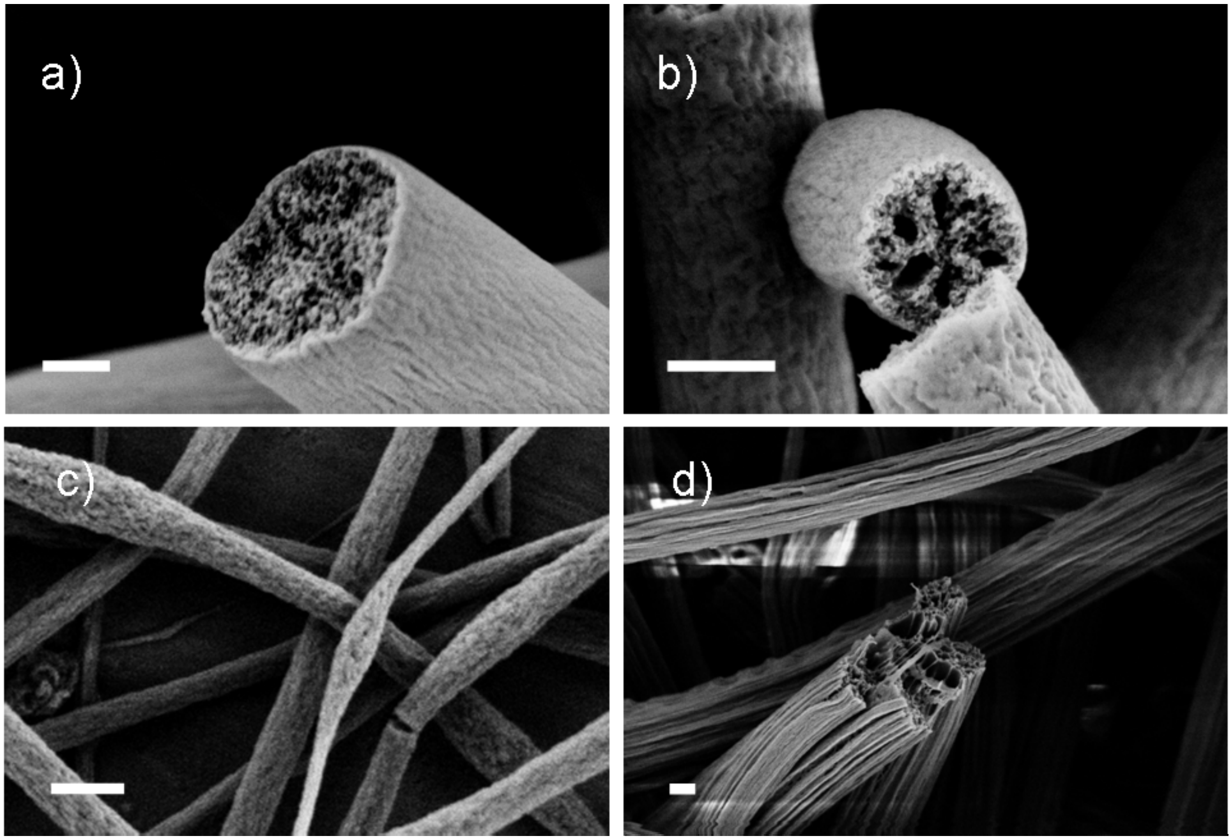

Figure 4.17. PPFPMA fibers break due to their brittleness as it is visible from the SEM micrographs (a-c) Using 12 wt% (solid content) PCL as elasticizer like PCL improved the issue a bit (d) (parameters. a: $CHCl_3$/DMF(3:1), 32% w/v solid/solvent, b: THF/DMF(3:1), 30% w/v, c: THF/DMF(1:1), 15.7% w/v, d: THF/DMF (1:1), 22.3% w/v related to solid content, all 7cm, 0.5-4.7mL/h, 5-10kV, 50-64%, scale bars = 1 µm).

In order to improve this effect, the content of PCL was increased to ~ 50 wt%. The ~ 12% w/v solutions of PCL/PPFPMA in THF/DMF (1:1, v:v) appeared turbid after a homogenization step just before electrospinning by vortexing or the use of an ultrasound finger. The morphology of the electrospun fiber meshes was similar to those of pure PCL mats spun at similar conditions (Figure 4.18a, Chapter 6.2, Figure S6). It should be noted that the fiber morphology changed during spinning as can be depicted from Figure 4.18b, which was electrospun from the same solutions as in Figure 4.18a. In addition, it was observed that the electrospinning behavior altered (i.e. the form of the jet) which correlated appropriately with the obtained structures, resulting in a bimodality of thick fibers (probably attributed to PPFPMA rich phase) and thin fibers (Figure 4.18b). SEM image analysis for as-synthesised meshes suggests that demixing occurs both during and before the spinning process, regardless of an initial homogenization (Figure 4.18a-c). In addition it was observed that increased beading occurred during processing under low humidity, which is consistent with the behavior of electospun polymer/bioconjugate blends from $CHCl_3$ (Figure 4.2c versus

Chapter 6.2 Figure S6). Importantly, the electrospun fiber mats shown in Figure 4.18 could be handled without obvious mechanical degradation also within 3 weeks reaction time with the model compound AE, which will be addressed in the next section.

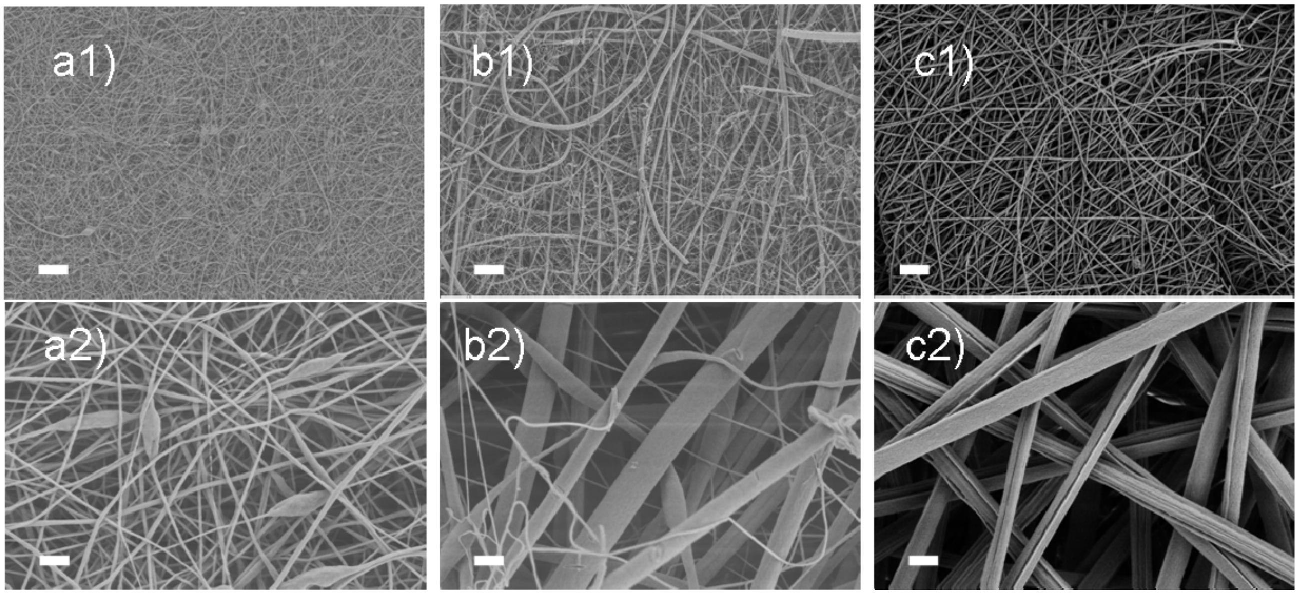

Figure 4.18. Different structured fiber meshes were obtained spinning a 1/1 (w/w) PCL/PPFPMA blend as indicated by the SEM images (a-c). Electrospinning was conducted using THF/DMF (1:1/v:v) solutions (parameters: 5.4-8 kV/ 7 cm, 0.8 mL/h, a)/b) 12.7% w/v, 53%, c) 12.1% w/v, 41%; scale bars a-c1)= 20 µm, a-c2) = 2 µm).

PCL/PPFPMA blend meshes with 12, 48 and 50 wt% PPFPMA were reacted with different concentrated AE solutions under dynamic conditions. Analogously to the meshes composed of pure PPFPMA the PFP release at a given reaction time was quantified and converted into yields (Table 6). Using fiber mats with only 12 wt% PCL blend content, the AE substitution reached 4.4% after 2 h and did not dramatically increase over the next 4 h (5%, 6 h). After 24 h the value increased to 14.7%, which was ~ 10 times higher compared to 2 h and the control reaction with pure methanol. The reaction seems to proceed first within 2 h at accessible spots. Then, continuing after the initial surface functionalization, the surface becomes increasingly hydrophilic, which encourages further reaction into the fiber bulk. This is also exemplified from the mesh prepared from the ~ 1:1 (w/w) PCL/PPFPMA blends. At 5.5 h, 11.1% of the theoretical PFP maxima was released, followed by a significant increase in PFP yield over the following 4 days (50.8%), eventually reaching 95.6% after 7 days. For the reported reactions so far, a large excess of AE was used. However, biomolecules are generally valuable substances, and therefore the procedure was replicated under a reaction condition ratio close to one, to study the resulting reaction kinetics. The resulting yields decreased dramatically to 2.7% after 3 days and 4.5% after 11 days. Still, all the yields were larger than conversions of reference reactions with pure methanol (e.g. 1.4%, 4 days).

Table 6. Conversion (y) of PPFPMA/PCL blend meshes with AE in methanol

time	sample	AE [µL]	m [mg]	eq. AE	c [wt%]	y [%]
2h	PCL1	145.631	2.1	329.5	88.0	4.4
6h		145.631	2.1	329.5	88.0	5.0
24h		145.631	2.2	314.5	88.0	14.7
24h, ref			2			1.3
5.5h	PCL9	145.6	2.6	487.3	48.1	11.1
4d		145.6	2.6	487.3	48.1	50.8
5d		145.6	2.6	487.3	48.1	59.8
7d		145.6	2.6	487.3	48.1	95.6
3d	PCL22	1.0	9.8	0.9	50.0	2.7
4d		1.0	9.8	0.9	50.0	3.5
11d		1.0	9.8	0.9	50.0	4.5
4d, ref	PCL22		8.7		50.0	1.4

Three samples were used PCL1/9/22, reference (ref) were conducted in pure MeOH, the amount of AE indicated is present in 5 mL AE/MeOH solutios, equivalence (eq.) AE compared to PPFPMA repeat unit, concentration (c) of PPFPMA in the blend).

To investigate the behavior of the same system using more challenging sterically hindered amines, the previous reaction was conducted using isopropyl amine (IPA) and a PPFPMA/PCL fiber blend (1:1, w:w). Using a large excess (87 eq.) the release seemed to be slower as 2% (4 h), 8.3% (8 days) and 12.7% (15 days) of the maximum PFP was released (Chapter 6.2, Table S4).

In order to examine the spatial uniformity of the functionalization, amino and as a control hydroxyl functional fluorescein dyes were reacted with PPFPMA/PCL fibers in methanol. After 7 and 17 h reaction time the difference in fluorescence demonstrated the successful immobilization of the amino-functional fluorecein on the PPFPMA in contrast to hydroxyl-functionalized fluorescein (Figure 4.19). In addition, the increase of the fluorescence intensity after 17 h, regarding also the decreased gain and exposure time of the fluorescence microscope, suggests higher conversion, which is in agreement with the UV-spectroscopy.

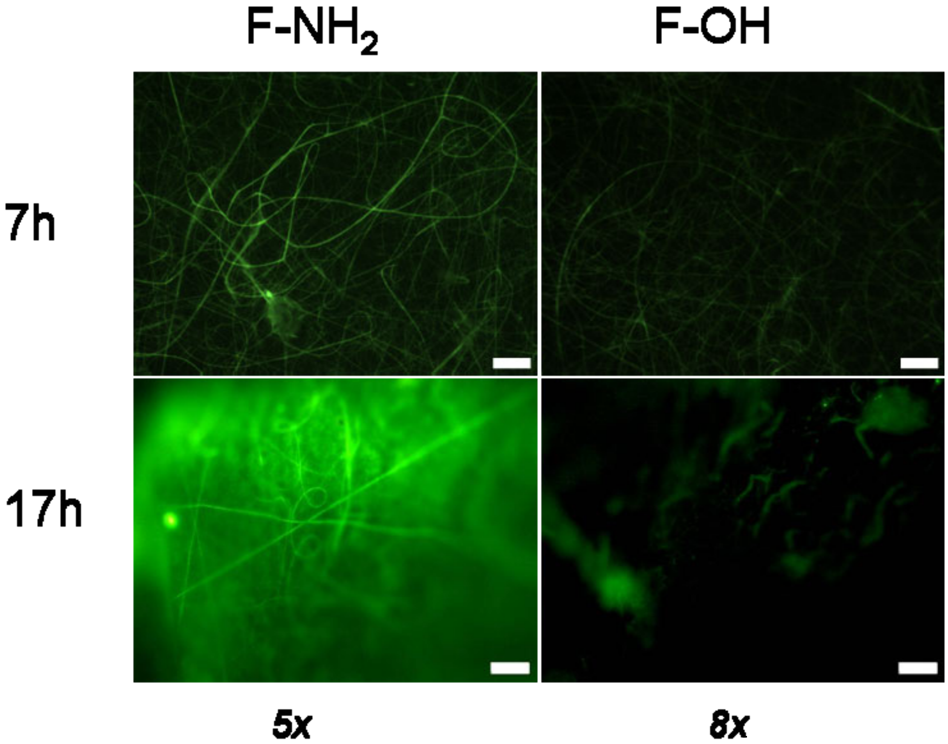

Figure 4.19. The reaction of fluorescein (F) functionalized with amino (-NH_2) or hydroxyl group (-OH) and PCL/PPFPMA fibers suggest a homogenious distribution as depicted from the fluorescence light micrographs (7h: 7.9x gain, 473.1ms, 17h: 5.6x gain, 250.9ms, scale bars = 10 µm).

In addition, contact angle measurements indicated an increase of hydrophilicity by decreasing the contact angle from 138° to 0° after 2 weeks reaction time (PCL10, 450 eq.). Together with the UV-studies and fluorescence microscopy data, these reactive fibers were considered suitable for further functionalization with complex biomolecules (e.g. peptides, sugars), which will be addressed in the next section.

4.2.2 Potential bioactive applications

Nonwovens functionalized with tritrpticin for antimicrobial nanofiber

Antimicrobial surfaces have important practical relevance, particularly in the food industry and biomedicine. An example for the latter is the development of implants to repel against bacteria and as such prevent infections. In Nature, commonly antimicrobial peptides are found in different species including human. Most natural antimicrobial peptides seem to act by damaging the bacterial membrane structure, as a result of their cationic nature due to multiple Arg and/or Lys residues. These residues can bind to the negatively charged lipid membranes of bacteria and initialize the membrane incursion triggering channel formation or rupture of membrane.

Tritrpticin (Trit), a member of the cathelicidin family with the sequence VRRFPWWWPFLRR, was used in this study as its antimicrobial effect is well described in literature.[205] The peptide was obtained, using solid-phase supported peptide synthesis with a KG spacer resulting in H_2N-KG-VRRFPWWWPFLRR-$CONH_2$. This sequence has two preferable amino-groups to anchor the peptide to the nanofibers.

Functionalizations were performed in a mixture of water/methanol (1:1, v:v) as Trit is not soluble in water or methanol alone. The PFP release could not be quantified by UV/Vis spectroscopy as Trit itself absorbs below λ = 300 nm due to Tryptophan residues. Model reactions with AE, resulted in lower yields as corresponding reactions in methanol. For example using a large excess of AE (324 eq.) resulted in 5.5% PFP release after 11 days in methanol/water compared to a 40.3% PFP release (6 days, 189 eq.) in pure methanol. This might be attributed to the increased nucleophilicity of amines in pure methanol compared to in water. At low AE with excess of 1 eq. the yield of PFP was 1.0% after 1.5 days and 1.2% after 8 days. Despite the low values for PFP release, these are still higher than from the control reaction with pure methanol (ref. 8 days: 0.24%, Chapter 6.2, Table S5).

In order to maximize the conversion with Trit, electrospun meshes on glass slides were reacted with 2 mL Trit-solution (4.5 mg/mL Trit/(MeOH/H_2O), 21 eq.) for 2 weeks. The meshes were then characterized with XPS. As shown in Table 7 the electrospun PCL fibers only indicated carbon and oxygen atoms. The blend system was also composed of fluorine atom, attributed to the pentafluorophenyl side group of the PPFPMA. After reaction with Trit fluorine at the surface decreased from 5.4 to 2.4 at%, suggesting a release of pentafluorophenol from the polymer backbone upon reaction. In addition the nitrogen content increased to 5.3 at%, attributed to the successful surface anchoring of the Trit moiety to the fibers. Together with the decrease in fluorine content this highly suggested the successful reaction of Trit with the PPFPMA at the fiber surface. These materials are currently under investigation as potential antimicrobial materials by the group of Prof. J. Tiller (TU Dortmund).

Table 7. XPS quantification data of functionalization as followed by fluorine (F) and nitrogen content (N).

sample	C [at%]	O [at%]	N [at%]	F [at%]
PCL431	83.3	16.4		
PCL/PPFPMA27	69.0	25.6		5.4
Tritrpticin, 27	67.2	25.2	5.3	2.4

The values were corrected for noise of background signals (raw data: Chapter 6.2 Table S6).

Functional nanofiber meshes for macrophage stimulation

The interaction of pathogens, such as bacteria, with natural interfaces is not limited to peptides (e.g. antimicrobial), but also essential to the molecular recognition of sugar units. The latter is important in several ways, more importantly, in the stimulation of immune response cascades of organisms in diseases like, for example, Malaria in humans. The immune system indentifies microorganism-specific motifs by innate immune receptors. A common receptor–ligand complex is formed between the mammalian Toll-like receptor 4 (TLR4)–MD2–CD14 complex and bacterial lipopolysaccharide (LPS).[206] Host recognition of pathogenic microorganisms induces the immune response, by producing antimicrobial substances and by recruitment of phagocytic cells like macrophages. One simple but important substance identified is D-Mannose. Its presentation is specifically detected by macrophages via D-Mannose receptors, which mediate endocytosis or cytokine production.[207] The latter are important compounds for signaling cascades to trigger the immune reaction.

In this context electrospun PPFPMA/PCL fibers were functionalized with amino-functional D-mannose (D-man) or D-galactose (D-gal) (Figure 4.20). Both sugars have been synthesized in the group of Prof. P. Seeberger (MPI-KG). The resulting functional meshes were subsequently tested to activate the cytokine production of macrophages.

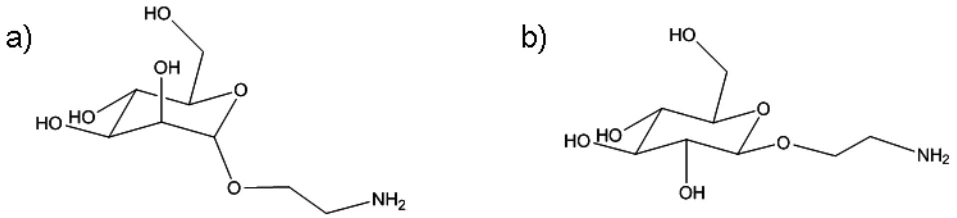

Figure 4.20. Structure of the amino-functional (a) D-Mannose and (b) D-Galactose.

Active ester surface functionalization of the meshes was conducted by soaking the meshes in methanol solutions of the two saccharides. In a first test reaction, the PFP release was studied, as monitored by UV/Vis spectroscopy, indicating a rather low yield of 2.5% within 9 days for D-Man, but still larger than the control experiment (i.e. reaction with pure methanol). In contrast the conversion with D-Gal was higher reaching 4% in 8 days (Table 8).

Table 8. Conversion of PPFPMA/PCL blend meshes with D-Man and D-Gal.

time	sample	sug. [mg]	m [mg]	eq. sug.	c [wt]	y [%]
Mannose						
15h	PCL21	8.9	4.0	4.9	51.0	3.3
2d		8.9	4.0	4.9	51.0	3.5
9d		8.9	4.0	4.9	51.0	3.6
Galactose						
15h	PCL21	9.4	3.6	5.8	51.0	1.9
1d		9.4	4.6	4.5	51.0	3.5
8d		9.4	4.6	4.5	51.0	5.5

5 mL Sugar (sug.) MeOH solutions were used, equivalence (eq.) sug. compared to PPFPMA repeat unit, concentration (c) of PPFPMA in the blend.

In order to further insure the immobilization of saccharides onto the PPFPMA/PCL fiber surface, XPS was performed and the elemental surface composition was quantified (Table 9). Comparing the pure PCL/PPFPMA with each other, indicates differences in the fluorine content and therefore in PCL/PPFPMA ratios, which is consisted with the observed differences in fiber morphology (Figure 4.18). After reaction with D-Man or D-Gal the corresponding fluorine content decreased, indicative of PFP release. In addition, for D-Gal functionalized fibers the nitrogen atom from the linker unit could also be detected. This coincided with the findings from the UV spectroscopy that D-Gal seemed to be immobilized to a higher extent than D-Man (sample: PCL/PPFPMA21). However, using a higher excess of D-Man (sample: PCL/PPFPMA 34: 279 eq., compared to 21: 4.9 eq.) and D-Gal (PCL/PPFPMA 29: 360 eq. compared to 21:4.5 eq.) did not further decrease the fluorine ratio after the reaction. This might be explained by the presence of non-accessible groups as detected by XPS and the small scale mass used for this reaction due to the value of the saccharide molecules (sample: PCL/PPFPMA 29/34: 0.3 mg).

Table 9. XPS quantification data for sugar modified PCL/PPFPMA fibers.

sample	t [d]	m [mg]	eq. Sug.	C [at%]	O [at%]	N [at%]	F [at%]
PCL/PPFPMA29				63.3	32.9		3.8
PCL/PPFPMA21				62.1	14.8		23.1
PCL/PPFPMA34				47.4	45.5		7.0
Mannose 21	9	4	4.9	65.0	23.1		12.0
Mannose 34	12	0.3	4.5	56.1	38.6		5.3
Galactose 21	8	4.6	279.0	54.7	30.2	1.5	13.6
Galactose 29	12	0.3	368.0	70.0	26.7		3.3

The values were corrected for background signals and DMF traces (raw data: Chapter 6.2 Table S6), t: reaction time in days (d), m: mass of PCL/PPFPMA meshes, eq. equivalence amount of sugar.

In summary, mesh characterizations by XPS and UV- spectroscopy confirmed an effective functionalization and introduction of functional saccharides onto the fiber surface. To investigate whether macrophage cultivation on the fiber mesh could lead to cytokine production, cytokine stimulation studies using macrophages (cell line RAW264.7) with functionalized and nonfunctionalized fiber meshes were performed in collaboration with Dr. B. Lepenies, and Prof. P. Seeberger (MPI-KG). The cells were seeded on functional meshes carrying D-Gal and D-Man (functionalization: similar conditions as XPS sample Mannose 34, Galactose 29). As control, meshes functionalized with aminoethanol (AE3) and un-functional PCL/PPFPMA meshes (blank) were used. As expected, the meshes alone did not stimulate macrophages to the production of different cytokines as TNF-α, IL-6, IL-12, and IL-1 (Figure 4.21 and data not shown). Lipopolysaccharide (LBS) are found in the outer membrane of gram-negative bacteria and induce cytokine production in antigen-presenting cells through stimulation of the (TLR)-4 signaling pathway.[206] Stimulation of RAW macrophages in the presence of LPS induced marked production of TNF-α (Figure 4.21A), IL-6 (Figure 4.21B), and IL-12 (Figure 4.21C), but only marginal release of IL-1 (data not shown). However, in the presence of the D-Man-functionalized fiber meshes the production of TNF-α and IL-6 was significantly increased (Figure 4.21A and B), whereas no alteration was observed for IL-12 and IL-1 (Figure 4.21C and data not shown).

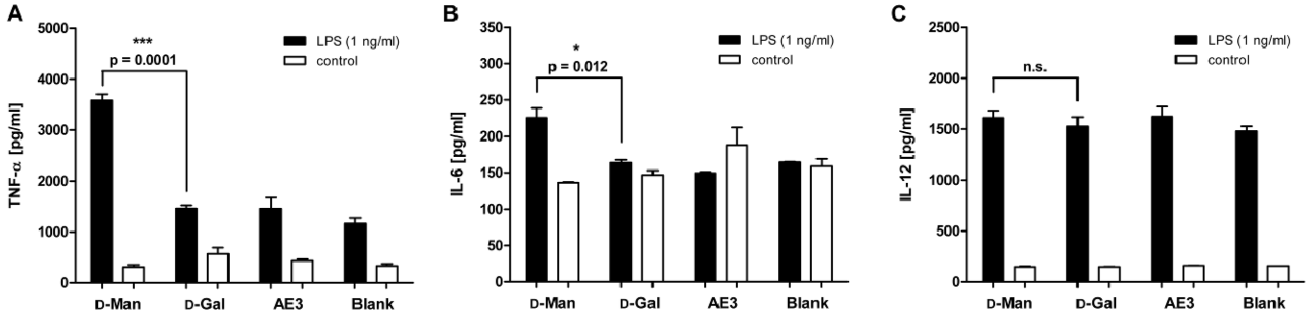

Figure 4.21 Cytokine production by RAW246.7 macrophages upon stimulation with LPS in combination with the functionalized meshes. Raw macrophages were seeded on the meshes and stimulated in the presence (black bars) or absence (white bars) of 1 ng/mL LPS overnight. TNF-α (A), IL-6 (B), and IL-12 (C) were measured in supernatants of stimulated macrophages. Measurements were performed in triplicates. Data are expressed as mean ± SEM for each group. Significance was tested with the two-tailed unpaired t-test.

To elucidate if the D-Man-functionalized fiber meshes also had an impact on the expression of co-stimulatory molecules, CD80/CD86 expression was measured on CD11b$^+$ macrophages by flow cytometry. Indeed, stimulation of RAW macrophages with LPS on the D-man-functionalized fiber resulted in a weak, but detectable increase in CD86 expression (Figure 4.22). Similar results were obtained for CD80 expression upon stimulation of RAW macrophages (data not shown).

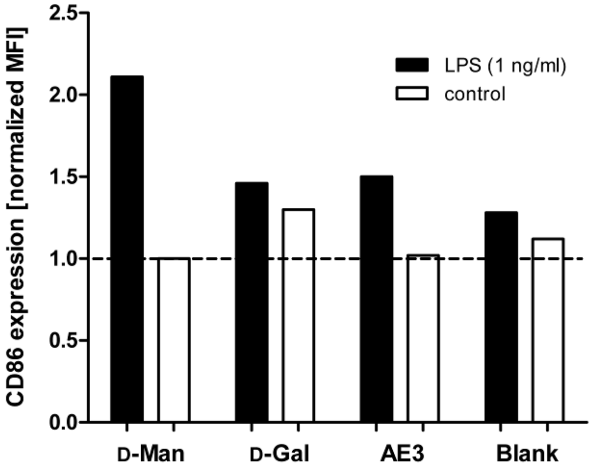

Figure 4.22 Expression of co-stimulatory molecules by RAW246.7 macrophages upon stimulation with LPS in combination with the functionalized meshes. Raw macrophages were seeded on the meshes and stimulated in the presence (black bars) or absence (white bars) of 1 ng/mL LPS overnight. Cells were gated on live CD11b+ cells (=macrophages). The mean fluorescence intensity (MFI) is shown. MFI was normalized to the MFI of unstimulated macrophages cultivated on the mannose-functionalized fiber mesh.

The results presented here indicate that stimulation with the D-Man-functionalized fiber meshes in the presence of LPS had a synergistic effect for cytokine production and expression of co-stimulatory molecules. These findings indicate that the sugar-functionalized fibers are biologically active and also in agreement with previous publications where murine macrophages were efficiently targeted by mannosylated proteins such as mannosylated bovine serum albumin.[208]

In summary peptide and sugar functionalization of PPFPMA/PCL fibers has successfully conducted, indicating the versatility of reactive fiber meshes for immobilization of biomolecules and preparation of biologically active meshes. Furthermore, the sugar functionalizations imply specific interactions with biological systems. In future studies, more complex sugar molecules will be employed for more biologically significant applications.

5 Summary and outlook

This thesis addresses the structural and functional control of electrospun fiber mats. The aim was to establish straightforward processes to obtain mats, which enable cellular ingrowth through designed porosity and functionalized fiber surfaces to control cell behavior (e.g. adhesion).

In the first section, it is shown that fiber meshes with bimodal size distribution could be obtained in a single-step process by electrospinning. A standard single syringe set-up was used to spin concentrated poly(ε-caprolactone) (PCL) and poly(lactic-*co*-glycolic acid) (PLGA) solutions in chloroform and meshes with bimodal-sized fiber distribution could be directly obtained by reducing the spinning rate at elevated humidity. A mechanism for the formation of these meshes was proposed based on analysis of high speed camera images of the spin jet. Scanning electron microscopy (SEM) and mercury porosity of the meshes suggested a suitable pore size distribution for effective cell infiltration.

The mixed meshes (e. g. nano- and microfiber fabrics) together with unimodal fiber meshes were evaluated for cellular infiltration. While the micrometer fibers in the mixed meshes generate an open pore structure, the submicrometer fibers support cell adhesion and facilitate cell bridging on the large pores. This was revealed by initial cell penetration studies, showing superior ingrowth of epithelial cells into the bimodal meshes compared to a mesh composed of unimodal 1.5 µm fibers. As epithelial cells are known to be more receptive to planar surfaces, additional cell studies investigated osteoblast and chondrocyte interactions with such meshes. However, no distinct effect of mixed sized fiber meshes on adhesion and production of glycoaminoglycans could be shown.

Degradation and mechanical tests were performed in order to further investigate the biomedical potential of such mixed fiber PCL meshes. The nanofibers resulted in a faster degradation behavior compared to microfibers, as demonstrated for wetting (plasma-treated) and nonwetting fiber meshes. Mechanical characterizations of micron- and nano-sized fiber meshes were conducted on macro- and microscale. While tensile testing indicated increased elastic modulus and lower strength of micron- versus nano-sized fiber meshes, force deformation measurements using a colloidal probe atomic force microscopy (AFM) confirmed an increased stiffness behavior.

The bimodal fiber meshes together with electrospun nano- and microfiber meshes were further used for the inorganic/organic hybrid fabrication of PCL with calcium carbonate or calcium phosphate, two biorelevant minerals. Such composite structures are attractive for the potential improvement of properties such as stiffness or bioactivity as in the case of calcium phosphate (e.g.

for osteoblasts). It was possible to encapsulate nano and mixed sized plasma-treated PCL meshes to areas > 1 mm^2 with calcium carbonate using three different mineralization methods including the use of poly(acrylic acid). The additive seemed to be useful in stabilizing amorphous calcium carbonate to effectively fill the space between the electrospun fibers resulting in composite structures. The organic part could be removed by leaching and the resulting inorganic pore system did not collapse upon a subsequent calcination step.

Micro-, nano- and mixed sized fiber meshes were successfully coated within hours by fiber directed crystallization of calcium phosphate using a ten-times concentrated simulated body fluid. It was shown that nanofibers accelerated the calcium phosphate crystallization, as compared to microfibers. In addition, initial soaking, longer crystallization times and the use of dynamic conditions were beneficial for the thickness of the calcium phosphate coating. Crystallizations performed at static conditions led to hydroxyapatite formations whereas in dynamic conditions brushite coexisted.

In the second section, nanofiber functionalization strategies are investigated. First, a one-step process was introduced where a peptide-polymer-conjugate (PLLA-*b*-CGGRGDS) was co-spun with PLGA in such a way that the peptide is enriched on the surface. It was shown that by adding methanol to the chloroform/blend solution, a dramatic increase of the peptide concentration at the fiber surface could be achieved as determined by X-ray photoelectron spectroscopy (XPS). Peptide accessibility was demonstrated via a contact angle comparison of pure PLGA and RGD-functionalized fiber meshes. In addition, the electrostatic attraction between a RGD-functionalized fiber and a silica bead at pH ~ 4 confirmed the accessibility of the peptide. A possible mechanism for the observed enrichment using chloroform/methanol solutions was discussed on the basis of dynamic light scattering measurements.

The bioactivity of these RGD-functionalized fiber meshes was demonstrated using blends containing 18 wt% bioconjugate. These meshes promoted adhesion behavior of fibroblast compared to pure PLGA meshes. In addition the direct production of hydrophilic PLGA-based fibers was used for electrospinning into cell culture without any toxic effects on cell proliferation.

In a second functionalization approach, a modular strategy was investigated. In a single step, reactive fiber meshes were fabricated and then functionalized with bioactive molecules. While the electrospinning of the pure reactive polymer poly(pentafluorophenyl methacrylate) (PPFPMA) was feasible, the inherent brittleness of PPFPMA required to spin a PCL blend to improve the mechanical stability of the fiber meshes. Blends and pure PPFPMA showed a two-step functionalization kinetics. An initial fast reaction of the pentafluorophenyl esters with aminoethanol as a model substance was followed by a slow conversion upon further hydrophilization. This was analysed by UV/Vis-spectroscopy of the pentaflurorophenol release upon nucleophilic substitution with the amines. The conversion was confirmed by increased hydrophilicity of the resulting meshes.

The PCL/PPFPMA fiber meshes were then used for functionalization with more complex molecules such as peptides and saccharides. Tritrpticin, an antibacterial peptide, was attached to the fibers in a methanol/water mixture. Although the conversion in a pre-test with aminoethanol, a model substance, suggested slower conversion kinetics in water/methanol, XPS clearly indicated a successful functionalization with tritrpticin via an observed decrease in fluorine and increase in nitrogen content.

In addition, aminofunctionalized D-Mannose or D-Galactose was reacted with the active pentafluorophenyl esters as followed by UV/Vis spectroscopy and XPS. The functionality was shown to be bioactive using macrophage cell culture. The meshes functionalized with D-Mannose specifically stimulated the cytokine production of macrophages when lipopolysaccharides were added. This was in contrast to D-Galactose- or aminoethanol-functionalized and unfunctionalized PCL/PPFPMA fiber mats.

In summary, this work provides simple and versatile routes to structure and functionalize meshes. Reactive fiber meshes were successfully functionalized with different biomolecules which make these meshes an attractive toolbox for diverse bioactive substances. RGD-functionalized fibers together with their hydrogel-like appearance upon wetting, might be useful for chondrocyte infiltration and other bioassays. In addition, fabricated mixed sized fibers and especially its calcium phosphate composite are attractive scaffolds, which are currently under investigation for extensive cell studies.

6 Appendix

6.1 Experimental part section

6.1.1 Methods

6.1.1.1 Materials characterization

NMR measurements were carried out at room temperature using a Bruker DPX-400 spectrometer operating at 400 MHz (^{1}H-NMR) or 100 MHz (^{13}C-NMR). As solvent, $CDCl_3$ (Deutero GmbH, Kastellaun, Germany), DMF d7 or DMSO d6 (Carl Roth, Karlsruhe, Germany) were used. Calibration was carried out using signals corresponding to deuterated solvents ($CDCl_3$: 7.26 ppm; DMSO d6: 2.50 ppm; DMF d7: 8.02 ppm).

FTIR spectroscopy was conducted on a BioRad 6000 spectrometer using single reflection diamond ATR. Samples were measured as dried powders.

Mass spectrometry was performed on a high performance liquid chromatograph electro spray ionization mass spectrometer (**LC-ESI-MS**) (Shimadzu, qp8000α, Duisburg, Germany) without chromatographic separation.

Matrix-assisted laser desorption ionization time of flight mass spectrometry (**MALDI-TOF-MS**) was performed on a Voyager-DE STR BioSpectrometry workstation with matrix-assisted laser desorption/ionization and time of flight detector (Perseptive Biosystems, Inc., Framingham, MA, USA). Measurements were performed in linear mode at an acceleration voltage of 20 kV using a metal acetylacetonate matrix and standard sample preparation protocols.

GPC measurements with simultaneous UV and RI detection was performed in (*i*) THF at 25 ^oC, flow rate: 1 mL/min, column settings: two MZ-SD*plus* columns, 300×8 mm (dimensions), 5 µm (particle size), 10^3 and 10^5 Å (porosity), (*ii*) NMP + 5 g/L LiBr at 70 °C, flow rate: 0.8 mL/min, column settings: two PSS-GRAM columns, 300×8 mm, 7 µm, 10^2 and 10^3 Å or (*iii*) DMSO + 5 g/L LiBr at 70 °C, flow rate: 1 mL/min, column settings: one PSS-GRAL column, 10 µm, linear. Solutions containing ~ 0.15 wt% polymer were stirred overnight and filtered through 0.45 µm filters; injected volume was 100 μL. Calibration was done with PS, PLA or PMMA standards (PSS, Mainz, Germany).

Differential scanning calorimetry measurements were performed on a NETZSCH **DSC** 204 (NETZSCH Gerätebau GmbH, Selb, Germany) under N_2 at a rate of 10°C/min and the glas/melting temperature values were determined from the 2nd heating curve (inflection/peak). To determine the decomposition temperature, thermogravimetric analysis (**TGA**) was carried out on a NETZSCH TG 209 F1 at 20 K min^{-1} in a nitrogen atmosphere.

6.1.1.2 Characterization of solutions

Polymer solutions were prepared by dissolving the polymer overnight by stirring, shaking (shaker, ~ 200 /min) or mixing with a rock and roll shaker. Polymer/polymer-blends were mixed by shaking 5 min in advance before spinning. The different polymer solutions were characterized with CDM83 **Conductivity Meter** (Radiometer, Copenhagen, Denmark) using a 0.05% NaCl/water (50 mg/100 mL) solution for calibration.

Viscosity measurements of different polymer solutions were conducted at 25°C on an automated microviscometer AMVn (Anton Paar, Graz, Austria), using glass capillary systems for different viscosity ranges (4 (3) mm diameter capillary/steel ball with 3 (2.5) mm in diameter). Viscosity (n) were determined by the falling time (t_l) of the steel ball according to the following equation:

$$n = K_l*(d_K-d_P)*t_l$$

K_l= calibration constant, d_K= density of steel ball, and d_P=density of polymer solution.

The **pH** measurements were conducted on a computer controlled measurement system (Metrohm, Filderstadt, Germany) using the software tiamo 1.1. The pH-electrode (Nr. 6.0256.100) used was calibrated with 3 buffer solutions provided by Metrohm at pH = 4, pH = 7.0 and pH = 9.

Peptide-polymer conjugate solutions in chloroform and chloroform/methanol (3:1/v:v) were investigated by dynamic light scattering (**DLS**) using ALV-7004 Multiple tau digital correlator equipped with CGS-3 Compact Goniometer system, 22 mW He-Ne laser (wavelength λ = 632.8 nm) and a pair of avalanche photodiodes operated in a pseudo-cross-correlation mode (ALV-GmbH, Langen/Hessen, Germany). To remove dust, samples were filtrated. Measurements were performed at room temperature at a fixed scattering angle of 90°.

6.1.1.3 Electrospinning

The **electrospinning** setup was composed of a high voltage power supply (DC, HCP-serie 14-20000, FuG Electronik GmbH, Rosenheim, Germany) and a syringe pump (KD Scientific Inc., Holliston, MA, USA) (see Figure A1). Plastic 1 mL syringes with disposable blunted tips (Howard electronics, JG20-2, nominal inner diameter: 0.584 mm, El Dorado, KS, USA) were charged positively and an aluminum foil or a grounded water bath was used as a collector in a vertical setup. The water ground was used for the samples in epithelial cell studies and porosimetry. The whole setup was protected by an custom-made PMMA box. The humidity and temperature were measured with a sensor (Thermohygrometer P330, Carl Roth, Karlsruhe, Germany) and humidity control was possible by purging the chamber with dry or humid air. While the humidity changed from 13 to 70% the temperature stayed around 21 °C. The polymer solution was fed at a rate between 0.2-1 mL/h by the syringe pump to the blunted needle tip, where a voltage of 4-15kV was applied. The spinning distance between tip and ground collector was 7-10 cm.

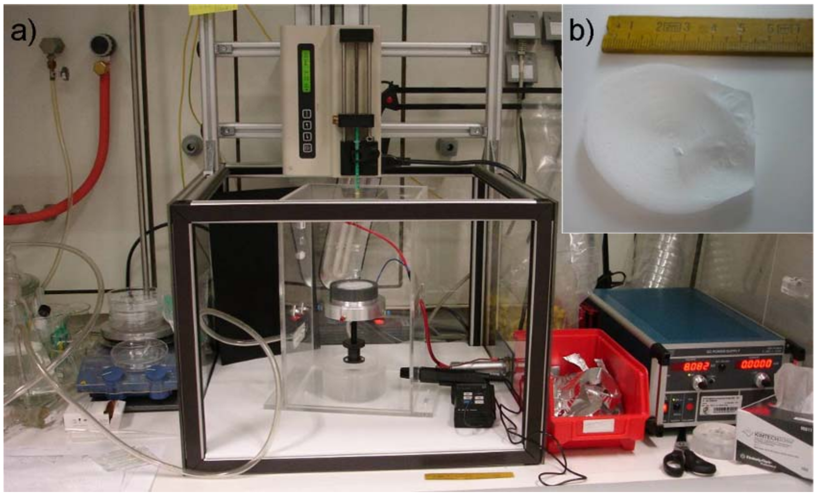

Figure A1. The vertical electrospinning setup with the humidity chamber (a) and an electrospun PCL mesh (b).

To investigate the formation of the bimodality the electrospinning process was illuminated with diffused xenon light (100 W) and observed with a **CMOS high speed** camera from PCO 1200 hs s/w (PCO AG, Kelheim, Germany) using 1995 fps and an exposure time of 50 µs.

6.1.1.4 Mesh and fiber characterizations

The resulting fiber meshes were dried, cut into 0.5×0.5 cm^2 pieces and sputtered with Pd/Au for **SEM** measurements (LEO 1550-GEMINI, Zeiss, Oberkochen, Germany) or further used for cell studies. To evaluate the fiber diameter the software ImageJ (1.38x, Wayne Rasband, National Institutes of Health, Bethesda, MD, USA) was used.

For evaluating the **pore characteristics** mercury intrusion measurements were carried out on a Pascal 440 apparatus by Thermo Finnigan (Rodano, Italy) using roughly 50 mg of untreated PCL meshes which were cut into stripes. A contact angle of 141.3° for Hg was used. The cumulative pore volume at a given pressure represents the total volume of mercury taken up by the sample at that pressure (range of pressure used was between 0.01 to 400 MPa). The mean pore diameter was calculated by applying the Washburn equation and a cylindrical pore model.

Wide angle X-Ray scattering (**WAXS**) of the PCL and PCL/composites were conducted on a PDS 120 diffractometer (Nonius GmbH, Solingen, Germany) with Cu Kα-radiation.

Tensile tests (MPI-KG, Dr. M. Eder, Dr. habil. I. Burgert) were performed on four ~ 2.5 mm wide and several centimeter long strips, cut out of an electrospun fiber mat. The strips were attached to a microtensile testing device by clamping and strained with a test speed of 20 µm/s until the end of the measurement range which was limited by both the traverse part of the motor and the optical strain measurement system. The strain was measured by videoextensometry within an area of uniform sample thickness, labeled by black markers which were attached to the sample surface by gluing. Stress calulations were based on the cross-sectional areas of the samples.

The **force measurements** (University of Bayreuth D. Kluge, Prof. A. Fery) were performed on a Nanowizard I **AFM** with the CellHesion Stage (JPK Instruments, Berlin, Germany). A tipless cantilever (NSC12/tipless/AlBS, Mikromasch, Tallinn, Estonia) that was modified with a colloidal glass bead (diameter ~ 35 µm) was used. Before modification, the spring constant of the cantilever was calibrated using the thermal noise method and obtained a value of 8.93 N/m. For the force-deformation measurements, the setpoint for the maximum applied load was set to 1 µN with a movement speed of 5 µm/s. For every type of network, at least two arbitrarily chosen positions were investigated. On each position, a force map with the size of 50x50 µm that consisted of 10x10 pixels (which corresponded to 100 measurements with a spacing of 5 µm) was made.

For the **XPS** measurements (Fh-IAP, F. Pippig, Dr. A. Holländer), an Axis 165 instrument (Kratos Analytical, Manchester, UK) with monochromatic Al K_a radiation in hybrid mode, i.e., with electrostatic and with magnetic lenses, was used. Thermal electrons from a filament were used to compensate for the charging of the sample. The filament was set to a potential that ensured a complete compensation for the charge and usually resulted in an overcompensation. The Kratos vision 2 software was used for the data processing. A linear background correction was applied and the high resolution spectra were fitted with Gaussian functions. Constraints were set to related components. Typically, different points within one sample and different samples were measured. The corresponding values were then averaged. In order to delete background (e.g. aluminium foil, glass, silicon wafer) and known impurities signal (silicon sealing grease, DMF), a correction according its chemical surface chemical composition was performed.

The colloidal **probing of electrostatic interactions** (MPI-KG, Dr. S. Schmidt) was performed on a Nanowizard I AFM (JPK Instruments AG, Berlin, Germany) in a closed liquid cell (Small Cell, JPK Instruments AG, Berlin, Germany) filled with 10^{-4} M hydrochloric acid. The AFM head was mounted on an optical microscope (IX51, Olympus, Japan). Using brightfield optics (objective 63×/1.25 Oil Ph3, Antiflex EC Plan-Neofluar, Carl Zeiss AG, Jena, Germany) single fibers could be resolved. The microscope stage allowed for µm-accurate positioning of the cantilever in order to map the fibers via so-called force mapping (also known as force-volume mode).

The adhesion data was collected by conducting the force mapping at the apex of the fibers in a 100x100 nm sized grid. To aim for the apex the topography of the fiber was imaged by force mapping over its whole width in the first step. Then the colloidal probe was positioned using the AFM software, which can be done with nanoscopic precision. As force colloidal probe, silica particles (Microparticles GmbH, Berlin, Germany) were used with a diameter of 10 µm glued to the apex of the AFM cantilevers (with a nominal spring constant of 0.2 N/m; NSC 12 tipples, Mikromasch, Tallin, Estonia). Prior to the measurements, the cantilevers and colloidal probes were rinsed with analytical grade isopropanol and water followed by treatment in air plasma at a pressure of 1 mbar for 2 min while applying an intensity of 18 W (PDC-32G Plasma Cleaner, Harrick Plasma, Ithaca, NY, USA).

UV-visible spectroscopy was done by a PerkinElmer Lambda 2 UV/Vis spectral photometer (PerkinElmer, Waltham, MA, USA) at 60 nm min-1 in 1 nm intervals. For the pentafluorophenol release studies PFP/MeOH solutions or PFP/(MeOH/H_2O) with known concentrations were measured with UV-Vis spectroscopy. Plotting the absorption intensity at 267 nm for MeOH (266 nm MeOH/H_2O) against concentration calibration was conducted using linear regression. For MeOH the resulting equation was $y = 3.7225\ x$ and for MeOH/H_2O $y = 7.886\ x$ with correlation coefficients (least square method) $R^2 = 0.99796$ and $R^2 = 0.99989$, respectively.

6.1.1.5 Cell studies:

Epithelial cells (Fh-IBMT, Dr. A. Lankenau) type **CHO-K1** (DSMZ, Braunschweig, Germany) were plated in monolayer in 25 cm^2 tissue culture flasks and cultured to near-confluence in Dulbecco’s modified Eagle's medium (DMEM) medium containing 10% fetal bovine serum (FBS) and 1% penicillin/streptomycin (Invitrogen, Darmstadt, Germany). The medium was replaced every 3 days and cultures were maintained in a tissue culture incubator at 37 °C with 5% CO_2.

Cells were seeded on fiber meshes at a density of 1750 cells/cm^2 and grown for 8 days. Cell-containing fiber meshwes were fixed in 4% paraformaldehyde for 20 min rinsed with PBS, washed twice with ultrapure water and refixed in 2% glutaraldehyde in PBS for 10 min. Afterwards samples sequentially dehydrated in 10%, 30%, 40%, 50%, 60%, 70%, 80%, 90% ethanol for 10 min. each and subsequently in 99.8% and 100% ethanol for 15 min. twice for each respective ethanol change. After a short incubation in tetramethylsilane the samples were vacuum dried and used for SEM analysis.

To compare cellular infiltration into different substrates, CHO-K1 cells were seeded on ca. 8×8 mm^2 large samples at 1750 cells/cm^2, allowed to grow for 8 days and finally washed twice in PBS and stained with 0.1% crystal violet in 50% methanol for 1 min. After washing with Millipore water, meshes were air-dried and embedded into cryo-matrix (Jung Tissue Freezing Medium) at -20 °C using the Leica Precision Cryoembedding System for small samples. Sections of 10 µm thickness using a CM1900 cryotome with Leica 819 disposable blades (all by Leica, Nussloch, Germany) were transferred onto plain glass slides (Carl Roth, Karlsruhe, Germany) without any fixation and examined/photographed within 2 min. The obtained microscopy images were rotated, cropped and modified using a homemade Mathematica script (Wolfram Research, Oxfordshire, UK) which removed all grey pixels as those were assigned to the non-stained fibers. The remaining purple structures were considered to be derived from the crystal-violet stained cells. From each processed image, three representative subsections were profiled for cell density dependent to the penetration depth using ImageJ. The resulting data was a table with an averaged color value for each segment of depth.

L929 mouse fibroblasts (No.: ACC 2, DSMZ, Braunschweig, Germany) were cultivated in DMEM/HEPES without pyruvate (Sigma Aldrich, Steinheim, Germany), with 10% FCS, 1% Penicillin-Streptomycin solution and 2 mM L-glutamine (all from Biochrom AG, Berlin, Germany) at 37 °C and 5% CO_2.

The 90% confluent cell layer was passaged every 3 days using trypsin/EDTA (0.25%/0.05% w/v). 1×10^5 of dissociated cells were resuspended in cell medium and seeded onto the fiber-coated glass substrates (RGD specifity) or tissue culture plate (toxicity) inside a 3.5 cm Petri dish and allowed to adhere. Proper cell spreading on the surface was assumed by microscopic control (DMIL, Leica, Nussloch, Germany). Phase contrast images were taken every 1 h (RGD specifity) or 1 d (toxicity) using a Nikon Digital Sight DS-L1 (Nikon, Düsseldorf, Germany).

Human osteosarcoma **U-2-OS** expressing Tag-FP635-Actin (Marinpharm GmbH, Luckenwalde, Germany) were cultured using DMEM, 10% fetal calf serum, 2 mM L-alanyl-glutamine and 1% non-essential amino acids at 37 °C and 5% CO_2. $1\text{-}2\times10^5$ cells were grown on 25 cm² or 5×10^5 cells 75cm², respectively for 3-4 days (80 - 90% confluence) and passaged using 0,25% Trypsin/ 0.1% EDTA (5-8 min at 37°C). 1×10^6 /ml of dissociated cells were resuspended in cell medium and seeded onto the fiber meshes.

NIH 3T3 fibroblast (MPI-MF, Dr. J. Polleux) were cultivated in using DMEM, 10% FBS (both from Gibco, Invitrogen, Darmstadt, Germany), 1% penicillin / streptomycin (PAA, Cölbe, Germany) in a tissue culture incubator at 37 °C with 5% CO_2. After reaching 80% confluence, cells were first rinsed with sterile PBS and than released with a 1% trypsin-EDTA solution (Gibco, Invitrogen, Darmstadt, Germany) for about 3-5 minutes. Trypsinization was stopped by adding 10% FBS containing DMEM to the released cells and centrifugation at 1000 rpm for 3 min. The resulting cell pellet was resuspended in pre-warmed growth medium and the cells were replated in cell culture dishes containing growth medium. After trypsination, approximately 1.2×10^5 cells in DMEM containing 0.2% FBS were seeded on these dishes. Cell spreading assays were conducted on the fibers during 24 h. Images were recorded with a Zeiss Axiovert 40 CFL microscope (Carl Zeiss, Jena, Germany).

Adult bovine middle/deep zone **chondrocytes (P2)** (QUT, Prof. D.W. Hutmacher) were cultured in expansion media (LG-DMEM, 10% FBS) or chondrogenic media (HG-DMEM, 1.25 mg/mL BSA, 100nM DEX, 1mM ITS+1, 10ng/mL TGF-b1). The PCL meshes were cut into 6mm diameter discs and seeded with 2×10^5 cells/disc.

Human primary **osteoblast** were cultured and seeded according to a previous protocol.[209]

The mouse **macrophage** cell line **RAW 264.7** (MPI-KG, Dr. B. Lepenies, Prof. P. Seeberger) was cultivated in medium consisting of 50% RPMI 1640 and 50% DMEM (GIBCO Invitrogen, Karlsruhe, Germany) at 37 °C and 5% CO_2. Cell culture medium was supplemented with 10% FBS, L-glutamine (2 mM), sodium pyruvate (1 mM), and 1% penicillin/streptomycin. All medium additives were obtained from PAN Biotech (Aidenbach, Germany).

Fibers functionalized with D-Mannose, D-Galactose, aminoethanol or unfunctionalized fibers were placed in the wells of a 96-well plate. Subsequently, 1 x 105 RAW macrophages were seeded in each well and were allowed to adhere to the fiber meshes for at least 3 h. Cells were then stimulated by adding the Toll-like receptor-4 (TLR-4) agonist lipopolysaccharide (LPS, Sigma-Aldrich, Munich, Germany) at a final concentration of 1 ng/mL. Cells were cultivated overnight, the culture supernatant was removed from the cells and cytokine concentrations were analyzed by enzyme-linked immunosorbent assay (ELISA).

Indirect sandwich ELISAs were performed for quantification of IL-1, IL-6, IL-12, and TNF-α. Antibody (Ab) pairs and cytokine standards were purchased from PeproTech (Hamburg, Germany). ELISA was performed according to manufacturer’s instructions. After incubation with the detection antibody plates were washed three times and incubated with Avidin-HRP (PeproTech) for 30 minutes at RT. ELISA development was performed by using the ABTS substrate (Sigma-Aldrich, Steinheim, Germany). Absorbance was measured with an ELISA plate reader (TECAN Infinite® M200 NanoQuant, Crailsheim, Germany) at 405 nm (reference wavelength was 650 nm).

After removal of the supernatant, macrophages were dissolved from the mesh by incubation with PBS/EDTA (0.05%). Cells were then washed with FACS buffer (PBS, 0.5% BSA, 2 mM EDTA), and FC receptors were blocked with anti-mouse CD16/32 Ab (1:100, BD Biosciences, Heidelberg, Germany) for 15 min. Double stainings were performed for the macrophage marker CD11b and the co-stimulatory molecules CD80/DC86. For this purpose, cells were incubated with allophycocyanin (APC)-labeled anti-CD11b Ab and either FITC-labeled anti CD80 Ab or PE-labeled anti CD86 Ab (BD Biosciences, each antibody was diluted 1:200). Cells were incubated at 4 °C for 30 min and washed twice with 200 µl FACS buffer. Expression levels of CD80 and CD86 were measured by flow cytometry using a FACSCanto II flow cytometer (Becton Dickinson, Franklin Lakes, NJ, USA). Cells were gated on living CD11b+ cells and CD80/CD86 expression was measured as mean fluorescent intensity (MFI). All data were analyzed with the FlowJo software (Tree Star Inc., Ashland, OR, USA).

Statistical analyses were performed with unpaired Student's t-test. All statistical analyses were performed with the Prism software (Graph Pad Software, San Diego, CA, USA).

6.1.2 Materials

Part 3: Poly(ε-caprolactone) (PCL, GPC: $M_n = 113$ kDa, PDI = 1.65), polystyrene (PS) and poly(methyl methacrylate) (PMMA) were purchased from Sigma-Aldrich (Steinheim, Germany). Polylactic-co-glycolic acid (PL(L)GA, 85/15 mol/mol, PUROSORB PLG8531) was friendly provided by Purac (Gorinchem, Netherlands). The PCL granulate was dissolved in chloroform, reprecipitated in methanol and dried in a vacuum chamber overnight at room temperature. The molecular weight changed after the treatment ($M_n = 78$ kDa, PDI = 1.61). Chloroform, methanol, ($CHCl_3$, 99+%, Merck, Darmstadt, Germany), tetrahydrofurane (THF), and *N*,*N*-dimethylformamide (DMF, 99+%, Sigma-Aldrich, Steinheim, Germany), were used as received as well as PLGA, PMMA, and PS. For aqueous solutions, bidistilled water was used (0.055 μS/cm, 23.4° C). All salts used for crystallizations were bought from sigma-aldrich (high purity grade, Steinheim, Germany).

Part 4: L-lactide (98%) was recrystallized 3 times from ethyl acetate prior to use and toluene was distilled over Na/K (all obtained from Sigma-Aldrich, Steinheim, Germany). Maleic anhydride, ethanol amine, magnesium sulfate, stannous octoate, acetic anhydride (Ac_2O), fluorescein isothiocyanate (all obtained from Sigma-Aldrich), methanol (Biosolve), chloroform (Merck), ethanol (VWR), N,N-dimethylformamide (DMF, 99+%), triethylsilane (TES, 99%, both from Sigma-Aldrich), trifluoroacetic acid (TFA), N-methyl-2-pyrrolidone (NMP, 99.9%), N,N-diisopropylethylamine, and piperidine (all peptide grade, Acros) have been used as received. Dichloromethane (DCM; peptide grade, IRIS Biotech GmbH) was distilled from CaH_2 and N-methyl-2-pyrrolidone (NMP, 99.9% peptide synthesis grade) was purified over an Al_2O_3 column. Fmoc-amino acid derivatives (Fmoc-Arg(Pbf)-OH), Fmoc-Asp(tBu)-OH, Fmoc-Gly-OH, Fmoc-Ser(tBu)-OH, Fmoc-Cys(Trt)-OH and all others), 2-(1H-benzotriazole-1-yl)-1,1,3,3-tetramethyl-uronium hexafluoro phosphate (HBTU), N-hydroxybenzotriazole (HOBt), and polystyrene-(2-chloro-trityl chloride) resin (loading: 1.57 mmol/g) were used as received from IRIS Biotech.

TentaGel SRAM resin (loading: 0.24 mmol/g) was ordered from Rapp Polymere (Tübingen, Germany).

Aminoethanol, ethylene diamine and isopropyl amine were bought from Sigma-Aldrich and were distilled prior to use.

6.1.3 Experimental procedures

6.1.3.1 Calcium Carbonate crystallizations

The conditions of the performed crystallizations with nano and mixed sized PCL fiber mesh are summarized in the table below:

Nr	crystallization details	time	fct	volume	characteristics morphology
1	GD 10 mM CC	3 d	P/ WT	~10 mL	C, A, V, ACC on mesh, partially penetrated
	GD 10 mM, turning	2/5 d	P		C, V, no improvement
	GD 10 mM, pertubation	2/5 d			smaller crystals, increasingly defected with time, mainly C
	GD 10 mM, pertubation	7 d		~10 mL	ACC like glueing of pores
2	DD, 10 mM CC/ NC	2 d		~20-50 mL	incorporated in mesh, mostly still at surface
	DD, 10 mM	6.5 d	WT		not much CaC, lack of infiltration
	DD, 2.3 mM (falcon)	2 w	P	2x ~15 mL	penetrated, defected, more crystals than 1.25 mM
	DD, 1.25 mM (eppendorf)	3 w (2 w)		2x ~2.3 mL	some defected C (not even penetrated, rotated -)
	DD, 1.25 mM (falcon)	3 w (2 w)		2x ~15 mL	rotated: some defected C (not penetrated), worse than ep
	saturated solution (closed)	1.5 d		~5-10 mL	coating on mesh surface
	different seeds DD 1.25 (2 w)/2.3 mL				
	saturated solution (open)	1.5 d			coating on mesh surface
	different seeds DD 1.25 (2 w)/2.3 mL , Ref				
	DD, 0.02 M CC/NC, 4°C fridge	2 d		~20-50 mL	still most on surface, potential too fast mixing/precipitation
		8 d			
	DD, 0.02 M CC/NC, 4°C fridge, mix mesh	7 d		~20-50 mL	still rather at the surface
3	vac, 8 mM CC/ NC	1 min		~0.5 mL	large ACC zone, fibers encapsulted
	", time: 2, 3.5, 5, 20 min, no vacuum; volume: 1, 2, 5 mL; temperature: RT, cooled: fridge 30 min, freezer 5 min => no improvement				
	vac, 16 mM	1 min		~0.5 mL	small ACC/C spots
4	Cen, 0.1 M CC/PAA/NC, 10 min, 9000 RPM	20/60 min			coating on mesh surface
	Cen, 10/30 min, 9000 RPM	1.5 h			coating on mesh surface
5	vac 0.1 M CC/PAA/NC	5-10 min			few precipitation
	vac 0.1 M CC/PAA/NC	20 min			encapsulated films
	prec. 0.1 M CC/PAA/NC	1.5h			encapsulated thin films
	vac 0.1 M CC/PAA/NC, mixed mesh	5 min			few precipitation
		20 min			encapsulated films
		60 min			encapsulated films increased in size
6	Precipitation, pH shift: 3.6-7, mixed mesh	12 h		~10 mL	fiber encappsulated by ACC-like coating
7	GD, PAA 50 mM, 25 mM CC	1 d			some encapsultation, particle like coating
	GD, PAA 50 mM, 25 mM CC	4.5 d			good encapsulation, also after leaching self-sustainable
	GD, PAA 50 mM, 25 mM CC	1 w		10 mL	good coverage, nearly entire coated
8	GD, PAA7 50 mM, 25 mM CC, upscaling	12 d		50 mL	not completely coated
	GD, PAA9 50 mM, 25 mM CC	1 w		20 mL	"

GD = gas diffusion, DD = double diffusion, vac = vacuum assisted, cen = centrifuge assisted, CC = $CaCl_2$, NC = Na_2CO_3, PAA = poly(acrylic acid), 1) = 1min, 18 W PDC-32G plasma cleaner (Harrick Plasma, Ithaca, NY, USA), WT = without treatment, most crystallizations done with nanosized fiber meshes unless specifically noted that mixed sized fiber meshes were used.

6.1.3.2 Calcium phosphate crystallizations

Using 2×SBF mineralization method, Ca and P solutions were prepared separately and mixed in ratio 1:1 before an experiment. The amount of salts described below, were used to prepare 0.5 L of

Ca solution and 0.5 L of P solution, where the final pH was adjusted to 7.4. For the mesh mineralizaton 50 mL of each solution was added to a plastic beaker. The latter was shaken for 2 weeks, obtaining the PCL calcium phosphate composite.

Ca solution:	**amount**	**P solution:**	**amount**
NaCl:	15.99 g	$Na_2SO_4 \times 10H_2O$:	0.322 g
KCl:	0.44 g	$NaHCO_3$:	0.706 g
$MgCl_2 \times 6H2O$:	0.610 g	K_2HPO_4:	0.348 g
$CaCl_2 \times 2H_2O$:	0.735 g	Tris:	6.055 g
Tris:	6.055 g	HCl (2M):	21.85 mL
HCl (2M):	21.85 mL		

For the 10×SBF the following salts were dissolved in 1 or 0.97 L water in the indicated order:

order	**salts**	**amount [g]**
1	NaCl	58.43
2	KCl	0.37
3	$CaCl_2 \cdot 2H_2O$	3.68
4	$MgCl_2 \cdot 6H_2O$	1.02
5	Na_2HPO_4	1.42
6	$NaHCO_3$	0.84

The last component was added prior to mineralization while shaking the mineralization beaker. For the mineralization experiments, 100 mL or 50 mL mineralization solution in a plastic or 10 mL in glass beaker were used. The meshes were then added. The meshes were mostly treated with plasma (air, oxygen, 0.05-0.1 mbar) using 18 W PDC-32G plasma cleaner. The mineralization was started by the addition of the respective $NaHCO_3$ amount (84, 42 or 8.4 mg).

The conditions of the performed crystallizations are summarized in below:

Nr	SBF (c)	time	fct	fct time	crystallization	volume	mesh	characteristics morphology
1	*2*	*2 w*	*P Air*	*1 min*		*100 mL*	*mix*	*blocks/crystals/particles, inhomogeneous*
2	*10 (1)*	*2 h*		*2x1 min*		*50 mL*	*mix*	*inhomogeneous, partial coating, encapsulation*
3		*140 min*					*mix*	*uncoated, coated and fully encapsulated areas*
4a		*120 min*	*P Air*	*2x1 min*	*40 min soaked*	*50 mL*	*mix*	*thick coating, inhomogeneous*
		5.5 h						*films, particles*
		18 h						films, particles
		2 h	P O_2	2x1 min	40 min soaked	50 mL	mix	coated fibers, inhomogeneous
		5.5 h						particles
		18 h						more particles
		2 h	NaOH	6.5 h	40 min soaked	50 mL	mix	coated fibers, inhomogeneous
		5.5 h						more coated
		18 h						films, inhomogeneous
4b		130 min	WT			10 mL	mix	inhomo, uncoated, coated encapsulated
		135 min	P Air	10 min	~30 min soaked		micro	few coating between fibers
				15 min				more coating, fully encapsulated parts
				2x10 min				*nice coating, spots, inhomogeneous*
		2 h		2x10 min				CaP between fibers, some CaP on fiber
		2 h		2x10 min	16.5 h soaked			more crystals on fibers
		3 h	P O_2	7 min	11.5 h soaked		micro	more or less homogeneous
			P Air	11 min				inhomogeneous, uncoated, coated
				20 min			mix	noncoated, coated, fully encapsulated
				11+11 min				inhomogeneous, uncoated, coated
				2 min				inhomogeneous, uncoated, coated, particles
			P O_2	2 min			nano	uncoated, coated, fully encapsulated
5		*2 h*	*P Air*	*15+10 min*		*100 mL*	*micro*	*nice, fully encapsulated parts*
		135 min	*P Air*	*5 min*		*100 mL*	*mix*	*encapsulated, coated*
		2.5 h	*P* O_2	*5 min*		*50 mL*	*nano*	*coated, particles, mostly encapsulated*
6		*30 min*					*micro*	*little coating, particles; or no coating*
		90 min						*coating on small spots on the mesh*
		150 min						*larger spots with coatings, platelets*
		30 min	*P Air*	*5 min*		*50 mL*	*nano*	*inhomo, encapsulation, coating, uncoated*
		90 min						*", thicker coating*
		150 min						*films, encapsulations, all over, platelets*
7	10 (0.97)	1 h			dynamic conditions	100 mL	micro	few encapsulated, mostly uncoated, inhomo., particles
		2 h			50-150 mot (1/min)			coated, uncoated, particles
		4 h			solution change after 2 h			platelets, coated, uncapsulation
		1 h					nano	fibers glued together or encapsulation, inhomo.
		2 h						CaP between fibers, inhomo., films, particles, platelets
		4 h						CaP between fibers, a lot of platelets

The crystallizations marked in italics, SEM images are shown in the thesis, for the SBF 2x and 10x solutions (1 L and 0.97 L H_2O) were prepared, the crystallization time ranged from 30 min to 2 weeks, different functionalization (fct, P: plasma, NaOH: 0.025 M in MeOH, WT: without treatment)

6.1.3.3 Synthesis of PLLA-*b*-CGGRGDS

Synthesis of maleimide initiator (II)

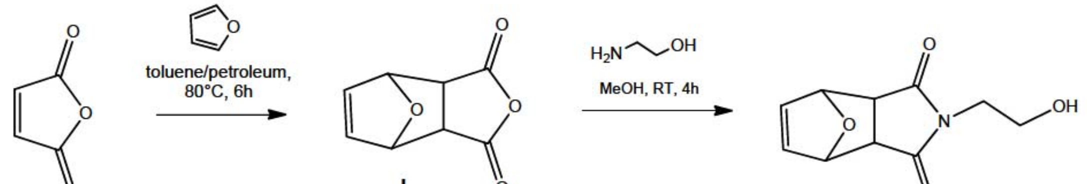

10.14 g (103 mmol) maleic anhydride was suspended in 50 mL toluene and heated up to 80°C. Then 10.76 g furan (159 mmol) in 20 mL petrol ether was added. The mixture was stirred for 6h. The solution was then allowed to cool down to room temperature. The obtained white crystals were filtrated, washed, and dried overnight to yield 12.90 g (75%) of product **I**.

^{1}H-NMR ($CDCl_3$), δ (ppm): 3.18 (m, 2H, C$\underline{H}$CO), 5.45 (m, 2H, C$\underline{H}$O), 6.57 (m, 2H, C$\underline{H}$ vinyl)
^{13}C-NMR ($CDCl_3$), δ (ppm): 48.9, 82.4, 137.1, 170.0

10 g (60 mmol) of **I** were suspended in 250 mL methanol and cooled to 0°C. 3.66 g ethanol amine dissolved in 100 mL methanol were added dropwise. After stirring the mixture for 5 minutes at 0°C, the temperature was raised to room temperature to give a clear solution and allowed to react for 4 h. The solvent was removed under vacuum and the crude product was purified in a silica column with ethyl acetate as eluent. The product was freeze-dried from benzene yielding 5.84 g (47%) of **II**.
^{1}H-NMR ($CDCl_3$). δ (ppm): 2.26 (s, 1H, OH), 2.89 (m, 2H, CH), 3.70 (m, 2H, NCH2), 3.76 (m, 2H, OCH_2), 5.28 (m, 2H, CHO), 6.52 (m, 2H, CH vinyl)
FTIR-ATR (υ in cm^{-1}): 3473 (m), 2895 (w), 1767 (m), 1686 (vs), 1435 (m), 1406 (s), 1334 (s), 1269 (m), 1169 (s), 1099 (m) 1053 (s), 1014 (vs), 918 (m), 876 (vs), 851 (s), 808 (s), 723 (s), 674 (vs)

Synthesis of maleimide functional poly(L- lactide acid) (PLLA, III)

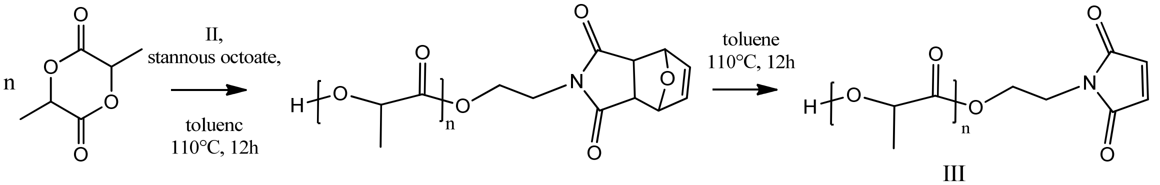

2.078 g (14.4 mmol) of freshly distilled L-lactide ((3S)-cis-3,6-dimethyl-1,4-dioxane-2,5-dione) and 300 mg (1.4 mmol) of **II** were dissolved in 6.5 mL dried toluene. Then 4.0 mg (0.010 mmol) of stannous octoate was added to the solution and the polymerization was conducted at 110°C stirring for 12 h under reflux. After precipitation in ethanol, 1.430 g of the polymer were yielded.
^{1}H-NMR ($CDCl_3$). δ (ppm): 1.58 (d, 108H, OCH-C$\underline{H}_3$), 2.88-2.94 (m, 1H, OH), 3.79 (m, 2.5H, O-CH_2-C$\underline{H}_2$-N), 4.27-4.34 (m, 3.5H, O-C$\underline{H}_2$-CH_2-N, HOC$\underline{H}$-CH_3), 5.17 (q, 30H, OC$\underline{H}$-CH_3), 6.51 (bs, 0.28H, CH vinyl protected), 6.72 (bs, 1.72H, CH vinyl deprotected)
GPC (NMP, PS standard): $M_{n,\,app}$ = 3000 g/mol, PDI = 1.5.

In order to fully deprotect the maleimide 1.15 g of the polymer were dissolved in toluene and stirred over night at 110°C stirring for 12 h under reflux. After precipitation in ethanol 1.07 g of **III** were yielded.

^{1}H-NMR (CDCl$_3$). δ (ppm): 1.47-1.59 (d, 109H, OCH-C$\underline{H}_3$), 3.79-3.80 (m, 2.7H, O-CH$_2$-C$\underline{H}_2$-N), 4.26-4.36 (m, 3.8H, O-C$\underline{H}_2$-CH$_2$-N, HOC$\underline{H}$-CH$_3$), 5.17 (q, 34H, OC$\underline{H}$-CH$_3$), 6.72 (m, 2H, CH vinyl)
$DP_{n,\ NMR}$ = 34, $M_{n,\ NMR}$ = 2600 g/mol
FTIR-ATR (υ in cm^{-1}): 2997 (w), 1757 (vs), 1456 (m), 1360 (m), 1182 (vs), 1132 (vs), 1088 (vs), 1043 (s), 872 (m), 756 (m), 696 (m)

Synthesis of the oligopeptide (H-Cys(Trt)-Gly-Gly-Arg(Pbf)-Gly-Asp(tBu)-Ser(tBu)-OH) (IV)

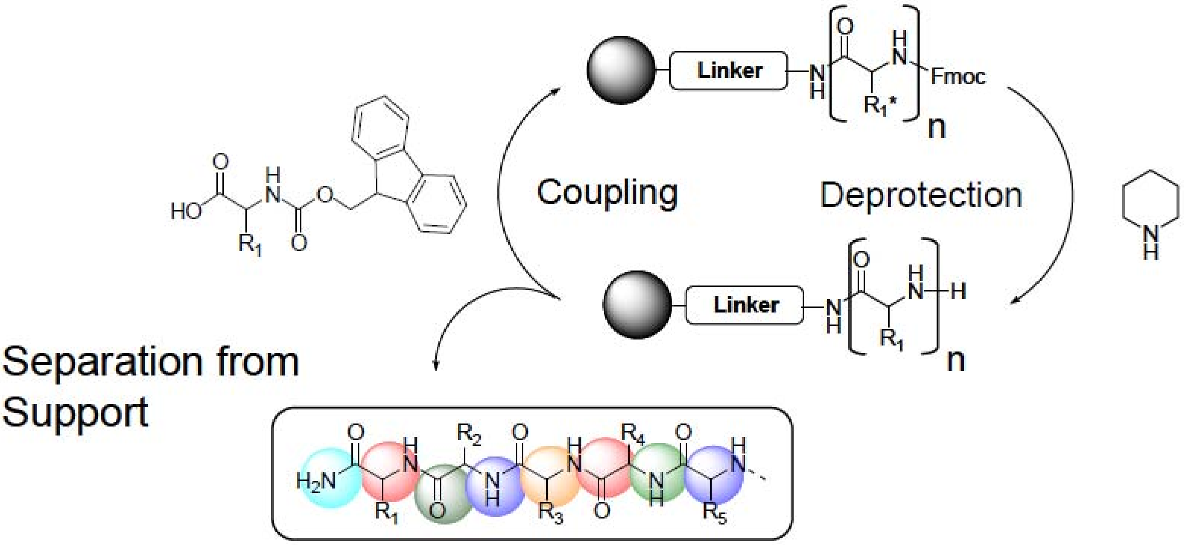

The peptide synthesis was performed on a fully automated ABI 433a peptide synthesizer (Applied Biosystems, Darmstadt, Germany). 2.7 g of polystyrene-(2-chlorotrityl chloride) resin were loaded with Fmoc-Ser(tBu)-OH. After a capping step with Ac$_2$O, the loading was determined to be 0.37 mmol/g by an analytical Fmoc test, using UV spectroscopy. The sequential assembly of the standard amino acids was carried out on the synthesizer, using NMP as the solvent by following standard ABI Fastmoc protocols (single coupling + capping with Ac$_2$O). Fmoc amino acid coupling was facilitated by HBTU/DIPEA in NMP. The cleavage from the resin and removal of the protecting groups was accomplished by 2 h treatment of the dried resin with a mixture of TFA/TES/ H$_2$O (94/1/5 v/v/v%). The peptide was isolated by precipitation in diethyl ether. The precipitate was then centrifuged and washed with diethyl ether, followed by lyophilization from acetonitrile/milliQ water.

ESI-MS (acetonitrile/H_2O), (m/z, Da): $[M+H]^+ = 651$ (100%, $M_{theo} = 651$)

H-NMR (DMF-d7). δ (ppm): 1.30 (s, 1H, SH), 1.60-1.88 (m, 4H, C<u>H</u>$_2$-C<u>H</u>$_2$-CH Arg), 2.80-3.25 (m, 6H, C<u>H</u>$_2$-SH, C<u>H</u>$_2$ Asp, C<u>H</u>$_2$-NH Arg), 3.50-4.43 (m, 7H, α-CH, C<u>H</u>$_2$-OH Ser), 4.80-4.82 (m, 2H, NH_2 Cys)

FTIR-ATR (υ in cm^{-1}): 3275 (m), 3059 (m), 2936 (m), 1645 (s), 1521 (s), 1409 (m), 1334 (m), 1182 (m), 1130 (m), 1022 (s), 837 (m), 800 (m)

Synthesis of the polymer-oligopeptide conjugate: PLLA-*b*-CGGRGDS (V)

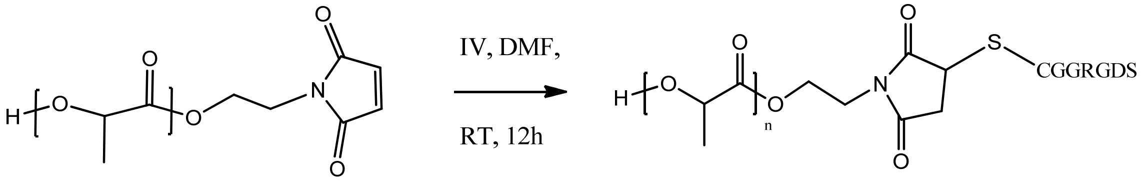

V

1 g (0.38 mmol, assuming M_n = 2600 g/mol) of **III** and 410 mg (0.63 mmol) of **IV** were dissolved separately in 20 mL DMF and flushed with argon gas. Then the two solutions were mixed, flushed again with argon and stirred overnight at room temperature. Then the solution was precipitated, centrifuged and the precipitate in ethanol was freeze-dried from acetonitrile/H_2O to yield 1.14 g (92%) product.

MALDI-TOF-MS ($CHCl_3$): $m/z_{\text{(max intensity)}} = 2521 = [M(PLLA_{23}\text{-}b\text{-}CGGRGDS) + H]^+ \pm 1$, mass distribution with peaks in interval of $\Delta M = 72$ Da ($M_{[L\text{-lactide}]} = 72$)

H-NMR (DMF-d7). δ (ppm): 1.37-1.57 (m, 98H, OCH-C<u>H</u>$_3$, C<u>H</u>$_2$-CH$_2$-CH Arg), 1.70-1.98 (2H, CH$_2$-C<u>H</u>$_2$-CH Arg), 3.95 (m, 4H, C<u>H</u>$_2$-OH Ser, O-C<u>H</u>$_2$-CH$_2$-N maleimide), 4.26-4.39 (m, 5H, α-CH), 5.27-5.29 (q, 29H, OC<u>H</u>-CH$_3$)

FTIR-ATR (υ in cm^{-1}): 3287 (w), 2999 (w), 2945 (w), 1757 (s), 1655 (m), 1456 (m), 1360 (m), 1184 (vs), 1130 (s), 1090 (vs), 1043 (s), 872 (m), 754 (m), 687 (m)

6.1.3.4 Functionalized Fluorescein isothiocyanate

A solution of 85.8 µL/ 30 mL (1.28mmol) ethylene diamine / methanol was added dropwise to 0.5 g (1.28 mmol) of fluorescein isothiocyanate (FITC) dissolved in 20 mL of methanol. In analogy, 76.9 µL (1.28 mmol) aminoethanol dissolved in 30 mL methanol was added dropwise to 0.1 g (0.257 mmol) FITC dissolved in 20 mL of methanol. Both solutions were stirred for 3 h at RT. The solvent was removed under vacuum, the product was freezed-dried from water to yield 0.56 g (97%) of amino-functionalized and 0.11 g (95%) hydroxyl-functionalized fluorescein, respectively.

Amino-FITC: H-NMR (MeOD). δ (ppm):3.27 (m, 4H, C<u>H</u>$_2$-C<u>H</u>$_2$), [6.75 (m, 3H), 6.87-6.90 (m, 6H), 7.26 (m, 1H), 7.86 (m, 1H), all aryl fluorescein]

Hydroxyl-FITC: H-NMR (MeOD). δ (ppm): 3.00 (m, 4H, C<u>H</u>$_2$-C<u>H</u>$_2$), [6.57-6.67 (m, 8H), 6.87 (m, 4H), 7.18 (m, 2H), 7.77 (m, 1H), all aryl fluorescein]

6.1.3.5 Tritrpticin

The Tritrpticin with the sequence KG-VRRFPWWWPFLRR-CONH$_2$ was synthesized on the fully automated ABI 433a peptide synthesizer (Applied Biosystems,Germany). 1.024 g of TentaGel SRAM resin with a 0.24 mmol/g loading was used and therefore the C-terminus was an amide. On the N-terminus a glycine and lysine were added to the native tritrpticin sequence. The sequential assembly of the standard amino acids was carried out on the synthesizer, using NMP as the solvent following this protocol: double coupling until first Tryptophan, then triple coupling and capping with Ac$_2$O. Fmoc amino acid coupling was facilitated by HBTU/DIPEA in NMP. The cleavage from the resin and removal of the protecting groups was accomplished by 2 h treatment of the dried resin with a cleavage mixture of TFA/TES/H$_2$O (94/1/5 vol.%). The peptide was isolated by precipitation in diethyl ether and the precipitate centrifuged and washed with diethyl ether, followed by lyophilization from acetonitrile/milliQ water.

H-NMR (DMSO-d6). δ (ppm): 0.83-0.84 (s, 12H, δ-Ile, γ-Val), 1.59 (m, 37H, β+γ-Arg, β+γ+δ-Lys, β+γ-Ile, β+γ-Pro), 2.69-3.05 (m, 22H, ε-Lys, δ-Arg, β-Trp), 3.5 (s, 4H, β-Phe), 3.88 (s, 3H, δ-Pro), 4.14-4.24 (s, 10H, α-CH), 4.55 (s, 6H, α-CH), 7.11-7.58 (m, 49H, aryl Trp and Phe)

ESI-MS (acetonitrile/H$_2$O), (m/z, Da):M_{theo} = 2085.18

$[M+Na]^{3+}$ + Na + K = 767 (21%), $[M+2Na]^{3+}$ + Na = 729 (72%), $[M+2H]^{3+}$ + H = 697 (45%), $[M+3H]^{4+}$ + H = 523 (100%)

6.2 Supporting experimental data

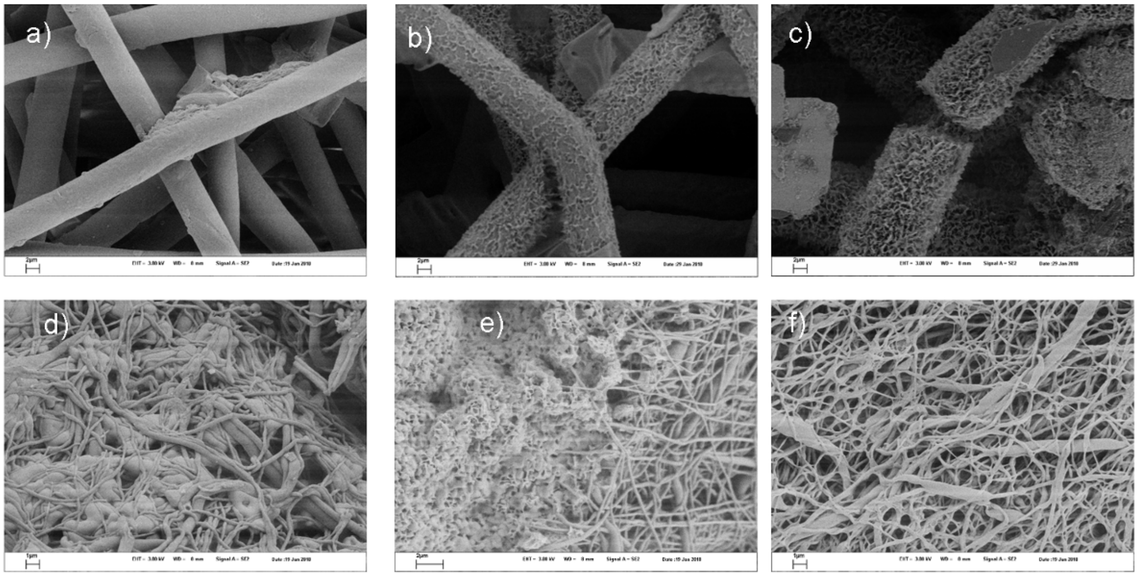

Figure S1. SEM images of crystallization performed under dynamic conditions using micron (a-c) and nanosized (d-f) fiber meshes (crystallization time: a/d) 1 h, b/e) 2 h, c/f) 4 h; after 2 h the reaction solution was renewed, plasma: 5 min, air, 18 W, scale bars: a-c/e) = 2 µm, d/f) = 1 µm).

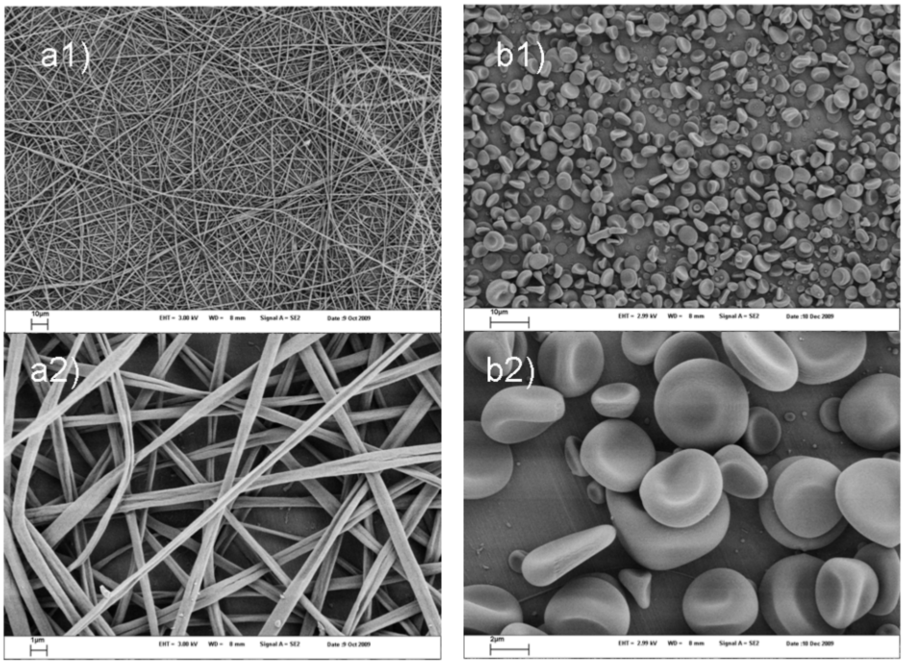

Figure S2. SEM images of meshes fabricated by electrospinning PLGA (a) and PLLA-CGGRDGS (b) from $CHCl_3$/MeOH (3:1) solutions (parameters: a) 5% w/v, 7 cm, 5.4 kV, 1.2 mL/h 50% humidity b) 10% w/v, 1 mL/h, 7-10 kV, 22-30% humidity, scale bars: a/b1) = 10 µm, a2 = 1 µm, b2 = 2 µm).

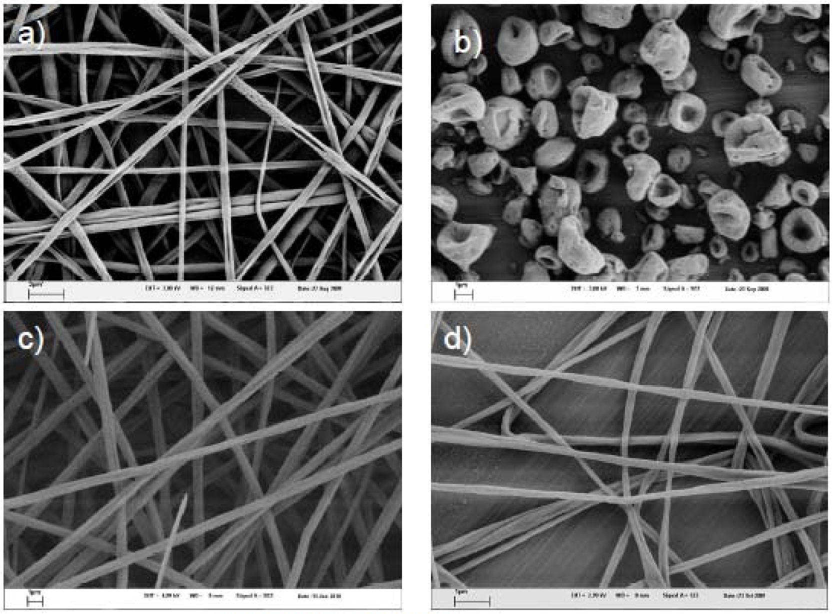

e)

PL(L)GA (84/16 mol/mol)

condition	Mw [kDa]	PDI	Mn exp	Mw exp	PDI exp
fresh (26.03.2008)	Mw~560	1,4-1,5	160,90	335,30	2,08
15.12.2009			127,25	284,90	2,23
28.9. - 15.12.2009 (sol.)			36,24	63,33	1,75

Figure S3. SEM images (a-d) of spun/sprayed PLGA from CHCl3/MeOH (3:1) solutions at various concentrations (% w/v) a/b) 8, c) 5 and d) 3. In b) the effect of the MeOH induced degradation (e) is obvious (parameters: a) 7 cm, 7.2kV, 0.8 mL/h, 75% humidity, b) 7cm, 7.1kV, 1mL/h, 63% humidity, c) 10 cm, 8.3 kV, 1 mL/h, 29%, d) 7 cm, 6.1kV, 1 mL/h, 49%, scale bars: a) = 2 µm, b-d) = 1 µm, e) M_n/M_w = [kg/mol]).

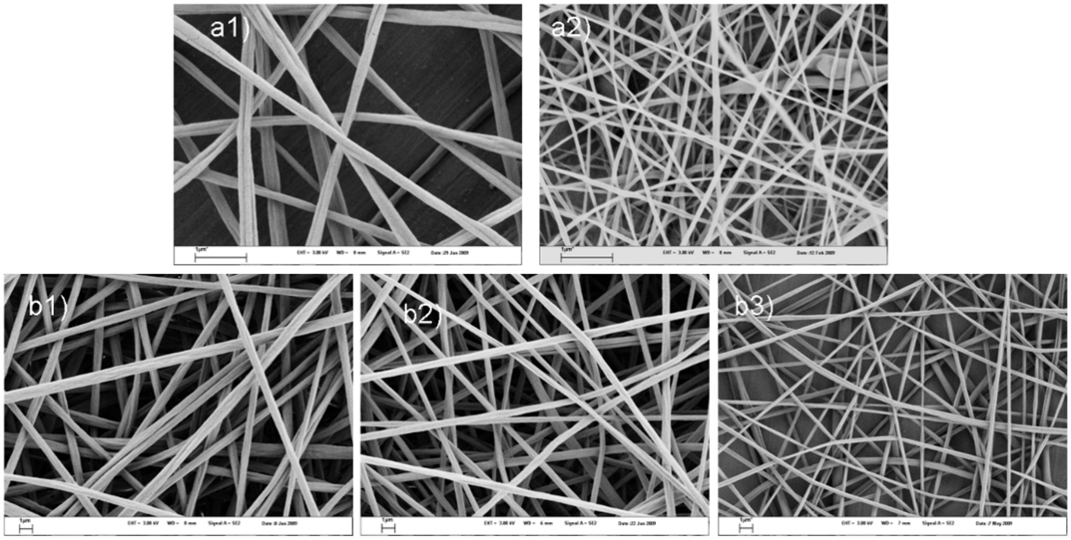

Figure S4. SEM images revealing the degradation behavior by a decrease in fiber diameter of electrospun fibers from 2 peptide/polymer solutions (a1-2: 3% w/v, 2 wt% peptide; b1-3: 5% w/v, 9.1 wt% peptide). However electrospraying was not observed (parameters: 7-10 kV/ 10 cm, 0.7-1 mL/h, 24-40% humidity; a1) reference, a2) after ~ 2 weeks; b1) reference, b2) after 1 month, b3) after ~ 5 months, scale bars: 1 µm)

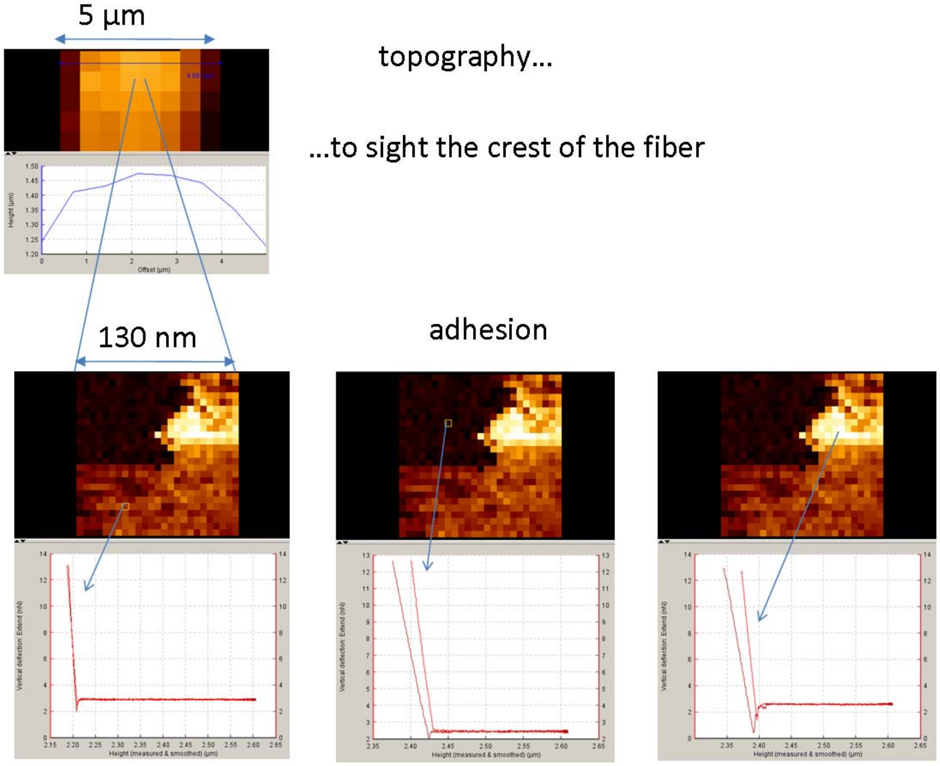

Figure S5. AFM interaction images together with the force displacement curves demonstrated the adhesion distribution over a selected 130×130 nm^2 area (see top), shows the variation in adhesion forces over the fiber surface (18 wt% peptide solid content).

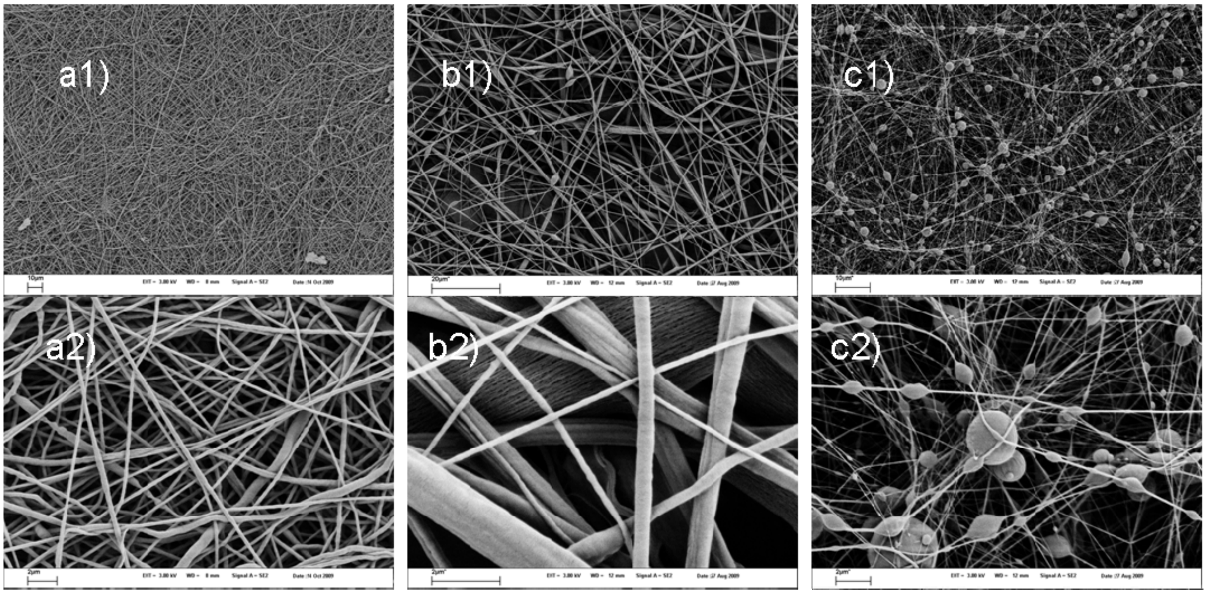

Figure S6. SEM images of PCL fibers (a) and PCL/PPFPMA blend (b-c) fibers revealing the similarity in the fiber structure (a/b) and the effect of humidity (c). (parameter: 1 mL/h, 5.5- 9.2 kV, 7-8 cm, a) 12.5% w/v, 42% humidity, b) 12.4% w/v, 56%, c) 12.4% w/v, 15.4%, scale bars: a/c1) = 10 µm, b1 = 20 µm, a-c2) = 2 µm)

Table S1. The viscosity values for PLGA and PLGA/polymer-peptide conjugate solutions composed of chloroform and chloroform methanol mixtures.

	c [%]	den. [g/cm3]	dyn n [mPa.s]	fall time [s]	system
$CHCl_3$					
PLGA	5	1.452	**307.3244**	34.49	3/4, 70°
PLGA	6	1,4569	376.2658	42,26	3/4, 70°
PLGA/RGD	5/9,1	1,459	**344.6319**	38.72	3/4, 70°
$CHCl_3$/MeOH (3:1)					
PLGA	5	1,294	**46.8596**	5.13	3/4, 70°
PLGA/RGD	5/9,1	1,299	**268.8004**	29.45	3/4, 70°
PLGA fresh	3	1,2850	**35.8555**	32.01	2.5/3, 30°
2 weeks later		1,283424	10.03	13.34	2.5/3, 20°
1 month later		1,300	4.2384	5.65	2.5/3, 20°
	3/4,8	1,2830	**37.5986**	33.56	2.5/3, 30°
2 weeks later		1,280686	34.33	45.64	2.5/3, 20°
	3/9,1	1,2817	**38.0374**	33.94	2.5/3, 30°
2 weeks later		1,280070	**33.5**	44.53	2.5/3, 20°
	3/18	1,2987	**48.1075**	43.04	2.5/3, 30°
2 weeks later		1,2987	**39.58**	52.75	2.5/3, 20°

c: concentration PLGA/solvent (% w/v) and peptide (wt% solid composition)

Table S2. Conductivity of PLGA and PLGA/peptide-conjugate solutions composed of chloroform and chloroform methanol mixtures.

$CHCl_3$				$CHCl_3$/MeOH (3/1)			
solutions	**c [%]**	**σ [µS/cm]**	**T [°C]**	**solutions**	**c [%]**	**σ [µS/cm]**	**T [°C]**
pure $CHCl_3$		0,007	20,8	pure MeOH		3,9	20,9
PLGA	5	0.007	22.7	PLGA	5	0.45	21.2
PLGA/RGD	5/9,1	0.02	21.4	PLGA/RGD	5/9,1	1.76	22.0
				PLGA fresh	3	0.42	21.8
				2 weeks	3	1.33	22.4
				PLGA/RGD fresh	3/2	0.92	22.3
					3/4,8	1.22	21.2
				2 weeks		2.55	22.4
	3/9,1	0.01	20.9		3/9,1	1.59	21.6
				2 weeks		3.04	21.2
	3/18	0.01	20.4		3/18	2.54	21.7
				2 weeks		1.83	21.4

c: concentration PLGA/solvent (% w/v) and peptide (wt% solid composition)

Table S3. Raw data of the nitrogen composition of different PLGA/PLA-CGGRGDS blend fibers derived from XPS.

samples	conj. c [wt%]	sol. c [% w/v]	form	N [at%]	±	N_{corr} [at%]	±	N_{theo} [at%]
PLA-CGGRGDS	100	10	particles	5.0				4.9
PLA-CGGRGDS/ PLGA blends	9.1	5	film (SC 3000)	4.7		4.9		0.4
	9.1		film (SC 1000)	4.3	0.4	4.6	0.4	
	9.1		fibers	4.3	0.7	4.5	0.5	
	6.4	5	film (SC 1000)	4.6	0.1	4.7	0.1	0.3
	6.4		fibers	1.9	0.7	2.0	0.7	
	4.8	5	film (SC 1000)	2.8	0.2	2.8	0.1	0.2
	4.8		fibers	0.6	0.1	0.6	0.1	
	2	5	film (SC 1000)	0.9	0.3	0.9	0.3	0.1
	2		fibers	0.6	0.2	0.6	0.2	
PLGA	0	5	fibers	0.0				0.0
PLA-CGGRGDS/ PLGA blends	18	3	fibers	2.8	0.2	2.9	0.4	0.9
	9.1	3	fibers	2.3		2.3		0.4
	4.8	3	fibers	2.3				0.2
	2	3	fibers	0.4	0.2			0.1

SC: spin-coating at 1000 RPM, sol. c: solution concentration related to PLGA mass, peptide c: peptide concentration related to total solid content

Table S4. Yields (y) of the reaction of PPFPMA/PCL fibers with isopropyl amine (IPA) derived from UV-Vis spectroscopy

time	sample	IPA [µL]	m [mg]	eq. IPA	c [wt]	y [%]
4h	PCL10	49.5	3.5	86.5	48.1	2
8d		49.5	3.5	86.5	48.1	8.3
15d		49.5	3.5	86.5	48.1	14.9
26d		49.5	3.5	86.5	48.1	25.2
32d		49.5	3.5	86.5	48.1	28.8
10d	PCL20	49.5	4.2	67.9	51.0	11.7
16d		49.5	4.2	67.9	51.0	14.1

Two samples were used (PCL10/20). The amount of IPA indicated was present in 5 mL IPA/MeOH solutios. (Equivalence (eq.) IPA as compared to PPFPMA repeting unit, concentration (c) refers to PPFPMA in the blend)

Table S5. Yields (y) of the reaction of AE with PCL/PPFPMA fibers in water/methanol (1:1, v:v)

time	sample	AE [µL]	m [mg]	eq.	c [wt]	y [%]
11h	PCL10	145.6	3.9	324.8	48.1	1
11d		145.6	3.9	324.8	48.1	5.5
17d		145.6	3.9	324.8	48.1	7.4
32h	PCL21	1.0	8.6	1.0	51.0	0.98
4d		1.0	8.6	1.0	51.0	0.99
7d		1.0	8.6	1.0	51.0	1.1
8d		1.0	8.6	1.0	51.0	1.2
32h	PCL21, 40 °C	1.0	8.1	1.0	51.0	1.1
4d		1.0	8.1	1.0	51.0	1.5
8d		1.0	8.1	1.0	51.0	1.8
8d, ref	PCL10		2.7		48.1	0.24
32h, ref	PCL21, 40°C		8.5		51.0	0.74
4d			8.5		51.0	0.77
8d			8.5		51.0	0.93

Two samples were used (PCL10/20). The amount of AE indicated was present in 5 mL AE/MeOH/H_2O solutios. (Equivalence (eq.) AE as compared to PPFPMA repeating unit, concentration (c) refers to PPFPMA in the blend)

Table S6. Raw data of the surface compositions derived from XPS of PCL/PPFPMA fiber functionalized with Tritrpticin, mannose, and galactose

sample	C [at%]	O [at%]	N [at%]	F [at%]	Si [at%]
PCL/PPFPMA27	67.8	26.0	0.0	5.3	0.9
Tritrpticin, 27	60.7	27.3	4.8	2.1	4.5
PCL/PPFPMA29	54.3	36.6	1.4	3.0	4.6
PCL/PPFPMA21	62.1	14.8		23.1	
PCL/PPFPMA34	23.7	55.3	1.1	2.6	17.3
Mannose 21	65.0	23.1		12.0	
Mannose 34	32.1	50.7		2.9	14.3
Galactose 21	50.5	33.0	1.4	12.5	2.5
Galactose 29	63.5	30.6		2.7	3.2

6.3 Abbreviation

6.3.1 methods

SEM	scanning electron microscopy
AFM	atomic force micrsocopy
DLS	dynamic light scattering
DSC	differential scanning calorimetry
FTIR	Fourier transform infrared spectroscopy
GPC	gel permeation chromatography
UV/Vis	ultraviolet/visible
WAXS	wide-angle X-ray scattering
TGA	thermogravimetric analysis
LC-ESI-MS	liquid chromatography-electrospray ionization-mass spectrometry
NMR	nuclear magnetic resonance

6.3.2 materials

MeOH	methanol
DMF	N-dimethylformamide
THF	tetrahydrofuran
DMAc	dimethylacetamide
Tris	Tris(hydroxymethyl)aminomethane
FITC	fluoresceine isothiocyanate
PEO	poly(ethylene oxide)
PnBA	poly(n-butyl acrylate)
PCL	poly(ε-caprolactone)
PLGA	poly(lactic-co-glycolic acid)
PMMA	poly(methyl methacrylate)
PS	polystyrene
PPFPMA	poly(pentafluorophenyl methacrylate)
PLLA	Poly(L-lactide)

6.4 Ackknowledgements

I am very grateful to Prof. Markus Antonietti and Prof. Hans Börner for the supervision of my doctoral thesis. I especially, thank Prof. Börner is thanked for his enthusiasm and great support during the course of this work.

I would also like to thank the following collaborators for their contribution:

The high speed camera was generously provided by PCO AG, and support with the recording was provided by T. Bauersachs and S. Karpitschka. Different measurements were performed were by J. Bienias (Dr. D. Enke, Martin Luther University Halle-Wittenberg, Mercury porosimetry), Daniel Kluge (Prof. Andreas Fery, University Bayreuth, AFM mechanics), Dr. Michael Eder, (Dr. Ingo Burgert, MPIKG, tensile testing), Falko Pippig (Dr. Andreas Holländer, IAP, XPS), Dr. Peter Cernoch (DLS), and Dr. Stephan Schmidt (MPIKG, AFM electrostatic interaction). Assistance with crystallizations was provided by Dr. Helmut Cölfen, Dr. Andronico Neira (calcium carbonate) and Prof. Andreas Taubert, Mathias Junginger (University of Potsdam, calcium phosphate). Materials were provided by PD Dr. Patrick Theato (Mainz, PPFPMA synthesis) and, Dan Grünstein, Dr. Raghavendra Kikkeri (Prof. Peter Seeberger, sugar synthesis). Cell studies were performed by several people including, Björn Boysen, Beate Morgenstern, Katja Uhlig (Dr. Andreas Lankenau, IBMT, epithelial, L929, U2OS), Dr. Julien Polleux (murine fibroblast), June Jeon, Nicola Detta (Prof. Dietmar Hutmacher, chondrocyte, osteoblast), and Dr. Bernd Lepenies, Uwe Vogel, Maha Maglinao (Prof. Peter Seeberger, macrophages).

I am also indepted to the technicians in the institute are thanked for their support especially Jessica Brandt and Katharina Ostwald for polymer, peptide-synthesis and positive inspirations, and also G. Haselhoff and H. Pitas for their assistance in building the electrospinning setup.

I would also thank Maha, Robin, Florian, Johannes, Jing, Travis, Andreas, and Helmut for the revisions of my thesis.

Overall I want to thank my current and former colleagues of the peptide group, the Department of Colloid Chemistry, the rest of the MPI-KG members and my office mates for a pleasant working atmosphere, especially in Chez Briel. I would also like to thank The finishers, Erich C, the football and kicker team for enriching my academic life.

Financial support was given by the joined program of Max Planck Society & Fraunhofer Society (MPG-FhG Project on Bioactive Surfaces).

My last thanks go to my family and friends for their support and love. Stay groovy!

6.5 References

[1] R. Langer, J. P. Vacanti, *Science* **1993**, *260*, 920.

[2] M. P. Lutolf, J. A. Hubbell, *Nat. Biotechnol.* **2005**, *23*, 47.

[3] M. C. Branco, J. P. Schneider, *Acta Biomater.* **2009**, *5*, 817; V. Vogel, G. Baneyx, *Annu. Rev. Biomed. Eng.* **2003**, *5*, 441.

[4] E. S. Place, J. H. George, C. K. Williams, M. M. Stevens, *Chem. Soc. Rev.* **2009**, *38*, 1139.

[5] R. Langer, D. A. Tirrell, *Nature* **2004**, *428*, 487.

[6] I. Levental, P. C. Georges, P. A. Janmey, *Soft Matter* **2007**, *3*, 299.

[7] J. P. Spatz, B. Geiger, "Molecular engineering of cellular environments: Cell adhesion to nano-digital surfaces", in *Cell Mechanics*, Elsevier Academic Press Inc, San Diego, 2007, p. 89.

[8] A. J. Engler, S. Sen, H. L. Sweeney, D. E. Discher, *Cell* **2006**, *126*, 677.

[9] P. P. Girard, E. A. Cavalcanti-Adam, R. Kemkemer, J. P. Spatz, *Soft Matter* **2007**, *3*, 307.

[10] L. G. Griffith, M. A. Swartz, *Nat. Rev. Mol. Cell Biol.* **2006**, *7*, 211.

[11] E. Cukierman, R. Pankov, D. R. Stevens, K. M. Yamada, *Science* **2001**, *294*, 1708.

[12] M. M. Stevens, J. H. George, *Science* **2005**, *310*, 1135.

[13] V. Vogel, M. Sheetz, *Nat. Rev. Mol. Cell Biol.* **2006**, *7*, 265.

[14] M. Vanderrest, R. Garrone, *Faseb J.* **1991**, *5*, 2814; D. J. S. Hulmes, "The collagen superfamily - diverse structures and assemblies", in *Essays in Biochemistry, Vol 27*, Portland Press Ltd, London, 1992, p. 49.

[15] P. Fratzl, "Collagen: Structure and Mechanics", Springer, 2008 506.

[16] T. E. Hardingham, A. J. Fosang, *Faseb J.* **1992**, *6*, 861.

[17] E. Ruoslahti, *Annu. Rev. Biochem.* **1988**, *57*, 375.

[18] J. Engel, *Biochemistry* **1992**, *31*, 10643.

[19] J. Taipale, J. KeskiOja, *Faseb J.* **1997**, *11*, 51.

[20] C. D. Roskelley, A. Srebrow, M. J. Bissell, *Curr. Opin. Cell Biol.* **1995**, *7*, 736; J. R. Sanes, *Annu. Rev. Neurosci.* **1989**, *12*, 491.

[21] J. C. Adams, F. M. Watt, *Development* **1993**, *117*, 1183.

[22] J. C. Adams, *Cellular and Molecular Life Sciences* **2001**, *58*, 371; K. Burridge, M. Chrzanowska-Wodnicka, *Annu. Rev. Cell Dev. Biol.* **1996**, *12*, 463.

[23] G. Maheshwari, G. Brown, D. A. Lauffenburger, A. Wells, L. G. Griffith, *J. Cell Sci.* **2000**, *113*, 1677.

[24] S. P. Palecek, J. C. Loftus, M. H. Ginsberg, D. A. Lauffenburger, A. F. Horwitz, *Nature* **1997**, *385*, 537.

[25] B. M. Gumbiner, *Cell* **1996**, *84*, 345; D. J. Behonick, Z. Werb, *Mech. Dev.* **2003**, *120*, 1327; D. E. Discher, P. Janmey, Y. L. Wang, *Science* **2005**, *310*, 1139.

[26] M. Schena, D. Shalon, R. W. Davis, P. O. Brown, *Science* **1995**, *270*, 467.

[27] R. S. Kane, S. Takayama, E. Ostuni, D. E. Ingber, G. M. Whitesides, *Biomaterials* **1999**, *20*, 2363.

[28] J. L. de Paz, P. H. Seeberger, *QSAR & Comb. Sci.* **2006**, *25*, 1027.

[29] D. Lehnert, B. Wehrle-Haller, C. David, U. Weiland, C. Ballestrem, B. A. Imhof, M. Bastmeyer, *J. Cell Sci.* **2004**, *117*, 41; D. G. Anderson, S. Levenberg, R. Langer, *Nat. Biotechnol.* **2004**, *22*, 863.

[30] D. S. Ginger, H. Zhang, C. A. Mirkin, *Angew. Chem., Int. Ed.* **2004**, *43*, 30.

[31] C. Wei, A. Haroon, *Appl. Phys. Lett.* **1993**, *62*, 1499.

[32] K. von der Mark, J. Park, S. Bauer, P. Schmuki, *Cell Tissue Res.* **2010**, *339*, 131.

[33] C. J. Bettinger, R. Langer, J. T. Borenstein, *Angew. Chem., Int. Ed.* **2009**, *48*, 5406.

[34] M. J. Dalby, N. Gadegaard, R. Tare, A. Andar, M. O. Riehle, P. Herzyk, C. D. W. Wilkinson, R. O. C. Oreffo, *Nat. Mater.* **2007**, *6*, 997; C. J. Bettinger, Z. Zhang, S. Gerecht, J. T. Borenstein, R. Langer, *Adv. Mater.* **2008**, *20*, 99.

[35] A. Curtis, C. Wilkinson, A. Curtis, C. Wilkinson, *Mater. Today* **2001**, *4*, 22; C. S. Chen, M. Mrksich, S. Huang, G. M. Whitesides, D. E. Ingber, *Science* **1997**, *276*, 1425.

[36] A. Curtis, C. Wilkinson, *Biomaterials* **1997**, *18*, 1573.

[37] R. L. Price, K. Ellison, K. M. Haberstroh, T. J. Webster, *J. Biomed. Mater. Res. Part A* **2004**, *70A*, 129.

[38] O. Zinger, G. Zhao, Z. Schwartz, J. Simpson, M. Wieland, D. Landolt, B. Boyan, *Biomaterials* **2005**, *26*, 1837.

[39] S. J. Eichhorn, W. W. Sampson, *J. R. Soc. Interface* **2005**, *2*, 309.

[40] P. Friedl, *Curr. Opin. Cell Biol.* **2004**, *16*, 14.

[41] J. L. West, J. A. Hubbell, *Macromolecules* **1998**, *32*, 241.

[42] M. P. Lutolf, J. L. Lauer-Fields, H. G. Schmoekel, A. T. Metters, F. E. Weber, G. B. Fields, J. A. Hubbell, *Proc. Natl. Acad. Sci. U. S. A.* **2003**, *100*, 5413.

[43] Y. Li, T. Ma, D. A. Kniss, L. C. Lasky, S.-T. Yang, *Biotechnol. Prog.* **2001**, *17*, 935; D. W. Hutmacher, H. Singh, *Trends Biotechnol.* **2008**, *26*, 166.

[44] M. P. Lutolf, J. L. Lauer-Fields, H. G. Schmoekel, A. T. Metters, F. E. Weber, G. B. Fields, J. A. Hubbell, *Proc. Natl. Acad. Sci. U. S. A.* **2003**, *100*, 5413.

[45] C. D. Roskelley, P. Y. Desprez, M. J. Bissell, *Proc. Natl. Acad. Sci. U. S. A.* **1994**, *91*, 12378.

[46] V. Vogel, G. Baneyx, *Annu. Rev. Biomed. Eng.* **2003**, *5*, 441.

[47] T. Sun, D. Norton, R. J. McKean, J. W. Haycock, A. J. Ryan, S. MacNeil, *Biotechnol. Bioeng.* **2007**, *97*, 1318.

[48] Y. Yang, D. Bolikal, M. L. Becker, J. Kohn, D. N. Zeiger, J. C. G. Simon, *Adv. Mater.* **2008**, *20*, 2037.

[49] J. C. M. van Hest, D. A. Tirrell, *Chem. Commun.* **2001**, 1897.

[50] J. A. Hubbell, *Bio-Technology* **1995**, *13*, 565.

[51] A. Kikuchi, T. Okano, *J. Control. Release* **2005**, *101*, 69.

[52] R. O. Hynes, *Cell* **1992**, *69*, 11.

[53] E. Ruoslahti, M. D. Pierschbacher, *Science* **1987**, *238*, 491.

[54] S. P. Massia, J. A. Hubbell, *J. Cell Biol.* **1991**, *114*, 1089.

[55] W. A. Comisar, N. H. Kazmers, D. J. Mooney, J. J. Linderman, *Biomaterials* **2007**, *28*, 4409.

[56] A. B. Pratt, F. E. Weber, H. G. Schmoekel, R. Muller, J. A. Hubbell, *Biotechnol. Bioeng.* **2004**, *86*, 27.

[57] M. Ehrbar, S. M. Zeisberger, G. P. Raeber, J. A. Hubbell, C. Schnell, A. H. Zisch, *Biomaterials* **2008**, *29*, 1720.

[58] G. P. Chen, T. Ushida, T. Tateishi, *Biomaterials* **2001**, *22*, 2563; Q. L. Zhou, Y. H. Gong, C. Y. Gao, *J. Appl. Polym. Sci.* **2005**, *98*, 1373; M. H. Ho, P. Y. Kuo, H. J. Hsieh, T. Y. Hsien, L. T. Hou, J. Y. Lai, D. M. Wang, *Biomaterials* **2004**, *25*, 129; Q. P. Hou, D. W. Grijpma, J. Feijen, *Biomaterials* **2003**, *24*, 1937; J. J. Yoon, T. G. Park, *J. Biomed. Mater. Res.* **2001**, *55*, 401.

[59] D. Lickorish, L. Guan, J. E. Davies, *Biomaterials* **2007**, *28*, 1495.

[60] A. S. Goldstein, G. M. Zhu, G. E. Morris, R. K. Meszlenyi, A. G. Mikos, *Tissue Eng.* **1999**, *5*, 421.

[61] M. Groenewolt, M. Antonietti, S. Polarz, *Langmuir* **2004**, *20*, 7811.

[62] H. D. Kim, E. H. Bae, I. C. Kwon, R. R. Pal, J. D. Nam, D. S. Lee, *Biomaterials* **2004**, *25*, 2319.

[63] K. Whang, C. H. Thomas, K. E. Healy, G. Nuber, *Polymer* **1995**, *36*, 837; J. H. Degroot, A. J. Nijenhuis, P. Bruin, A. J. Pennings, R. P. H. Veth, J. Klompmaker, H. W. B. Jansen, *Colloid Polym.*

Sci. **1990**, *268*, 1073; H. Elema, J. H. Degroot, A. J. Nijenhuis, A. J. Pennings, R. P. H. Veth, J. Klompmaker, H. W. B. Jansen, *Colloid Polym. Sci.* **1990**, *268*, 1082.
[64] S. Förster, M. Antonietti, *Adv. Mater.* **1998**, *10*, 195; I. W. Hamley, *Nanotechnology* **2003**, *14*, R39.
[65] C. J. Hawker, T. P. Russell, *Mrs Bulletin* **2005**, *30*, 952.
[66] D. E. Discher, F. Ahmed, *Ann. Rev. Biomed. Eng.* **2006**, *8*, 323; X. S. Wang, G. Guerin, H. Wang, Y. S. Wang, I. Manners, M. A. Winnik, *Science* **2007**, *317*, 644; A. Aggeli, I. A. Nyrkova, M. Bell, R. Harding, L. Carrick, T. C. B. McLeish, A. N. Semenov, N. Boden, *Proc. Natl. Acad. Sci. U. S. A.* **2001**, *98*, 11857.
[67] C. E. MacPhee, D. N. Woolfson, *Curr. Opin. Solid State Mat. Sci.* **2004**, *8*, 141.
[68] J. D. Hartgerink, E. R. Zubarev, S. I. Stupp, *Curr. Opin. Solid State Mat. Sci.* **2001**, *5*, 355.
[69] S. G. Zhang, *Nat. Biotechnol.* **2003**, *21*, 1171.
[70] T. C. Holmes, *Trends Biotechnol.* **2002**, *20*, 16.
[71] R. Fairman, K. S. Akerfeldt, *Curr. Opin. Struct. Biol.* **2005**, *15*, 453.
[72] A. R. Hirst, B. Escuder, J. F. Miravet, D. K. Smith, *Angew. Chem., Int. Ed.* **2008**, *47*, 8002; D. N. Woolfson, M. G. Ryadnov, *Curr. Opin. Chem. Biol.* **2006**, *10*, 559; H. G. Börner, H. Schlaad, *Soft Matter* **2007**, *3*, 394; M. J. Webber, J. A. Kessler, S. I. Stupp, *J. Intern. Med.* **2010**, *267*, 71.
[73] H. G. Börner, *Prog. Polym. Sci.* **2009**, *34*, 811.
[74] K. Rajagopal, J. P. Schneider, *Curr. Opin. Struct. Biol.* **2004**, *14*, 480.
[75] A. Muenter, J. Hentschel, H. G. Börner, G. Brezesinski, *Langmuir* **2008**, *24*, 3306; H. G. Börner, *Macromol. Chem. Phys.* **2007**, *208*, 124; M. G. J. ten Cate, N. Severin, H. G. Börner, *Macromolecules* **2006**, *39*, 7831; H. Kühnle, H. G. Börner, *Angew. Chem., Int. Ed.* **2009**, *48*, 6431; J. M. Smeenk, M. B. J. Otten, J. Thies, D. A. Tirrell, H. G. Stunnenberg, J. C. M. van Hest, *Angew. Chem., Int. Ed.* **2005**, *44*, 1968.
[76] C. L. Nesloney, J. W. Kelly, *Bioorg. Med. Chem.* **1996**, *4*, 739; R. V. Ulijn, A. M. Smith, *Chem. Soc. Rev.* **2008**, *37*, 664; J. Kopecek, J. Y. Yang, *Acta Biomater.* **2009**, *5*, 805.
[77] S. G. Zhang, X. J. Zhao, *J. Mater. Chem.* **2004**, *14*, 2082.
[78] D. Papapostolou, E. H. C. Bromley, C. Bano, D. N. Woolfson, *J. Am. Chem. Soc.* **2008**, *130*, 5124.
[79] M. G. Ryadnov, D. N. Woolfson, *Nat. Mater.* **2003**, *2*, 329.
[80] D. Eckhardt, M. Groenewolt, E. Krause, H. G. Börner, *Chem. Commun.* **2005**, 2814.
[81] H. G. Börner, B. Smarsly, J. Hentschel, A. Rank, R. Schubert, Y. Geng, D. E. Discher, T. Hellweg, A. Brandt, *Macromolecules* **2008**, *41*, 1430.
[82] J. Hentschel, E. Krause, H. G. Börner, *J. Am. Chem. Soc.* **2006**, *128* 7722
[83] M. G. Ryadnov, D. N. Woolfson, *Angew. Chem., Int. Ed.* **2003**, *42*, 3021.
[84] D. Papapostolou, A. M. Smith, E. D. T. Atkins, S. J. Oliver, M. G. Ryadnov, L. C. Serpell, D. N. Woolfson, *Proc. Natl. Acad. Sci. U. S. A.* **2007**, *104*, 10853.
[85] J. F. Smith, T. P. J. Knowles, C. M. Dobson, C. E. MacPhee, M. E. Welland, *Proc. Natl. Acad. Sci. U. S. A.* **2006**, *103*, 15806.
[86] G. H. Altman, F. Diaz, C. Jakuba, T. Calabro, R. L. Horan, J. S. Chen, H. Lu, J. Richmond, D. L. Kaplan, *Biomaterials* **2003**, *24*, 401.
[87] M. O. Guler, L. Hsu, S. Soukasene, D. A. Harrington, J. F. Hulvat, S. I. Stupp, *Biomacromolecules* **2006**, *7*, 1855.
[88] G. A. Silva, C. Czeisler, K. L. Niece, E. Beniash, D. A. Harrington, J. A. Kessler, S. I. Stupp, *Science* **2004**, *303*, 1352.
[89] Y. Ma, H. G. Börner, J. Hartmann, H. Cölfen, *Chem. Eur. J.* **2006**, *12*, 7882 ; M. G. Page, N. Nassif, H. G. Börner, M. Antonietti, H. Cölfen, *Cryst. Growth Des.* **2008**, *8*, 1792; T. Wang, A. Verch, H. G. Börner, H. Cölfen, A. Antonietti, *J. Ceram. Soc. Jpn.* **2009**, *117*, 221.

[90] S. Kessel, A. Thomas, H. G. Börner, *Angew. Chem., Int. Ed.* **2007**, *46*, 9023; S. Kessel, H. G. Börner, *Macromol. Rapid. Commun.* **2008**, *29*, 419.

[91] S. Kessel, H. G. Börner, *Macromol. Rapid Commun.* **2008**, *29*, 316.

[92] J. D. Hartgerink, E. Beniash, S. I. Stupp, *Science* **2001**, *294*, 1684.

[93] K. Rajangam, M. S. Arnold, M. A. Rocco, S. I. Stupp, *Biomaterials* **2008**, *29*, 3298.

[94] M. W. Tibbitt, K. S. Anseth, *Biotechnol. Bioeng.* **2009**, *103*, 655.

[95] J. Hentschel, H. G. Börner, *J. Am. Chem. Soc.* **2006**, *128*, 14142.

[96] K. Y. Lee, D. J. Mooney, *Chem. Rev.* **2001**, *101*, 1869.

[97] J. Hentschel, M. G. J. ten Cate, H. G. Börner, *Macromolecules* **2007**, *40*, 9224.

[98] M. M. Stevens, *Mater. Today* **2008**, *11*, 18; D. Eyrich, F. Brandl, B. Appel, H. Wiese, G. Maier, M. Wenzel, R. Staudenmaier, A. Goepferich, T. Blunk, *Biomaterials* **2007**, *28*, 55.

[99] B. Rihova, *Adv. Drug Deliv. Rev.* **2000**, *42*, 65; G. Orive, R. M. Hernandez, A. R. Gascon, A. Dominguez-Gil, J. L. Pedraz, *Curr. Opin. Biotechnol.* **2003**, *14*, 659; G. Orive, R. M. Hernandez, A. R. Gascon, R. Calafiore, T. M. S. Chang, P. de Vos, G. Hortelano, D. Hunkeler, I. Lacik, J. L. Pedraz, *Trends Biotechnol.* **2004**, *22*, 87.

[100] J. Kisiday, M. Jin, B. Kurz, H. Hung, C. Semino, S. Zhang, A. J. Grodzinsky, *Proc. Natl. Acad. Sci. U. S. A.* **2002**, *99*, 9996.

[101] D. J. Pochan, J. P. Schneider, J. Kretsinger, B. Ozbas, K. Rajagopal, L. Haines, *J. Am. Chem. Soc.* **2003**, *125*, 11802; J. P. Schneider, D. J. Pochan, B. Ozbas, K. Rajagopal, L. Pakstis, J. Kretsinger, *J. Am. Chem. Soc.* **2002**, *124*, 15030.

[102] K. Rajagopal, M. S. Lamm, L. A. Haines-Butterick, D. J. Pochan, J. P. Schneider, *Biomacromolecules* **2009**, *10*, 2619.

[103] R. A. Hule, R. P. Nagarkar, B. Hammouda, J. P. Schneider, D. J. Pochan, *Macromolecules* **2009**, *42*, 7137.

[104] S. J. Hollister, C. Y. Lin, *Comput. Meth. Appl. Mech. Eng.* **2007**, *196*, 2991.

[105] C. Y. Lin, N. Kikuchi, S. J. Hollister, *J. Biomech.* **2004**, *37*, 623.

[106] S. J. Hollister, *Nat. Mater.* **2005**, *4*, 518.

[107] R. W. Goulet, S. A. Goldstein, M. J. Ciarelli, J. L. Kuhn, M. B. Brown, L. A. Feldkamp, *J. Biomech.* **1994**, *27*, 375.

[108] S. J. Hollister, *Nat. Mater.* **2005**, *4*, 518; D. W. Hutmacher, T. Schantz, I. Zein, K. W. Ng, S. H. Teoh, K. C. Tan, *J. Biomed. Mater. Res.* **2001**, *55*, 203.

[109] R. A. Barry, R. F. Shepherd, J. N. Hanson, R. G. Nuzzo, P. Wiltzius, J. A. Lewis, *Adv. Mater.* **2009**, *21*, 2407.

[110] M. N. Cooke, J. P. Fisher, D. Dean, C. Rimnac, A. G. Mikos, *J. Biomed. Mater. Res. Part B* **2003**, *64B*, 65.

[111] J. M. Williams, A. Adewunmi, R. M. Schek, C. L. Flanagan, P. H. Krebsbach, S. E. Feinberg, S. J. Hollister, S. Das, *Biomaterials* **2005**, *26*, 4817.

[112] S. S. Kim, H. Utsunomiya, J. A. Koski, B. M. Wu, M. J. Cima, J. Sohn, K. Mukai, L. G. Griffith, J. P. Vacanti, *Ann. Surg.* **1998**, *228*, 8; C. X. F. Lam, X. M. Mo, S. H. Teoh, D. W. Hutmacher, *Mater. Sci. Eng. C-Biomimetic Supramol. Syst.* **2002**, *20*, 49.

[113] D. W. Hutmacher, T. Schantz, I. Zein, K. W. Ng, S. H. Teoh, K. C. Tan, *J. Biomed. Mater. Res.* **2001**, *55*, 203.

[114] J. Malda, T. B. F. Woodfield, F. van der Vloodt, F. K. Kooy, D. E. Martens, J. Tramper, C. A. van Blitterswijk, J. Riesle, *Biomaterials* **2004**, *25*, 5773.

[115] A. Yeo, W. J. Wong, H. H. Khoo, S. H. Teoh, *J. Biomed. Mater. Res. Part A*, *92A*, 311.

[116] X. Tao, J. Joyce, G. Cassie, H. J. J., B. Thomas, *Biomaterials* **2005**, *26*, 93.

[117] R. Landers, U. Hubner, R. Schmelzeisen, R. Mulhaupt, *Biomaterials* **2002**, *23*, 4437.

[118] S. Kessel, H. G. Börner, *Macromol. Rapid Commun.* **2008**, *29*, 316.

[119] D. W. Hutmacher, S. Cool, *J. Cell. Mol. Med.* **2007**, *11*, 654.

[120] B. Rai, S. H. Teoh, D. W. Hutmacher, T. Cao, K. H. Ho, *Biomaterials* **2005**, *26*, 3739.

[121] S. Ramakrishna, K. Fujihara, W.-E. Teo, T.-C. Lim, Z. Ma, "*An introduction to Electrospinning and Nanofibers*", World Scientific Publishing Co. Pvt. Ltd., Singapore, 2005, p. 275.

[122] A. Greiner, J. H. Wendorff, *Angew. Chem. Int. Ed.* **2007**, *46*, 5670.

[123] M. M. Hohman, M. Shin, G. Rutledge, M. P. Brenner, *Phys. Fluids* **2001**, *13*, 2221; A. L. Yarin, S. Koombhongse, D. H. Reneker, *J. Appl. Phys.* **2001**, *90*, 4836.

[124] M. G. McKee, G. L. Wilkes, R. H. Colby, T. E. Long, *Macromolecules* **2004**, *37*, 1760.

[125] Z. C. Sun, E. Zussman, A. L. Yarin, J. H. Wendorff, A. Greiner, *Adv. Mater.* **2003**, *15*, 1929.

[126] M. Bognitzki, W. Czado, T. Frese, A. Schaper, M. Hellwig, M. Steinhart, A. Greiner, J. H. Wendorff, *Adv. Mater.* **2001**, *13*, 70.

[127] Y. Dror, W. Salalha, R. Avrahami, E. Zussman, A. L. Yarin, R. Dersch, A. Greiner, J. H. Wendorff, *Small* **2007**, *3*, 1064.

[128] C. L. Pai, M. C. Boyce, G. C. Rutledge, *Macromolecules* **2009**, *42*, 2102.

[129] S. Koombhongse, W. X. Liu, D. H. Reneker, *J. Polym. Sci. Part B: Polym. Phys.* **2001**, *39*, 2598.

[130] S. L. Chen, H. Q. Hou, P. Hu, J. H. Wendorff, A. Greiner, S. Agarwal, *Macromol. Mater. Eng.* **2009**, *294*, 265.

[131] A. Holzmeister, A. Greiner, J. H. Wendorff, *Polym. Eng. Sci.* **2009**, *49*, 148.

[132] W. E. Teo, S. Ramakrishna, *Nanotechnology* **2006**, R89; D. Li, Y. L. Wang, Y. N. Xia, *Nano Lett.* **2003**, *3*, 1167.

[133] S. Patel, K. Kurpinski, R. Quigley, H. F. Gao, B. S. Hsiao, M. M. Poo, S. Li, *Nano Lett.* **2007**, *7*, 2122.

[134] C. Hellmann, J. Belardi, R. Dersch, A. Greiner, J. H. Wendorff, S. Bahnmueller, *Polymer* **2009**, *50*, 1197.

[135] O. O. Dosunmu, G. G. Chase, W. Kataphinan, D. H. Reneker, *Nanotechnology* **2006**, *17*, 1123; J. S. Varabhas, G. G. Chase, D. H. Reneker, *Polymer* **2008**, *49*, 4226.

[136] U. Boudriot, R. Dersch, A. Greiner, J. H. Wendorff, *Artificial Org.* **2006**, *30*, 785; G. T. Christopherson, H. Song, H. Q. Mao, *Biomaterials* **2009**, *30*, 556.

[137] X. M. Mo, C. Y. Xu, M. Kotaki, S. Ramakrishna, *Biomaterials* **2004**, *25*, 1883.

[138] I. K. Kwon, S. Kidoaki, T. Matsuda, *Biomaterials* **2005**, *26*, 3929.

[139] J. Johnson, M. O. Nowicki, C. H. Lee, E. A. Chiocca, M. S. Viapiano, S. E. Lawler, J. J. Lannutti, *Tissue Eng. Part C* **2009**, *15*, 531.

[140] C. H. Lee, H. J. Shin, I. H. Cho, Y. M. Kang, I. A. Kim, K. D. Park, J. W. Shin, *Biomaterials* **2005**, *26*, 1261.

[141] C. Y. Xu, F. Yang, S. Wang, S. Ramakrishna, *J. Biomed. Mater. Res. Part A* **2004**, *71A*, 154.

[142] A. S. Badami, M. R. Kreke, M. S. Thompson, J. S. Riffle, A. S. Goldstein, *Biomaterials* **2006**, *27*, 596.

[143] J. L. Lowery, N. Datta, G. C. Rutledge, *Biomaterials* **2010**, *31*, 491.

[144] A. Thorvaldsson, H. Stenhamre, P. Gatenholm, P. Walkenstrom, *Biomacromolecules* **2008**, *9*, 1044.

[145] A. K. Ekaputra, G. D. Prestwich, S. M. Cool, D. W. Hutmacher, *Biomacromolecules* **2008**, *9*, 2097.

[146] Q. P. Pham, U. Sharma, A. G. Mikos, *Biomacromolecules* **2006**, *7*, 2796.

[147] A. Holzmeister, M. Rudisile, A. Greiner, J. H. Wendorff, *Eur. Polym. J.* **2007**, *43*, 4859.

[148] B. M. Baker, A. O. Gee, R. B. Metter, A. S. Nathan, R. A. Marklein, J. A. Burdick, R. L. Mauck, *Biomaterials* **2008**, *29*, 2348.

[149] J. Nam, Y. Huang, S. Agarwal, J. Lannutti, *Tissue Eng.* **2007**, *13*, 2249.

[150] S. In Jeong, S. Y. Kim, S. K. Cho, M. S. Chong, K. S. Kim, H. Kim, S. B. Lee, Y. M. Lee, *Biomaterials* **2007**, *28*, 1115.
[151] G. Kim, W. Kim, *J. Biomed. Mater. Res.* **2007**, *81B*, 104.
[152] M. Simonet, O. D. Schneider, P. Neuenschwander, W. J. Stark, *Polym. Eng. Sci.* **2007**, *47*, 2020.
[153] A. Townsend-Nicholson, S. N. Jayasinghe, *Biomacromolecules* **2006**, *7*, 3364.
[154] X. C. Yang, J. D. Shah, H. J. Wang, *Tissue Eng. Part A* **2009**, *15*, 945.
[155] D. I. Zeugolis, S. T. Khew, E. S. Y. Yew, A. K. Ekaputra, Y. W. Tong, L. Y. L. Yung, D. W. Hutmacher, C. Sheppard, M. Raghunath, *Biomaterials* **2008**, *29*, 2293.
[156] N. Bhattarai, D. Edmondson, O. Veiseh, F. A. Matsen, M. Q. Zhang, *Biomaterials* **2005**, *26*, 6176.
[157] C. S. Reddy, A. Arinstein, R. Avrahami, E. Zussman, *J. Mater. Chem.* **2009**, *19*, 7198.
[158] S. Kidoaki, I. K. Kwon, T. Matsuda, *Biomaterials* **2005**, *26*, 37.
[159] X. Y. Sun, R. Shankar, H. G. Borner, T. K. Ghosh, R. J. Spontak, *Adv. Mater.* **2007**, *19*, 87.
[160] M. L. Ma, K. Titievsky, E. L. Thomas, G. C. Rutledge, *Nano Lett.* **2009**, *9*, 1678; V. Kalra, J. Lee, J. H. Lee, S. G. Lee, M. Marquez, U. Wiesner, Y. L. Joo, *Small* **2008**, *4*, 2067.
[161] X. L. Xu, L. X. Yang, X. Y. Xu, X. Wang, X. S. Chen, Q. Z. Liang, J. Zeng, X. B. Jing, *J. Control. Release* **2005**, *108*, 33; J. C. Sy, A. S. Klemm, V. P. Shastri, *Adv. Mater.* **2009**, *21*, 1814.
[162] H. S. Yoo, T. G. Kim, T. G. Park, *Adv. Drug Deliv. Rev.* **2009**, *61*, 1033; D. Liang, B. S. Hsiao, B. Chu, *Adv. Drug Deliv. Rev.* **2007**, *59*, 1392.
[163] T. G. Kim, T. G. Park, *Tissue Eng.* **2006**, *12*, 221.
[164] K. C. Krogman, J. L. Lowery, N. S. Zacharia, G. C. Rutledge, P. T. Hammond, *Nat. Mater.* **2009**, *8*, 512.
[165] M. Schindler, I. Ahmed, J. Kamal, A. Nur-E-Kamal, T. H. Grafe, H. Y. Chung, S. Meiners, *Biomaterials* **2005**, *26*, 5624.
[166] X. Li, J. Xie, J. Lipner, X. Yuan, S. Thomopoulos, Y. Xia, *Nano Lett.* **2009**, *9*, 2763.
[167] M. E. Davis, J. P. M. Motion, D. A. Narmoneva, T. Takahashi, D. Hakuno, R. D. Kamm, S. G. Zhang, R. T. Lee, *Circulation* **2005**, *111*, 442.
[168] W. Hu, Z.-M. Huang, *Polym. Int.* **2009**, *59*, 92.
[169] X. S. Li, C. Yao, F. Q. Sun, T. Y. Song, Y. H. Li, Y. P. Pu, *J. Appl. Polym. Sci.* **2008**, *107*, 3756.
[170] F. T. Moutos, L. E. Freed, F. Guilak, *Nat. Mater.* **2007**, *6*, 162.
[171] D. Briggs, M. P. Seah, "*Practical surface analysis by Auger and x-ray photoelectron spectroscopy*", John Wiley & Sons Ltd., 1990.
[172] D. E. N. J. I. Goldstein, P. Echlin, D. C. Joy, C. Fiori, E. Lifshin, "*Scanning electron microscopy and x-ray microanalysis. A text for biologists, materials scientists and geologists*", Plenum Press, 1981.
[173] G. Binnig, C. F. Quate, C. Gerber, *Phys. Rev. Lett.* **1986**, *56*, 930.
[174] W. A. Ducker, T. J. Senden, R. M. Pashley, *Nature* **1991**, *353*, 239.
[175] C. M. Mate, G. M. McClelland, R. Erlandsson, S. Chiang, *Phys. Rev. Lett.* **1987**, *59*, 1942.
[176] G. C. Rutledge, J. L. Lowery, C. L. Pai, *J. Eng. Fiber Fabr.* **2009**, *4*, 1.
[177] R. Pirard, S. Blacher, F. Brouers, J. P. Pirard, *J. Mater. Res.* **1995**, *10*, 2114.
[178] H. Yoshimoto, Y. M. Shin, H. Terai, J. P. Vacanti, *Biomaterials* **2003**, *24*, 2077.
[179] A. Lendlein, R. Langer, *Science* **2002**, *296*, 1673.
[180] C. L. Casper, J. S. Stephens, N. G. Tassi, D. B. Chase, J. F. Rabolt, *Macromolecules* **2004**, *37*, 573.
[181] H. Fong, I. Chun, D. H. Reneker, *Polymer* **1999**, *40*, 4585.
[182] M. H. Moses, S. Michael, R. Gregory, P. B. Michael, *Phys. Fluids* **2001**, *13*, 2221.
[183] G. C. Rutledge, S. V. Fridrikh, *Adv. Drug Delivery Rev.* **2007**, *59*, 1384.

[184] L. Rayleigh, *Proc. London Math. Soc.* **1878**, *s1-10*, 4.
[185] Z. W. Ma, W. He, T. Yong, S. Ramakrishna, *Tissue Eng.* **2005**, *11*, 1149.
[186] C. Li, L. M. Qi, *Angew. Chem.-Int. Edit.* **2008**, *47*, 2388.
[187] E. Loste, R. J. Park, J. Warren, F. C. Meldrum, *Adv. Funct. Mater.* **2004**, *14*, 1211.
[188] K. H. Lee, H. Y. Kim, M. S. Khil, Y. M. Ra, D. R. Lee, *Polymer* **2003**, *44*, 1287.
[189] Y. Oaki, S. Kajiyama, T. Nishimura, H. Imai, T. Kato, *Adv. Mater.* **2008**, *20*, 3633.
[190] Y. Abe, T. Kokubo, T. Yamamuro, *J. Mater. Sci.-Mater. Med.* **1990**, *1*, 233.
[191] S. Schweizer, A. Taubert, *Macromol. Biosci.* **2007**, *7*, 1085; M. J. Larsen, S. J. Jensen, *Arch. Oral Biol.* **1989**, *34*, 963.
[192] A. C. Tas, S. B. Bhaduri, *J. Mater. Res.* **2004**, *19*, 2742.
[193] F. Yang, J. G. C. Wolke, J. A. Jansen, *Chem. Eng. J.* **2008**, *137*, 154.
[194] M. Ngiam, S. Liao, A. J. Patil, Z. Cheng, C. K. Chan, S. Ramakrishna, *Bone* **2009**, *45*, 4.
[195] A. Shkilnyy, J. Brandt, A. Mantion, O. Paris, H. Schlaad, A. Taubert, *Chem. Mat.* **2009**, *21*, 1572.
[196] W.-J. Li, C. T. Laurencin, E. J. Caterson, R. S. Tuan, F. K. Ko, *J. Biomed. Mater. Res.* **2002**, *60*, 613; U. Boudriot, R. Dersch, A. Greiner, J. H. Wendorff, *Artificial Organs* **2006**, *30*, 785.
[197] R. W. Farndale, D. J. Buttle, A. J. Barrett, *Biochim. Biophys. Acta* **1986**, *883*, 173.
[198] C. X. F. Lam, S. H. Teoh, D. W. Hutmacher, *Polym. Int.* **2007**, *56*, 718.
[199] X. H. Zong, S. F. Ran, K. S. Kim, D. F. Fang, B. S. Hsiao, B. Chu, *Biomacromolecules* **2003**, *4*, 416.
[200] R. B. Merrifield, *J. Am. Chem. Soc.* **1963**, *85*, 2149.
[201] S. S. Ghosh, P. M. Kao, A. W. McCue, H. L. Chappelle, *Bioconjugate Chem.* **1990**, *1*, 71.
[202] L. F. Wang, C. L. Pai, M. C. Boyce, G. C. Rutledge, *Appl. Phys. Lett.* **2009**, *94*, 3.
[203] G. A. Parks, *Chem. Rev.* **1965**, *65*, 177.
[204] M. Eberhardt, R. Mruk, R. Zentel, P. Theato, *Eur. Polym. J.* **2005**, *41*, 1569.
[205] S. T. Yang, S. Y. Shin, C. W. Lee, Y. C. Kim, K. S. Hahm, J. I. Kim, *FEBS Lett.* **2003**, *540*, 229.
[206] S. I. Miller, R. K. Ernst, M. W. Bader, *Nat. Rev. Microbiol.* **2005**, *3*, 36.
[207] M. E. Taylor, J. T. Conary, M. R. Lennartz, P. D. Stahl, K. Drickamer, *J. Biol. Chem.* **1990**, *265*, 12156.
[208] I. Takata, K. Chida, M. R. Gordon, Q. N. Myrvik, M. J. Ricardo, L. S. Kucera, *J. Leukoc. Biol.* **1987**, *41*, 248; Y. Shimizu, H. Takagi, T. Nakayama, K. Yamakami, T. Tadakuma, N. Yokoyama, N. Kojima, *Parasite Immunol.* **2007**, *29*, 229; K. Un, S. Kawakami, R. Suzuki, K. Maruyama, F. Yamashita, M. Hashida, *Hum. Gene Ther.* **2010**, *21*, 65.
[209] Y. F. Zhou, V. Sae-Lim, A. M. Chou, D. W. Hutmacher, T. M. Lim, *J. Biomed. Mater. Res. Part A* **2006**, *78A*, 183.